Correlation of electron and x-ray spectroscopies in nanoscale systems

Angela Erin Goode

Department of Materials
Imperial College London

This thesis is submitted in fulfilment of the requirements for
the degree of Doctor of Philosophy (PhD), Imperial College London

© Angela Erin Goode, 2012

Declaration of originality

I declare that this work is my own and that any references to other work are appropriately referenced. Some of the work in this thesis has been published in the following journal article.

Angela E. Goode , James M. Perkins , Ann Sandison , Chithra Karunakaran , Huikai Cheng , David Wall , John A. Skinner , Alister J. Hart , Alexandra E. Porter , David W. McComb and Mary P. Ryan *Chemical speciation of nanoparticles surrounding metal-on-metal hips,* **Chem. Commun**., 48, 8335-8337 (2012).

Abstract

The huge growth in nanotechnology brings with it an increasing need for techniques capable of structural and chemical analysis on the nanoscale. Two such techniques are electron energy-loss spectroscopy in the scanning transmission electron microscope (STEM-EELS) and x-ray absorption spectroscopy in the scanning transmission x-ray microscope (STXM-XAS). Despite the different probe-specimen interactions of EELS and XAS, these techniques both excite transitions from core states into unoccupied excited states, providing remarkably similar chemical information, but with different spatial and spectral resolutions, as well as different electron/photon induced damage properties.

Due to advances in the fabrication of diffractive x-ray optics, soft x-ray probes in the STXM can now achieve ~15 nm spatial resolution, while the STEM probe can routinely reach sub-nanometre dimensions. At the same time, the spectral performance of EELS is becoming more competitive with the ~0.1 eV resolutions of x-ray instruments, due to the development of monochromators in the electron microscope. While the spatial and spectral performances of these two techniques are continually converging, the gaps which still exist may be bridged by employing a correlative approach.

The motivation of this thesis is to apply both STEM-EELS and STXM-XAS to a range of nanoscale systems, and to investigate the benefits and limitations of this correlative approach. In order to understand the biodegradation of carbon nanotubes (CNTs), spectral signatures corresponding to graphitic carbon have been used to map CNT aggregates within the cellular environment. The nature and distribution of functional groups on oxidised CNTs have also been characterised using EELS, and compared to XAS data from the literature. Lastly, wear debris generated from CoCr hip prostheses has been investigated within explanted tissue. For the first time, detailed chemical analysis was performed of debris particles, which were found to be composed of mainly oxidised Cr as well as trace amounts of oxidised Co. Additionally, some nanoparticles were observed to have metallic Co and Cr cores.

Acknowledgements

First and foremost I would like to thank my supervisors, Prof. Mary Ryan, Dr. Alexandra Porter and Prof. David McComb for their patient guidance throughout my PhD. I have learnt so much over the last few years, and I am truly grateful for their support and continued enthusiasm. I wish to thank Dr. Mahmoud Ardakani and Dr. Ecaterina Ware for their wonderful technical support and kindness. I owe huge thanks to Dr. James Perkins, Dr. Catriona McGilvery, Dr. Liam Spillane, Dr. Sehban Husain, Dr. Ai Leen Koh and Dr. Vaso Tileli, all of whom have given up many hours of their time to ensure I received extensive training on the Titan microscope, not to mention their dedication at answering out-of-hours phone requests for Titan support.

I would like to thank Mr. Alister Hart and his group in the Faculty of Medicine, Imperial College London, for providing wear samples, and for many helpful discussions. I have received a lot of advice and assistance on all matters relating to carbon nanotubes from Prof. Milo Shaffer and his group in the Department of Chemistry, Imperial College London. In particular I would like to thank Dr. Robert Menzel and Dr. Ainara Garcia for being ever-willing to answer my questions, and Dr. Shane Bergin and Dr. Shu Chen for all their help preparing samples, and for teaching me the ways of the chemistry lab. I also wish to thank Prof. Valeria Nicolosi, now at Trinity College Dublin, who kindly shared her protocol for grid preparation. I am grateful to Dr. Jeremy Skepper and Dr. Karin Muller at the University of Cambridge who have provided macrophage samples, and given invaluable advice. I also wish to thank the synchrotron scientists, Dr. Sue Wirick at Brookhaven National Laboratory and Dr. Chithra Karunakaran, Dr. Yingshen Lu and Prof. Adam Hitchcock at the Canadian Light Source for their excellent support and expertise. I acknowledge Prof. Kostas Kostarelos of UCL for providing functionalised nanotube samples.

I would like to thank the members of the Electron Microscopy group at Imperial College, as well as Weili, Hannah, Preetma and Naidu, who have all been a constant source of support, friendship, and tea. It has been a lot of fun to work with you all! I am also grateful to Fiona, Sonya and Rob for empathising with their own PhD experiences, to Priyan for much needed cinematic distractions, and of course to Shamini, who has been a wonderful flatmate and friend.

Mum and Ian — for your unwavering love and support, despite my refusal to get a proper job, I am more grateful than I can say. I hope this makes you proud. Ravi — for cake at the high points, hugs at the low points, and your encouragement and understanding throughout, thank you.

Table of Contents

List of Figures 9
List of Tables 17
1. Introduction 18
2. Probing electronic interactions with electrons and x-rays 21
2.1. Electron-sample interactions in the electron microscope 21
2.1.1. Elastic scattering 21
2.1.2. Inelastic scattering and Bethe theory 22
2.2. Photon-sample interactions in the x-ray microscope 24
2.3. The spectrum 25
2.3.1. Origin of fine structure 26
2.3.2. Dipole selection rules 27
2.3.3. Determination of species, valence and coordination 28
3. Literature Review 29
3.1. Introduction to STXM and EELS 29
3.2. Spatial Resolution 31
3.3. Spectral resolution 33
3.4. Elemental quantification and detection limits 35
3.5. Bonding states and fine structure 36
3.6. In situ measurements 39
3.6.1. Gas cells and Fischer-Tropsch catalysts 39
3.6.2. Liquid cells and biofilms 41
3.7. Damage studies 43
3.8. The carbon K edge 45
3.9. Summary 50
4. Instrumentation 51
4.1. Instrumentation for EELS 51
4.1.1. The transmission electron microscope 51
4.1.2. Contrast 53
4.1.3. TEM hardware 55
4.1.4. FEI Titan hardware 59
4.1.5. EELS Spectrum Image Acquisition 66
4.1.6. EELS Processing 67

4.2. STXM-XAS 67
4.2.1. Synchrotrons 68
4.2.2. Monochromation in the beamline 69
4.2.3. NSLS Beamline X1A1 69
4.2.4. CLS beamline 10ID1 (SM spectromicroscopy) 70
4.2.5. Zone Plates 71
4.2.6. The scanning transmission x-ray microscope 73
4.2.7. STXM-XAS data acquisition 74
4.3. Processing large datasets 76
4.3.1. Singular value decomposition 76
4.3.2. Principal component analysis 77
5. Fate of MWNTs in macrophage cells 79
5.1. Introduction 79
5.2. Bonding and the Carbon K edge 81
5.2.1. Linear combinations of atomic orbitals 82
5.2.2. Hybridisation 82
5.2.3. Symmetry considerations 83
5.2.4. Electronic structure of graphitic carbon 83
5.3. Sample History 85
5.3.1. Carbon nanotube functionalisation 85
5.3.2. Cell exposure 86
5.3.3. STXM-XAS 86
5.3.4. STEM-EELS 87
5.4. Results 87
5.4.1. Characterisation of unexposed a-MWNTs 87
5.4.2. STXM-XAS results 89
5.4.3. STEM-EELS Results 97
5.4.4. Comparison of EELS and XAS 102
5.5. Discussion 105
5.5.1. Characterisation of a-MWNTs 105
5.5.2. Uptake and Distribution of a-MWNTs 106
5.5.3. Fate of a-MWNTs in macrophage cells 106
5.5.4. EELS versus XAS 107
5.6. Conclusions 109

6. Functionalised Carbon Nanotubes 110
6.1. Introduction 110
6.1.1. Identification of functional groups 111
6.1.2. Distribution of functional groups 113
6.2. The Carbon K edge 115
6.2.1. Orientation dependence 115
6.2.2. Chemical Shifts 117
6.3. Methods 118
6.3.1. Sample history 118
6.3.2. TEM grid preparation 119
6.3.3. Microscope parameters 120
6.4. Results 122
6.4.1. EELS of ox-MWNTs 122
6.4.2. Comparison with XANES literature 123
6.4.3. Spatial distribution of peak B' 125
6.4.4. Statistical analysis of peak B' 130
6.5. Discussion 131
6.5.1. Assignment of peak B' 132
6.5.2. Spatial distribution of peak B' 132
6.5.3. Frequency of occurrence of peak B' 133
6.6. Conclusions 134
7. Characterising wear debris from MOM hips 135
7.1. Introduction 135
7.1.1. Morphological characterisation 136
7.1.2. Chemical characterisation 136
7.2. The transition metal $L_{2,3}$ edge 137
7.3. Sample History and Methods 139
7.3.1. Wear debris identification 140
7.3.2. STXM-XAS 140
7.3.3. STEM-EELS 140
7.3.4. STEM-EDX methods 143
7.4. Results 143
7.4.1. Locating wear debris 143
7.4.2. STXM-XAS results 146

7.4.3. STEM-EELS results 151
7.4.4. EELS Quantification 154
7.5. Discussion 157
7.6. Conclusions 160
8. Conclusions and further work 162
8.1. Fate of MWNTs in cells 162
8.2. Functionalised CNTs 164
8.3. MOM hip debris 165
8.4. Correlative EELS/XAS 166
Appendix 1 167
References 169

List of Figures

Figure 2.1 Wavevector diagram showing the incident electron wavevector $\mathbf{k_0}$, and the transmitted wavevector $\mathbf{k_f}$ which has been scattered through an angle θ. The scattering vector **q** is defined as $\mathbf{q} = \mathbf{k0} - \mathbf{kf}$. Reproduced from [7]. 22
Figure 2.2 Diagram showing the features present in a typical EEL spectrum. Reproduced from [7]... 25
Figure 2.3 Schematic showing the nomenclature of different inner-shell ionization edges. Adapted from [7, 8]. 26
Figure 2.4 Diagrams showing some basic edge shapes, calculated using a free atom model: (a) the K edge has a saw-tooth shape, and (b) some $L_{2,3}$ edges and $M_{4,5}$ edges display a delayed maximum. (c) Bound states have been included to recreate the shape of white lines seen in 3d and 4d transition metals. Adapted from [7]. 26
Figure 2.5 Diagram showing that the near edge fine structure of an inner-shell ionization edge is related to the density of states above the Fermi level E_F. Reproduced from [7]. 27
Figure 3.1 Schematic diagrams of (a) STXM-XAS and (b) STEM-EELS. 30
Figure 3.2 Schematic diagram showing the order of data acquisition in a) a STXM "stack", in which images at different photon energies are acquired sequentially, and b) an EELS "spectrum image" in which a whole EEL spectrum is acquired at a given position before the probe is moved, and the spectrum acquisition repeated. 31
Figure 3.3 Graph of the evolution of spatial resolution in light and electron microscopy. Adapted from [19]. 32
Figure 3.4 Fine structure at the Mn $L_{2,3}$ edges of various Mn oxides show good agreement between EELS (a) and XAS (b) spectra. Adapted from [6]. 34
Figure 3.5 Chemical maps of gadolinium (red) and carbon (blue) calculated from EELS data of Gd-metallofullerene molecules confined in a SWNT. Points a, b and i indicate single Gd atoms. From [39]. 36
Figure 3.6 (a) EELS spectrum from a 1.2nm point on a single nanotube. The area of the shaded region was used to calculate the concentration of oxygen present. (b) XAS spectrum of nanotube (solid line) and a bulk V_2O_5 reference (dashed line) From [43]. 37
Figure 3.7 Nitrogen K edge XAS spectra of N-CNTs before and after annealing (a), and spectra showing the peak at 401 eV in more detail (b). This feature can be deconvoluted into seven peaks, which is indicative of gaseous nitrogen. From [46]. 38
Figure 3.8 STXM chemical maps of a group of N-CNTs, showing the presence of gaseous N_2 (red) within the hollow of the tubes, and substituted nitrogen (green) in tube walls. From [45]. 38
Figure 3.9 High resolution TEM micrograph of FT catalyst which was carburised at 20 Torr CO in situ using a differentially pumped TEM. The pressure was lowered to < 3.5 Torr during imaging. Lattice spacings consistent with α-Fe are marked. From [50]. 40
Figure 3.10 Schematic cross-section of a nanoreactor composed of two silicon nitride windows. From [52]. 41
Figure 3.11 XAS spectra (a), x-ray absorption image (b) and TEM micrograph (c) recorded from a resin-embedded biofilm sample. The spectra of the resin and a bacterium are very similar, indicating that the embedding methods have not preserved cell contents well. However the ability to image this sample in the TEM provides highly spatially resolved morphological information. From [53]. 42

Figure 3.12 a) CLSM image of the quantum dot stains (red). Yellow box indicates the region imaged in the STXM (b) and TEM (c). From [55]. 43
Figure 3.13 Images of the same atmospheric particle taken with a) TEM and b) STXM. c) The TEM-EEL spectrum and d) STXM-XANES spectrum from this particle. From [58]. 44
Figure 3.14 (a) X-ray absorption spectra 1-3 are from resin-rich, cell-rich and C_{60}-rich regions of a cell section. Spectra from both SVD and PCA analysis are shown. Spectrum 4 is a C_{60} reference spectrum. (b) and (c) Corresponding thickness maps and cluster maps from SVD and PCA analysis respectively. Adapted from [63]. 46
Figure 3.15 (a) STEM dark field image of a single layer graphene edge and (b) overlaid atomic positions. (d) Monochromated EEL spectra taken from the coloured atoms show different fine structure due to the different coordination environments of the carbons (c). From [65]. 47
Figure 3.16 Chemical maps calculated from EELS measurements of hybrid nanoparticles at different stages of production (a-c). Cadmium (grey), silicon (blue), carbon (green) and gadolinium (red) relative profiles across the nanoparticle diameters are plotted opposite (d-f). From [66]. 48
Figure 3.17 STXM-XAS spectra of the five components present in dodecyl-functionalised SWNTs: horizontal SWNTs (a), vertical SWNTs (b), oxidised SWNTs (c), carbon contaminants (d) and dodecyl (e). The corresponding chemical maps obtained from fitting these reference spectra to a region of SWNT bundles are displayed to the right. From [69]. 49
Figure 4.1 Ray diagram of the condenser lens system used to form (a) parallel illumination at the specimen for TEM imaging, or (b) a condensed probe at the specimen in STEM mode. Adapted from [70]. 52
Figure 4.2 Ray diagrams of the projector system for TEM imaging and diffraction. Adapted from [2]. 53
Figure 4.3 Ray diagram showing that highly scattered rays are blocked by the objective aperture, and so do not contribute to the bright field TEM image. From [2]. 54
Figure 4.4 Schematic diagram of a thermionic electron source, adapted from [2]. 56
Figure 4.5 Schematic diagram of field emission gun, adapted from [2]. 56
Figure 4.6 Illustration of a) a perfect lens where a point source is focused to a point, b) chromatic aberration where the rays of different energy are indicated by different colours, and c) spherical aberration where rays at different angles are focused to different points. The plane drawn, in which paraxial rays are focused, is known as the Gaussian image plane [19]. 58
Figure 4.7 Schematic showing the optics of the FEI Titan (S)TEM. Adapted from [75]. 60
Figure 4.8 Diagram showing the paths of the electrons through a simple Wien filter. (a) Electrons which enter with average velocity (green) experience equal electric and magnetic deflection and travel along the optic axis. For faster or slower electrons, these forces are unbalanced and the electrons are deflected away from the optic axis. As they approach the electrode, their energies are altered, bringing them back towards the optic axis again. (b) Ray diagram showing the action of the Wien filter on off-axial electrons. Adapted from [76]. 62
Figure 4.9 Ray diagrams of a zoom system in two settings. In both cases the object of lens 1 and the image of lens 2 are in the same positions. By changing the position of the image of lens 1, the convergence angle at the image of lens 2 also changes. Adapted from [70]. 62
Figure 4.10 Ray diagrams showing a range of different 'spot numbers', i.e. different image positions of condenser lens 1. The image positions of C1 are marked with green arrows. Changing the spot number alters the amount of current in the beam. From [70] 63

Figure 4.11 Ray diagrams showing how the image position of condenser lens 2 alters the size of the parallel illumination in TEM mode. The image positions of C2 are marked with green arrows. From [70]. 63
Figure 4.12 Ray diagram of the minicondenser lens in (a) TEM and (b) STEM modes. Adapted from [70]. 64
Figure 4.14 Diagram showing the geometry of HAADF, ADF and BF STEM detectors and their collection angles adapted from [2]. 65
Figure 4.15 Diagram of the focusing and dispersing actions of a magnetic prism EEL spectrometer. Adapted from [8]. 66
Figure 4.16 Schematic showing the acquisition of STEM-EELS data in the Titan microscope. An entire EELS spectrum is acquired at one position on the sample, after which the STEM probe can be moved to acquire EELS data at the next location. This can be done systematically to form a 3D data cube known as a spectrum image. Dark field images e.g. HAADF-STEM images may be acquired simultaneously with EELS data. 67
Figure 4.17 Spectra emitted from a) a bending magnet b) wiggler and c) undulator. Adapted from [26]. 69
Figure 4.18 Schematic diagrams of the optics in the beamlines (a) X1A1 at BNL and (b) SM beamline at CLS. Adapted from [79] and [80]. 70
Figure 4.19 Schematic of a zone plate with N zones. The radius of zone N is r_N and its width is δr_N. Rays are brought to focus a distance f_m from the zone plate where m is the diffraction order. Adapted from [78]. 72
Figure 4.20 Schematic showing the focusing optics of the STXM. The order sorting aperture (OSA) is used to block all higher order beams, so that only the first order beam is used to form the probe at the sample. Adapted from [81]. 72
Figure 4.21 Schematic showing the two sub-patterns of zones which are manufactured individually, then combined to form the finished zone plate. Adapted from [84]. 73
Figure 4.22 Diagrams of a) a STXM and b) a TXM. Reproduced from [14]. 74
Figure 4.24 Diagram showing the acquisition of STXM-XAS data. An x-ray absorption images at a particular incident x-ray energies is acquired. Images are acquired at a range of different incident energies, and built up into a 3D dataset called a 'stack'. 75
Figure 5.1 Cartoon showing the engulfing and degradation of foreign material by a macrophage cell. Adapted from [107]. 80
Figure 5.2 Diagrams of the five lowest-energy hydrogenic atomic orbitals: 1s, 2s and $2p_{x,y,z}$. 81
Figure 5.3 Energy level diagram showing the relative energies of two 1s atomic orbitals, and their bonding and antibonding molecular orbitals. Graphs of the molecular wavefunctions are inset. Adapted from [125]. 82
Figure 5.4 Diagram showing the geometries of σ and π bonds in a graphene sheet lying in the xy plane. (a) Head-on overlap of sp^2 orbitals form σ bonds while (b) side-on overlap of two p_z-orbitals results in the formation of a π bond. 83
Figure 5.5 Energy level diagrams showing the molecular orbitals of a sp^2 hybridised carbon atom. Adapted from [126]. 84
Figure 5.6 Energy level diagrams showing the formation of band structure. Adapted from [127]. ... 84
Figure 5.7 EEL spectra of graphite and CNT, which both exhibit a sharp peak at 285 eV and a broader structure at ~300 eV. Figure adapted from [128]. 85

Figure 5.8 TEM and STXM data of unexposed a-MWNT samples which had been dispersed in dextrose. (a) STXM X-ray absorption image reveals a-MWNT aggregates, although individual a-MWNTs cannot be resolved. (b) BF-TEM image and (c) XAS and EEL spectra of a-MWNTs, with peak labels corresponding to Table 5.2. (Scale bars 500 nm.) 88
Figure 5.9 A range of X-ray absorption images of macrophage cells after 1 day of exposure to a-MWNTs (a-c) and after 14 days of exposure (d-f). X-ray absorption images acquired at different photon energies contain contrast from different sample components. High contrast between a-MWNTs and the cell is seen at 285.5 eV (a & d) while contrast between the cell and resin is visible at 287.7 eV (b & e). Holes in the section (red arrows) due to damage from the X-ray probe are visible in images (c) and (f). 90
Figure 5.10 Reference spectra used for SVD fitting of the 1-day (a) and 14 day (b) STXM datasets. Cell-rich and resin spectra were obtained by summing over relevant regions in each STXM stack. The a-MWNT spectrum was taken from the sample of unexposed tubes shown in Figure 5.8. 91
Figure 5.11 Chemical maps of 1-day and 14-day cells, calculated by SVD analysis. Maps show the spatial distribution of resin (a & f), cell-rich (b & g) and a-MWNT (c & h) components. The residual signal is plotted in (d) and (i). RGB images with resin displayed in blue, cell in green and nanotubes in red are also shown (e) and (j) (scale bars 5 µm). 92
Figure 5.12 Results of PCA analysis of 1-day and 14-day exposed cells. (a) and (b) are maps showing the PCA clusters. (c) and (d) display the XAS spectra obtained by summing over all pixels in a cluster (scale bars 2 µm). 94
Figure 5.13 Overlaid spectra of the PCA clusters from the centre of CNT aggregates, after 1 and 14 days exposure. 94
Figure 5.14 Linear deconvolution results for a selection of PCA spectra from cells exposed for (a-b) 1 day and (c-d) 14 days. The PCA spectra (red/purple lines), fitted spectra (dashed lines) and residuals, i.e. difference between the two (dotted lines) are plotted. Fitting was performed by linear deconvolution using three reference spectra, and their coefficients are displayed in the bar graphs: cell-rich (green), resin (blue) and a-MWNT (red). 95
Figure 5.15 Analysis of PCA clusters calculated from an STXM stack which contains spatial drift. (a) PCA cluster map (scale bar = 5 µm), in which the purple cluster corresponds to the edge of the nanotube aggregate (arrow). (b) The spectrum of the edge cluster (purple) is overlaid with cell and nanotube spectra for comparison. (c) shows the functions which are used to recreate the edge spectrum, according to Equation 5.1. (d) The recreated spectrum (dashed line) agrees well with the original PCA cluster of the aggregate edge (purple), demonstrating that this cluster arises from drift artefacts. 96
Figure 5.16 Correlative electron and X-ray imaging of the 1-day cell. (a) X-ray absorption image of the whole cell and nanotube aggregates. (b) BF-TEM image of the boxed region in (a). Arrows indicate thinner regions and holes which formed after electron irradiation. Cell cytoplasm is labelled cyt. (c) Higher magnification HAADF-STEM image of the boxed region in (b), showing aggregated and individual a-MWNTs associated with the cell membrane (dots). 98
Figure 5.17 Correlative HAADF and X-ray imaging of the 14-day exposed cell. (a) X-ray absorption image of the whole cell and nanotube aggregates. (b) HAADF-STEM image of the boxed region in (a) showing the aggregates over which EELS data were acquired (green box). Contrast from the nuclear membrane is also visible (arrows) in this image. 99
Figure 5.18 SVD results for EELS data of 1-day and 14-day samples. (a,h) The component spectra used for SVD fitting: resin (blue), cell-rich (green) and a-MWNT (red) spectra. (b,i) HAADF-STEM

images of the cells, showing the area over which EELS data were acquired (red boxes). (c-e, j-l) Chemical maps showing the spatial distribution of each chemical component (f,m) Maps of the residual signal as defined in section 5.4.2.1. (g,n) RGB images showing regions of high resin concentration in blue, cell-rich regions in green and a-MWNT regions in red. (Overlapping cell and MWNT regions appear yellow). 100
Figure 5.19 Results of PCA analysis of the 1-day and 14-day EELS datasets. (a,b) PCA clusters and (c,d) corresponding cluster spectra. 101
Figure 5.20 Shows overlaid spectra of the PCA clusters from the centre of CNT aggregates, after 1 and 14 days exposure. 102
Figure 5.21 Comparison of XAS (dotted line) and EEL spectra (solid line) of the resin and cell-rich components, as well as spectra from nanotube aggregates after 1 day and 14 days of exposure. .. 103
Figure 5.22 Profiles showing the spatial variation of chemical components as calculated from EELS (solid lines) and XAS experiments (dashed lines). (a) HAADF-STEM image of a section of the 14-day cell discussed previously. Profiles are calculated along the yellow arrow, and signals are summed over the width of the red box in order to reduce noise. (b) Resin and (c) cell-rich profiles are plotted, and show that EELS profiles have a low SNR. (d) Profiles of the combined resin and cell contributions, showing improved SNR in the EELS profile. (e) a-MWNT and (f) residual profiles. Note that the residual profile is multiplied by a factor of 10 to enhance its visibility. 104
Figure 5.23 Deconvolution of EELS a-MWNT profile with the XAS a-MWNT profile from Figure 5.22(e). This gives an estimation of the instrument function of the STXM, which is found to have a full width at half maximum of 280 nm. 105
Figure 6.1 Schematic illustrating the variety of oxygen-containing groups which may be present on ox-MWNT surfaces. Figure from [160] 111
Figure 6.2 Graph showing the concentrations of different functional groups on the surface of MWNTs oxidised using a variety of acids. Functional groups were quantified using chemical derivatisation. Reproduced from [163]. 112
Figure 6.3 Studies of the spatial distribution of functional groups on MWNTs (a) SEM image of sulphur-functionalised MWNTs tagged with gold nanoparticles (b) SEM of MWNTs without sulphur containing groups (c) XANES of three chemical components present in a sample of ox-MWNTs and (d) STXM chemical map of the components showing the distribution of oxidizes carbon in blue. Adapted from [171] and [168]. 114
Figure 6.4 (a) Schematic showing the orientation of π* (orange) and σ* (purple) orbitals when viewing a CNT end-on, along the long axis. The scattering geometry is illustrated for two situations: (b) when the electron probe is located in the centre of the MWNT and (c) when the probe is at the edge. (d) Shows the variation in orientation of the orbitals from the multiple carbon walls probed by an electron probe. 116
Figure 6.5 STEM and EELS analysis of ox-MWNT samples at -170°C (a) Dark field STEM image of MWNTs over a hole in the support film, and (b) STEM image of the same MWNT after exposure to an electron probe scanned over the tip. (c) Carbon K edge EEL spectrum of the support film (green) compared to a previously reported low-temperature spectrum (blue) [175] (d) Oxygen K edge spectrum of the support film (green) compared with EELS of ice (blue) from reference [175]..... 121
Figure 6.6 EEL spectra of the different MWNT samples. Two spectra of pristine (green) and oxidised (red) MWNTs from each batch are shown. Peaks corresponding to graphitic carbon at 285.5 and 292.7 eV are labelled. The peaks occurring at 287.7 eV are also marked. 122

Figure 6.7 (a) EELS data of the ox-MWNTs investigated here are compared with XANES spectra from the literature, including acid oxidised MWNTs from reference [166], acid oxidised SWNTs (i)-(iv) from references [167], [67], [132] and [169] respectively, as well as oxidised and pristine graphene from reference [133]. The position of EELS peaks A, B' and C have been marked, as well as a new peak B" at ~288.7 eV which appears only in XANES data. (b) Expanded spectrum of the region between peaks A and C of ox-SWNT (ii) showing additional features at 287.7 and 288.2 eV. 124
Figure 6.8 EEL spectra showing the orientation-dependence of MWNTs at the carbon K edge. The reference spectra were taken at the edge (orange) and centre (purple) of a MWNT. 125
Figure 6.9 Four spectra taken at different positions across a MWNT (grey) overlaid with a linear superposition of the reference spectra from Figure 6.8. The coefficients of the reference spectra were calculated using linear decomposition, and are displayed in the bar graphs on the right. 126
Figure 6.10 Linear regression analysis of the experimental spectra of ox-MWNTs. (a) The four reference spectra, gaussian peak (red) graphitic carbon from two positions: q ∥ c axis (green) and q ⊥ c axis (blue) and amorphous carbon (purple). (b) Dark field STEM image of a ox-MWNT, from which two EEL spectra are taken. (c-d) The fitted spectra and scaled reference components are overlaid. The difference between experimental and fitted spectra is plotted as the residual signal, in grey. Bar graphs to the right show the coefficients of each fitted component, where the colours correspond to the key in (a). 127
Figure 6.11 Chemical distribution maps across various ox-MWNTs from Batch 1. (a-d) Dark field STEM images of the MWNT bundles. Maps of (e-h) graphitic carbon and (i-l) peak B' are shown, and overlaid to form false colour images (m-p) where the graphitic carbon is green, and peak B' is red. 128
Figure 6.12 Chemical distribution maps across various ox-MWNTs from Batch 2. (a-d) Dark field STEM images of the MWNT bundles. Maps of (e-h) graphitic carbon and (i-l) peak B' are shown, and overlaid to form false colour images (m-p) where the graphitic carbon is green, and peak B' is red. 129
Figure 6.13 (a) XANES of the three chemical components present in a sample of ox-MWNTs and (b) STXM chemical map of the components showing the distribution of oxidizes carbon in blue. Adapted from [168]. 130
Figure 6.14 Bar graph showing the percentage of EEL spectra which contained a statistically significant peak B' at 287.7 eV. 131
Figure 7.1 Schematic describing the effect of an octahedral crystal field on 3d energy levels. a) Example of octahedral geometry, in which six oxygen ligands surround a central metal ion. b) Energy level diagram of 3d levels showing the loss of five-fold degeneracy due to the different orientations of the d-orbitals with respect to the ligands. Diagram adapted from [204]. 139
Figure 7.2 Examples of elemental quantification in Digital Micrograph. All spectra have been deconvolved with low loss spectra in order to remove the effects of plural scattering. The background-removed edges are shown in green, the first derivative in black, and the calculated edge in blue. (a) and (c) show the oxygen K and Co $L_{2,3}$ edges. (b) Quantification at the Cr $L_{2,3}$ edge was more difficult due to the proximity of the O K edge. Background of the form AE^{-r} was removed from the O K edge, after which the O K edge itself was fitted and subtracted from the experimental spectrum. The fitting at the onset of the O K edge is poor (seen as the peak at ~530 eV), however this procedure results in a relatively flat signal in the region 540-570 eV showing that the oxygen signal has been removed effectively in this region. 142

Figure 7.3 Light micrographs showing a section of hip capsule tissue across the synovial surface. (a) The presence of a subsurface band (arrow) of macrophage cells indicates an inflammatory response in the tissue sections. (b) Higher magnification image of the macrophages, revealing dark regions (arrows) in the cell cytoplasm. 144
Figure 7.4 Electron micrographs of wear debris contained in macrophage cells. (a-b) HAADF-STEM imaging shows that macrophages are laden with wear debris (bright particles). The arrows indicate abnormal nuclear membrane structures, where the outer nuclear membrane is separating from the inner membrane. (c-f) Bright field TEM images in which the wear debris is imaged as dark particles. Debris is seen clustered in the cytoplasm. Mitochondria with damaged ultrastructure are marked with arrows. (g-h) EDX analysis of the circled particles in (e) and (f) shows that particle A contains Cr while particle B contains both Cr and Co. The high Cu signal originates from the TEM grid. 145
Figure 7.5 FIB-SEM analysis of a volume of macrophage cell containing wear debris, in two and three dimensions. (a-c) Three backscattered electron images, from a set of 200 slice-and-view images, are shown. (scale bars 750 nm) Wear debris (dark particles) and lipid bilayers are visible. (d) A snapshot of a 3D reconstruction of the volume, showing the distribution of wear particles (green). 146
Figure 7.6 Bright field TEM micrograph of a representative macrophage cell laden with wear debris, where the cell membrane is marked (red dots). Although STXM-XAS and STEM-EELS data were acquired from multiple cells, for ease of comparison, all subsequent data presented in this chapter were acquired within the boxed region of this macrophage cell. 147
Figure 7.7 SVD and PCA analysis of a STXM stack at the Cr $L_{2,3}$ edge. (a) The three component spectra (red, green and blue) used for SVD fitting are shown, along with an RGB image displaying the spatial distribution of these components. (b) Seven PCA clusters were identified, and cluster spectra and locations are shown. 148
Figure 7.8 SVD and PCA results of a STXM stack at the Co $L_{2,3}$ edge. (a) The three component spectra used for SVD fitting are shown, along with an RGB image displaying the spatial distribution of these components. (b) Spectra of the PCA clusters and a map of the cluster locations. 149
Figure 7.9 Comparison of experimental XAS spectra with reference compounds. (a) At the Cr $L_{2,3}$ edge, the blue phase contains no Cr and corresponds to the cell cytoplasm. The green phase is most similar to the Cr(III) reference compounds. The red phase is similar to the green spectrum, but exhibits a more intense peak at 576 eV (arrow). (b) At the Co $L_{2,3}$ edge, the red phase matches the spectrum of Co metal, while the green phase contains only trace amounts of Co and does not correspond to any reference samples studied. The $LiCoO_2$ and CoO reference spectra are taken from Morales et al. [207]. 150
Figure 7.10 Comparison of the Cr $L_{2,3}$ edge of the red phase with a linear combination of 70% Cr(III) and 30% Cr metal. Ratios of each component were calculated using linear regression fitting. 150
Figure 7.11 Comparison of images of the same cellular region, taken with STXM and (S)TEM. (a) X-ray absorption image taken with 540 eV photons. (b) Bright field TEM image and (c) HAADF-STEM image taken with an inner collection semi-angle of 129 mrad, showing the morphology of debris and cellular ultrastructure on a higher length scale. 151
Figure 7.12 Different clusters of wear debris analysed by STXM and dark field STEM) (scale bars 400 nm). Cr (a,d,g,j) and Co (b,e,h,k) chemical thickness maps and dark field STEM images (c,f,i,l) of wear debris clusters are correlated. Circled particles in (l) were selected for further EELS analysis (see Figure 7.15). 152
Figure 7.13 Comparison of XAS and EEL spectra of the different chemical phases of the wear debris at the Cr $L_{2,3}$ edge (a) and the Co $L_{2,3}$ edge (b). 153

Figure 7.14 XAS spectra of the green phase at the Cr $L_{2,3}$ edge, after different degrees of smoothing. Spectra have been overlaid with corresponding EELS for comparison. 153
Figure 7.15 Quantitative EELS analysis of a 50 nm wear particle. (a) Higher magnification HAADF-STEM image of the wear particles shown in Figure 7.12(j-l). EEL spectra were acquired at each pixel in the boxed area. (b-d) Chemical maps showing the distribution of oxygen, chromium and cobalt were calculated. (e) Absolute numbers of atoms per unit area are plotted as a function of distance across the nanoparticle (red arrow in (b)). The chemical composition changes through the particle, showing an oxygen-rich and cobalt-deficient shell. 155
Figure 7.16 STEM-EDX analysis of wear debris in an adjacent area of cell. (a) HAADF-STEM image and corresponding EDX maps of elemental O, Cr, Co and additionally, Mo (b-e)..... 156

List of Tables

Table 5.1 Table detailing photon energies at which X-ray absorption images were acquired to form STXM 'stacks'. 87
Table 5.2 List of the peaks present in the carbon K edge XAS and EEL spectra of unexposed a-MWNTs, and the origins of each peak. 88
Table 6.1 XANES peak energies for a range of functional group, reproduced from [136]. 117

1. Introduction

Growth in the development and applications of nanotechnology brings with it an increasing need for structural and chemical characterisation on the nanometre scale. Even outside of the field of nanotechnology, the bulk properties of many materials are often determined by their composition at the nanometre level. Despite this, many commonly used laboratory-based characterisation techniques, such as ultra-violet and infra-red spectroscopies, mass spectrometry and thermogravimetric analysis, provide spatially averaged information of comparatively large volumes of sample. While these techniques provide a representative overview of the sample, their averaged signals often probe not only the nanostructures of interest, but also any surrounding material, debris and impurities in the sample. In addition, averaged properties miss statistical outliers, which may be critical for the function of the material. For characterisation of interfaces or individual nanostructures, techniques with much higher spatial resolution are essential.

Only a handful of techniques are capable of providing chemical information on the nanometre scale, including electron energy-loss spectroscopy (EELS) and x-ray absorption spectroscopy (XAS) in x-ray microscopes and scanning probe methods such as scanning tunnelling microscopy (STM)[1]. Of these, EELS and XAS provide remarkably similar chemical information despite the fact that their probe specimen interactions are very different: electron scattering and photon absorption, respectively.

Both electrons and x-rays can be focussed to nanometre scale probes. Electron microscopes were originally developed to overcome the diffraction limited spatial resolution of optical instruments. A 300 kV electron beam, whose wavelength λ is 2 pm[*] has a theoretical spatial resolution of ~1 pm[†][2]. However, the typical spatial resolution achievable in a transmission electron microscope (TEM) is much poorer due to the limitations of electromagnetic lenses. Advances such as aberration correctors mean that current state of the art STEM instruments have probe sizes of <1 Å [3]. The

[*] From de Broglie wave equation, $\lambda = h/p$ where h is Planck's constant and p is the relativistic momentum of the electron.

[†] Using the Rayleigh criterion whereby the smallest distance which can be resolved, δ, is given by $\delta = \frac{0.61\lambda}{NA}$ Here, NA is the numerical aperture, which can be approximated to unity for simplicity (see Appendix 1).

spatial resolution of STXMs has always lagged behind that of electron microscopes, although recent advances in diffractive x-ray optics mean that soft x-ray instruments (which operate in the 100 eV to 2 keV range [4]) now boast probe sizes of <15 nm [5]. While further advances in x-ray optics can be expected to improve probe sizes in the future, STXMs will never match the spatial resolution of STEM-EELS due to the fundamental diffraction limit for x-rays. Meanwhile, the development of monochromators for electron microscopes means that the spectral resolutions of the two instruments are also converging [6]. However, it is unlikely that the combination of high flux and high energy-resolution achievable in the STXM will ever be matched in the electron microscope. Thus, a correlative approach that brings together the STXM and STEM-EELS methods will be very powerful to bridge the gaps in spatial and spectral resolutions and obtain new insights into nanostructured systems.

The aim of this thesis is to explore the possibilities of correlating EELS and XAS experiments; to determine if it is possible to perform both experiments on the exact same nanostructures, and to determine the advantages of such a correlative approach. This thesis is structured as follows: chapter 2 explains the theory of interactions between electrons, or x-rays, and matter in order to understand why EELS and XAS provide such compatible chemical information on samples. Chapter 3 reviews the technological developments which have brought about a convergence in the spectral and spatial capabilities of both instruments. Previous studies which employ both techniques to answer questions on a particular system are also discussed. In chapter 4, the STEM-EELS and STXM-XAS instruments used are described, and the procedures for collecting large datasets which contain spatially resolved chemical information - the EELS spectrum image and the STXM stack - are also discussed. The techniques used here to process these large datasets are also introduced.

Chapter 5 presents results of a correlative EELS/XAS study of the fate of multi-walled carbon nanotubes (MWNT) in human macrophage cells. In particular, to determine the extent to which intracellular nanotubes retain their graphitic structure, whether any degradation of carbon nanotubes (CNTs) occurs at long time points (up to two weeks) and whether these questions can be answered in resin embedded cells at the carbon K edge in both microscopes.

In chapter 6, the claim that EELS is too damaging to detect fine structure at the carbon K edge is investigated. The aim of this work was to map the location of functional groups across acid oxidised MWNTs, using changes in electronic structure which are characteristic of oxygen-containing functional groups. An additional peak was observed and was shown to be indicative of acid-oxidised MWNTS. The findings of this work were compared with current STXM studies which are attempting to address the same question.

In chapter 7, EELS and XAS techniques have been applied to debris from metal-on-metal hip prostheses. Nanoparticulate debris containing CoCr can be found in soft tissue surrounding the failed prostheses; however it is unclear how the presence of these particles is linked to the overall failure of the implant. The aim of this work was to determine the chemical speciation of the debris within macrophage cells, which would provide insights into the interaction between debris and the cell. Finally, conclusions and further work are discussed in chapter 8.

2. Probing electronic interactions with electrons and x-rays

In many studies of the electronic structure of materials, x-ray absorption near-edge structure (XANES) and energy-loss near-edge structure (ELNES) are often dealt with interchangeably. Yet it is not immediately obvious that electron scattering events and photon absorption events should give rise to the same spectral signatures. Both these events probe electronic transitions within the target atom, from a filled initial state into *the same* unfilled final states. In order to understand this phenomenon, this chapter will describe the interaction of electrons and x-rays with matter within the framework of time-dependent perturbation theory. The interpretation of near-edge spectral features, and the chemical information provided about a sample, will also be discussed.

2.1. Electron-sample interactions in the electron microscope

In the TEM, when an electron passes through a thin sample, it has some probability of being scattered. The scattering is either elastic or inelastic: elastic scattering involves a Coulombic interaction, generally between probe electrons and the atomic nucleus[‡]; inelastic scattering largely results from probe electrons interacting with atomic electrons [2]. The energy lost by inelastically scattered electrons can be measured and displayed in an EEL spectrum. In this section, the theory of electron scattering is introduced with emphasis on those scattering events which are relevant to core-loss EELS.

2.1.1. Elastic scattering

Elastic scattering, often called Rutherford scattering, conserves both kinetic energy and momentum (to a good approximation) as the nucleus is far more massive than the probe electron. The

[‡] The interaction between a probe electron and the nucleus may result in energy transfer if e.g. a bremsstrahlung x-ray is produced, or if the atom is displaced [2].

probability of an electron being scattered elastically into a solid angle dΩ can be expressed by the Rutherford differential cross-section[§] $d\sigma_{el}/d\Omega$, where [2]

$$\frac{d\sigma_{el}}{d\Omega} = \frac{e^4 Z^2}{16(E_0)^2 \sin^4 \frac{\theta}{2}} \qquad \textit{Equation 2.1}$$

Here, e is the electron charge, Z is the atomic number, E_0 is the incident beam energy and θ is the scattering angle, as shown in Figure 2.1.

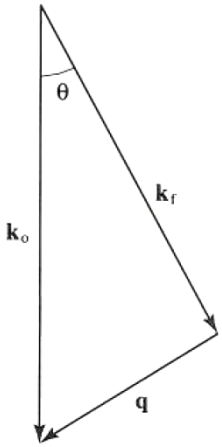


Figure 2.1 Wavevector diagram showing the incident electron wavevector $\boldsymbol{k_0}$, and the transmitted wavevector $\boldsymbol{k_f}$ which has been scattered through an angle ϑ. The scattering vector $\boldsymbol{q}$ is defined as $\boldsymbol{q} = \boldsymbol{k_0} - \boldsymbol{k_f}$. Adapted from [7].

Although elastic scattering is the main contributor to diffraction patterns and images in the TEM, it can also indirectly affect an EEL spectrum. For example, this occurs when a) an electron undergoes both an elastic and an inelastic scattering event and b) when channelling occurs, redistributing the electron flux in crystalline materials [8].

2.1.2. Inelastic scattering and Bethe theory

For inelastic scattering, the mechanisms of energy-loss include plasmon and phonon excitations, direct radiative losses and single electron excitations [7]. In this section we will consider only the last of these processes. When the incident electron interacts with an atomic electron, it can lose

[§] The Rutherford model is based on a simple unscreened nuclear field. When screening is accounted for, the cross-section is a function of Z^n where $n \lesssim 2$ [7].

some energy E and promote the atomic electron from its initial state into an unoccupied final state [7].

When discussing the probability that a probe electron will interact with an atomic electron, the double differential cross-section is used. This represents the fraction of electrons that are scattered into a solid angle dΩ with an energy between E and E + dE [7]. The double differential cross-section can be derived quantum mechanically using Fermi's Golden Rule. We start by treating the incident and scattered electrons as plane waves, of the form $\exp(i\underline{k}\cdot\underline{r})$ [7]. The Born approximation assumes that energy loss and momentum transfer are small in comparison with the energy and momentum of the incident beam, thereby allowing the electron and atom to be dealt with in separate terms [7]. A further simplification is the one-electron approximation, in which other electrons do not contribute to the excitation process [8]. The double differential cross-section then has the form [9]

$$\frac{d^2\sigma}{dEd\Omega} \propto \frac{4\gamma^2}{{a_0}^2 q^4}\left|\left\langle\psi_f\right|\exp\left(i\underline{q}\cdot\underline{r}\right)\left|\psi_i\right\rangle\right|^2 \rho(E) \qquad \textit{Equation 2.2}$$

Where a_0 is the Bohr radius, $\underline{r}$ is the position of the atomic electron, $\underline{q}$ is the scattering vector as shown in figure 2.1, $|\psi_i\rangle$ and $|\psi_f\rangle$ are the initial and final states respectively, ρ(E) is the density of states (DOS) and γ is the relativistic factor for a particle with velocity v [9],

$$\gamma = \frac{1}{\sqrt{1-{v^2}/{c^2}}} \qquad \textit{Equation 2.3}$$

If a small collection aperture is used at the spectrometer entrance, only those electrons scattered by small angles will contribute to the EEL signal, and hence $\underline{q}$ will be small. This allows us to neglect second order and higher terms in the Taylor-expanded exponential term in equation 2.2,

$$\exp\left(i\underline{q}\cdot\underline{r}\right) \approx 1 + i\underline{q}\cdot\underline{r} - \frac{1}{2!}(\underline{q}\cdot\underline{r})^2 + \cdots \qquad \textit{Equation 2.4}$$

Furthermore, the first term of the Taylor-expansion, 1, does not contribute to the integral as $|\psi_i\rangle$ and $|\psi_f\rangle$ are orthogonal [8, 9]. Thus equation 2.2 becomes

$$\frac{d^2\sigma}{dEd\Omega} \propto \frac{4\gamma^2}{{a_0}^2 q^4}\left|\left\langle\psi_f\right|\underline{q}\cdot\underline{r}\left|\psi_i\right\rangle\right|^2 \rho(E) \qquad \textit{Equation 2.5}$$

This is known as the dipole approximation, and has important implications for the final states which can be reached from a given initial state, as discussed in section 2.3 [7]. An important related

quantity is the generalized oscillator strength (GOS), f. This is an atom-dependent quantity which describes the response of the atom as a function of energy E and momentum $\underline{q}$ gained from the fast electron [7, 8]. The GOS is often defined per unit energy [7]:

$$\frac{df}{dE} = \frac{E}{Ra_0{}^2 q^2} \left| \left\langle \psi_f \right| \exp\left(i\underline{q} \cdot \underline{r}\right) \left| \psi_i \right\rangle \right|^2 \qquad \textit{Equation 2.6}$$

It is used to calculate the partial scattering cross-sections for quantitative analysis of edges (see section 7.3.3.1) [7].

2.2. Photon-sample interactions in the x-ray microscope

Photon absorption is described by the Beer-Lambert law [10]

$$I(E) = I_0(E) e^{-\mu(E)t} \qquad \textit{Equation 2.7}$$

where the transmitted flux $I(E)$ is dependent on the incident flux $I_0(E)$ and the x-ray absorption coefficient μ.

A photon which is incident on a sample has some probability of being absorbed, causing an inner shell electron to be excited into a higher final state. The form of the x-ray absorption coefficient may also be derived from Fermi's Golden Rule [11]:

$$\mu \propto \sum_f \left| \left\langle \psi_f \left| e^{i\underline{k}\cdot\underline{r}} \, \underline{\varepsilon} \cdot \underline{p} \right| \psi_i \right\rangle \right|^2 \delta(\hbar\omega - E_f + E_i) \qquad \textit{Equation 2.8}$$

Where $|\psi_i\rangle$ and $|\psi_f\rangle$ are the initial and final states, $\underline{\varepsilon}$ and $\underline{k}$ are the polarization vector and wavenumber of the light respectively, $\underline{p}$ is the momentum operator and $\underline{r}$ is again the position of the atomic electron. For soft x-rays, $\underline{k} \cdot \underline{r} \ll 1$, and so we can approximate the exponential term to unity. This reduces Equation 2.9 to [11]

$$\mu \propto \sum_f \left| \left\langle \psi_f \left| \underline{\varepsilon} \cdot \underline{p} \right| \psi_i \right\rangle \right|^2 \delta(\hbar\omega - E_f + E_i) \qquad \textit{Equation 2.9}$$

which looks very similar to equation 2.5 with the electron-electron interaction operator $\underline{q} \cdot \underline{r}$ being replaced by another dipole operator, $\underline{\varepsilon} \cdot \underline{p}$ [11]. Unlike the electron-electron transition which requires a small collection angle for the dipole approximation to be valid, the electron-photon dipole approximation is based on the much greater photon wavelength compared to the extent of the initial state. This condition is satisfied for all soft x-rays.

2.3. The spectrum

Figure 2.2 shows the basic features of an energy-loss spectrum. The features at low energy-loss arise from elastic scattering, as well as from collective excitations such as phonons and plasmons [7]. Since low loss features have no direct analogue in soft x-ray XAS, these will not be discussed further here. Instead, this section will concentrate on the features which are common to both spectroscopies: inner shell ionization edges. Inner shell edges occur between about 40 eV and several thousand eV and each is labelled according to the initial state from which the transition occurs, as shown in Figure 2.3. The fine structure that is present at a core loss edge is divided into two regions [7, 8]:

a) **Near-edge**, which occurs within ~30 eV of the edge threshold. This is called energy-loss near-edge structure (ELNES) in EELS and x-ray absorption near-edge structure (XANES) in XAS. Some x-ray studies also refer to this region as the near edge x-ray absorption fine structure (NEXAFS) region.
b) **Extended structure**, which occurs more than ~30 eV above the edge threshold. This is known as extended energy-loss fine structure (EXELFS) in EELS and extended x-ray absorption fine structure (EXAFS) in XAS.

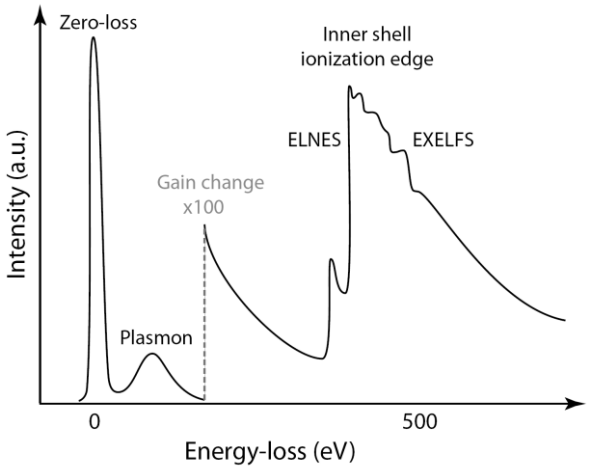


Figure 2.2 Diagram showing the features present in a typical EEL spectrum. Adapted from [7].

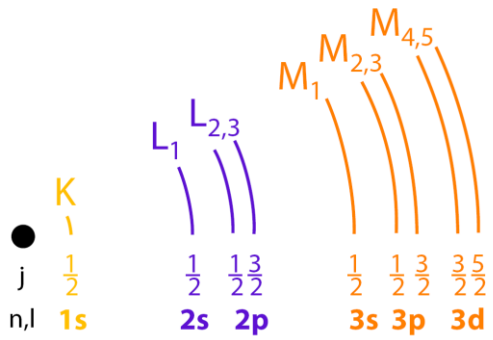


Figure 2.3 Schematic showing the nomenclature of different inner-shell ionization edges. Adapted from [7, 8].

2.3.1. Origin of fine structure

In Equation 2.5Equation 2.9 we found that the interaction cross-section contains a transition-matrix term and a DOS term. The form of an ionization edge can be understood by considering these terms separately. The transition-matrix term describes the spatial overlap between initial and final states. It varies slowly with energy, giving basic edge shapes for each class of edge listed in Figure 2.3 [7]. Figure 2.4 shows these edge shapes for a free, unbound atom.

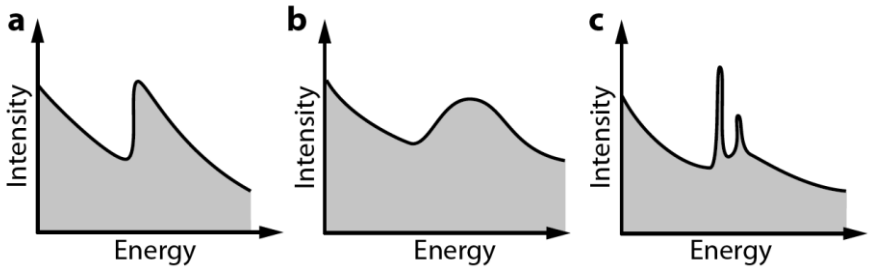


Figure 2.4 Diagrams showing some basic edge shapes, calculated using a free atom model: (a) the K edge has a saw-tooth shape, and (b) some $L_{2,3}$ edges and $M_{4,5}$ edges display a delayed maximum. (c) Bound states have been included to recreate the shape of white lines seen in 3d and 4d transition metals. Adapted from [7].

Superimposed on the basic edge shape is fine structure arising from the DOS term (Figure 2.5) [9]. In principle, $\rho(E)$ is a joint DOS *i.e.* the DOS of the final state, convolved with that of the initial core state. A core state is strongly bound, and so its DOS is a sharp peak with width Γ_{i}. Using the Heisenberg uncertainty principle and the lifetime of the core hole, τ_h, the width of the core state is given by [8]

$$\Gamma_{\mathrm{i}} \approx \frac{\hbar}{\tau_h} \qquad \textit{Equation 2.10}$$

Therefore $\rho(E)$ can be thought of as the unoccupied DOS, broadened by Γ_{i}.

One other broadening effect which contributes to the fine structure is the lifetime of the *final* state, τ_f [8]. The excited electron can be thought of as an ejected, free electron with a mean free path which is inversely proportional to its kinetic energy. Therefore at higher energy losses, τ_f decreases and the DOS structure is increasingly broadened. This results in a decreasing amplitude of near edge structure with increasing energy-loss [8].

2.3.2. Dipole selection rules

Only a subset of all unoccupied final states contribute to the DOS term; these are known as the 'allowed' final states. The transition-matrix determines which final states can be reached from a given initial state, as all other combinations of initial and final states give a matrix element of zero. Conditions under which the transition-matrix is non-zero are [7]:

a) When the change in angular momentum quantum number is $\Delta l = \pm 1$, and the spin is conserved; $\Delta s = 0$. This is a consequence of the dipole form of the interaction operators, and means that the initial and final states must have different symmetry e.g. s → p, and p → s or d. Thus the density of states term is a partial or symmetry-projected DOS. When large collection angles are used in EELS, the dipole approximation breaks down and it becomes possible to probe extra transitions, into dipole-forbidden final states.

b) When there is spatial overlap between initial and final wavefunctions. For core loss spectroscopy, we are interested in inner-shell initial states, which are highly localized on a particular atom. Therefore the final state must also have some component that is localized on the atom. The DOS which fulfils this requirement is known as the site-projected or local DOS [7].

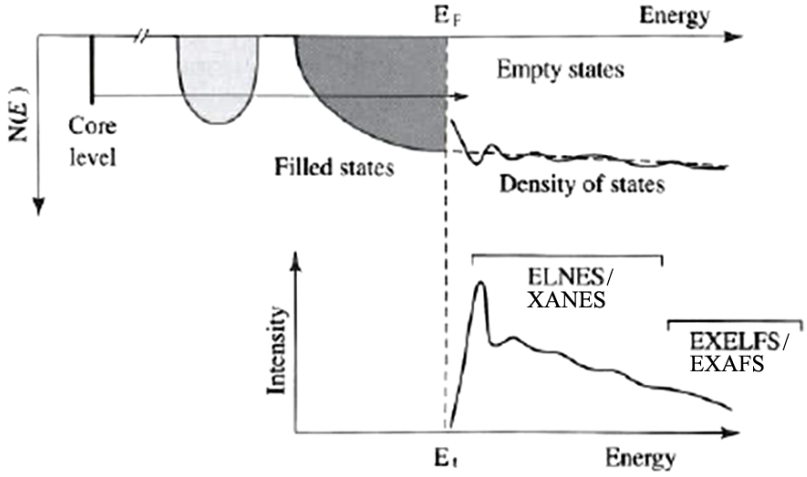


Figure 2.5 Diagram showing that the near edge fine structure of an inner-shell ionization edge is related to the density of states above the Fermi level E_F. Adapted from [7].

2.3.3. Determination of species, valence and coordination

The energy at which an edge threshold occurs corresponds to the energy difference between an inner-shell state and the lowest unoccupied state in the same atom. This energy is characteristic of different elemental species, and so different elements can easily be identified. Additionally, smaller shifts in the position of the edge threshold (on the order of 1 eV) can provide information on the valence of this atom. This is due to changes in the binding energies of both the initial and the final states when the effective charge on the atom changes [7].

Fine structure, through its relation to the DOS, provides information on the bonding and local coordination of the atom. For example, an effect called crystal field splitting can influence the 'white line' $L_{2,3}$-edges of some transition metal compounds. This happens when coordinating atoms lift the degeneracy of the unfilled final states, resulting in a single white line splitting into multiple peaks [8]. This will be discussed in more detail in section 7.2. In general, the exact interpretation of fine structure can be complex. For this reason, a combination of computer modelling and fingerprinting techniques, in which known reference spectra are compared to the unknown spectrum, are often used [7].

3. Literature Review

This chapter compares STXM-XAS and STEM-EELS, and discusses case studies in which electrons and/or x-rays have been employed to gain understanding of nanometer scale systems. The examples have been chosen to illustrate potential benefits and limitations of a correlative approach. For more comprehensive reviews of each technique individually, readers are referred elsewhere [1, 12, 13].

3.1. Introduction to STXM and EELS

The STXM was developed in 1985 by Kirz and Rarback, and makes use of Fresnel zone plates as focusing elements [14]. These diffractive optics consist of concentric alternating transmitting and absorbing rings, and are able to focus x-ray beams to spots as small as 15 nm in diameter. In the STXM, monochromated x-rays are focused by the zone plate onto a thin sample which is scanned across the x-ray probe while the transmitted x-ray intensity is detected (Figure 3.1). Chemical information can be obtained from a single spot, a line, or it can be mapped over an area of the sample. For the latter, an absorption image is collected at a single photon energy by recording the transmitted flux while the sample is raster-scanned across the x-ray probe. The photon energy is then changed and another absorption image is recorded. This process is repeated and a 3D data cube or 'stack' (two spatial dimensions and one energy dimension) is recorded. Although the transmitted x-ray signal is the most direct measure of x-ray absorption, total electron yield (TEY) is often used as an equivalent measure of XAS. TEY, a measure of the total current associated with non-radiative decay of core holes, has the advantage of being surface sensitive and does not require thin samples. However it relies on the assumption that the number of electrons created is proportional to the number of photons absorbed [15].

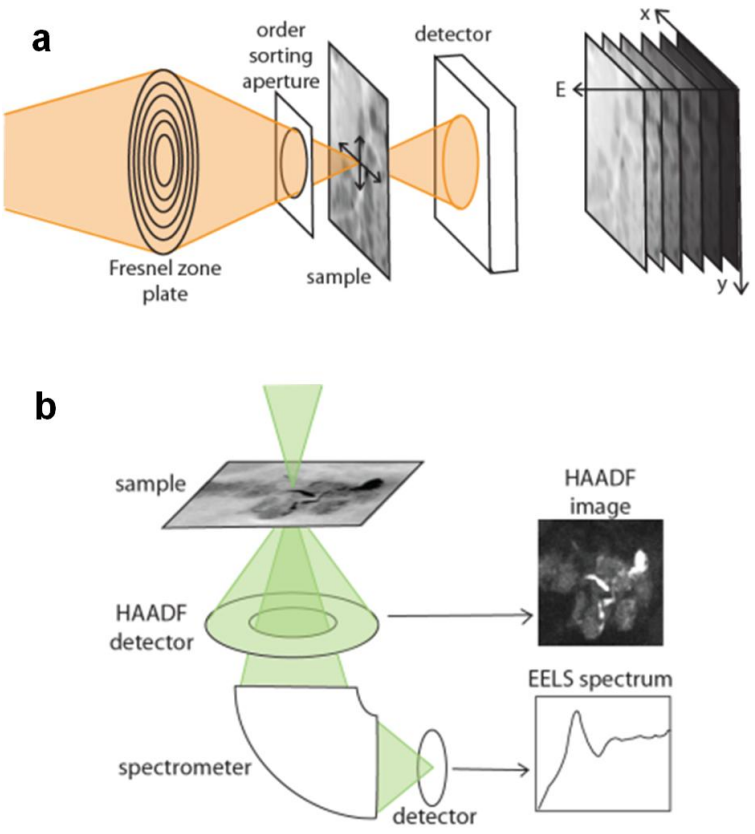


Figure 3.1 Schematic diagrams of (a) STXM-XAS and (b) STEM-EELS.

In STEM 'spectrum imaging' the electron beam is focussed to a probe, and EELS measurements are made using a spectrometer, commonly a magnetic prism in which the electrons are dispersed according to their energy-loss (Figure 3.1). EEL spectra are usually acquired in parallel, where the whole spectrum is detected at once on a position sensitive detector [2, 16]. At each probe position, a complete EELS spectrum is acquired. By scanning the electron probe across the sample and recording an EEL spectrum at each point, EELS data can be recorded in a spatially resolved manner. The 3D dataset that is created is known as a "spectrum image" (SI), and is analogous to a STXM stack, although the data are acquired in a different order as illustrated in Figure 3.2.

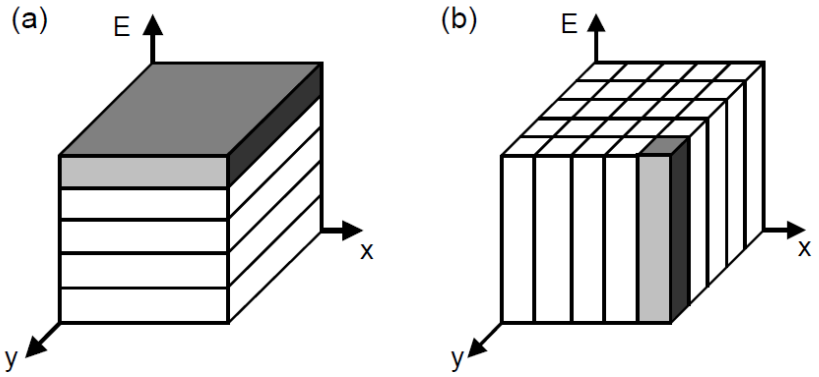


Figure 3.2 Schematic diagram showing the order of data acquisition in a) a STXM "stack", in which images at different photon energies are acquired sequentially, and b) an EELS "spectrum image" in which a whole EEL spectrum is acquired at a given position before the probe is moved, and the spectrum acquisition repeated.

3.2. Spatial Resolution

For spectroscopy techniques, spatial resolution is a measure of the volume of sample which gives rise to the spectroscopic signal. In EELS this volume is determined by a number of factors including the size of the electron probe, the amount that this probe broadens within the sample and the delocalisation of inelastic scattering. The effect of beam broadening can be minimised through use of an angle-limiting aperture placed before the EEL spectrometer which removes high angle electrons, or by using high accelerating voltages or sufficiently thin samples [17]. Delocalisation is more fundamental and describes the phenomenon of core electrons being excited when a fast electron passes some distance from the atom [18]. However this effect is small [2], and so it is usually the size of the electron probe which limits the spatial resolution of core-loss EELS.

Figure 3.3 shows the evolution of spatial resolution in optical and electron microscopy. Electromagnetic lenses are poor compared to their optical counterparts, being subject to severe lens aberrations. By the late 1990s these aberrations caused the resolution of the electron microscope to reach a plateau far below the diffraction limit [19]. In 1936, Scherzer showed that by using only spherically symmetric lenses, it was not possible to fully correct spherical and chromatic aberrations [20]. Since the development of non-spherical lenses was beyond the technology available at this time, aberration correction had to be performed numerically using techniques such as deconvolution. Whilst improving the effective spatial resolution, care must be taken when applying such post-acquisition methods as they have been reported to give rise to artefacts [21]. It is only recently, with the help of sophisticated computer control, multipole lens systems have been developed to correct for spherical aberrations [22].

The first results from a commercial spherical aberration corrected TEM were published in 1998. In this instrument, two hexapoles and four additional lenses allowed an improvement in point resolution from 0.24 nm to better than 0.14 nm [23]. In most new generation TEMs, only spherical aberrations are corrected, however chromatic aberrations have also been successfully corrected in a small number of TEMs, allowing spatial resolutions of up to 50 pm to be achieved [24]. Chromatic aberrations can also be reduced through use of a monochromator (see section 4.1.4.1).

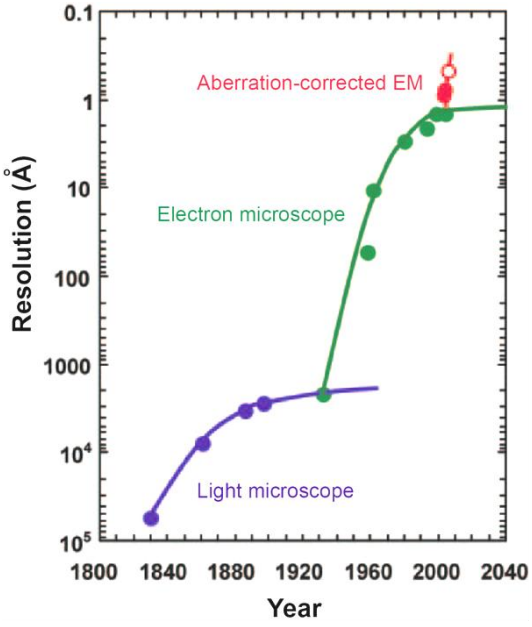


Figure 3.3 Graph of the evolution of spatial resolution in light and electron microscopy. Adapted from [19].

While electron microscopy has already achieved sub-nanometre resolution with potential for improvement, the fundamental diffraction-limit of soft x-ray probes is much higher, on the order of 10nm. Other factors will also affect the spatial resolution of the x-ray microscope, depending on the technique used. In spectromicroscopy, where the spectrum is recorded from a single spot on the sample, the spatial resolution is determined by three factors of similar magnitude: a) the size of the x-ray probe, b) thermal drift, and c) an effect called 'run out'. Run out refers to the unintentional lateral movement of the x-ray beam on the sample, which happens when the zone plate is moved along the optic axis to maintain focus at different x-ray energies. Using STXM techniques, drift and run out effects can be removed. Since stacks of images are acquired instead of a single spot, both effects can be corrected post-acquisition through the use of cross-correlation procedures [25]. The remaining factor limiting the spatial resolution is once again the size of the probe, which in the case of the STXM, is formed using zone plates [26].

Zone plates have been used to focus soft x-rays for decades. The earliest versions were made mechanically in the 1960s, while holography techniques allowed zone plates with more zones to be constructed. By 1979, the outermost zone width was as small as 0.12 μm, which corresponds to a diffraction-limited beam size of 140 nm (see section 4.2.5) [27]. In 1998, using electron beam nanofabrication, Warwick *et al*. reported a zone plate of gold on silicon nitride with a theoretical diffraction limited spot diameter of 40nm, and an actual full width at half maximum (FWHM) of 130 nm [25]. They put this discrepancy down to ambient vibrations and imperfections in the zone plate. By 2005, spatial resolution had been reduced by an order of magnitude. Chao *et al*. overcame the limited feature density that could be created using nanofabrication by splitting the zone plate rings into two complementary patterns [5]. These were fabricated separately and then overlaid, resulting in a zone plate with a sub-15nm spatial resolution. These zone plates are installed in a TXM at the Advanced Light Source in Berkeley, and give the best spatial resolution in a soft x-ray microscope to date. Most STXMs currently operate with spatial resolutions of 25-50 nm [28, 29].

3.3. Spectral resolution

The grating monochromators used in soft x-ray beamlines are well-developed [26] and energy resolutions of 0.05 to 0.10 eV are readily available [30-32]. These values are below the natural linewidths[**] of most core loss spectra [33, 34], and so the principle reason to pay attention to energy resolution in the STXM is to enable meaningful comparisons between spectra measured at different facilities [35]. Using beams of higher than necessary monochromaticity (defined as $E/\Delta E$) is detrimental since the photon flux will be lowered. In addition, as an XAS spectrum is acquired sequentially, the x-ray dose will also increase if many energies are to be sampled.

In EELS, many factors deteriorate the energy resolution of the electron beam. Energy broadening from electron interactions in the illumination system, the design of the spectrometer and the stability of power supplies all contribute, but the main limiting factor is the energy spread of the electron source [8]. Thermionic, Schottky-emission and cold field-emission guns have typical energy spreads of 2 eV, 0.7 eV and 0.3 eV, respectively [2, 16]. These energy spreads are greater than many natural line widths, with the result that fine structure is not fully resolved in such EELS spectra, and information on chemical environments is reduced.

[**] A 'natural linewidth' refers to the fact that a spectral line from an atomic transition is not completely sharp - there is an energy spread associated with the transition that is a consequence of the Heisenberg uncertainty principle and the finite lifetime of the states [33].

This situation has been greatly improved with the development of electron monochromators. These filters, located below the electron source, disperse source electrons and then select only a certain energy range using a slit [17]. Monochromated instruments allow energy resolutions of < 0.1 eV to be reached and their introduction has led to huge advances in the detection of EELS fine structure. For example, Figure 3.4 shows monochromated EELS and XAS spectra of manganese oxides [6]. In this instance the energy resolutions of the EELS and XAS were 0.2 eV and 0.1 eV, respectively. Both these values are below the 0.3 eV natural line width of the Mn $L_{2,3}$ edge, explaining the good agreement between the two techniques.

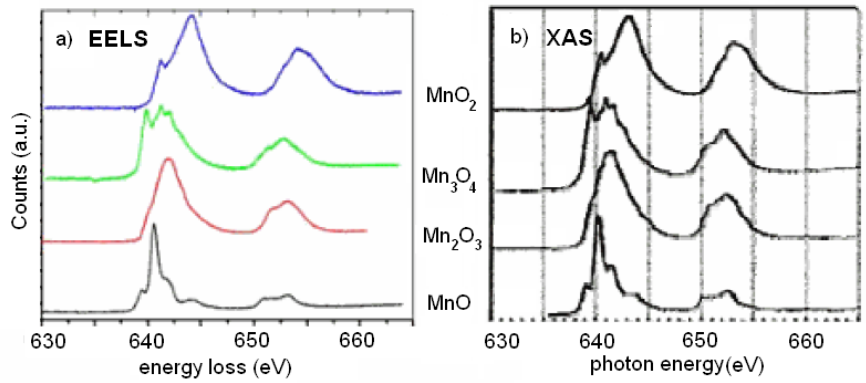


Figure 3.4 Fine structure at the Mn $L_{2,3}$ edges of various Mn oxides show good agreement between EELS (a) and XAS (b) spectra. Adapted from [6].

In the case of single crystal V_2O_5, additional EELS structure was observed at the vanadium $L_{2,3}$ edge when the monochromator was turned on and the energy resolution was improved from 0.6 to 0.22 eV [36]. XAS data that were acquired with a resolution of 0.08 eV revealed no additional fine structure, although features which appeared as shoulders in the monochromated EEL spectra were more clearly resolved as peaks in the x-ray spectra.

Some care needs to be taken when comparing EELS and XAS spectra acquired using different detection modes, as these can influence the measured spectral shape. For example, when performing total electron yield (TEY) measurements on insulating systems, McComb *et al.* found that the charging of insulating ZrO_2 grains during spectrum acquisition modified the relative intensities of the peaks in the x-ray data compared to their ELNES measurements [37].

The examples above demonstrate that the spectral performance of monochromated EELS is competitive with XAS measurements. As long as care is taken to ensure no saturation of the signal occurs, and that the dipole conditions are met, XAS and EEL spectra should be directly comparable.

Any remaining differences between the spectra would be due to differences in damage mechanisms, and sample preparation and environments, which will be discussed later in this report.

3.4. Elemental quantification and detection limits

EELS and energy filtered transmission electron microscopy (EFTEM) techniques have long been used to map *elemental* distributions at the nanometre scale. The intensity under a particular edge gives a measure of the amount of that element present, which can be quantified and mapped across the sample. In EELS, the quantification procedure involves background removal and signal integration. Then the partial ionisation cross-section is determined, which enables the edge intensity to be converted into an elemental concentration. Details of this procedure can be found elsewhere [38]. The accuracy of this quantification is limited by the accuracy of the background subtraction and the determination of ionisation cross-section, and is typically around 5 at%.

The detection sensitivity of EELS varies greatly with experimental variables, sample parameters and the particular element under investigation. Concentrations of 0.1-1% are typically detectable. Figure 3.5 shows work by Suenaga *et al*. which demonstrates that even single-atom detection is achievable using STEM-EELS [39]. Using a model system of Gd-metallofullerene molecules trapped within a single walled nanotube (SWNT), individual Gd atoms were mapped using the Gd N edge. However, this was a challenging experiment, and even with this ideal system, measurements were acquired with barely sufficient counting statistics. An additional complication of single-atom detection was that during the short acquisition time of 35 ms per pixel, the Gd atoms were found to move within their fullerene cages. Due to this motion, an increase in acquisition time alone may not be suitable for improving the signal-to-noise ratio (SNR) for such unstable samples, and that more sensitive detectors are required if single-atom measurements are to become routinely achievable in EELS.

The diffraction-limited spatial resolution of the x-ray probe means that single atom detection will most likely never be achieved in the STXM despite the high chemical sensitivity of this technique. Amongst the lowest concentrations that have been reported in the STXM is a 2 nm layer of Co within 250 nm of other metals [40]. A vanadium concentration of 0.23 at% ± 0.05 at% has also been measured in a recent STXM investigation of cometary particles [41]. In this work, STXM elemental maps were directly compared to energy dispersive analysis (EDX), however EDX failed to provide a quantitative analysis of the vanadium due to its low concentration and the overlap of the Ti and V peaks.

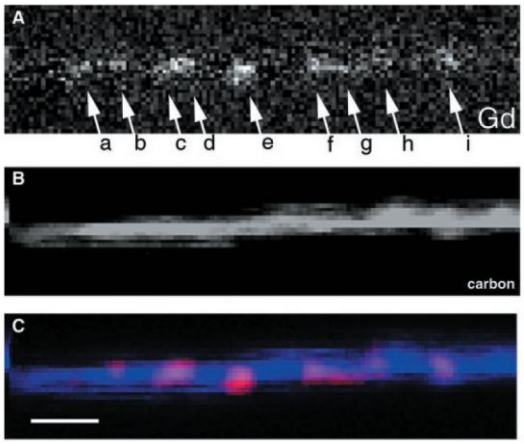


Figure 3.5 Chemical maps of gadolinium (red) and carbon (blue) calculated from EELS data of Gd-metallofullerene molecules confined in a SWNT. Points a, b and i indicate single Gd atoms. From [39] Reprinted with permission from AAAS .

The STXM-XAS detection limit of ~0.1% is expected to improve if one switches from measuring transmission signals, in which the measurement of interest is a small drop in a large number of background counts, to yield techniques such as x-ray fluorescence (XRF). The XRF-STXM technique is currently being developed, and its increased sensitivity compared to x-ray absorption measurements has already been demonstrated in a study of trace amounts of As and Mg in bacterial samples [42].

3.5. Bonding states and fine structure

So far we have considered using EELS and XAS only to identify and map different elements. However, far more chemical information is present in the spectra in the form of fine structure, although accessing this information places higher demands on the spectral resolutions of the techniques.

In a correlative EELS-XAS study of vanadium oxide nanotubes, bulk XAS measurements revealed double peaks at 531 and 533 eV in the oxygen K edge, which were used to confirm the chemical speciation of the tubes as V_2O_5 [43] (Figure 3.6). As the EELS measurements were not monochromated and had an energy resolution of 1.1 eV, this fine structure was not resolved, and could only be inferred from the asymmetry in the oxygen edge. EDX and EELS signals were, however, useful for mapping oxygen and vanadium elemental concentrations across the diameter of the tubes, with 1.2 nm spatial resolution. In addition, TEM bright field imaging had the spatial resolution to reveal variations in the spacing of layers across the tube diameters, which ranged from 2.5 to 4 nm. This combined approach therefore provided a more complete characterisation of the nanometre scale structure and chemistry of the tubes.

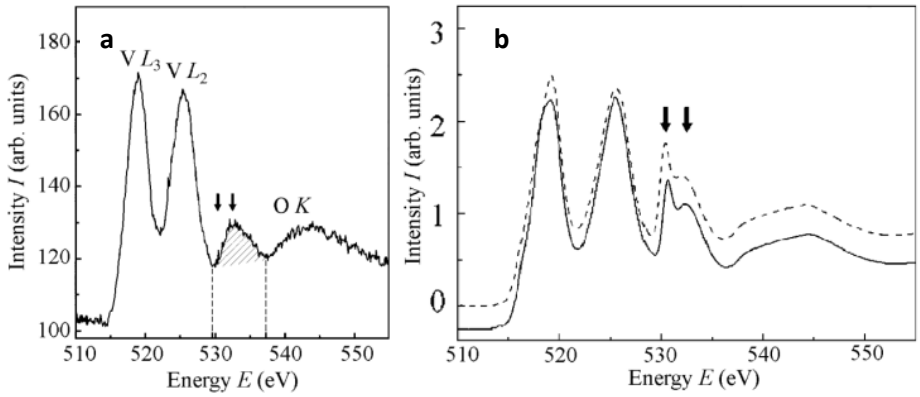


Figure 3.6 (a) EELS spectrum from a 1.2nm point on a single nanotube. The area of the shaded region was used to calculate the concentration of oxygen present. (b) XAS spectrum of nanotube (solid line) and a bulk V_2O_5 reference (dashed line) Reprinted with permission from [43]. Copyright 2007 American Institute of Physics.

Another system which has benefited from both XAS and EELS investigations is the nitrogen-doped carbon nanotube (N-CNT). Nitrogen doping is performed either to tailor electrical properties of the CNTs themselves, or as a means of storing nitrogen gas [44, 45]. In order to assess the suitability of N-CNTs for these applications, and to understand the doping process, it is important to be able to distinguish between the different chemical forms of the nitrogen present, and to map their distributions across individual N-CNTs.

Park *et al.* used XAS at the N K edge to demonstrate the presence of pyridine-like and graphite-like nitrogen in the N-CNTs (Figure 3.7). They were also able to resolve the vibronic structures of a gaseous N_2 peak [46]. These XAS measurements were not spatially resolved however, and EFTEM elemental mapping was performed on the same tubes. EFTEM revealed that the nitrogen signal was concentrated at the inner walls of the N-CNTs. Further evidence of the presence of N_2 gas within the hollow of the tubes was provided by a STEM-EELS study [44]. In this work, the peak at 401 eV corresponding to gaseous N_2 disappeared after the electron probe had created holes in the graphitic tube walls, suggesting that the N_2 gas had been released.

Using STXMs, it is now also possible to obtain spatially resolved XAS across *individual* N-CNTs. A recent study by Zhou *et al.* [45] mapped the different nitrogen species across the tubes, providing direct confirmation that substituted nitrogen is located in the nanotube walls and molecular nitrogen is trapped within tube compartments (Figure 3.8). Furthermore, the nitrogen pressure was calculated to be ~50 atm. As the spatial resolution of the STXM was 30 nm, such detailed analysis can only be applied to larger diameter tubes (>200 nm), although these results are consistent with STEM-EELS analysis of smaller tubes.

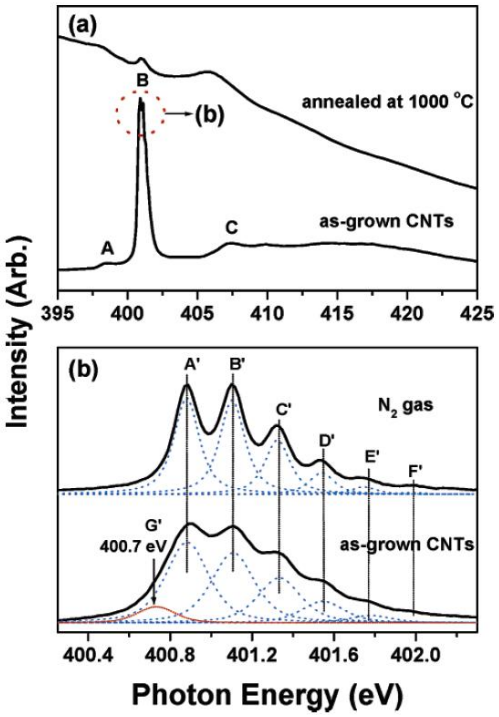


Figure 3.7 Nitrogen K edge XAS spectra of N-CNTs before and after annealing (a), and spectra showing the peak at 401 eV in more detail (b). This feature can be deconvoluted into seven peaks, which is indicative of gaseous nitrogen. Reprinted with permission from [46]. Copyright 2005 American Chemical Society.

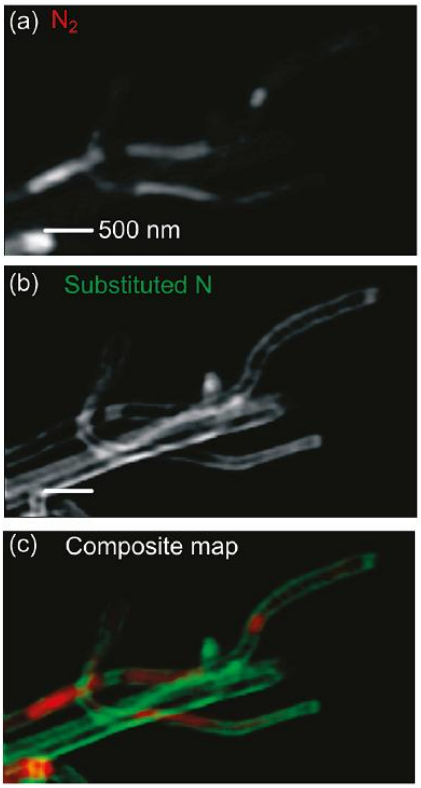


Figure 3.8 STXM chemical maps of a group of N-CNTs, showing the presence of gaseous N_2 (red) within the hollow of the tubes, and substituted nitrogen (green) in tube walls. Reprinted with permission from [45]. Copyright 2010 American Chemical Society.

3.6. In situ measurements

Both electrons and soft x-rays interact strongly with matter. The transmission requirement poses strict limitations on sample thickness, which means that ultrathin sections are usually prepared from solid samples and then studied under low pressure conditions. However, many chemical processes occur at gas-solid or liquid-solid interfaces, and in order to study these systems nanoreactors have been developed which confine the gas or liquid to a layer that is transparent to the electron/x-ray beam. Another option for environmental studies in the TEM is a differentially pumped vacuum system, in which the sample chamber is separated from the rest of the column by apertures and kept at a higher pressure on the order of 50 mbar [47]. The applications of environmental spectro-microscopy will be illustrated in the following case studies.

3.6.1. Gas cells and Fischer-Tropsch catalysts

Fischer-Tropsch (FT) synthesis involves the conversion of CO and H_2 (syngas) into hydrocarbons for use as synthetic fuels and oils. Iron-based FT catalysts are mainly composed of iron oxide on silicon dioxide. In this complex iron-oxygen-carbon system, questions remain about the identity of the active phase responsible for catalysing the reaction. As the FT reaction occurs at high temperatures and pressures, conventional microscopy analysis can only be carried out on catalysts after the reaction. However, these *ex situ* experiments are difficult to perform as samples are highly air-sensitive. To overcome this, Janbroers *et al.* used a protective atmosphere sample holder to transfer the catalyst sample from the reactor into the electron microscope [48]. TEM-EEL spectra of these quasi-*in situ* samples yielded significantly different results to previous studies: iron carbides were present in the activated catalyst, which would otherwise have been re-oxidised on exposure to air.

A fundamental issue when investigating any dynamic process like catalytic activity is that the state of the catalyst *after* activation may not accurately reflect its state *during* the reaction [49]. Environmental methods are then needed to study the evolution of the system *in situ*, whilst the reaction is occurring. A differentially pumped TEM allowed atomic-resolution images and EEL spectra to be obtained *during* catalyst activation [50]. Due to the considerable engineering challenge of confining a gas environment around the sample whilst maintaining high-vacuum conditions in the rest of the microscope, the maximum pressure obtainable with this setup was < 0.1 bar, two orders of magnitude lower than normal working conditions. Within these limitations, the authors observed the evolving reduction of the iron oxide precursors during CO treatment at 270°C. The low Fe L_3/L_2 ratio combined with a high Fe/O ratio suggested that *metallic* iron was present along with iron

carbides. This was confirmed by TEM analysis, which had sufficient spatial resolution to image lattice spacings consistent with α-Fe (Figure 3.9).

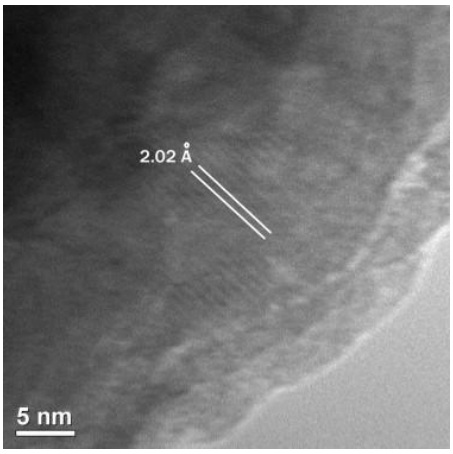


Figure 3.9 High resolution TEM micrograph of FT catalyst which was carburised at 20 Torr CO in situ using a differentially pumped TEM. The pressure was lowered to < 3.5 Torr during imaging. Lattice spacings consistent with α-Fe are marked. Reprinted from [50] with permission from Elsevier.

Nanoreactors may be used to achieve even higher pressures *in situ*. De Groot *et al*. performed an STXM study of FT catalysts under pressures of 1 bar, achieved by containing the catalyst and gas between two 1.2 µm thick SiN_x membranes [51]. A schematic of such a nanoreactor is shown in Figure 3.10. A Pt resistive heater was also used to provide temperatures of up to 500°C. This work examined the catalysts during activation in H_2, as well as FT synthesis. XAS at the Fe $L_{2,3}$ and O K edges were used to follow the evolution and spatial distribution of different iron species (metal, oxides, carbides). The spectra obtained were similar to the EELS measurements discussed above, but with high enough spectral resolution to resolve crystal field effects, revealing iron in an octahedral coordination probably due to Fe_2SiO_4. In addition to this, changes in the fine structure at the C K edge allowed different carbon species to be identified as either iron carbides or reaction products. Once again this analysis was limited by the 15 nm spatial resolution of the STXM, which is the same size as the iron oxide crystallites which make up the catalyst (Janbroers *et al*., 2011). However, as this nanoreactor was originally designed for the electron microscope [52], future *in situ* EELS studies may be able to provide complimentary information on a smaller length scale.

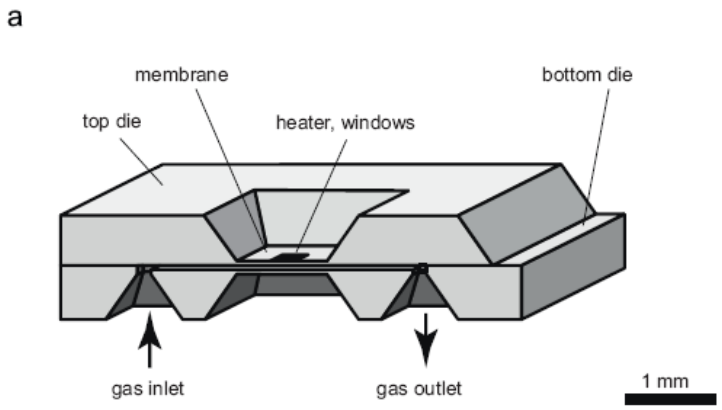


Figure 3.10 Schematic cross-section of a nanoreactor composed of two silicon nitride windows. Reprinted from [52] with permission from Elsevier.

3.6.2. Liquid cells and biofilms

Many systems (including biological cells and other soft matter) are hydrated in their native state, and typically need to be dried before studying in the vacuum of the TEM or STXM. Much work has gone into developing techniques to fix and dehydrate samples, but these techniques invariably result in undesirable structural and morphological modification of the sample. There are now a number of routes available which avoid these artefacts, such as wet cell technology and cryo-methods [14, 53, 54]. These techniques have recently been employed to understand the morphology and structure of biofilms – communities of bacterial cells and their surrounding organic matrix of polysaccharides, proteins and nucleic acids [53, 55].

Silicon nitride windows are also used in this field, to enclose fluid samples in a 'wet cell' and allow biofilms to be kept hydrated throughout the experiment [53]. In a study by Lawrence *et al.*, a river biofilm was tagged with a range of fluorescent markers which bound specifically to nucleic acids, proteins and lipids. Confocal laser scanning microscopy (CLSM) was then used to provide spatially resolved compositional information on length scales of under 1 μm. One limitation of fluorescent staining is that the technique relies on the specificity of the markers to bind to the right component. It is also affected by dense samples, through which the stain may not be able to penetrate. By applying the direct chemical analysis of XAS-STXM methods alongside the indirect CLSM analysis, the specificity of the fluorescent probes could be confirmed. Component maps of the same region of biofilm are compared in Figure 3.11. As the wet cell used in this study was too thick to be electron transparent, biofilm samples were prepared through a different route - resin-embedding - for TEM analysis. Thin sections of resin-embedded biofilms were imaged in the TEM, and compared to chemical analysis performed in the STXM. TEM imaging provided much more morphological

information of the cells and extracellular matrix. However, XAS spectra taken from a bacterium cell was very similar to spectra of the embedding resin, suggesting that resin-embedding had failed to preserve the organic material within the cells.

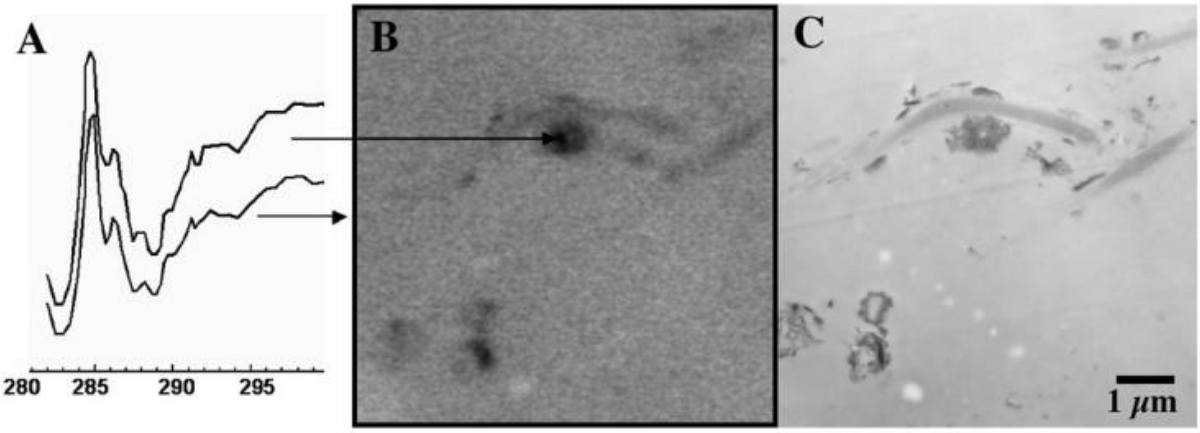


Figure 3.11 XAS spectra (a), x-ray absorption image (b) and TEM micrograph (c) recorded from a resin-embedded biofilm sample. The spectra of the resin and a bacterium are very similar, indicating that the embedding methods have not preserved cell contents well. However the ability to image this sample in the TEM provides highly spatially resolved morphological information. From [53].

In an attempt to preserve cell composition to a greater degree than resin-embedding, a later correlative STXM-TEM study used freeze-dried cryo-sections [56]. Biofilm samples were frozen at high pressure to ensure consistent vitrification, microtomed at liquid nitrogen temperatures, and then gradually warmed up to 25°C. XAS carbon K edge spectra showed fine structure characteristic of proteins, lipids and polysaccharides within cells, demonstrating that the macromolecular composition of cells had been better preserved through freeze-drying. Additionally, the absence of resin and its associated absorptions at the C K edge allowed the biological macromolecules to be more easily identified. TEM imaging once again revealed morphological structure, and XAS spectra this time revealed protein signals in the bacteria. However, lower than expected lipid and polysaccharide signals indicated some movement of organic matter during sample preparation.

Dynes *et al.* [55] demonstrated that it is possible to perform correlative CLSM, TEM and STXM on a single sample. In this work, cryo-ultramicrotomed biofilm sections were labelled with CdSe/ZnS quantum dots. These nanocrystal probes are designed to bind to polysaccharides. They provide contrast in all three microscopes via a) fluorescence in light microscopy b) z-contrast in TEM and c) absorption at the Se, Zn or Cd edges in STXM, allowing the distribution of polysaccharides to be imaged at three different length scales (Figure 3.12).

These studies have shown that it is possible to perform correlative studies of the same sections of sample across different microscopes. However, they have mostly been limited to using TEM for imaging purposes only. The use of additional EELS techniques could reduce the need for probes, with their associated specificity problems, allowing the full spectral and spatial benefits of a correlative spectroscopy approach to be exploited. However, damage from the electron beam will need to be considered.

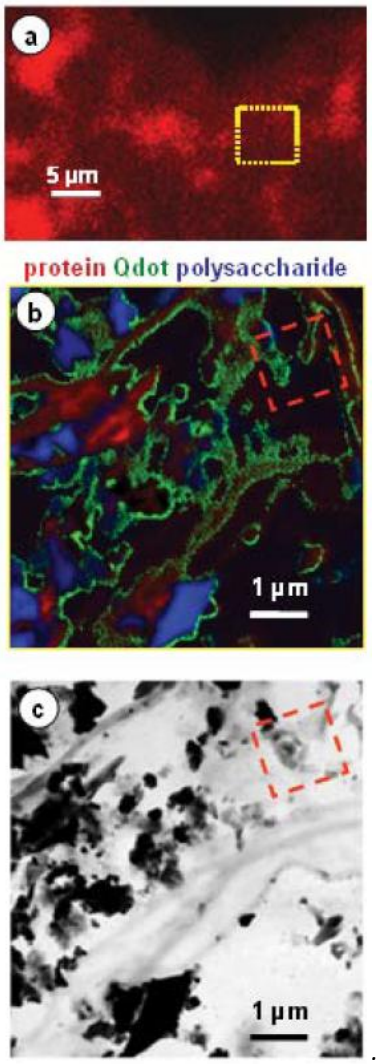


Figure 3.12 a) CLSM image of the quantum dot stains (red). Yellow box indicates the region imaged in the STXM (b) and TEM (c). From [55].

3.7. Damage studies

It is often assumed that EELS is more damaging than XAS, however it is still unclear to what degree this is true, and direct comparisons of damage are few and far between. Such comparisons are

difficult because the mechanisms of damage are complex and not completely understood. In addition, relevant parameters such as probe brightness and diameter are constantly changing as instruments improve. One widely cited study comparing EELS and XAS was carried out on particles of diesel soot [57]. In this study the electron beam was defocused to 100 nm to reduce the dose, however EEL spectra still showed only π* and σ* features with no fine structure and no variation between different particles. In contrast, XAS spectra contained multiple peaks between 285 and 290 eV, indicative of the presence of carbonyl and carboxyl groups. While it is probable that electron beam damage contributed greatly to the differences between the EELS and XAS spectra, the effects of a) the different sample preparation routes used and b) the different energy resolutions of EELS and XAS, also need to be quantified. Another correlative STXM/EELS study on similar carbonaceous airborne particles also found that EEL spectra lacked information on functional groups [58]. However, Figure 3.13 shows that the use of STXM alone misses important morphological and structural information, and so a correlative approach was suggested, in which STXM is first used for chemical analysis and subsequent TEM imaging is used to analyse particle morphology.

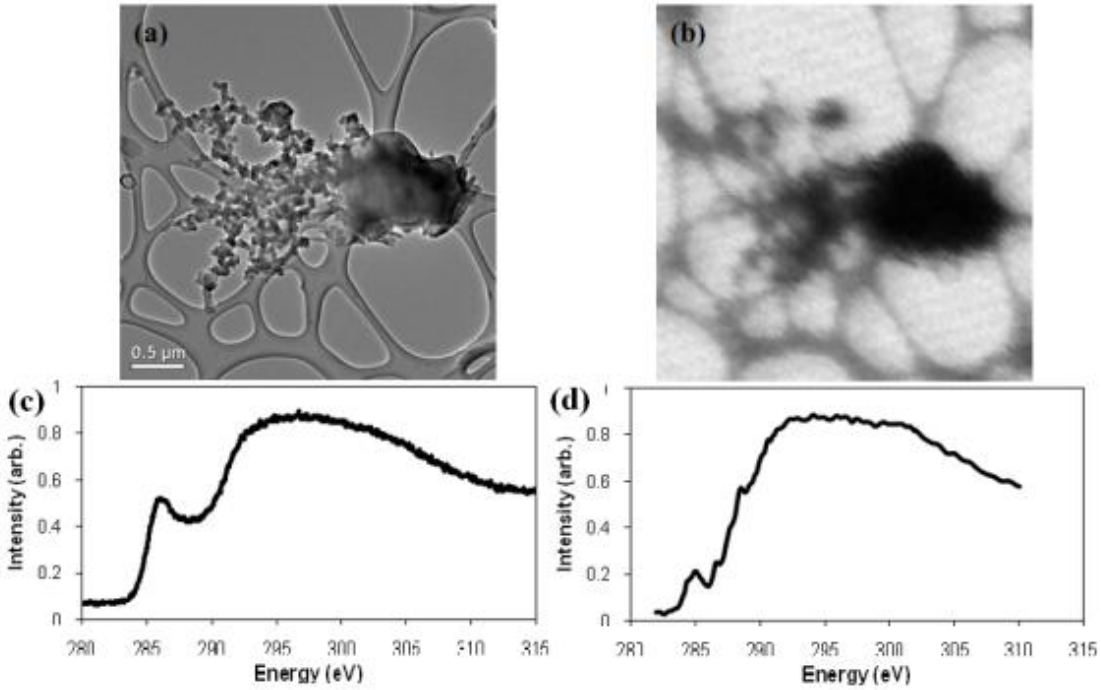


Figure 3.13 Images of the same atmospheric particle taken with a) TEM and b) STXM. c) The TEM-EEL spectrum and d) STXM-XANES spectrum from this particle. From [58].

More quantitative studies have investigated damage rates on poly(ethylene terephthalate) (PET), comparing 100 keV electrons with soft x-rays at the carbon and oxygen K edges [59]. Through analysis of the near edge structures, the damage products were found to be the same. The critical

dose for PET was found to be an order of magnitude higher for x-rays than for electrons. However, this comparison was limited by a number of factors, including:

a) The use of a 100 keV electron beam which is above the threshold for knock-on damage of carbon [60], thereby introducing an additional damage mechanism which is not present in x-ray spectroscopy, and

b) The use of different microscopes to evaluate the critical dose, i.e. the TEM was used to evaluate electron damage while the STXM was used to evaluate x-ray damage [14, 61].

These points were addressed in a subsequent study in which a) a lower energy electron beam of 80 keV minimised knock-on damage, and b) the spectral evaluation of both electron and x-ray damage was performed in the STXM [61]. PET samples were exposed to a range of doses of electrons and x-rays and afterwards XAS spectra were taken of the series of spots. Remarkably, using this method the critical dose for chemical changes in PET was then found to be 4.2×10^8 Gy for **both** x-rays and electrons. As there are considerable differences between the primary processes of electron and x-ray irradiation, this result indicates that secondary processes (the generation of low energy secondary electrons and ions in both electron and x-ray cases) must govern radiation damage.

In order to achieve the doses used in the studies above, the electron and x-ray beams were spread over areas of up to ~10 μm^2. In practice, it would be interesting to determine the highest spatial resolution at which undamaged spectra can be recorded with sufficient counting statistics in each instrument. Also, when discussing damage in terms of the amount of energy transferred, it is important to bear in mind that whilst XAS is a resonant process in which absorption events lead almost exclusively to analytically useful inner shell excitations, inelastic scattering of high energy electrons mainly results in valence electron excitations (both collective and single-electron transitions) which contribute to sample damage without contributing to the core loss spectrum. The fraction of electron scattering events which lead to inner shell transitions of interest is also smaller for edges at higher energy-loss.

3.8. The carbon K edge

One option to reduce *electron* beam damage is to make use of the low loss region of EELS spectra. Low-loss transitions have much larger cross-sections than core excitations, allowing shorter acquisition times, and therefore lower doses, to be used. In a study of the toxicity of C_{60} to human macrophage cells, Porter *et al.* used low loss EELS techniques to avoid degradation of C_{60} under the

high electron doses required for core-loss measurements [62]. They demonstrated that the shift in π+σ plasmon between 22 and 26 eV could be used to distinguish between C_{60} and cellular carbon, and thus mapped the distribution of C_{60} crystals within the cells. As the C_{60} was present in macrophages in clusters of ~200 nm, spatially-resolved studies were also possible in the STXM. The STXM study demonstrated that x-rays were not too damaging to perform core loss measurements of C_{60}. Using a 50 nm x-ray probe at the STXM at beamline X1A1 of BNL, areas containing C_{60} and cell cytoplasm were distinguished and mapped at the carbon K edge (Figure 3.14) [63]. The use of x-rays in this study provided more easily interpretable core loss spectra which show C_{60} distributions consistent with the previous work.

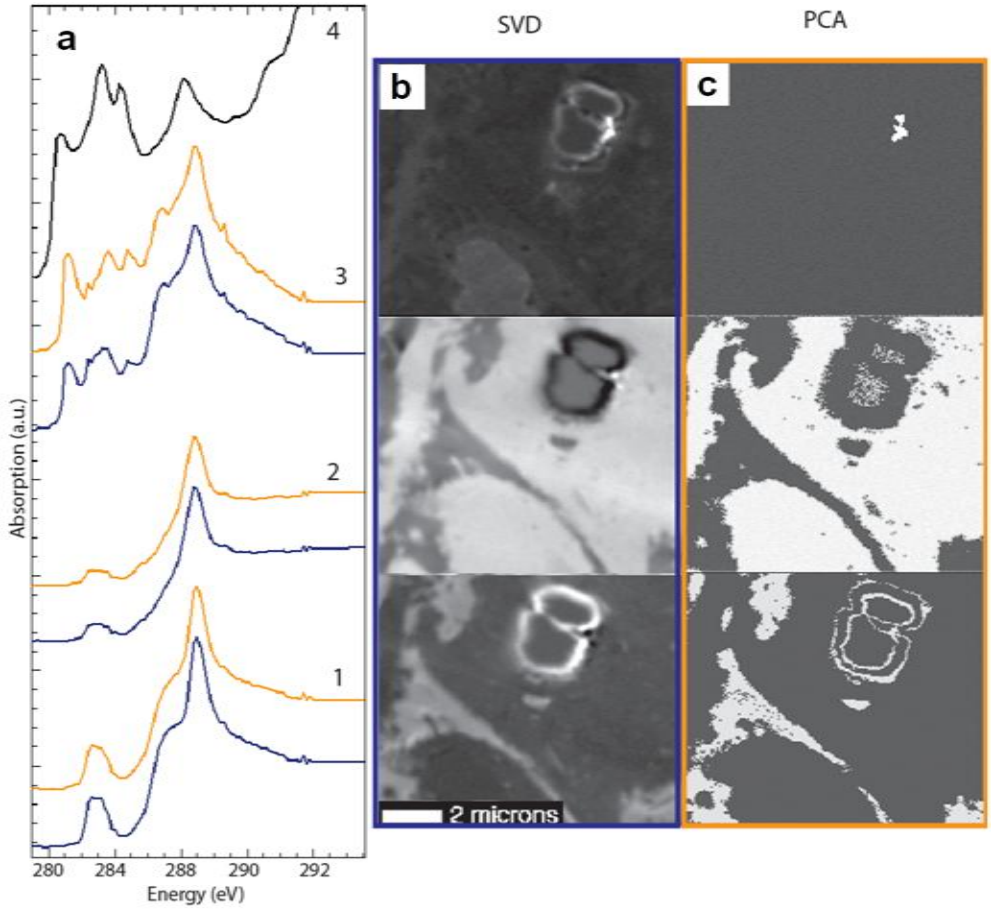


Figure 3.14 (a) X-ray absorption spectra 1-3 are from resin-rich, cell-rich and C_{60}-rich regions of a cell section. Spectra from both SVD and PCA analysis are shown. Spectrum 4 is a C_{60} reference spectrum. (b) and (c) Corresponding thickness maps and cluster maps from SVD and PCA analysis respectively. Adapted from [63].

Electron beam damage can be reduced by operating below the ~86 kV knock-on damage threshold of carbon [64]. Detailed EELS fine structure at the carbon edge has been reported in a study of graphene using a lower operating voltage of 60 kV [65]. The combination of low operating voltage

and a corrected electron probe allowed atom-by-atom measurements of different bonding states to be obtained at the edges of graphene sheets (Figure 3.15).

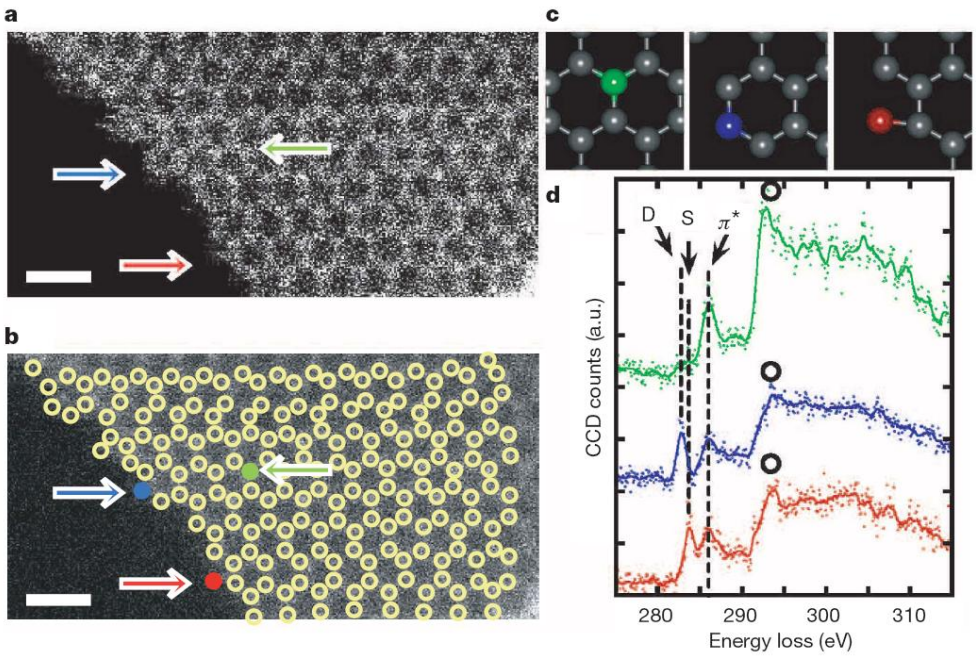


Figure 3.15 (a) STEM dark field image of a single layer graphene edge and (b) overlaid atomic positions. (d) Monochromated EEL spectra taken from the coloured atoms show different fine structure due to the different coordination environments of the carbons (c). Reprinted by permission from Macmillan Publishers Ltd:Nature [65] copyright 2010.

The studies above show that both electron and x-ray spectroscopies are able to distinguish graphitic carbon from amorphous carbon spectra. We now consider distinguishing between carbon species which are more similar in nature. Recent work by van Schooneveld *et al.* [66] demonstrated the huge capabilities of EELS for the characterisation of hybrid organic-inorganic nanoparticles. The nanoparticles studied were composed of a Cd-containing quantum dot core surrounded by a silica shell, and coated with octadecane and two lipids: a PEG lipid and a Gd-containing lipid. Figure 3.16 shows HAADF images which reveal particle morphology at different stages of their synthesis, while EELS SI data provided quantitative elemental maps of Cd, C, Si, Gd. EELS measurements of the lipid layer, however, were more difficult. The electron dose required to perform sub-nanometre EELS with adequate signal-to-noise ratio (SNR) was found to degrade the lipids, although small differences in the fine structure were observed between amorphous carbon and damaged lipid spectra. To avoid the damage associated with EELS, the authors used lower dose HAADF imaging to perform quantification of the lipid layer. As contrast in a HAADF image is approximately proportional to the square of the atomic number, the Gd atoms appeared brighter, allowing the PEG:Gd-lipid ratio to be estimated.

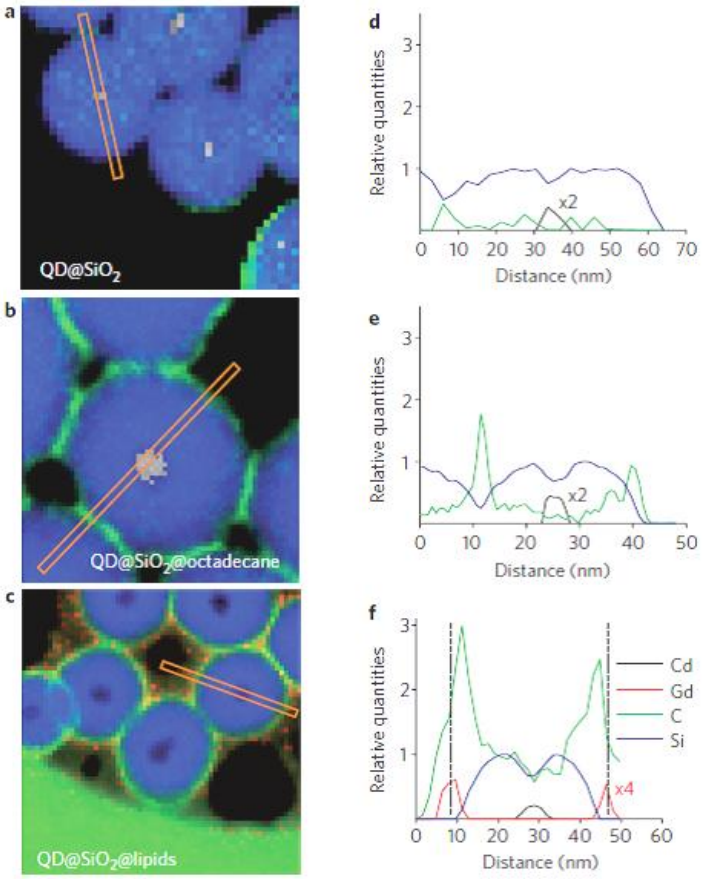


Figure 3.16 Chemical maps calculated from EELS measurements of hybrid nanoparticles at different stages of production (a-c). Cadmium (grey), silicon (blue), carbon (green) and gadolinium (red) relative profiles across the nanoparticle diameters are plotted opposite (d-f). Reprinted by permission from Macmillan Publishers Ltd:Nature Nanotechnology [66] copyright 2010.

Hitchcock *et al*. recently demonstrated the comparative ease of using STXM-XAS to distinguish between similar carbon compounds. In samples of SWNTs functionalised with dodecyl, they found signatures at the carbon K edge characteristic of a) graphitic carbon, b) oxidised SWNTs, c) carbon contaminants and d) dodecyl [67] (Figure 3.17). However, when trying to map the contributions of these components over bundles of SWNT, some fitting errors were observed due to the similarities between spectra of each component. Further work is therefore needed to refine reference spectra before fully quantitative characterisation can be carried out. However, analysis of very similar fine structure may always be difficult, and more indirect measures of functionalisation may need to be employed, such as tagging of functional groups [68].

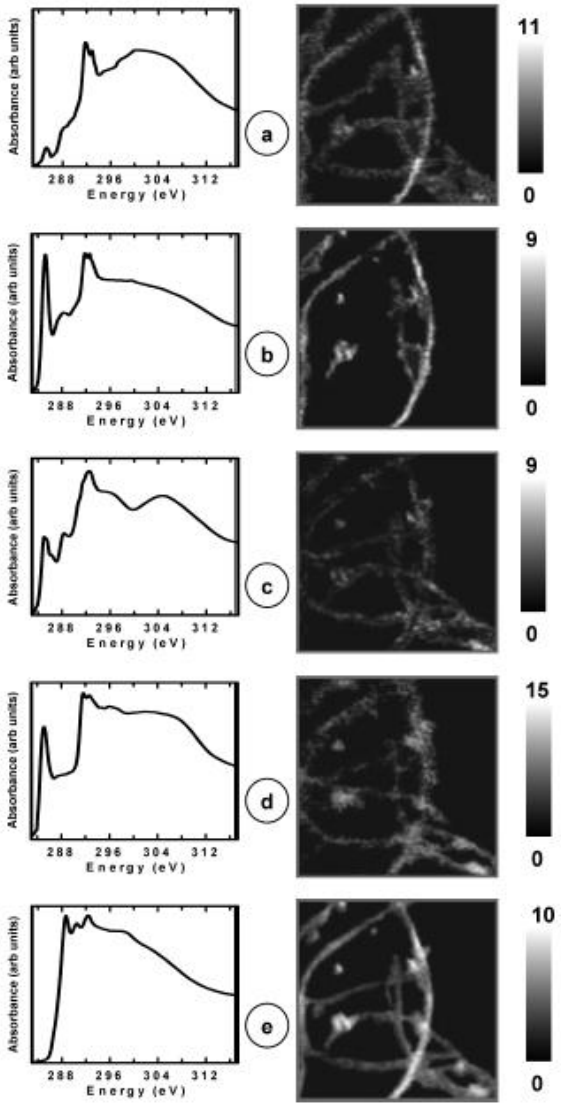


Figure 3.17 STXM-XAS spectra of the five components present in dodecyl-functionalised SWNTs: horizontal SWNTs (a), vertical SWNTs (b), oxidised SWNTs (c), carbon contaminants (d) and dodecyl (e). The corresponding chemical maps obtained from fitting these reference spectra to a region of SWNT bundles are displayed to the right. Reprinted with permission from [69]. Copyright 2010 American Chemical Society.

The examples discussed here demonstrate that STXM-XAS is capable of providing detailed spectral information of organic carbon species, whilst obtaining the same information in the electron microscope remains extremely challenging. However, a number of recent studies have shown that despite the limitations of electron beam damage, state of the art electron microscopes are capable of distinguishing between different carbon species using differences in fine structure of (damaged) EEL spectra. This situation can be expected to improve with the development of more efficient electron detectors, as well as furthered understanding of damage mechanisms, allowing optimised TEM conditions to be chosen.

3.9. Summary

This chapter has discussed advances in instrumentation which have brought the spatial and spectral resolutions of STEM-EELS and STXM-XAS closer together. However, the resolution gaps that exist today between each instrument are unlikely to be fully bridged by future technological advances, due to fundamental limitations e.g. the diffraction limit of soft x-rays. These differences, as well as the different damage mechanisms, and different requirements for sample preparation and environment, make a correlative approach to sample characterisation appealing. To date, no single study has employed both STXM-XAS and STEM-EELS to investigate the properties of systems on the nanoscale. The success of correlative TEM/STXM studies in fields such as biofilms suggests that there are more advantages to be gained in using the full chemical capabilities of both microscopes.

4. Instrumentation

The aim of this chapter is to describe the electron and x-ray microscopes used in this thesis. Each instrument will be briefly introduced, with emphasis on those developments that most affect the spatial and spectral resolutions of EELS/XAS measurements. Spectral processing techniques will also be discussed.

4.1. Instrumentation for EELS

In this section the overall operation of a TEM will first be described, followed by descriptions of individual components of basic TEMs such as the JEOL 2000, as well as the FEI Titan, which provides state of the art spatial and spectral resolution. The methods used to acquire and process EELS data in this thesis will also be discussed.

4.1.1. The transmission electron microscope

In a TEM, high-energy electrons are used to probe thin specimens. The transmitted electrons (or any x-rays generated) are analysed, providing structural and chemical information on the sample. Electrons are first generated by a source, and then accelerated to high energies using an electrostatic field. They are then focussed using a series of lenses known as the condenser system and upper objective lens. For TEM imaging, these lenses are used to provide parallel illumination at the specimen. For STEM imaging, the electron beam is focussed to a small probe at the specimen. Spatially-resolved information is acquired by raster-scanning the probe over the specimen while recording the transmitted beam intensity at each point. Typical condenser lens configurations required for each imaging mode are illustrated in Figure 4.1 [70]. The condenser lens system also controls the brightness of the beam, as well as the illuminated area (TEM) or beam convergence angle (STEM) [2, 70].

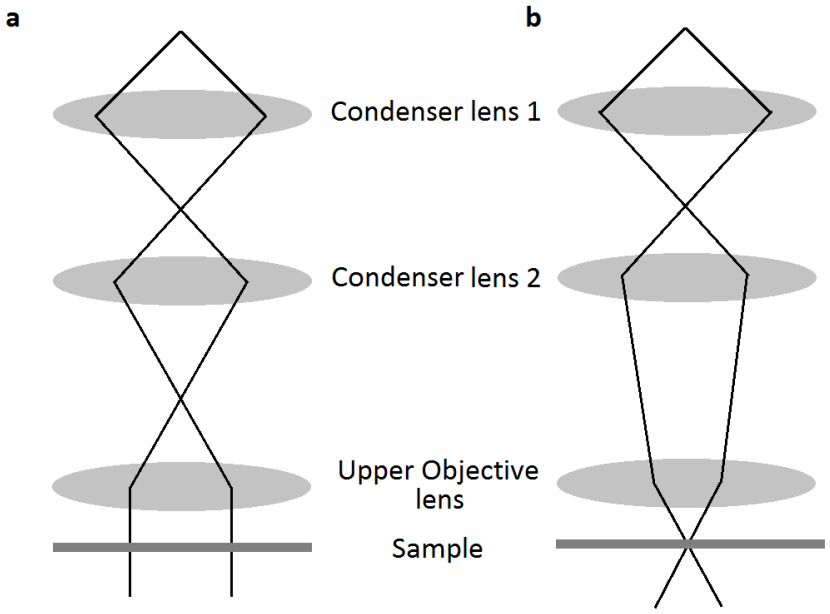


Figure 4.1 Ray diagram of the condenser lens system used to form (a) parallel illumination at the specimen for TEM imaging, or (b) a condensed probe at the specimen in STEM mode. Adapted from [70].

The lower objective lens is located after the specimen. In TEM mode, this lens takes the transmitted electrons and forms a diffraction pattern in the back focal plane. The projector lenses then transfer either the diffraction pattern or the image, on to a detector (Figure 4.2) [2]. This is done by choosing either the back focal plane, or the image plane of the lower objective lens, as the object of the first projector lens. Projector lenses control the magnification in TEM mode. Magnifications of several million times can now be achieved [16]. In contrast to TEM, STEM magnification is controlled by the dimensions over which the probe is scanned rather than the strength of the projector lenses. Although projector lenses are not used for image magnification in STEM mode, they are useful as transfer lenses so that the acceptance angles of the STEM detectors can be controlled [71].

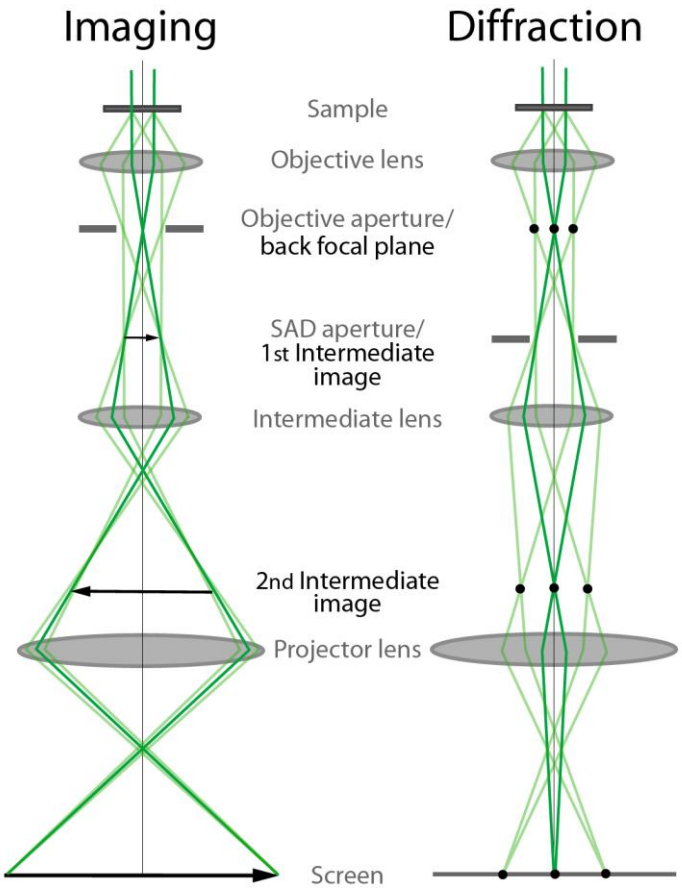


Figure 4.2 Ray diagrams of the projector system for TEM imaging and diffraction. Adapted from [2].

4.1.2. Contrast

Contrast in a TEM or STEM image arises when we select or exclude those post-specimen rays which are allowed to contribute to an image. In TEM mode, this selection is performed using the objective aperture, which is located in the back focal plane of the objective lens (*i.e*. at the diffraction pattern). In STEM mode, the selection is made at the level of the STEM detectors (see section 4.1.4.3) [2].

Figure 4.3 Ray diagram showing that highly scattered rays are blocked by the objective aperture, and so do not contribute to the bright field TEM image. From [2]. shows the effect of an objective aperture on the rays which contribute to a TEM image. If this aperture is centred around the optic axis, the direct beam is transmitted while electrons scattered to high angles are blocked, and do not contribute to the TEM image. This means that the regions within the sample which scatter highly appear darker. Such images are known as bright field (BF) images [2].

Incoherent (Rutherford) elastic scattering was discussed in section 2.1.1. From equation 2.1 we know that the Rutherford scattering cross-section is a function of Z^n where n~2 [8]. Therefore, high

Z regions will scatter more than low Z regions. Higher densities, ρ, and sample thicknesses, t, also increase scattering. Therefore this contrast mechanism is known as mass-thickness contrast. This is an important contrast mechanism in bright field images [2]. At low scattering angles, mass-thickness contrast also competes with diffraction contrast from coherent elastic scattering. In diffraction contrast, electrons are scattered into Bragg angles by a periodic crystal structure, and the intensity detected depends on the orientation of the sample [2].

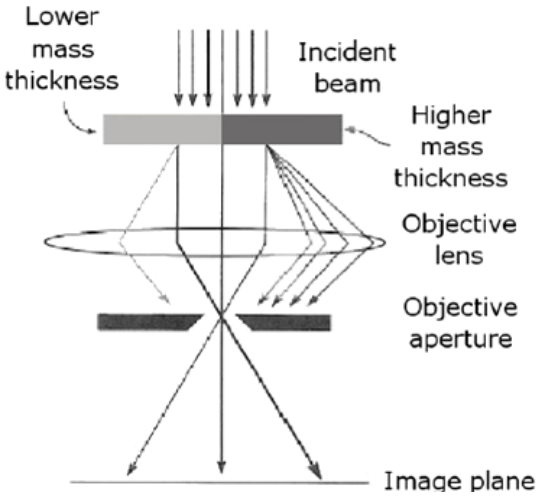


Figure 4.3 Ray diagram showing that highly scattered rays are blocked by the objective aperture, and so do not contribute to the bright field TEM image. From [2].

Dark field (DF) TEM images contain complementary contrast to BF images. DF TEM images may be obtained by selecting a portion of the scattered beam to form the image [2], which can be done in two ways:

a) by moving the objective aperture to a diffracted beam;
b) by tilting the diffraction pattern such that a diffracted beam travels down the optic axis (and hence through the centred objective aperture).

The transmitted electrons from a STEM probe can be recorded by a number of detectors simultaneously. The bright field (BF) detector is centred at the optic axis, and collects the direct beam. A range of annular detectors collect the scattered electrons to form dark field STEM images. The annular geometry of these detectors allows them to collect a larger proportion of scattered electrons, making dark field STEM imaging more efficient than dark field TEM. Additionally, electrons scattered to very high angles can be collected to form high angular annular dark field

(HAADF) images. Diffraction effects are not present in electrons scattered to high angles, and so do not contribute to the HAADF image [2].

4.1.3. TEM hardware

4.1.3.1. Electron sources

An electron gun is used to generate and accelerate a beam of electrons. The type of source determines the brightness and energy spread of the beam. Brightness is defined as the current density per unit solid angle [2]; a high brightness (and coherence) is needed for analytical or high spatial-resolution work [16]. The energy spread will determine the extent to which fine structure can be resolved in an EEL spectrum, and can also enlarge the probe through chromatic aberration (see section 4.1.3.2). Two main electron sources are used in TEMs. The JEOL 2000 has a thermionic source. Titan has a (thermally-assisted) FEG.

a) **Thermionic sources.** A filament which is heated resistively provides the electrons with enough energy to enable them to overcome their work function and leave the source. Filaments are commonly made of tungsten (for its high melting temperature) or lanthanum hexaboride (for its low work function). The electrons they produce are then accelerated and focused by an electric field. This field is generated between the filament, an anode and a grid called the Wehnelt cylinder. Thermionic sources produce beams of relatively low brightness and large energy spreads [16].
b) **Field emission guns** (FEGs). There are two types of FEG. Cold field emission guns (CFEGs) apply a high electric field to a metal surface, enabling the electrons to escape by tunnelling. A CFEG can emit over a thousand times more electrons than thermionic guns [17], and has the lowest energy spread of all guns, at ~0.3 eV. Thermally-assisted field emission (Schottky) guns use both an electric field to lower the work function and heating to provide electrons with energy, so much so that in this case tunnelling does not occur. Schottky emitters have intermediate energy spreads of ~0.7 eV [2].

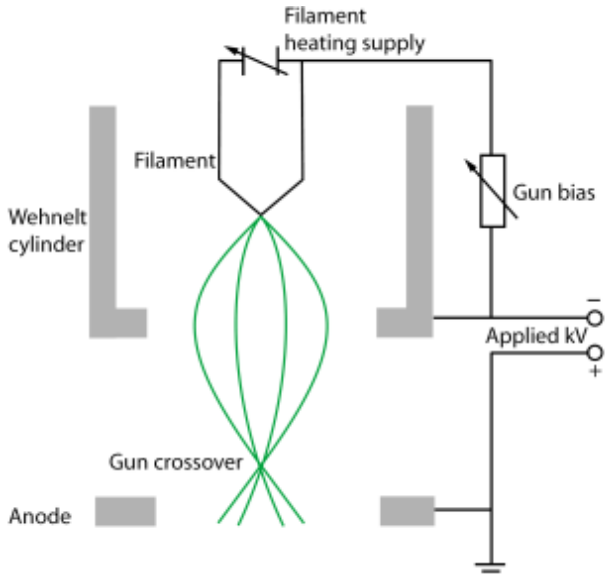


Figure 4.4 Schematic diagram of a thermionic electron source, adapted from [2].

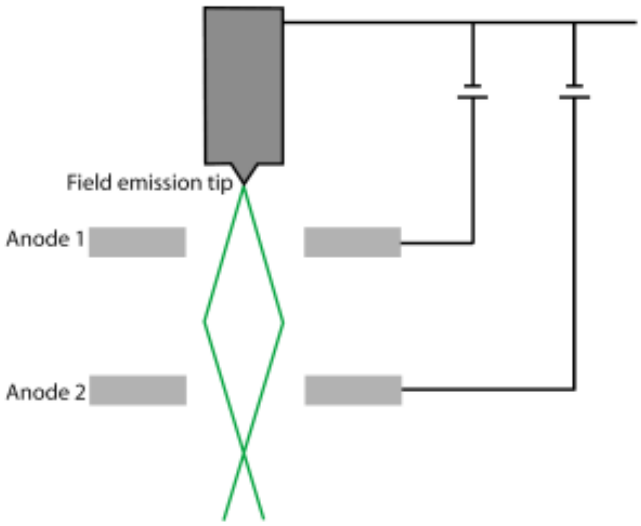


Figure 4.5 Schematic diagram of field emission gun, adapted from [2].

4.1.3.2. Electron lenses

The electron beam in a TEM is focussed using electromagnetic lenses. These lenses are composed of copper wire wound round a 'pole-piece', which is a cylindrical soft iron core with an axial borehole. Current passing through the wire creates an axially symmetric magnetic field in the bore. The lens makes use of the fact that a magnetic field B acts on an electron of velocity v with a force $F = -e(B \times v)$. Focus is achieved by deflecting electrons into a helical path of decreasing radius,

causing a parallel beam to converge to a point [2]. Electromagnetic lenses are limited by the following lens aberrations [2]:

1. Astigmatism is a distortion whereby a lens has different focal lengths for rays of different orientations. This can result, for example, in circular features appearing elliptical. Astigmatism occurs when the magnetic fields in the lenses are not cylindrically symmetric, due to defects in the pole-piece. The proximity of apertures, contamination and specimen charging can also disturb the magnetic field. This can be corrected using compensatory fields created by stigmators in the condenser and objective lens systems.
2. Chromatic aberration (Figure 4.6 (b)) occurs because the electrons in the beam are not completely monochromatic. Lower energy electrons are focused more strongly by the lens. This leads to a point object being imaged as a disk, with a radius r_{chr} of

$$r_{chr} = C_c \frac{\Delta E}{E_0} \beta \qquad \textit{Equation 4.1}$$

   where C_c is the chromatic aberration coefficient of the lens, ΔE is the deviation from initial beam energy E_0 and β is the semiangle of collection of the lens. This aberration is important in TEM images, as post-specimen electrons have a large ΔE after inelastic scattering. In STEM-EELS, as there is no imaging lens behind the specimen, chromatic aberration is only relevant in the condenser lens system where the pre-specimen energy spread of the beam is small. Therefore r_{chr} is small, though not negligible, in STEM mode.

3. Spherical aberration is caused by the lens over-focussing off-axis rays, as shown in Figure 4.6 (c). At the Gaussian image plane, where paraxial rays are focused, the radius of disk, r_{sph}, is given by

$$r_{sph} = C_s \beta^3 \qquad \textit{Equation 4.2}$$

   where C_s is the spherical aberration coefficient and β is the semi-angle of collection of the lens. It is spherical aberration that ultimately limits the spatial resolution in modern TEMs. For TEM imaging, the spherical aberration of the objective lens limits the image resolution. For STEM imaging, however, the spherical aberration of the *condenser* lens is most important, since it enlarges the probe [2].

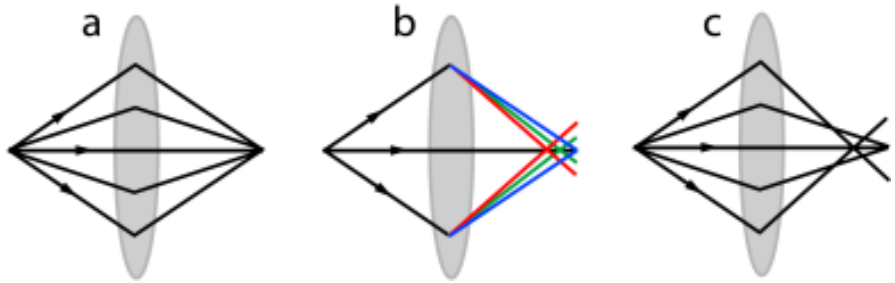


Figure 4.6 Illustration of a) a perfect lens where a point source is focused to a point, b) chromatic aberration where the rays of different energy are indicated by different colours, and c) spherical aberration where rays at different angles are focused to different points. The plane drawn, in which paraxial rays are focused, is known as the Gaussian image plane [19].

4.1.3.3. Spatially resolved electron detectors

TEM images and diffraction patterns are viewed on a detector, either a fluorescent screen or a camera such as charge coupled device (CCD) array [16]. In a CCD, electrons are incident on a scintillator (e.g. single crystal yttrium-aluminium garnet (YAG)), where the electrons produce photons. These photons are transferred by a lens system on to the CCD chip [16]. CCD chips typically contain 2048 × 2048 pixels, each one a metal-oxide semiconductor capacitor. Charge is stored in each capacitor, proportional to the transferred photon intensity. The charge can be read from individual pixels serially. Pixels can also be summed first before being read out, in a process called binning. This reduces the overall number of read-out events, and improves the signal-to-noise ratio (SNR). However, binning is done at the expense of the dynamic range, and in some cases, the spatial resolution [72].

4.1.3.4. X-ray detectors

To perform chemical analysis, an energy dispersive x-ray (EDX) detector can be fitted above the specimen. This detector collects x-rays emitted from the sample when outer shell electrons fall into the core holes created from inelastic scattering [2]. The x-rays have energies characteristic of the atoms that emitted them, allowing chemical species to be identified. EDX spectra are easier to acquire than EELS, and have low backgrounds arising from Bremstrahlung, or breaking radiation emitted when electrons are decelerated in the sample. This low background makes heavy elements easier to detect using EDX. However, there are some major drawbacks. The low energy resolution of the EDX detector (100-150 eV) means that more detailed chemical information can only be provided by EELS [7, 73]. In addition, most EDX detectors have very low efficiencies, collecting only

~1% of the x-rays compared to the ~50% efficiency of EELS systems. However, recently developed silicon drift detector systems, which have large collection solid angles of ~1 steradian, have improved the sensitivity of EDX by a factor of about ten [74].

4.1.4. FEI Titan hardware

All STEM imaging and EELS data in this thesis was acquired using the FEI Titan microscope at Imperial College London. As well as the standard components of a (S)TEM, the FEI Titan is equipped with a monochromator and EELS spectrometer. A three-condenser lens system provides greater user control over the illumination conditions at the specimen, and a spherical aberration corrector uses non-rotationally symmetric hexapole lenses to compensate for the spherical aberration of the objective lens. This improves the spatial resolution of TEM imaging, however as no HRTEM images were acquired in this thesis, details of the C_s corrector will not be discussed here. For a review of this type of corrector the reader is referred elsewhere [22].

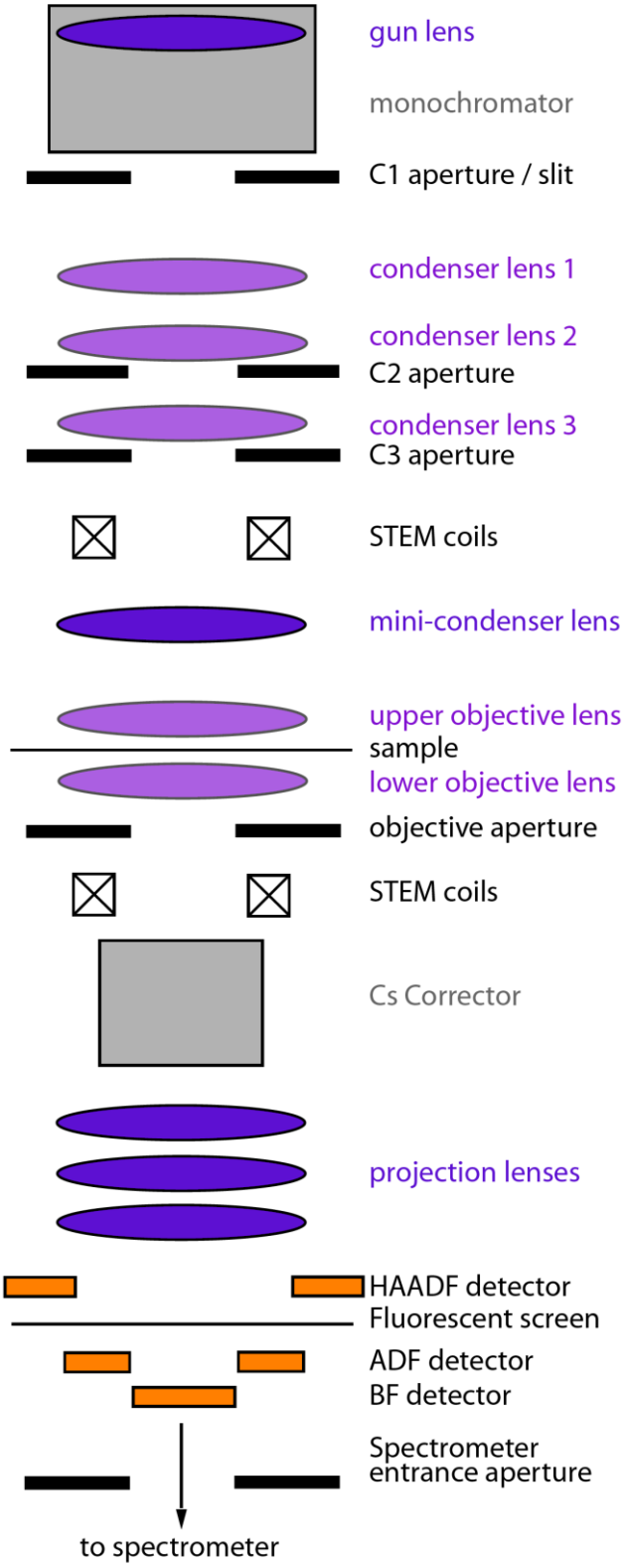


Figure 4.7 Schematic showing the optics of the FEI Titan (S)TEM. Adapted from [75].

4.1.4.1. Monochromator

A relatively new development in TEM design is the inclusion of a monochromator after the electron gun. This consists of a filter which disperses the electrons, and a monochromising slit which allows only those electrons within a small range of energies through. The monochromator thereby decreases the energy spread of the electron beam, which is particularly important for EELS [76].

The Titan is fitted with an in-column Wien filter monochromator. The action of the monochromator can be thought of simply by considering an electric field E and a perpendicular magnetic field B which are both constant along the length of the monochromator [76]. The deflecting electric and magnetic forces experienced by an electron of velocity v are therefore $-eE$ and $-eBv$, respectively. For electrons with average velocity $v = \frac{E}{B}$, the deflecting forces cancel and the electron passes straight through the monochromator, along the central axis. Electrons with higher velocities experience a larger magnetic deflection, which brings them towards the negative electrode. As the electron approaches the negative electrode, it loses kinetic energy. As a consequence of the lower electron velocity, the relative strengths of the deflective forces are also altered, and the electron is brought back to the central axis [76]. The deflective fields have an analogous effect on electrons with lower than average energies. The Wien filter also has a focussing effect on off-axial electrons, and so acts as a lens. Both the degree of dispersion and the lens strength depend on the strength of the deflective fields, known as the monochromator 'excitation'. Increasing the monochromator excitation increases the dispersion of the beam falling on the energy selecting slit at the exit of the monochromator, and hence decreases the energy range of the electrons which are selected to form the beam. This improvement in the energy resolution of the beam comes at the expense of lower beam currents, and hence longer acquisition times [8].

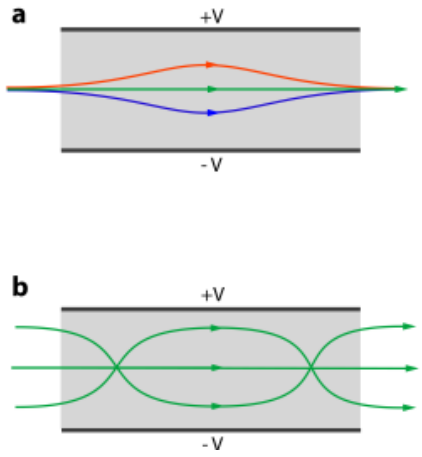


Figure 4.8 Diagram showing the paths of the electrons through a simple Wien filter. (a) Electrons which enter with average velocity (green) experience equal electric and magnetic deflection and travel along the optic axis. For faster or slower electrons, these forces are unbalanced and the electrons are deflected away from the optic axis. As they approach the electrode, their energies are altered, bringing them back towards the optic axis again. (b) Ray diagram showing the action of the Wien filter on off-axial electrons. Adapted from [76].

4.1.4.2. Condenser system

While many conventional TEMs operate with two condenser lenses, the Titan has three condenser lenses, as well as a minicondenser lens situated above the objective lens. These additional lenses provide greater control over the illumination area and convergence angle at the sample [70].

Neighbouring pairs of condenser lenses are coupled to form a 'zoom system'. In a zoom system, the object position of the first lens and the image position of the second lens remain constant. Then a change in the position of the intermediate image has the effect of changing the convergence angle at the image of the second lens [70].

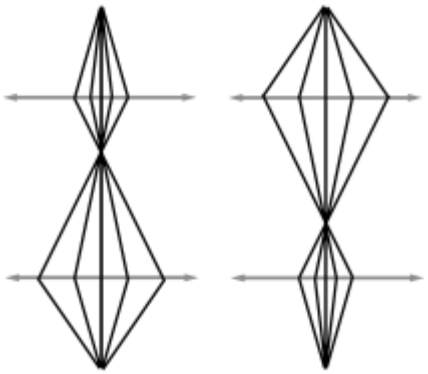


Figure 4.9 Ray diagrams of a zoom system in two settings. In both cases the object of lens 1 and the image of lens 2 are in the same positions. By changing the position of the image of lens 1, the convergence angle at the image of lens 2 also changes. Adapted from [70].

In the Titan, the C1 and C2 lenses form a zoom system. As the C2 aperture is beam defining, C1-C2 zoom controls the beam current (called the spot number). The C2-C3 zoom system defines the illumination area in TEM, or the convergence angle in STEM [70].

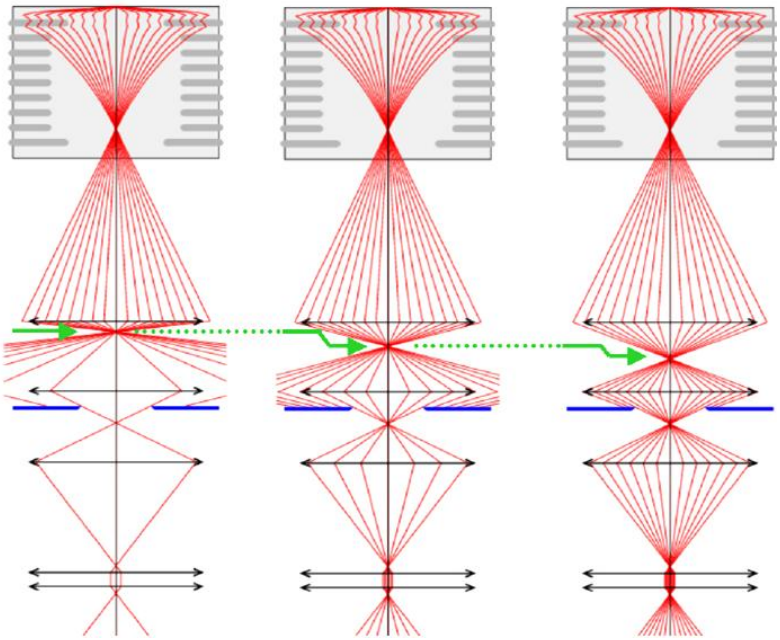


Figure 4.10 Ray diagrams showing a range of different 'spot numbers', i.e. different image positions of condenser lens 1. The image positions of C1 are marked with green arrows. Changing the spot number alters the amount of current in the beam. From [70].

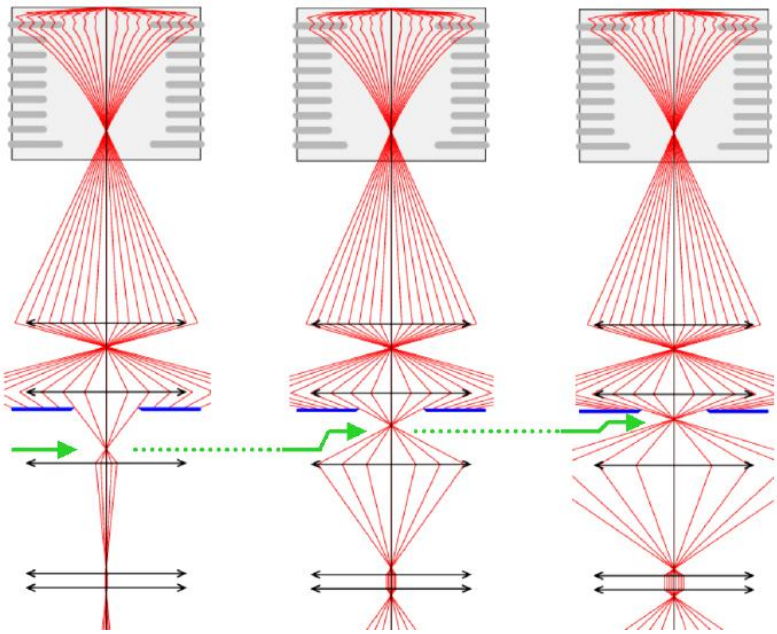


Figure 4.11 Ray diagrams showing how the image position of condenser lens 2 alters the size of the parallel illumination in TEM mode. The image positions of C2 are marked with green arrows. From [70].

The minicondenser lens is used to increase the range of areas over which parallel illumination can be obtained. In TEM mode the minicondenser lens focuses the beam to a cross-over point just above the upper objective lens. The upper objective lens is then used to form a parallel beam at the sample (Figure 4.12). This is useful for TEM imaging. However in STEM mode the probe is larger when the minicondenser lens is on, and for this reason the mincondenser lens is often switched off for STEM imaging (this is known as nanoprobe mode) [70].

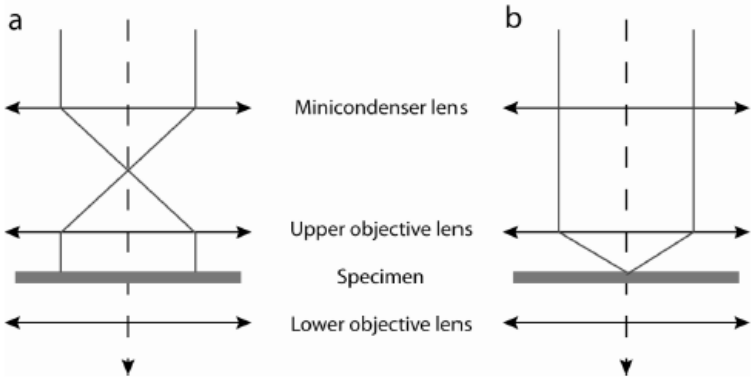


Figure 4.12 Ray diagram of the minicondenser lens in (a) TEM and (b) STEM modes. Adapted from [70].

Another advantage of the three-condenser lens system is realised when the monochromator is excited. Exciting the monochromator reduces the object distance of the C1 lens. The object, ~1 µm in size, is now located at the monochromising slit. At its maximum strength, the C1 lens provides a demagnification of ~1000×, which is insufficient to form a sub-nanometer probe from this image. Therefore the C2 lens is needed to provide additional demagnification of the source image. The strength of the C2 lens now controls the probe size, and the C3 aperture becomes the beam defining aperture [70].

4.1.4.3. STEM detectors

The Titan is equipped with four STEM detectors: a bright field (BF) detector, two annular dark field (ADF) detectors and a high angle annular dark field (HAADF) detector, some of which are shown in Figure 4.13. The BF detector collects the direct beam. The annular detectors, both above and below the viewing screen, collect only scattered electrons. The inner and outer collection angles of the ADF detectors are labelled β_{in} and β_{out} respectively. By varying the camera length and the detector used, the user can control the range of scattering angles used to form any image. As the annular detectors do not block the spectrometer entrance aperture, dark field images may also be obtained simultaneously with EELS data.

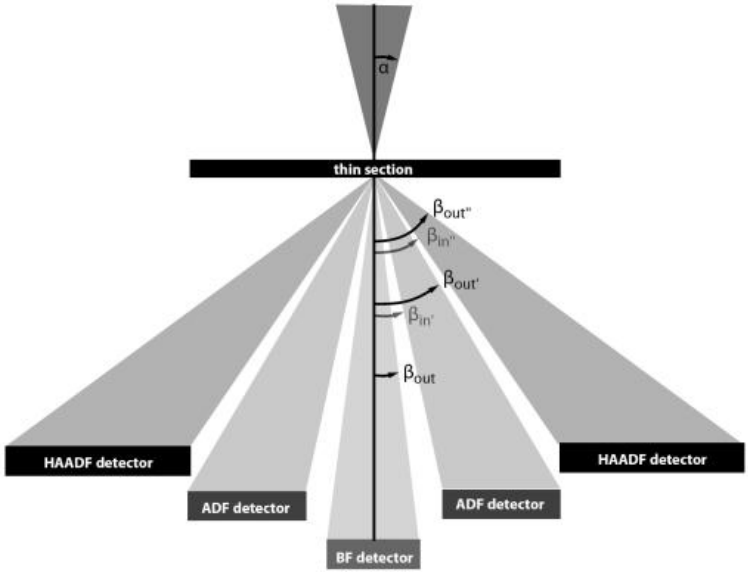


Figure 4.13 Diagram showing the geometry of HAADF, ADF and BF STEM detectors and their collection angles adapted from [2].

4.1.4.4. EELS Spectrometer

For EELS measurements a spectrometer is fitted under the detector system. This is commonly a magnetic prism, which produces a magnetic field perpendicular to the electron trajectory. Electrons are selected by an entrance aperture, travel through the spectrometer in an evacuated 'drift tube', and are deflected through about 90°. The radius of curvature R of the electron trajectory is given by

$$R = \frac{\gamma m_0 \boldsymbol{v}}{e\boldsymbol{B}} \qquad \textit{Equation 4.3}$$

where γ is the relativistic factor, m_0 is the rest mass of the electron, e is the electron charge, B is the magnetic field and v is the velocity of the electron [8].

The field causes electrons to be focused as well as dispersed. Focusing occurs as shown in Figure 4.14. If we consider electrons from a point object at O, those deviating from the central trajectory travel different distances through the magnetic field, and hence are deflected through different angles. The result is that electrons of the same energy are brought into focus at a point in the dispersion plane. Lower energy electrons are deflected slightly more than higher energy ones, and brought to focus at a different position. In this way the electrons are dispersed according to their energy-loss [8].

The dispersion D is defined as the displacement of the focus per unit change in energy-loss [8]. The Titan is fitted with a GIF Tridiem 865 spectrometer which has a maximum dispersion of 0.01 eV per

pixel. To select different elemental edges, the whole energy-loss spectrum can be shifted across the detector by applying a voltage to the drift tube, changing the kinetic energy of all the electrons [7].

The magnetic prism suffers from aberrations, which limit the focussing power of the spectrometer and hence the energy resolution of EELS. In the GIF Tridiem 865, up to 4th order aberrations are corrected using octupole and decapole lenses, resulting in a spectrometer resolution of 0.1 eV for a 200 keV beam [77].

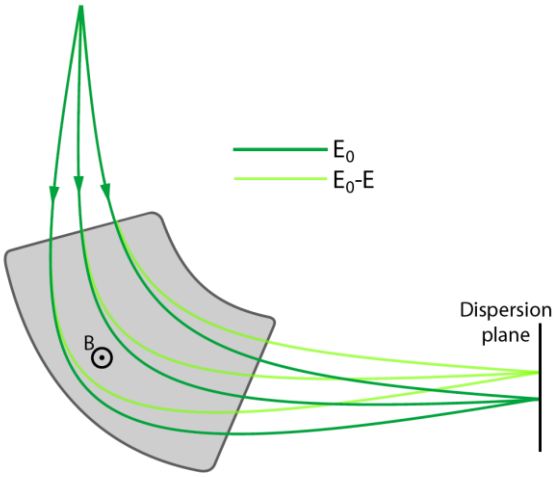


Figure 4.14 Diagram of the focusing and dispersing actions of a magnetic prism EEL spectrometer. Adapted from [8].

4.1.5. EELS Spectrum Image Acquisition

Early EEL spectra were collected in series, by scanning the spectrum across a slit on to a single detector [8]. EEL spectra are now collected in parallel, where the whole spectrum is detected at once on the position sensitive CCD detector. The latter is preferable, as it has the higher collection efficiency [2, 16].

In this thesis, EELS data is often acquired in the form of a spectrum image (SI). Here, a region of interest is selected and divided into an array of pixels. EEL spectra are then acquired sequentially at each pixel position. During acquisition of an individual spectrum, the STEM probe may either be held stationary at the centre of the pixel, or scanned over the entire pixel area. The latter is known as sub-pixel scanning, and may improve sample stability and reduce hole formation during SI acquisition of beam sensitive samples. The resulting spectrum image is a three dimensional dataset, with two spatial dimensions and one spectral dimension as shown in Figure 4.15. Spatial drift correction can be performed during SI acquisition. To do this, adjacent regions are imaged at

intervals during data acquisition. Cross correlation is then used to measure the spatial drift, and the STEM probe is deflected accordingly to compensate this drift.

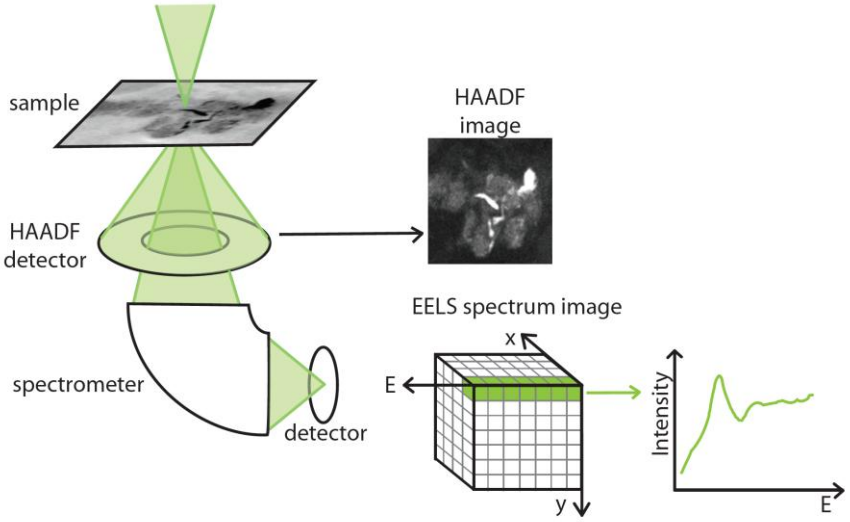


Figure 4.15 Schematic showing the acquisition of STEM-EELS data in the Titan microscope. An entire EELS spectrum is acquired at one position on the sample, after which the STEM probe can be moved to acquire EELS data at the next location. This can be done systematically to form a 3D data cube known as a spectrum image. Dark field images e.g. HAADF-STEM images may be acquired simultaneously with EELS data.

4.1.6. EELS Processing

Spectral drift can occur between different EEL spectra in a SI. This was corrected in all SIs by choosing a spectral feature which is present and unvarying in all spectra, and aligning the feature using an inbuilt cross correlation procedure in Digital Micrograph.

In EELS, ionisation edges are superimposed on a decreasing background, which must be removed. This is achieved by selecting a pre-edge energy window, no less than 30 eV wide. A power law function of the form $I=AE^{-r}$ is fitted to the signal within the window, and the extrapolated signal is subtracted from the raw data [7].

4.2. STXM-XAS

To achieve high spatial and spectral resolution XAS measurements, very intense x-ray beams are needed. For this reason, STXMs are located at synchrotron x-ray sources. Synchrotron facilities contain an electron storage ring which generates x-rays, and a beamline which conveys the x-rays to

the experimental chamber containing the STXM. The STXM experiments presented in this thesis were performed at soft x-ray beamlines of two synchrotron facilities: National Synchrotron Light Source (NSLS) at Brookhaven National Laboratory, Upton, USA and the Canadian Light Source in Saskatoon, Saskatchewan, Canada.

4.2.1. Synchrotrons

First generation synchrotrons were built as particle accelerators for high energy physics experiments. In these facilities, accelerated electrons are bent by dipole bending magnets into closed orbits in a storage ring. As a by-product of the curved trajectory of the charged particles, large quantities of x-rays were produced which were up to 10^6 times brighter than laboratory sources at that time [4]. Second and third generation synchrotrons were then built solely for x-ray experiments. These synchrotrons were fitted with 'insertion devices', designed to provide x-ray beams of very high brilliance, defined as the brightness per source area [4].

Insertion devices are periodic arrays of magnets which produce sinusoidal oscillations in the electron trajectory. They are categorized as wigglers and undulators depending on the size of the deflection angle they produce. Wigglers, with large deflection angles, generate a continuous spectrum of x-rays similar to that of bending magnets. Undulators emit photons in a forward beam cone, with a small spectral bandwidth (see Figure 4.16). The photon energy can be tuned by adjusting the magnetic field strength of the undulator [26]. This is done by changing the mechanical gap between the top and bottom magnets.

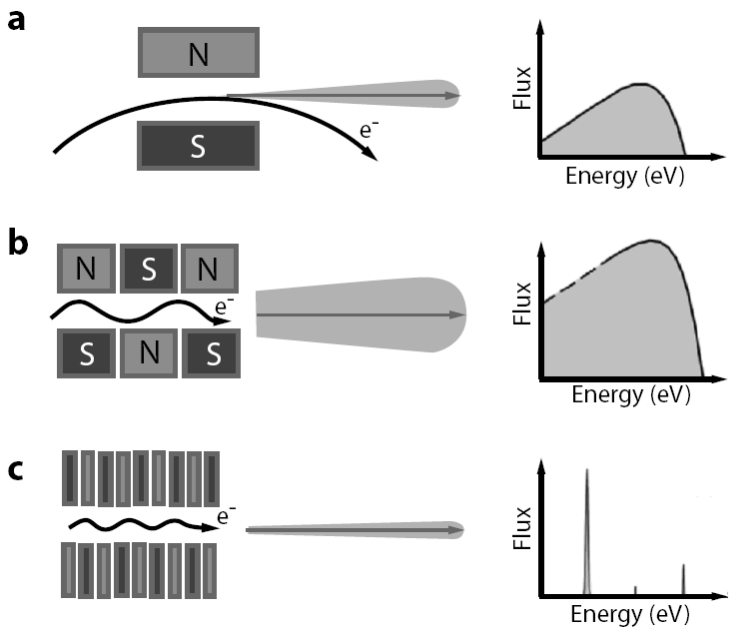


Figure 4.16 Spectra emitted from a) a bending magnet b) wiggler and c) undulator. Adapted from [26].

4.2.2. Monochromation in the beamline

Because of a lack of transparent and sufficiently phase shifting materials in the soft x-ray region, refractive optics are not used in x-ray facilities. The two main optical components in a beamline are mirrors to reflect, focus or split the x-ray beam and a monochromator, usually a diffraction grating. Grating monochromators are reflecting surfaces with a periodic array of lines, and these are rotated to scan through the photon energy. They increase the monochromacity of the beam, defined as $E/\Delta E$, to values of several thousand [78], high enough to resolve the fine structure in XAS spectra [26].

4.2.3. NSLS Beamline X1A1

In beamline X1A1, an undulator generates soft x-rays with energies between 250 and 800 eV. This beam is divided twice by mirrors to serve three beamlines, with the X1A1 beamline receiving ~20% of the illumination. In the horizontal plane, a toroidal mirror focuses the beam on to an entrance slit, after which the collimated beam is both dispersed and refocused by a spherical grating monochromator (SGM). An exit slit allows only a small bandwidth of photons through to the STXM. The same toroidal mirror simultaneously acts in the vertical plane to focus the beam at the exit slit [79].

4.2.4. CLS beamline 10ID1 (SM spectromicroscopy)

X-rays are generated by an elliptically polarized undulator (EPU). The EPU is an array of magnets with alternating magnetic orientations, and can produce either linearly polarized or circularly polarized x-rays. Monochromation is performed by a plane grating monochromator (PGM) which provides a nominal resolving power of 3000 (i.e. 0.1 eV for 300 eV photons) [80].

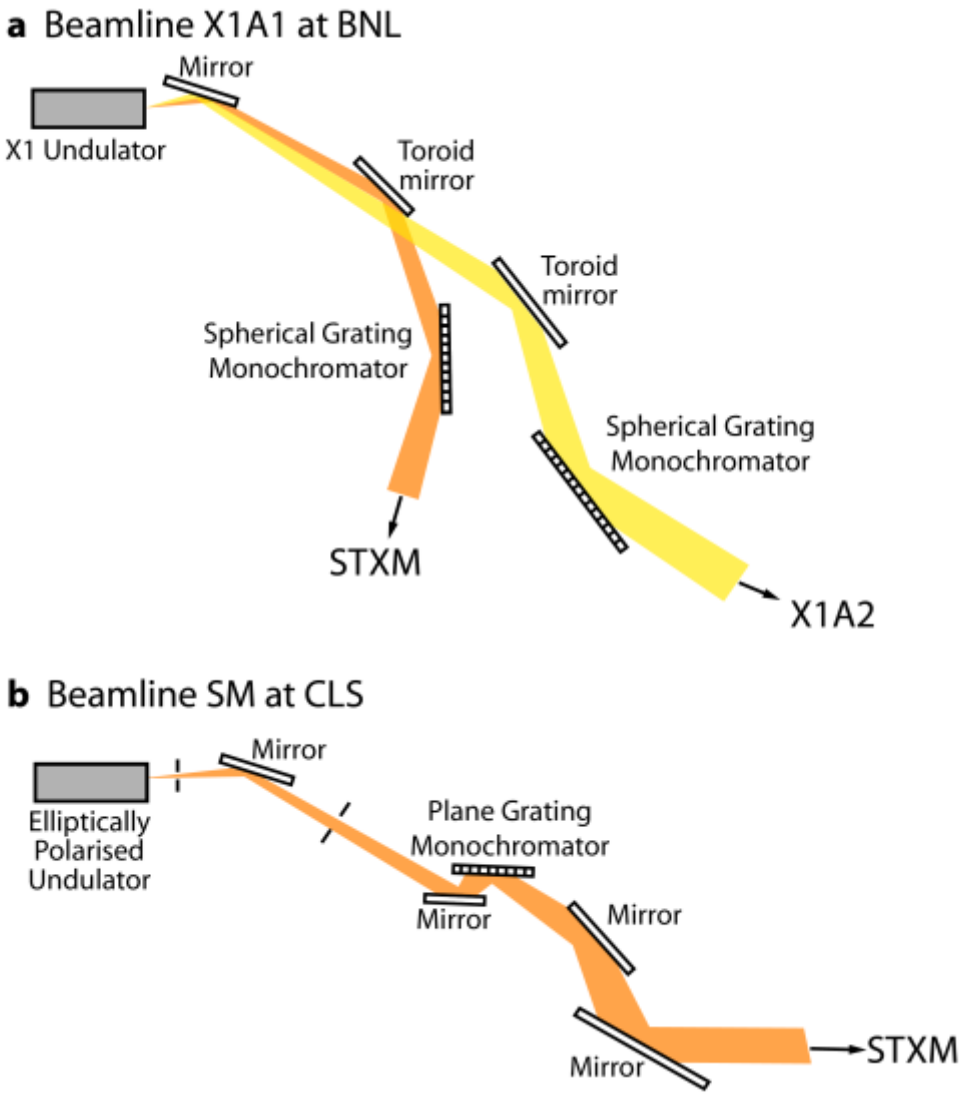


Figure 4.17 Schematic diagrams of the optics in the beamlines (a) X1A1 at BNL and (b) SM beamline at CLS. Adapted from [79] and [80].

4.2.5. Zone Plates

The limitation of refractive optics in the x-ray regime was discussed in section 4.2.2. For high resolution x-ray lenses, reflective optics are also inadequate as these are limited by the difficulty of fabricating surfaces with the required roughness and accuracy. Therefore, diffractive optics, in the form of Fresnel zone plates, are most often used as soft x-ray lenses [81].

A Fresnel zone plate is a circular diffraction grating. It is composed of N alternating transmitting and absorbing concentric rings (Figure 4.18), known as Fresnel zones. The widths of the zones are chosen so that for any two adjacent transmitting zones, the path lengths differ by mλ (where m is the diffraction order and λ is the wavelength). Constructive interference then occurs at a range of focal lengths f_m. This condition is satisfied when the radius r_n of the n^{th} zone is [81]

$$r_n{}^2 = mn\lambda f_m + \frac{m^2 n^2 \lambda^2}{4} \qquad \textit{Equation 4.4}$$

For large focal lengths, $f_m \gg m^2 n^2 \lambda^2 / 4$, and so the second term in Equation 4.4 can be ignored:

$$r_n \cong \sqrt{mn\lambda f_m} \qquad \textit{Equation 4.5}$$

An important parameter of the zone plate is the outermost zone width Δr (we will see later that this is closely related to the spatial resolution limit). The outer zone width is defined as [81]

$$\Delta r \equiv r_N - r_{N-1} \qquad \textit{Equation 4.6}$$

The focal length of the m^{th} diffraction order can be expressed as [81] (see Appendix 1)

$$f_m \cong \frac{4N(\Delta r)^2}{m\lambda} \qquad \textit{Equation 4.7}$$

In a Fresnel zone plate each positive diffractive order forms a separate focus point (Figure 4.19). Zone plates also give rise to negative diffraction orders, where the transmitted beam diverges. In order to use the zone plate as a focusing lens, only the first (positive) diffraction order can be transmitted. All other orders are blocked by an order-sorting aperture located close to the first

order focus, as well as a central beam stop on the zone plate itself (Figure 4.19). For a simple zone plate the first order diffraction efficiency is ~10%, though this can be improved by replacing the absorbing zones with material which shifts the phase by π [82].

Another important point to note from Equation 4.7 is that the focal length of a zone plate is inversely proportional to the x-ray wavelength. This means that the distance between a zone plate and the sample will need to be adjusted every time the incident photon energy is changed.

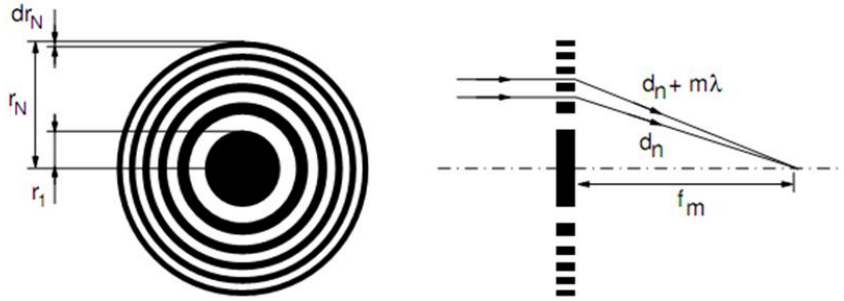


Figure 4.18 Schematic of a zone plate with N zones. The radius of zone N is r_N and its width is δr_N. Rays are brought to focus a distance f_m from the zone plate where m is the diffraction order. Adapted from [78].

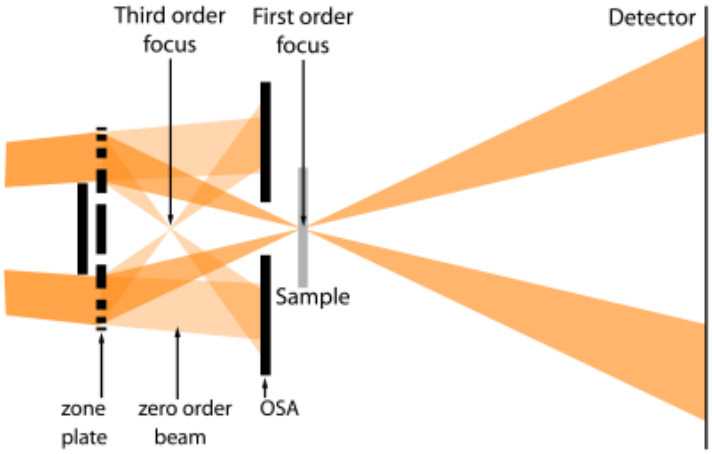


Figure 4.19 Schematic showing the focusing optics of the STXM. The order sorting aperture (OSA) is used to block all higher order beams, so that only the first order beam is used to form the probe at the sample. Adapted from [81].

The diffraction limited spatial resolution of a zone plate, δ, is related to the outermost zone width Δr by [78] (see Appendix 1).

$$\delta = 1.2\frac{\Delta r}{m} \qquad \textit{Equation 4.8}$$

The nanofabrication of such zone structures is technologically challenging. The zone plates used in this work were fabricated using electron beam lithography, which etches ring structures into metals

such as Ni or Ge [83]. Zone plates manufactured using these methods can have outer zone widths of ~20 nm [83]. Newer fabrication methods which divide a single zone plate into two sub-patterns (Figure 4.20) which are then overlaid can now provide zone widths of down to 12 nm [84].

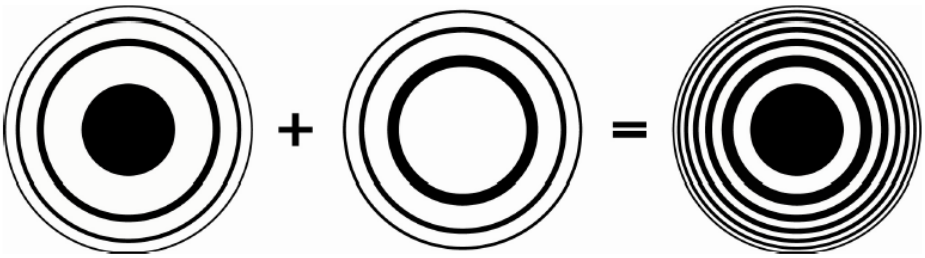


Figure 4.20 Schematic showing the two sub-patterns of zones which are manufactured individually, then combined to form the finished zone plate. Adapted from [84].

4.2.6. The scanning transmission x-ray microscope

The scanning transmission x-ray microscope (STXM) was developed in 1985 by Kirz and Rarback [14]. In this microscope, monochromated x-rays are focused by a zone plate on to a thin sample which is scanned across the probe while the transmitted x-ray intensity is detected. A schematic diagram of this microscope, as well as the related full-field transmission x-ray microscope (TXM) is shown in Figure 4.21. Unlike the TEM, full-field and scanning capabilities require the use of completely different microscopes. In the TXM, unmonochromated light is partially monochromated and condensed by a zone plate to a ~10 µm spot, and transmitted x-rays are imaged using a second zone plate on to a CCD camera. Although the TXM more easily achieves high spatial resolution [85], it is inferior to the STXM in two respects:

a) Since zone plates have typical efficiencies of 10%, the presence of a zone plate after the sample in the TXM means that the sample is exposed to ~10 times more dose than a STXM sample for a given number of photons detected.
b) The resolving power of a zone plate is ~100, compared to several thousand for a monochromator, so TXMs have limited spectral capabilities compared to STXM [14].

In an STXM, x-rays enter the chamber through a silicon nitride membrane. They are focussed by a zone plate and OSA, whose positions can be adjusted. The sample is also mounted on a number of scanning stages. A combination of piezo and stepper motors provides both high resolution positioning and large travel ranges. The detector used is a charge integrating detector. As the

absorption of soft x-rays is 10-100 times higher in air than helium, most experiments are performed in a helium atmosphere.

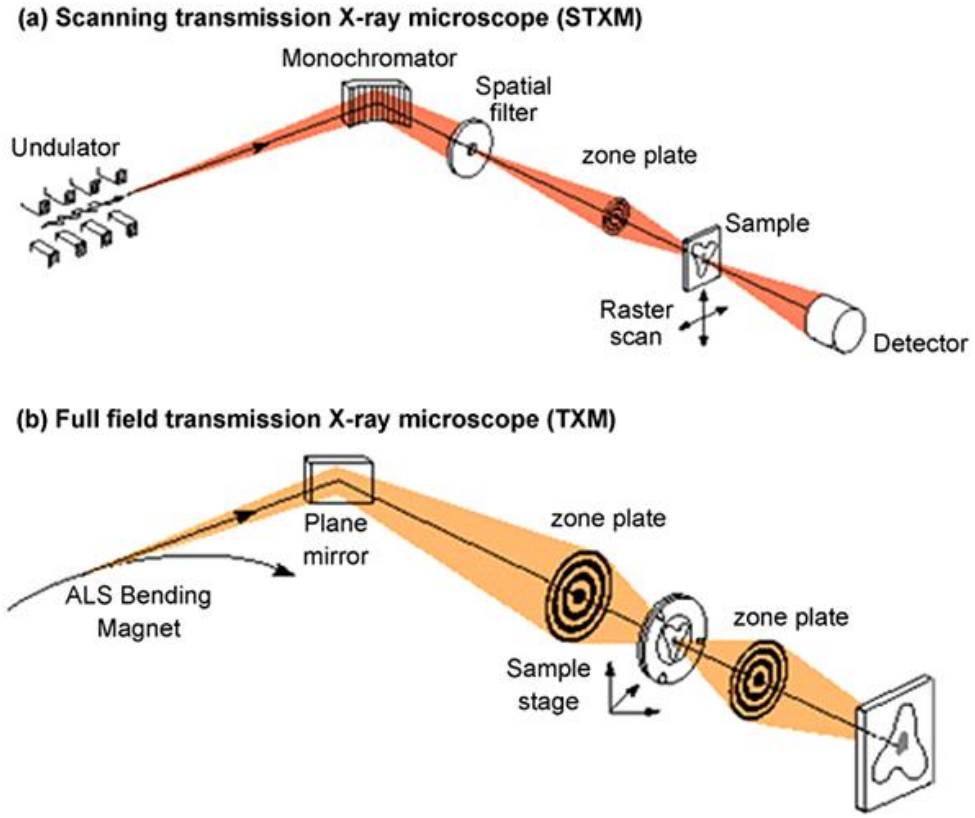


Figure 4.21 Diagrams of a) a STXM and b) a TXM. Reprinted from [14] with permission from Elsevier.

4.2.7. STXM-XAS data acquisition

Chemical information can be obtained from a single spot, a line, or it can be mapped over an area of the sample. For the latter, an absorption image is collected at a single photon energy by recording the transmitted flux while the sample is raster-scanned across the x-ray probe. The photon energy is then changed by rotating the grating monochromator and another absorption image is recorded. This process is repeated to acquire a 3D data cube or 'stack' (two spatial dimensions and one energy dimension), which is analogous to an EELS spectrum image (Figure 4.22). Since the focal length of a zone plate changes with photon energy, the zone plate needs to be moved along the optic axis at each energy step [15].

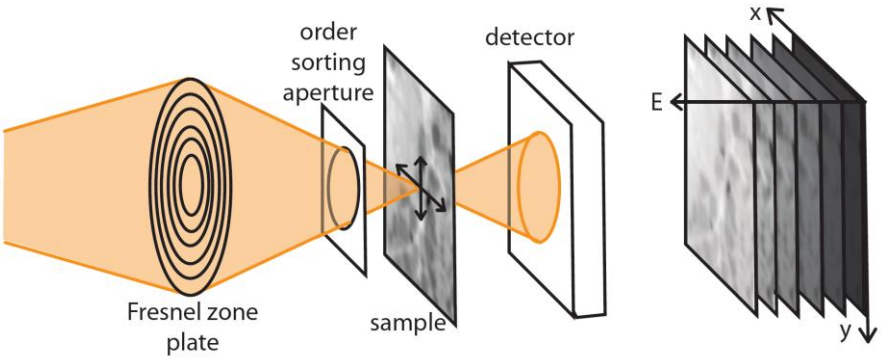


Figure 4.22 Diagram showing the acquisition of STXM-XAS data. An x-ray absorption images at a particular incident x-ray *energies is acquired. Images are acquired at a range of different incident energies, and built up into a 3D dataset called a 'stack'.*

For quantitative analysis, the transmitted x-ray intensity needs to be normalised against the incident intensity I_0, since this will vary as a function of time and photon energy. I_0 is ideally measured through a hole in the sample within the area over which the stack is acquired. If no hole is present in the area to be analysed, the I_0 spectrum can be recorded after stack acquisition, though errors may be introduced due to temporal variations in the incident flux. Stacks are then converted from transmitted flux to absorbance A, using

$$A = -ln\frac{I}{I_0} = \mu(E) \cdot t \qquad \textit{Equation 4.9}$$

Where μ(E) is the x-ray absorption coefficient and t is the sample thickness [86].

Although the transmitted x-ray signal is the most direct measure of x-ray absorption, total electron yield (TEY) is often used as an equivalent measure of XAS. TEY has the advantage of being surface sensitive and does not require samples to be thin, however it relies on the assumption that the number of electrons created is proportional to the number of photons absorbed [15, 87].

Normalisation against the incident flux (Equation 4.9) was performed using stack_analyze [88] and aXis2000 [89] software. Sequential images within a stack were then aligned using a cross-correlation function. This compensated for the lateral movement of the zone plate as well as thermal drift.

4.3. Processing large datasets

EELS SIs and STXM stacks contain rich and complex information. These 3D datasets may contain many hundreds of spectra, making it impractical to examine each spectrum individually. Often we are interested in mapping the variation in spectra features, or the different chemical components, across a dataset. Two common methods of calculating chemical maps have been used in this thesis: singular value decomposition (SVD) and principal component analysis (PCA). An overview of each technique is discussed below; for more complete treatment the reader is referred to dedicated reviews [10, 90, 91].

4.3.1. Singular value decomposition

Singular value decomposition (SVD) is also known as multiple linear least squares (MLLS) fitting in EELS literature. Strictly, this technique requires prior knowledge of all components in the sample, and their spectra.

In SVD, an experimental spectrum, I(E) (which is the absorbance for XAS, or the energy-loss electron counts for EELS), is recreated using a linear combination of each chemical component present in the sample:

$$I = I_1 \mathrm{t}_1 + I_2 \mathrm{t}_2 + \cdots + I_N \mathrm{t}_\mathrm{N} \qquad \textit{Equation 4.10}$$

where t_n is the mass thickness, and I_n is the spectral intensity of component *n*. The fit coefficients (t_n) are calculated by solving the linear Equation 4.10 at each pixel. The spatial variation of a coefficient can then be displayed in a 'chemical thickness map'.

The 'residual' is used as a measure of how well the calculated spectra fit the original data: at each pixel, the squared difference between a calculated spectrum and the experimental spectrum is summed to give a residual value. Residual maps can reveal poor fitting, which may be due to incorrect or missing components in the fitting model.

A major limitation of the SVD approach is that prior knowledge of the system, in terms of the components present or their spectra, is often incomplete [91]. In this case, internal reference spectra can be created. Regions containing different components are identified by inspection (when scrolling through a stack, different spectral components 'light up' at different energies). The spectra within each distinct region are summed to give an internal reference spectrum. These internal references can then be used chemical components for SVD fitting. Note that unless the specimen

contains regions in which only one chemical component is present throughout the thickness of the section, internal reference spectra will not be pure chemical phases.

4.3.2. Principal component analysis

PCA is also known as multivariate statistical analysis (MSA) in EELS literature. Unlike SVD, PCA does not require any prior knowledge of the physical components present in a sample. Instead, PCA analyses a dataset as a whole, and identifies the significant variations within the dataset. Variations are described by 'principal components', which can be thought of as *abstract* components. Just as we could decompose an experimental spectrum into a linear sum of real, chemical components in Equation 4.10, so we can use principal components [10]:

$$I = PC_1\mathrm{c}_1 + PC_2\mathrm{c}_2 + \cdots + PC_N\mathrm{c}_\mathrm{N} \qquad \textit{Equation 4.11}$$

where PC_n is the n^{th} principal component, and the coefficient c_n measures the contribution of PC_n to the experimental spectrum.

4.3.2.1. Calculating principal components

We start with our 3D dataset which contains P spectra, one for each spatial pixel. Each spectrum contains N energy points. This 3D dataset is arranged into a 2D data matrix, $D_{N\times P}$, which contains an experimental spectrum in each column (or an absorption/EFTEM image in each row). The covariance matrix, $Z_{P\times P}$, is calculated by multiplying D with its transpose [90]:

$$Z_{N\times N} = D_{P\times N} \cdot {D^T}_{N\times P} \qquad \textit{Equation 4.12}$$

Each element of Z gives a measure of the correlation between two absorption images. The eigenvectors of Z give us the principal components discussed above. Additionally, the eigenvalues measure the relative magnitudes of the statistical variations described by each principal component. Principal components with small eigenvalues describe low-amplitude statistical variations in the dataset [10]. These principal components often correspond to experimental noise, which can be removed. The remaining dataset is then a low-dimensional noise-filtered representation of the original data [10]. Thus, PCA is a very powerful technique allowing noise filtering without loss of spectral information. For further details on the calculation of principal components, readers are referred to dedicated reviews [10, 92, 93].

4.3.2.2. Cluster analysis

In effect, PCA has re-expressed the original dataset more concisely, using the eigenvectors of the covariance matrix as a basis set that was created from the data itself. Plots of the principal components can provide insights into the spectral variations in the dataset. However, a major limitation of this approach is that principal components are not always straightforward to interpret. They are abstract spectra, describing the differences between spectra in the dataset, with both positive and negative responses. Physically meaningful spectra of real chemical components can be recreated using a linear superposition of principal components, but this requires some prior knowledge of the components in the sample [90].

Often, in order to return to physical components, principal components are not examined directly but are used in 'cluster analysis' routines. Cluster analysis groups all pixels with similar experimental spectra into the same 'cluster'. This analysis is performed on the noise-filtered dataset, whose smaller size provides a great saving in computational cost compared to the original dataset. All pixels within the same cluster are identified, and their spectra are summed. The results of cluster analysis are displayed as a map of the distribution of clusters, as well as summed experimental spectra for each cluster. In this way, PCA can reveal subtle trends within datasets which may otherwise be missed by manual inspection [10, 92].

5. Fate of MWNTs in macrophage cells

5.1. Introduction

The huge and growing interest in carbon nanotubes (CNTs) has been fuelled by their exceptional electronic and mechanical properties, making them relevant to a wide range of applications, from field emission displays to ultra-strong composites **[94]**. CNTs are currently amongst the most commercially important nanostructures with annual production reaching hundreds of tonnes per year **[95]**.

One of the most promising potential applications of CNTs is in the field of nanomedicine. Their hollow structure and large surface area allows them to be loaded with drugs and targeting biomolecules **[96]**. These properties, combined with their high propensity to cross cell membranes **[97]**, make CNTs ideal for drug delivery applications. Already, there have been a number of proof-of-concept reports of functionalised CNTs used as drug delivery systems in mammalian cells **[98, 99]**. Hand in hand with this interest in CNTs for nanomedicine comes an urgent need to evaluate CNT biocompatibility and toxicity. This is particularly important as CNTs are perceived to be one of the most biologically non-degradable man-made materials **[100]**, and even functionalised, oxidised CNTs have been found to persist in animal models after four months **[101-103]**. Biopersistence has been found to be a critical factor in determining the chronic toxicity of similar systems such as carbon fibres and asbestos **[104-106]**.

CNTs administered for drug delivery applications are likely to encounter macrophage cells. These cells are involved in many immune processes, and their function is to clear pathogens and other foreign material, as well as cellular debris. Macrophages engulf and internalise foreign bodies via an active process called phagocytosis. Engulfed material is contained by a lipid membrane called a 'phagosome'. Phagosomes may fuse with an enzyme-containing lysosome, forming a phagolysosome, with the aim of degrading the material using oxidant-generating enzymes (Figure 5.1).

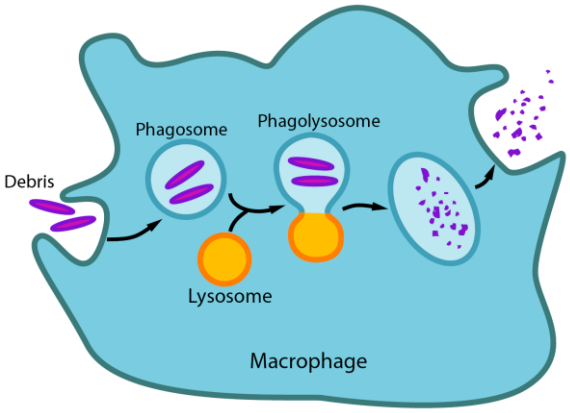


Figure 5.1 Cartoon showing the engulfing and degradation of foreign material by a macrophage cell. Adapted from [107].

There has been much focus on the toxicity of CNTs to macrophage cells, though results are often conflicting [108-113]. While some studies observe no cytotoxicity [111], others report increased cell death, inhibited cell proliferation and DNA damage, with increasing evidence that this toxicity is caused by oxidative stress [108, 112, 113]. The most likely cause of these inconsistent findings is the wide variation in the physico-chemical properties of the CNTs used in different toxicity studies [114]. Properties which have been found to influence CNT toxicity include tube dimensions, surface functionalisation, purity (i.e. presence of metallic catalyst particles) and aggregation state [115]. Clearly, it is necessary to characterise all relevant physico-chemical properties if the mechanism of CNT toxicity is to be fully understood. The aggregation state of CNTs is a particularly important parameter as this will determine what proportion of the CNT dose, i.e. how much *surface*, will be exposed to the cell. CNTs are notoriously difficult to disperse, and the stability of dispersions vary greatly with the solvent environment [116]. Aggregation state is often overlooked as it is difficult to quantify with the commonly used characterisation techniques such as Raman and UV-vis spectrometry, which have relatively low spatial resolution.

Few studies address the fate of CNTs which have been phagocytosed, in particular whether CNTs can be degraded by the action of the cell. One approach to understanding the action of macrophages on CNTs has been to use simulated physiological fluids to mimic the highly oxidising environment of the phagolysosome [117-121]. Recent studies using simulated fluids reported that functionalised, oxidised CNTs become degraded after 2-3 months [121, 122]. Currently there is no consensus on the exact mechanism of degradation, though these reports have demonstrated that the CNTs degrade either through shortening or layer-by-layer exfoliation, or a combination of both [118, 120]. The products of partial degradation are thought to be oxidised aromatic carbons, while complete degradation results in CO_2 formation [121].

The limitation of simulated fluid studies is that the cellular environment is oversimplified, and so these studies need to be replicated in *in vivo* and *in vitro* systems. It is not trivial to study CNTs within cells. Visualisation is often achieved using optical imaging of fluorescently labelled tubes [123]. Raman and Infrared spectroscopy have also been applied to CNT-cell systems [122], however none of these techniques has sufficient spatial resolution to characterise the aggregation state of the CNTs, or their location with respect to cell ultrastructure. Electron microscopy imaging provides a direct, high-spatial resolution method of characterising CNTs in cells, though difficulties may arise due to the low contrast between carbon-based nanotubes and the carbon-rich environment of the cell [108]. Low-loss EFTEM and EELS have been used to successfully increase the contrast between cells and carbon nanoparticles like C_{60} and SWNTs [62, 108, 124]. To date there have been no published spectroscopy studies of CNT-cell systems at the carbon K edge, even though such core loss information would provide more easily interpretable data. The aim of this work is to study the temporal evolution of the anatomical distribution and the electronic structure of the CNT aggregates inside human macrophage cells, after different exposure times, using a combination of STXM-XAS and STEM-EELS. Using changes in the structure at the carbon K edge, the distribution and degradation of CNT aggregates can be studied.

5.2. Bonding and the Carbon K edge[††]

To understand the bonding present in a CNT simply, we will start with the molecular orbital (MO) description of bonding in isolated molecules. These molecules can then be assembled into the solid state to explain the electronic structure of nanotubes.

The atomic orbitals (AOs) of a carbon atom may be approximated using hydrogenic orbitals, one-electron solutions of the Schrödinger equation. The solutions are written as wavefunctions, $\Psi(r)$, where the probability of finding an electron in a region of space is given by $|\Psi(r)|^2$. Figure 5.2 shows the forms of the five lowest-energy AOs: 1s, 2s and $2p_{x,y,z}$.

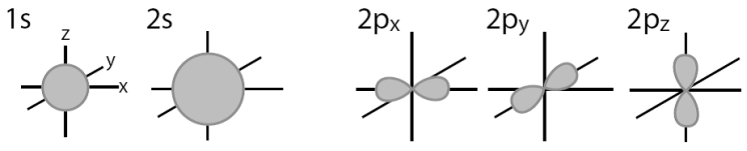


Figure 5.2 Diagrams of the five lowest-energy hydrogenic atomic orbitals: 1s, 2s and $2p_{x,y,z}$.

[††] This section is based on *Atkins' Physical Chemistry* [125], unless otherwise indicated.

5.2.1. Linear combinations of atomic orbitals

Bonding between two atoms can be described using the molecular orbital (MO) formulation, in which molecular orbitals are constructed from linear combinations of atomic orbitals (LCAO). Constructive interference between two AOs (bottom of Figure 5.3) raises the probability of finding an electron in the inter-nuclear region. The interaction between this electron and both nuclei results in a bonding effect. This is expressed as the formation of a new bonding molecular orbital of lower energy. Conversely, destructive interference results in antibonding orbitals, which contain a nodal plane between the nuclei where the wavefunction is zero. The relative energies of MOs constructed in this way can be displayed in a molecular orbital energy level diagram.

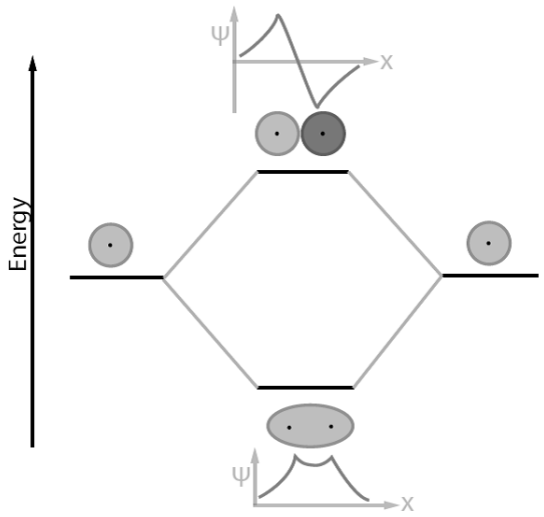


Figure 5.3 Energy level diagram showing the relative energies of two 1s atomic orbitals, and their bonding and antibonding molecular orbitals. Graphs of the molecular wavefunctions are inset. Adapted from [125].

5.2.2. Hybridisation

Now consider the bonding in, say, a saturated hydrocarbon chain or a graphitic sheet. In both these cases, the interatomic axes do not lie along the Euclidean axes. The concept of *hybridisation* can be used to create new orbitals which fit the geometry of the molecule. Similarly to above, hybrid orbitals are formed from linear combinations of AOs, this time from the same atom. Hybrid orbitals built from a single s-orbital and a pair of p-orbitals are known as sp^2 orbitals and have trigonal planar geometry, while one s- and three p-orbitals form tetrahedral sp^3 orbitals. It is the trigonal planar sp^2 orbital that is of interest for graphitic carbon systems.

5.2.3. Symmetry considerations

When forming a molecule, orbitals may overlap 'head-on', in which case the resulting molecular orbital displays cylindrical symmetry about the internuclear axis. Such a bond is labelled a σ bond. The sp^2 hybrid orbitals in graphene overlap in this way, forming a network σ bonds in the plane of the graphene sheet (Figure 5.4(a)). 'Side-on' overlap results in molecular orbitals with a nodal plane at the internuclear axis, and are known as π bonds (Figure 5.4(b)).

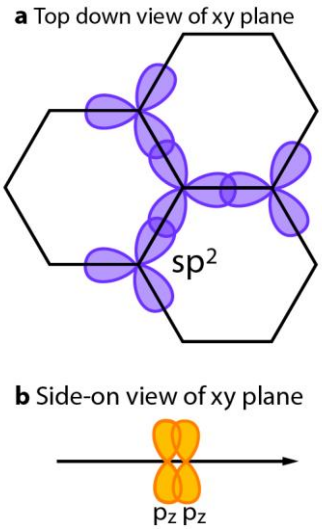


Figure 5.4 Diagram showing the geometries of σ and π bonds in a graphene sheet lying in the xy plane. (a) Head-on overlap of sp^2 orbitals form σ bonds while (b) side-on overlap of two p_z-orbitals results in the formation of a π bond.

5.2.4. Electronic structure of graphitic carbon

By bringing the above theories together, we arrive at the molecular orbital energy level diagram of sp^2 hybridised carbon (Figure 5.5). The n=2 atomic orbitals in a single carbon atom are composed of three hybrid sp^2 orbitals and an unhybridised $2p_z$ orbital. Each orbital is partially occupied in atomic carbon. To form a molecule, the sp^2 orbitals overlap head-on, forming three bonding and three anti-bonding molecular orbitals, which are labelled σ and σ* respectively. The σ orbitals are fully occupied. $2p_z$ orbitals overlap side-on, resulting in one bonding (π) and one anti-bonding (π*) molecular orbital. The π orbital is fully occupied, and so the lowest unoccupied orbital into which an electron may be excited is the π* orbital.

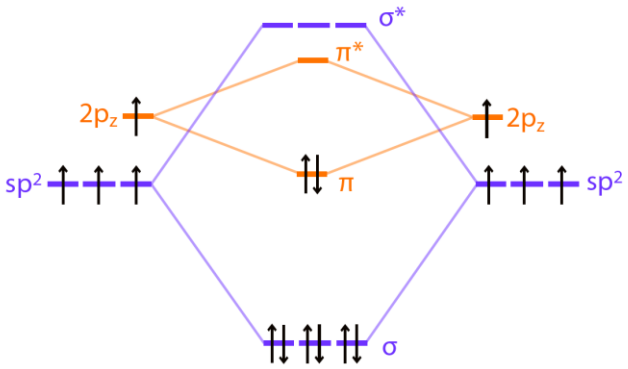


Figure 5.5 Energy level diagrams showing the molecular orbitals of a sp^2 hybridised carbon atom. Adapted from [126].

So far using molecular orbital theory, we have brought two atoms together, and their atomic orbitals produce an equal number of molecular orbitals. As the number of atoms increases, so does the number of molecular orbitals. In the solid state where we have essentially an infinite number of atoms, there will be essentially an infinite number of energy levels, spaced so closely together that they can be thought of as a continuum – a band. The energy difference between the lowest bonding and highest antibonding orbitals, known as the bandwidth, is determined by the overlap between neighbouring orbitals (Figure 5.6). The larger the overlap, the larger the bandwidth. Therefore for a graphene sheet, where the carbon bonds are sp^2 hybridised, the large overlap between σ-bonded sp^2 orbitals gives rise to wide σ bands. The π bonding between p_z orbitals produces narrower π bands.

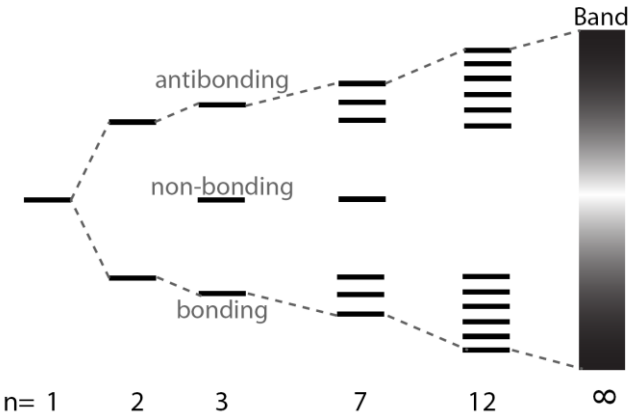


Figure 5.6 Energy level diagrams showing the formation of band structure. Adapted from [127].

For EELS and XAS measurements, we are interested in the *unoccupied* energy levels. Each carbon atom contributes 4 valence electrons to these bands, completely filling the bonding orbitals. Therefore in graphene, the first feature in an XAS or EEL spectrum corresponds to a transition into

the π* band, with the σ* resonance occurring at higher energies (Figure 5.7). Additionally, in order to satisfy the dipole selection rules (section 2.3.2), transitions only occur into orbitals with p-character. As we are interested in MWNTs of relatively low curvature, the local electronic structure is very similar to that of graphene, as demonstrated by the EEL spectra in Figure 5.7.

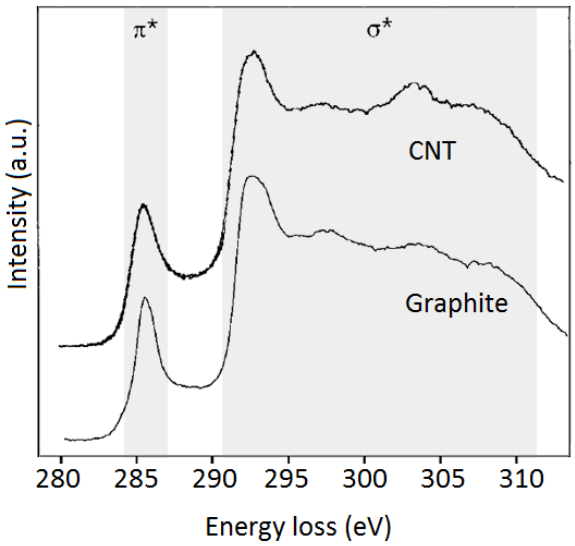


Figure 5.7 EEL spectra of graphite and CNT, which both exhibit a sharp peak at 285 eV and a broader structure at ~300 eV. Adapted from [128].

5.3. Sample History

5.3.1. Carbon nanotube functionalisation

The nanotubes used in this study were shortened, amine-functionalised MWNTs obtained from Prof. Kostas Kostarelos at the School of Pharmacy, University of London. The tubes had been prepared using the following two-step procedure [98].

Step one involved oxidising MWNTs to reduce their length to below one micron, and to introduce carboxylic acid surface functionalities. Pristine MWNTs were purchased from Nanostructured and Amorphous Materials Inc. (Houston, USA) and had 94% purity. 2.5 g of MWNTs were suspended in 120 ml of concentrated H_2SO_4/HNO_3 (3/1, v/v) and sonicated in a water bath for 24 h. The suspension was diluted with large amounts of water. Centrifugation was performed to remove the excess acid, and the black solid was then washed with water and acetone until a pH of 6 was obtained. 1.92 g of oxidised MWNT was obtained after drying *in vacuo* at room temperature [129].

Step two transformed the carboxylic functional groups to amine groups by amidation. 200 mg of oxidised MWNTs were heated in 10 ml of oxalyl chloride for 24 h at 62°C. Tubes were dried under vacuum, and then dispersed in tert-butyloxycarbonyl (Boc)-monoprotected diamino-

triethyleneglycol in distilled tetrahydrofuran and refluxed for 48 h. MWNTs were re-precipitated several times from methanol/diethyl ether by successive sonication and centrifugation. The protective Boc groups were then removed using 4 M HCl in dioxane. After the acid solution was evaporated, re-precipitation in diethyl ether yielded cationic amine functionalised MWNTs (a-MWNTs). The degree of amino group loading on the surface of MWNTs was determined by the Kaiser test to be 320 $\mu molg^{-1}$ [130].

5.3.2. Cell exposure

The cells chosen for a-MWNT exposure experiments are human monocyte-derived macrophages (HMMs) as, during an immune response, macrophages form the first line of defence in the body. The *in vivo* cell exposure experiments, fixation and embedding were performed by Dr. Karin Müller at the Multi-Imaging Centre of the University of Cambridge.

HMM cells were obtained by *in vitro* culture of human monocytes isolated from human buffy coat residues (National Blood Service, Brentwood, UK). The a-MWNTs were used as sterile stock solutions at 0.5mg/ml in 5% dextrose. The a-MWNT dispersions were bath sonicated for 15 minutes prior to use in cell culture studies. Cells were exposed to a-MWNTs at 50 µg/ml for 4 h, then washed and cultured in cell culture medium in the absence of nanotubes. After 1 and 14 days exposure, cells were processed for TEM.

Exposed cells were rinsed in saline (0.9% NaCl) to remove extracellular particles, then fixed in 4% gluteraldehyde in 0.1% PIPES buffer, pH 7.2, for one hour at 4C before being washed twice in deionized water. The cells were not stained with osmium tetroxide or uranyl acetate in order to avoid potential interference with the spectroscopy results. Samples were dehydrated in graded solutions of ethanol (70%, 95% and 100%), three times in each, for five minutes. After two further washes in 100% acetonitrile, samples were infiltrated with Quetol 651 resin over 4 days. Fresh resin was used each day. The resin was then cured at 60°C for 24 hours. A Leica Ultracut ultramicrotome with 35^{o} wedge angle diamond knife was used to cut ultrathin sections, nominally 150 nm, on to distilled water. Sections were collected on 300 mesh bare copper grids.

5.3.3. STXM-XAS

All sections were analysed in the STXM before the electron microscope, as EELS is the more damaging of the two techniques [59]. Six areas covering whole macrophage cells, approximately 20 µm × 20 µm, were analysed by acquiring a stack over the carbon K edge, from 280 to 300 eV. The photon energies and increments used are detailed in Table 5.1. Data processing was performed

using stack_analyze [88], pca_gui [10] and aXis2000 [59] software. The transmitted flux was normalised against the incident flux and stack images were aligned to correct for movements of the sections due to thermal drift. Component spectra and their chemical distribution maps were calculated using both SVD and PCA analysis.

Energy range (eV)	Energy increment (eV)
282-283.5	0.3
283.5-293	0.1

Table 5.1 Table detailing photon energies at which X-ray absorption images were acquired to form STXM 'stacks'.

5.3.4. STEM-EELS

Sections analysed by STXM were subsequently examined in the FEI Titan (S)TEM at 80 kV. Bright-field TEM images and high angle annular dark field (HAADF) STEM images were acquired. All EEL spectra presented here were acquired as spectrum images (SIs), with a monochromated energy resolution of 0.3 eV measured from the full width at half maximum of the zero loss peak. The convergence and collection semi-angles were 10 and 18 mrad respectively. Acquisition time and sample stability considerations limited the size of each SI to about 2 um × 100 nm. Pixel dimensions were chosen to be 25 nm x 25 nm, which provided spectra with sufficient signal-to-noise ratio (SNR) at low electron doses. In each spectrum image, background of the form AE^{-r} was removed using DM software, and the 1s-π* peak was aligned and calibrated to 285.5 eV. Singular value decomposition (SVD) and principal component analysis (PCA) were then performed using X-ray software as above. Linear regression fitting of experimental spectra was carried out in aXis2000 software.

5.4. Results

5.4.1. Characterisation of unexposed a-MWNTs

The physical and electronic structures of unexposed a-MWNTs were characterised in the STXM and TEM. X-ray absorption and bright-field TEM images of the a-MWNTs, which had been dispersed in dextrose, are shown in Figure 5.8(a) and (b). STXM imaging did not have high enough spatial resolution to resolve individual CNTs whereas TEM imaging revealed that the CNTs had diameters of ~50 nm. The lengths of the CNTs were more difficult to determine due to aggregation, but ranged between 50 and 500 nm. While some individual CNTs were observed in the TEM micrographs, many CNTs were found in aggregates on the support film.

XAS and EEL spectra of a-MWNTs are shown in Figure 5.8(c), and their peaks are summarised in table 5.2. Both spectra exhibit peaks at 285.5 eV and 292 eV (labelled A and D respectively) which can be assigned to 1s-π* and 1s-σ * transitions of sp^2 hybridised carbon respectively. These features are consistent with previously reported spectra of graphite and MWNTs [65, 131], and demonstrate that the graphitic structure of the CNTs had been preserved during amino functionalisation.

Peak label	Peak energy (eV)	Peak assignment
A	285.5	1s→ π* sp2 hybridised carbon
B	288.6	Oxygen-containing functionalities, defects or dextrose
C	291.7	1s→σ * sp2 hybridised carbon
D	~292	1s→σ * sp2 hybridised carbon

Table 5.2 List of the peaks present in the carbon K edge XAS and EEL spectra of unexposed a-MWNTs, and the origins of each peak.

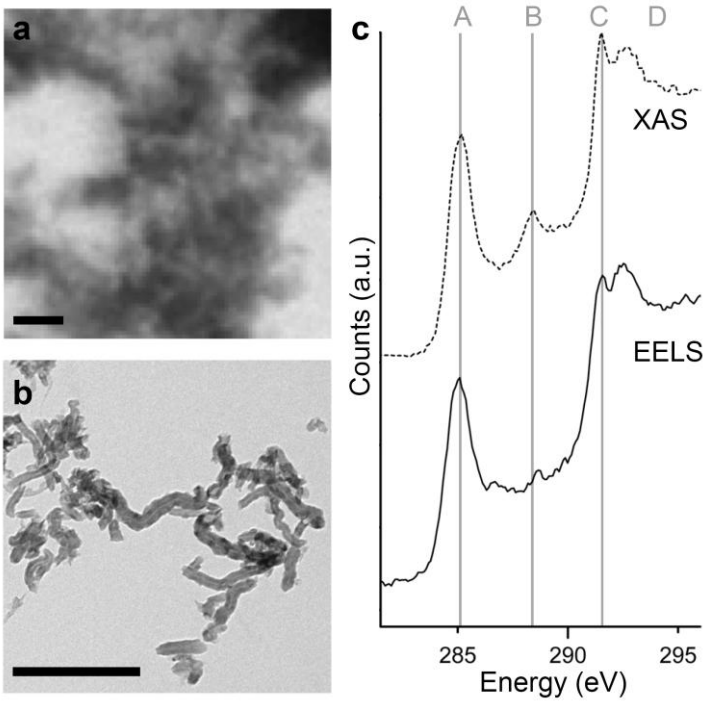


Figure 5.8 TEM and STXM data of unexposed a-MWNT samples which had been dispersed in dextrose. (a) STXM X-ray absorption image reveals a-MWNT aggregates, although individual a-MWNTs cannot be resolved. (b) BF-TEM image and (c) XAS and EEL spectra of a-MWNTs, with peak labels corresponding to Table 5.2. (Scale bars 500 nm.)

Compared to EELS, XAS data displays a more intense peak C at 291.7 eV, which is assigned to a 1s-σ* transition. The origin of peak B in XA spectra, at ~288 eV, could not be determined definitively due

to a variety of assignments in the literature. This peak could either arise from oxygenated functionalities [132], defects [133], or dextrose adsorbed on to the surface of the CNTs [134] (see section 6.4.2).

5.4.2. STXM-XAS results

STXM studies were performed on multiple cells exposed to a-MWNTs for 1 and 14 days. Figure 5.9 displays a selection of X-ray absorption images, acquired at different photon energies, for a representative cell at each time point. The most prominent features in images acquired at 285.4 eV are dark regions of a few hundred nanometres to a few microns across. These features are most likely aggregates of CNTs, which are highly absorbing at this photon energy. The images at 287.7 eV show maximum contrast between the cell and resin. As absorption images are acquired sequentially in order of increasing photon energy, so holes in the cell sections caused by X-ray beam damage are largest and most noticeable in the 288.4 eV images (Figure 5.9(c) and (f)). It is interesting to note a region of reduced absorption at 288.4 eV (arrows in Figure 5.9(c)) identified by later TEM studies as the cell nucleus. More detailed chemical analysis of these datasets was carried out using both SVD and PCA procedures.

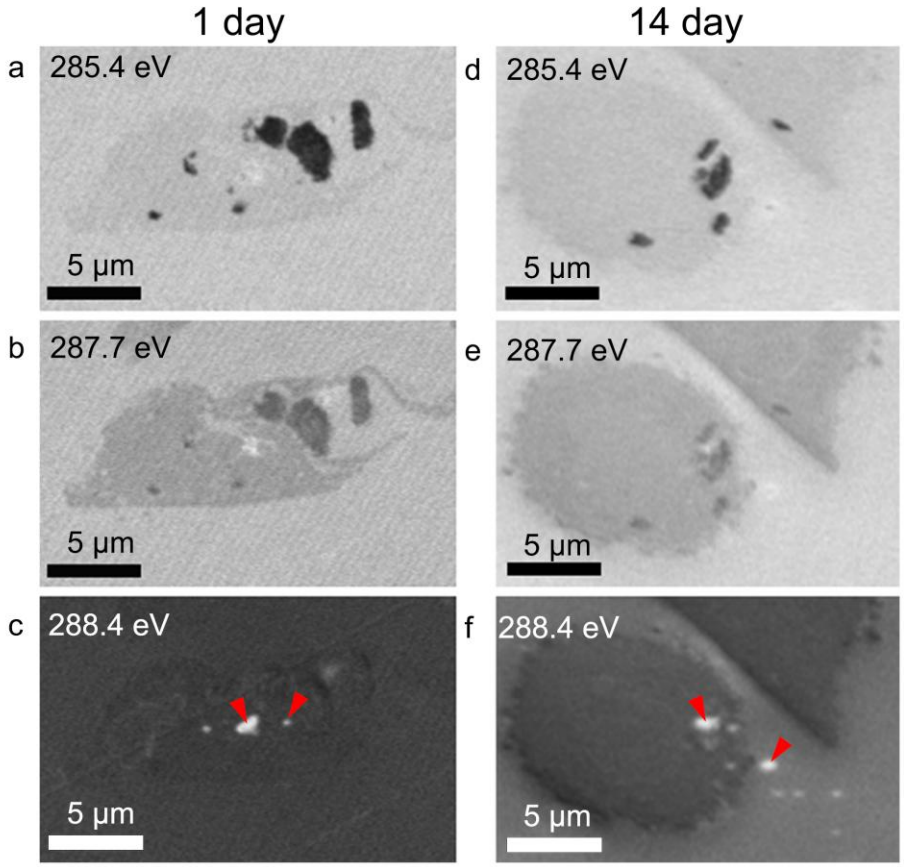


Figure 5.9 A range of X-ray absorption images of macrophage cells after 1 day of exposure to a-MWNTs (a-c) and after 14 days of exposure (d-f). X-ray absorption images acquired at different photon energies contain contrast from different sample components. High contrast between a-MWNTs and the cell is seen at 285.5 eV (a & d) while contrast between the cell and resin is visible at 287.7 eV (b & e). Holes in the section (red arrows) due to damage from the X-ray probe are visible in images (c) and (f).

5.4.2.1. SVD Analysis

Three reference spectra were used for SVD fitting (Figure 5.10):

1. the unexposed **a-MWNT** spectrum from Figure 5.8
2. an internal reference spectrum of the embedding **resin**
3. an internal reference spectrum from **cell-rich** regions

The a-MWNT spectrum displays peaks associated with graphitic carbon, as discussed in section 5.4.1. Resin spectra are dominated by a large peak around 288.7 eV, which can be assigned to the 1s-π* transition of C=O bonds in carboxyl groups present in the resin [135, 136]. As the cells have been infiltrated with epoxy resin during sample preparation, this peak is also present in the spectra from cell-rich regions. Cell-rich spectra display an additional shoulder on the 288.7 eV carboxyl peak, which makes it possible to distinguish them from resin spectra. A similar shift to lower energy has

been reported by Boese *et al.*, caused by the carboxyl groups on amino acids being converted to peptide bonds during polymerisation [137]. Therefore the shoulder in the cell-rich spectra could be associated with the presence of proteins within the cells. Additionally, small features at 285.5 and 287 eV indicate the presence of small amounts of aromatic carbons and C-H groups respectively [138].

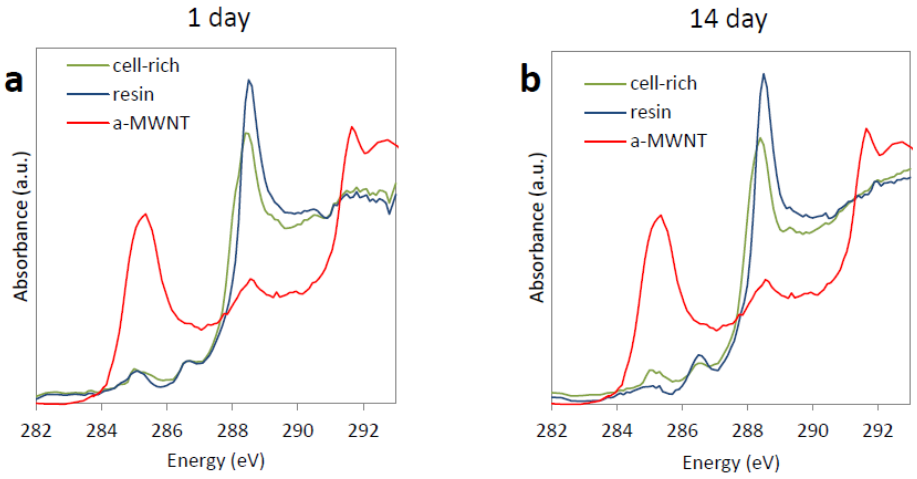


Figure 5.10 Reference spectra used for SVD fitting of the 1-day (a) and 14 day (b) STXM datasets. Cell-rich and resin spectra were obtained by summing over relevant regions in each STXM stack. The a-MWNT spectrum was taken from the sample of unexposed tubes shown in Figure 5.8.

The chemical maps of each reference component, calculated by SVD, are shown in Figure 5.11. Here, the image intensities correspond to the magnitude of the SVD fitting coefficients at that location: high intensity regions indicate large coefficients, and hence high concentrations of a component. Residual maps are also displayed in Figure 5.11. The residual is defined as the squared difference between experimental and fitted spectra, summed over the whole energy range. The magnitude of the residual can be used to give a qualitative measure of the goodness-of-fit between experimental and fitted spectra. The better the fit, the lower the residual value. Lastly, individual component maps have been combined to form RGB images (Figure 5.11(e) and (j)) for ease of analysis, where regions with high concentrations of a-MWNTs are red, cell-rich regions are green and resin regions are blue.

High intensity regions in the a-MWNT maps indicate regions in which the experimental spectra have large amounts of unexposed a-MWNT character. The maps show that after 1 day of exposure, some micron-sized aggregates of a-MWNTs (Figure 5.11(e)) appear to be in the process of being phagocytosed by the cells while smaller aggregates are already present within the cell body. After 14 days, nanotube aggregates are observed within the body of the cell, although there is insufficient resolution (both spatial and chemical) to determine the location of a-MWNTs with respect to the cell organelles.

Relatively high residual signals are observed in regions corresponding to nanotubes, indicating a poorer goodness-of-fit in these regions compared to their surroundings. Additionally, in Figure 5.11(d), even higher residual signals are observed at the *edges* of aggregates. This may be indication that aggregate edges exhibit changes in electronic structure. However, the anisotropic nature of the edge signal (brightest at the top left of nanotube aggregates) suggests that they are most likely an artefact caused by drift between successive images in the stack (see also section 5.4.2.3). To investigate both these results further, PCA was carried out on a reduced area of each dataset.

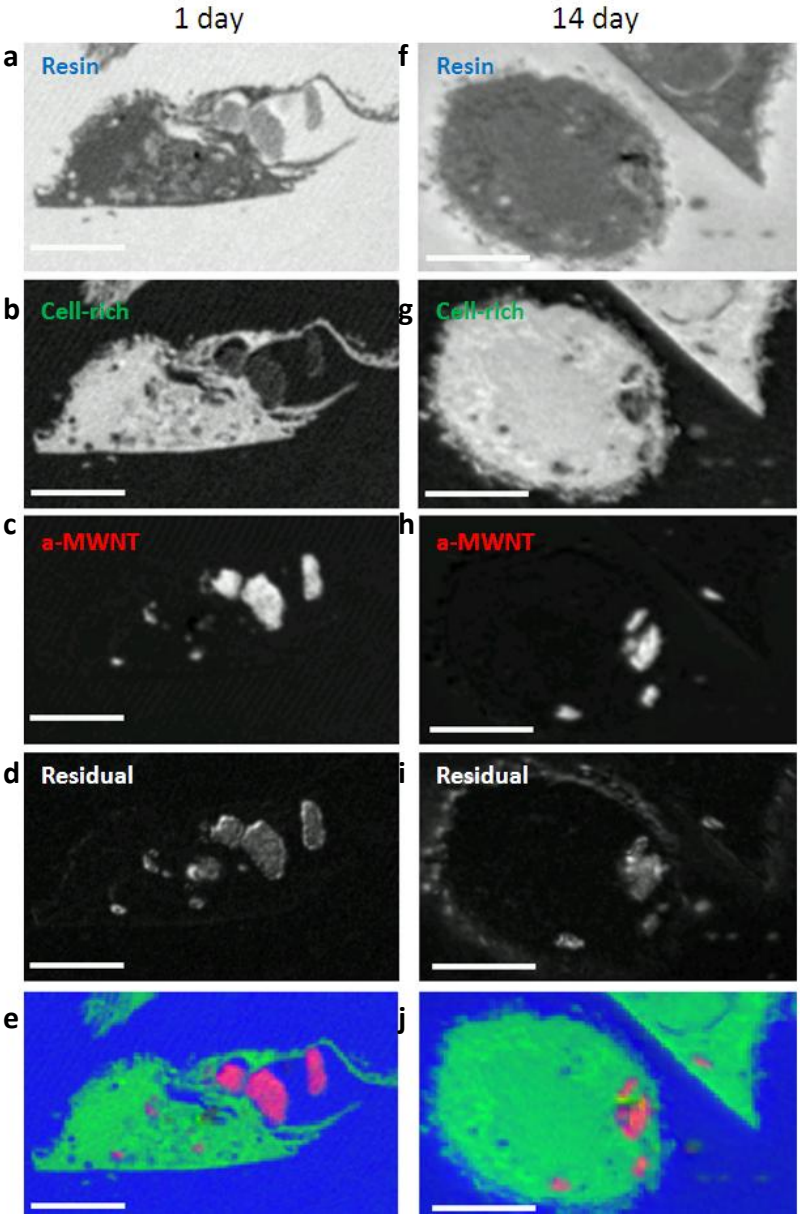


Figure 5.11 Chemical maps of 1-day and 14-day cells, calculated by SVD analysis. Maps show the spatial distribution of resin (a & f), cell-rich (b & g) and a-MWNT (c & h) components. The residual signal is plotted in (d) and (i). RGB images with resin displayed in blue, cell in green and nanotubes in red are also shown (e) and (j) (scale bars 5 µm).

5.4.2.2. PCA Results

The PCA routine sorts pixels into 'clusters' containing similar spectra, and sums all the spectra within each cluster. Five to six different clusters were identified in each dataset; their spatial distribution and colour-coded XA spectra are displayed in Figure 5.12. Large clusters corresponding to resin and cell-rich areas have been identified (the blue and green clusters respectively). Their spectra are in good agreement with SVD results reported in section 5.4.2.1. In areas containing a-MWNTs, a number of different PCA clusters have been identified. The largest of these clusters is located at the centre of the CNT aggregates. Figure 5.13 compares the PCA spectra corresponding to the centre of aggregates, after 1 day and 14 days exposure. Both display distinct π* and σ* transitions, indicating that the graphitic structure of the MWNTs is retained at 1 and 14 days. There are slight differences in the π* and σ* peak intensities between the two time points. Although these differences could be suggestive of altered electronic structure, they are most likely an artefact caused by different background contributions from the two cell sections which are not equally thick (note that no background has been removed from any XA spectra). Therefore, there is no evidence in these data of a change in the electronic structure of a-MWNTs at aggregate centres after 1 and 14 days.

The extra clusters corresponding to a-MWNT aggregates are located at the edges of the aggregates. The fact that these pixels are identified with a different cluster could indicate changes to the electronic structure of CNTs at aggregate edges. In order to determine if new chemical signatures were present at the edges of aggregates, the cluster spectra were compared with the unexposed a-MWNT reference spectrum. A direct comparison between cluster spectra and the unexposed a-MWNT reference is not possible as these pixels will also contain significant concentrations of cell and resin. Therefore, the PCA spectra of clusters were fitted with three reference spectra (section 5.4.2.1): unexposed a-MWNT, cell-rich and resin spectra. These reference spectra were fitted by linear regression analysis. The difference between a PCA cluster spectrum and the fitted spectrum can then be used to search for any changes in the electronic structure of the a-MWNTs. Figure 5.14 shows that there is very good agreement between fitted spectra and all PCA clusters - at the centre and the edges of aggregates, at both exposure time points. Instead, it is likely that the extra PCA clusters arise from changes in the sample composition at the edges of aggregates, i.e. the cell-rich:resin:a-MWNT ratios (inset bar graphs in Figure 5.14).

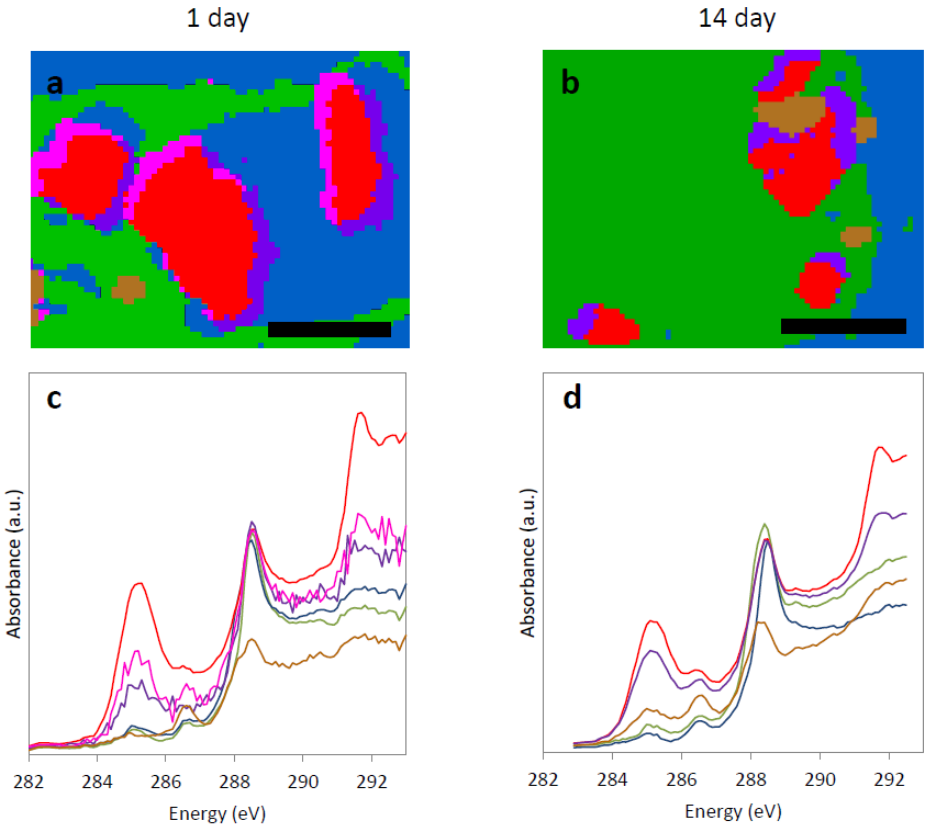


Figure 5.12 Results of PCA analysis of 1-day and 14-day exposed cells. (a) and (b) are maps showing the PCA clusters. (c) and (d) display the XAS spectra obtained by summing over all pixels in a cluster (scale bars 2 µm).

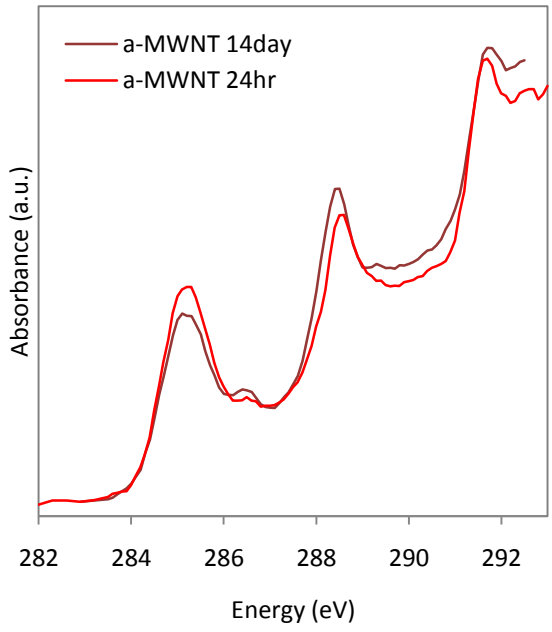


Figure 5.13 Overlaid spectra of the PCA clusters from the centre of CNT aggregates, after 1 and 14 days exposure.

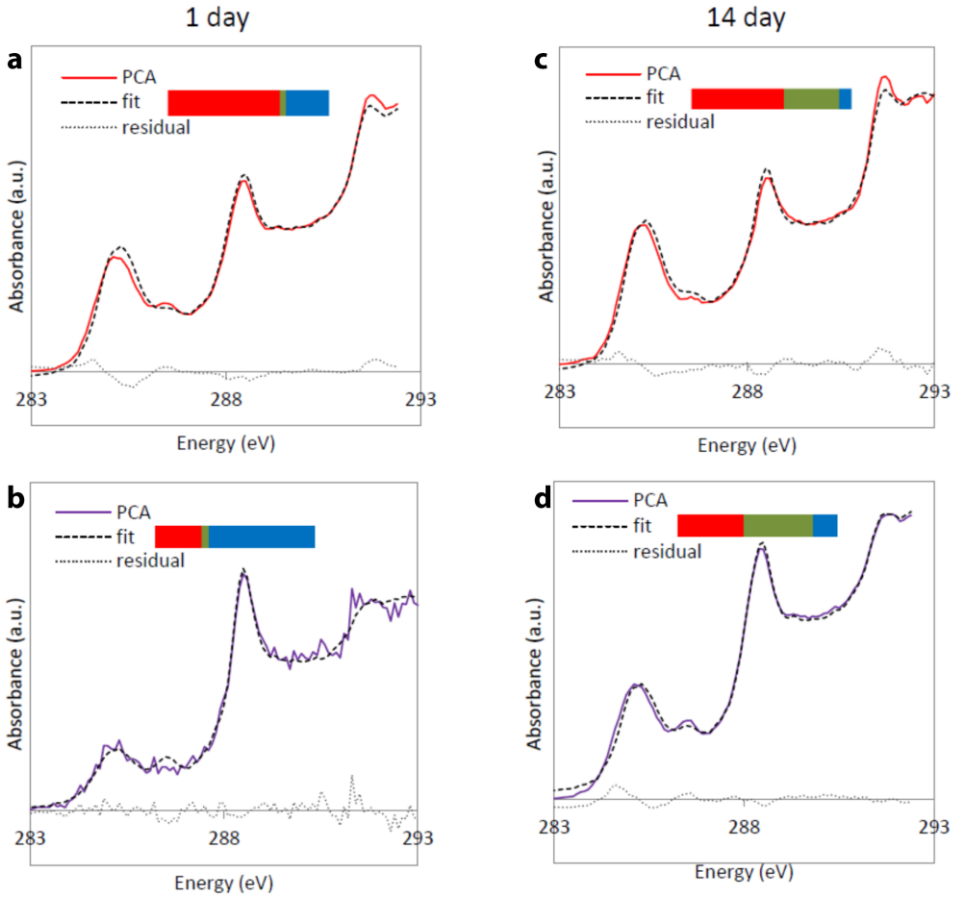


Figure 5.14 Linear deconvolution results for a selection of PCA spectra from cells exposed for (a-b) 1 day and (c-d) 14 days. The PCA spectra (red/purple lines), fitted spectra (dashed lines) and residuals, i.e. difference between the two (dotted lines) are plotted. Fitting was performed by linear deconvolution using three reference spectra, and their coefficients are displayed in the bar graphs: cell-rich (green), resin (blue) and a-MWNT (red).

5.4.2.3. Interpreting PCA results

There is an additional consideration when interpreting clusters at aggregate edges. Figure 5.15 shows a dataset in which the alignment algorithm failed to remove all the spatial drift in the dataset. PCA analysis of this misaligned dataset again yields clusters which are localised at aggregate edges. The spectrum of one of these edge clusters is shown in Figure 5.15(b), overlaid with cell and aggregate spectra for comparison. The edge spectrum contains a large 1s-π* peak at 285.5 eV which indicates the presence of graphitic carbons, however the characteristic graphitic σ* peak at 292 eV is absent. One possible cause for this inconsistency is the spatial drift within the dataset, which could have resulted in pixels, which originally were located over a nanotube aggregate, to drift out of this region during the acquisition of the dataset. The effect of this drift can be recreated by a linear

combination of the nanotube and cell spectra, modulated by the functions shown in Figure 5.15(c) so that

$$A_{edge}(E) = a(E)A_{MWNT}(E) + b(E)\,A_{cell}(E) \qquad \textit{Equation 5.1}$$

The fitted edge spectrum agrees well with the PCA cluster spectrum (Figure 5.15(d)), demonstrating that this cluster is caused by imperfect dataset alignment rather than any new chemical components.

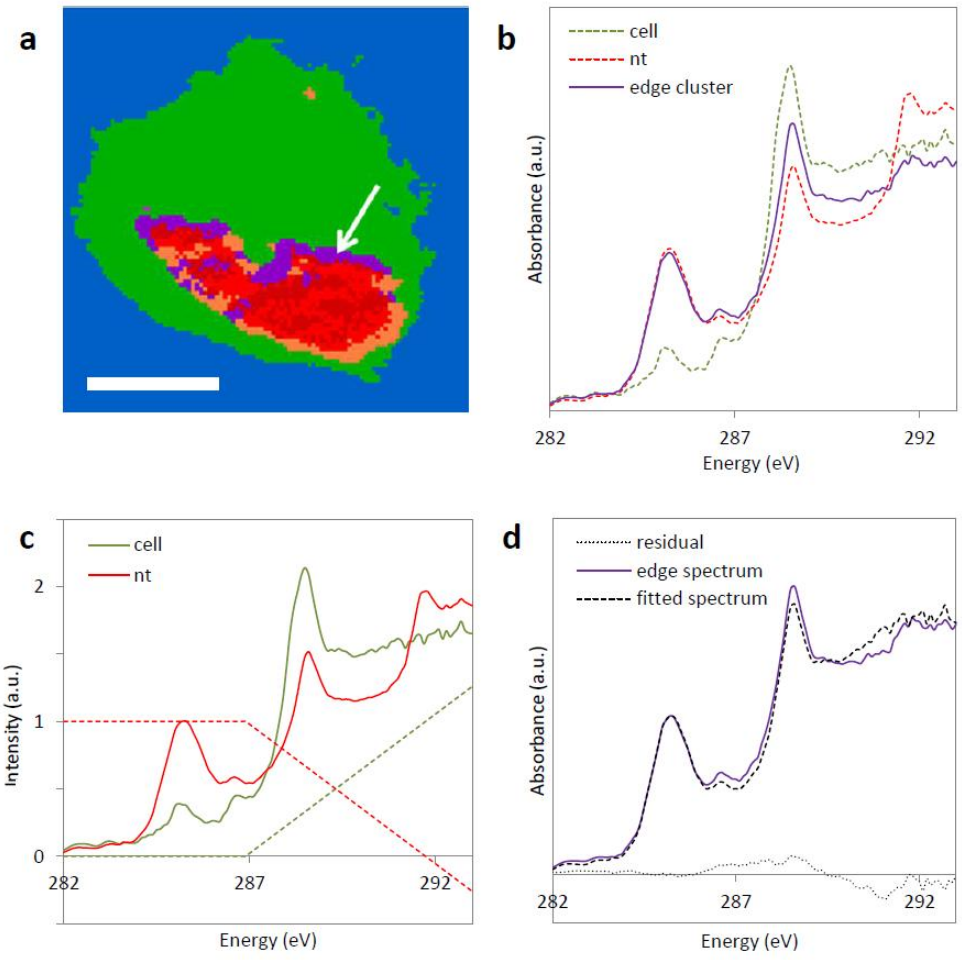


Figure 5.15 Analysis of PCA clusters calculated from an STXM stack which contains spatial drift. (a) PCA cluster map (scale bar = 5 µm), in which the purple cluster corresponds to the edge of the nanotube aggregate (arrow). (b) The spectrum of the edge cluster (purple) is overlaid with cell and nanotube spectra for comparison. (c) shows the functions which are used to recreate the edge spectrum, according to Equation 5.1. (d) The recreated spectrum (dashed line) agrees well with the original PCA cluster of the aggregate edge (purple), demonstrating that this cluster arises from drift artefacts.

5.4.3. STEM-EELS Results

5.4.3.1. TEM/STEM imaging

The thin sections which had been studied by STXM were then transferred into the TEM for imaging and EELS analysis at higher spatial resolution. Bright field TEM and HAADF-STEM images of the *exact same* cells analysed previously are shown in Figure 5.16 and Figure 5.17. Images were acquired in the following sequence, in order to minimise electron beam exposure prior to EELS analysis:

1. HAADF-STEM imaging was performed first to locate regions of interest for STEM-EELS analysis. Fast pixel dwell times of ~30 µs were chosen to lower the electron dose whilst providing adequate signal-to-noise ratios in the images.
2. TEM imaging was performed only after EELS data had been acquired.

Cell sections were found to thin rapidly under electron beam irradiation. The 14-day cell section ripped apart during acquisition of the EELS spectrum image, and so imaging in TEM mode could not be performed. Therefore only a low-dose HAADF-STEM image is shown for the 14-day cell (Figure 5.17(b)).

Contrast in the bright field TEM images arises from thickness and density variations in the sample, as well as diffraction from the crystalline a-MWNTs. Cell regions have lower image intensity as the cell cytoplasm is more electron dense than the surrounding resin. However, thinning of the sections due to electron beam damage also gives rise to contrast variations. For this reason, it is not possible to definitively distinguish between cell and resin regions in a TEM image, especially where areas have previously been exposed to the electron beam (see Figure 5.16(b)).

TEM imaging reveals that the majority of nanotubes at both exposure times are present within dense aggregates. High diffraction contrast in these regions makes it difficult to determine the morphological structure of CNTs within aggregates. Individual nanotubes are also present in Figure 5.16(b) but it is not possible to determine whether these tubes are inside the cell or merely associated with the cell membrane.

Diffraction effects are not present in electrons scattered to high angles, and so are not present in the HAADF-STEM images. Instead, the main contrast variations arise from density and thickness variations. It is even possible to identify the cell nucleus, due to the increased density of chromatin located at the nuclear membrane. As the resin, cell and a-MWNT components all contain low atomic number elements (H, C, O and N), atomic number Z contrast is of less importance in the HAADF-

STEM images. However, due to Z contrast, the iron catalyst particles present in some a-MWNTs appear as bright regions < 50 nm in size.

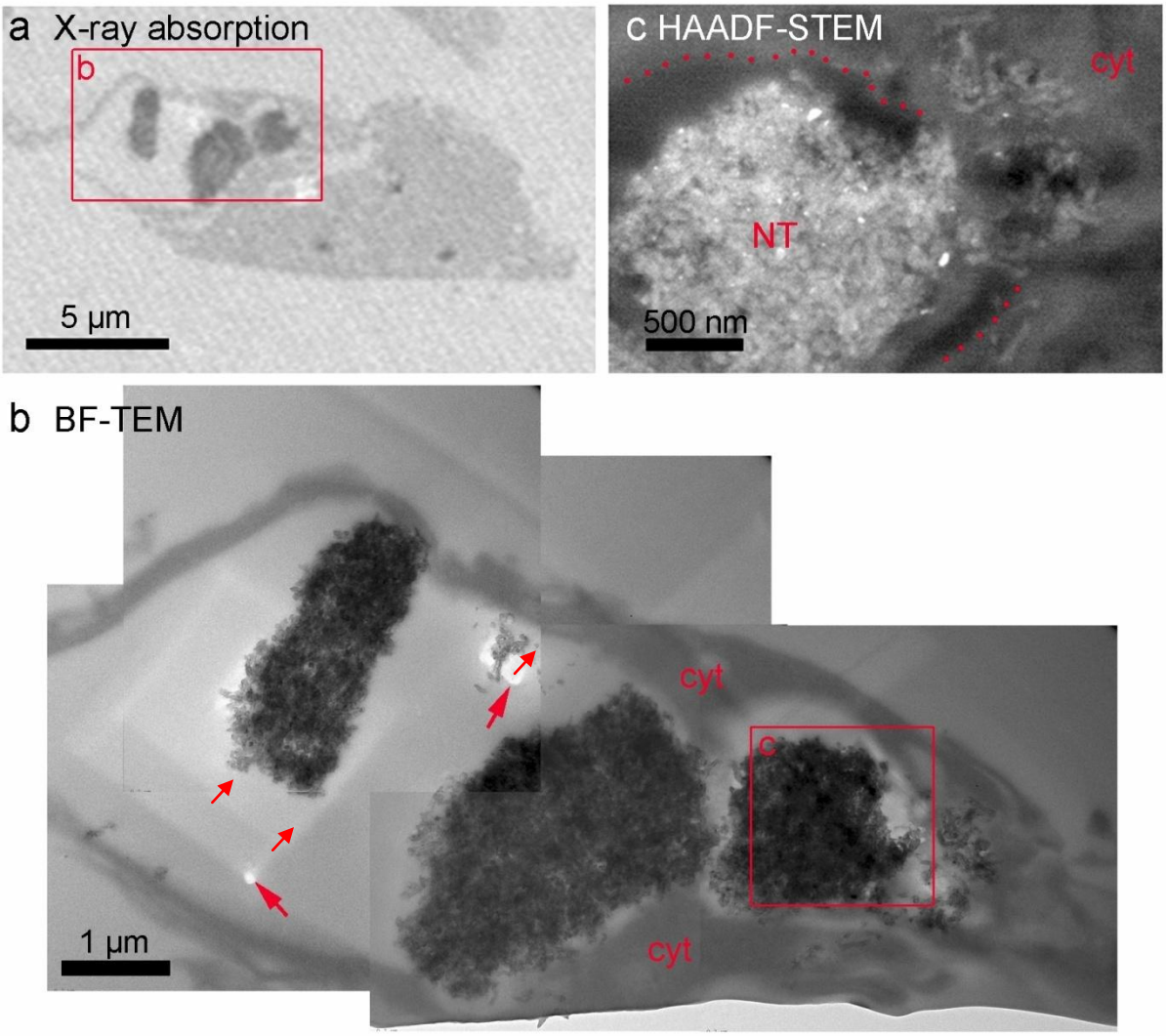


Figure 5.16 Correlative electron and X-ray imaging of the 1-day cell. (a) X-ray absorption image of the whole cell and nanotube aggregates. (b) BF-TEM image of the boxed region in (a). Arrows indicate thinner regions and holes which formed after electron irradiation. Cell cytoplasm is labelled cyt. (c) Higher magnification HAADF-STEM image of the boxed region in (b), showing aggregated and individual a-MWNTs associated with the cell membrane (dots).

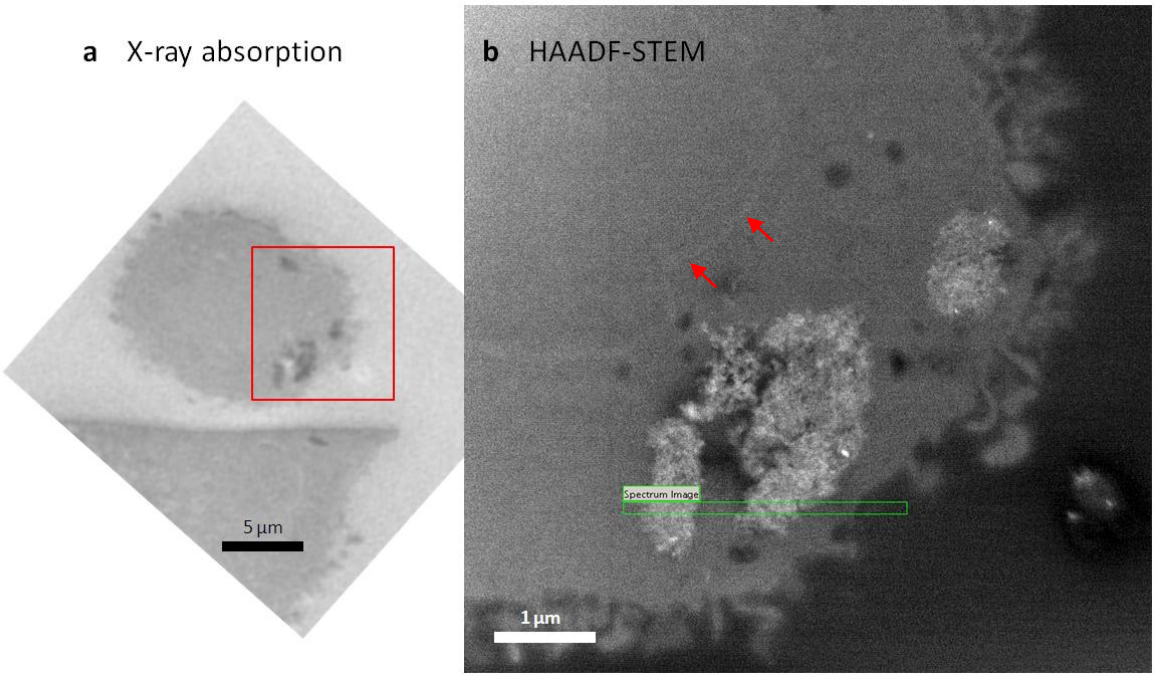


Figure 5.17 Correlative HAADF and X-ray imaging of the 14-day exposed cell. (a) X-ray absorption image of the whole cell and nanotube aggregates. (b) HAADF-STEM image of the boxed region in (a) showing the aggregates over which EELS data were acquired (green box). Contrast from the nuclear membrane is also visible (arrows) in this image.

5.4.3.2. SVD analysis

The three components used for SVD analysis of each EEL spectrum image are shown in Figure 5.18. The spectrum of unexposed a-MWNTs was discussed in section 5.4.1. EEL spectra of resin and cell-rich regions were obtained from EELS spectrum images. The EEL spectra of resin and cell-rich areas are very similar: both contain a small 1s-π* peak at 285.5 eV from unsaturated C=C bonds, and a broad featureless σ* resonance at ~292 eV.

Chemical maps calculated by SVD are also displayed in Figure 5.18. The resin and cell-rich maps are noisy in both SIs, but also display some long-range contrast variations. Regions which had been identified as a-MWNT aggregates in STEM images also appear bright in the a-MWNT chemical maps. However, regions corresponding to the centre of aggregates are noisy in the chemical maps, and appear brighter in the residual maps. This is most obvious at the bottom-right corner of the 1-day SI. The high noise in these regions is probably due to the high SBR and hence low SNR at the centre of aggregates. RGB images show regions of high a-MWNT concentration in red, cell-rich regions in green, and resin regions in blue.

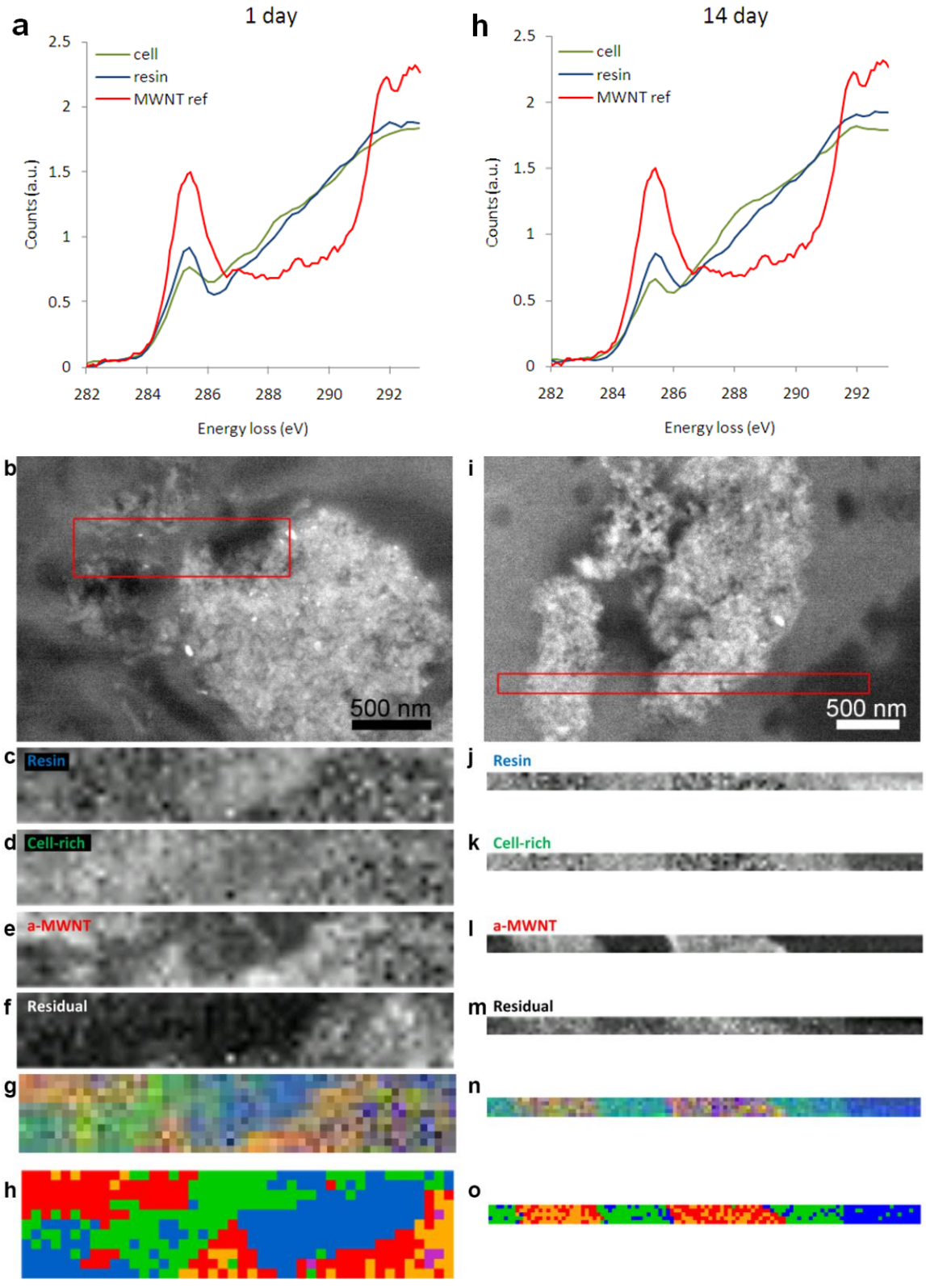


Figure 5.18 SVD results for EELS data of 1-day and 14-day samples. (a,h) The component spectra used for SVD fitting: resin (blue), cell-rich (green) and a-MWNT (red) spectra. (b,i) HAADF-STEM images of the cells, showing the area over which EELS data were acquired (red boxes). (c-e, j-l) Chemical maps showing the spatial distribution of each chemical component (f,m) Maps of the residual signal as defined in section 5.4.2.1. (g,n) RGB images showing regions of high resin concentration in blue, cell-rich regions in green and a-MWNT regions in red. (Overlapping cell and MWNT regions appear yellow).

5.4.3.3. PCA analysis

PCA analysis was again performed, and PCA maps and cluster spectra are displayed in Figure 5.19. Once again, PCA clusters have similar spectral and spatial signatures as SVD results. Although two clusters were identified at a-MWNT regions, these clusters relatively evenly distributed throughout the aggregates, and not segregated to the edges. Two PCA spectra corresponding to a-MWNT aggregates at different exposure times are compared in Figure 5.20. Once again, both spectra display distinct π* and σ* transitions, and there is no indication of a change in electronic structure after 14 days exposure to the macrophage cells.

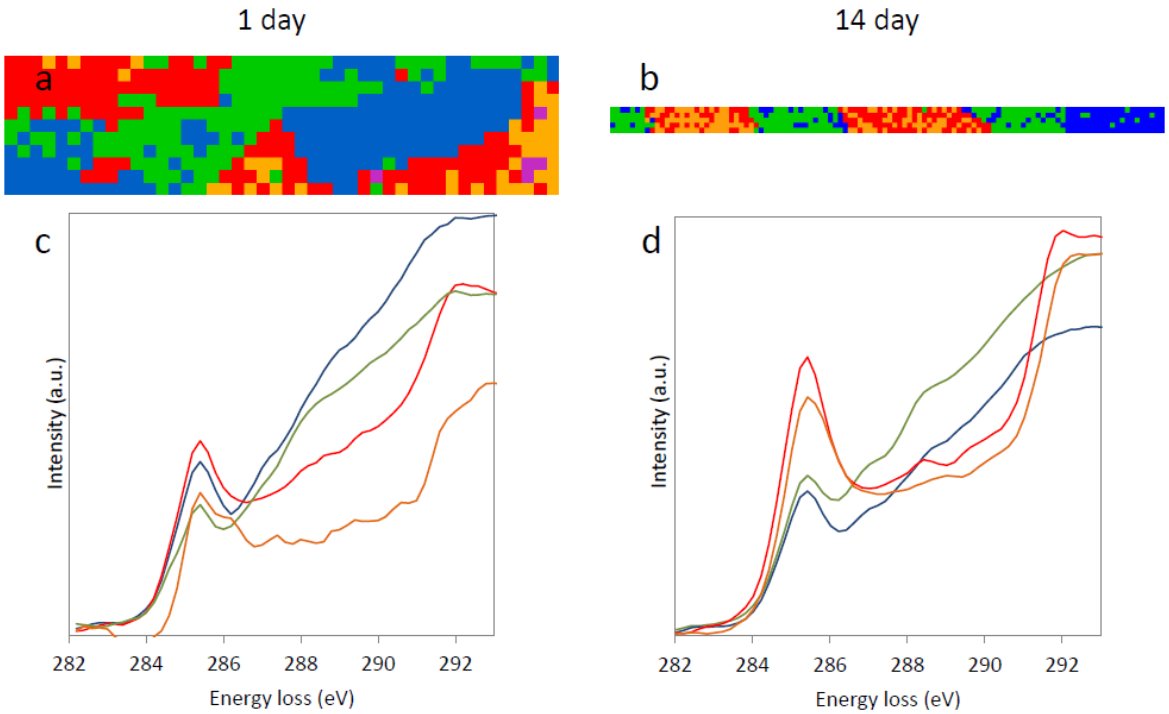


Figure 5.19 Results of PCA analysis of the 1-day and 14-day EELS datasets. (a,b) PCA clusters and (c,d) corresponding cluster spectra.

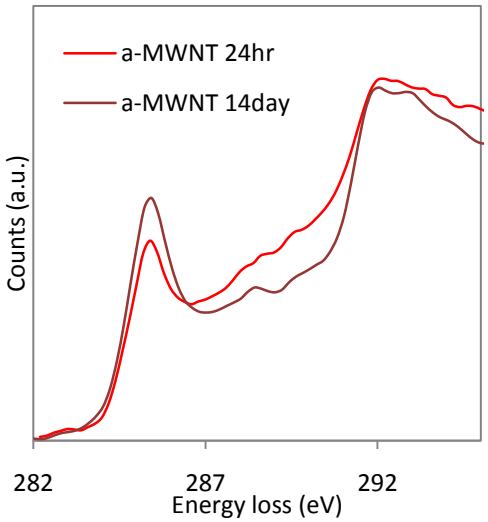


Figure 5.20 Shows overlaid spectra of the PCA clusters from the centre of CNT aggregates, after 1 and 14 days exposure.

5.4.4. Comparison of EELS and XAS

Figure 5.21 shows the PCA spectra corresponding of resin, cell and a-MWNT aggregates. XAS and EEL spectra have been overlaid for comparison. The most striking difference between EELS and XAS is present in the cell-rich and resin spectra. Much less fine structure is present in the EEL spectra of these components compared to XAS; most noticeably the sharp peak B at ~288 eV is missing in the EEL spectra. In spectra of MWNTs, large π* and σ* graphitic peaks (A and D respectively) are present after both 1 and 14 days in both XAS and EEL spectra. The sharp peak C at 291.4 eV, which also corresponds to a 1s-σ* transition, is present in XAS data, whereas only the broader σ* peak D at 292 eV is visible in the EEL spectra. Nevertheless, using EEL spectra at the carbon K edge, it is possible to differentiate between graphitic MWNT and organic carbons from cells and resin.

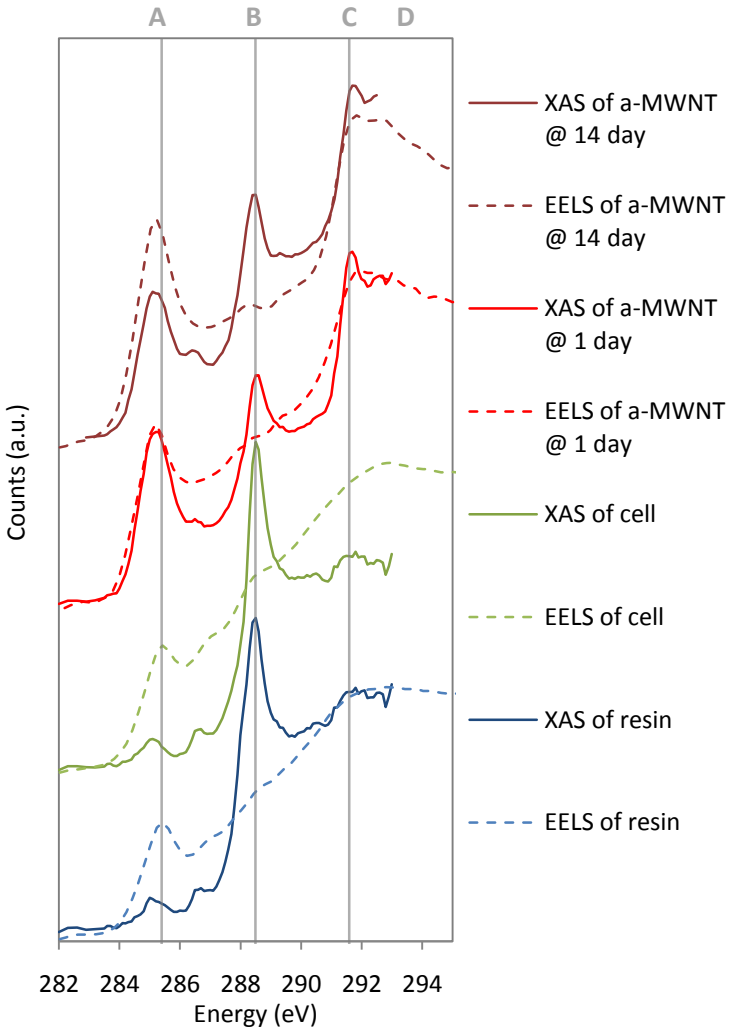


Figure 5.21 Comparison of XAS (dotted line) and EEL spectra (solid line) of the resin and cell-rich components, as well as spectra from nanotube aggregates after 1 day and 14 days of exposure.

Figure 5.22 compares the spatial variation of each SVD component. The graphs plot the fit coefficients as a function of distance along the line drawn in Figure 5.22(a). These profiles were calculated for both the EELS and XAS datasets of the 14-day cell. Figure 5.22(b) plots the variation in resin signal along the line. The XAS profiles indicate that there is no contribution from the resin signal within the cell, and that cell-rich contributions decrease in regions where a-MWNT aggregates are located, but do not fall to zero. The EELS profiles of resin and cell contributions are much noisier but follow the general trends of the XAS profiles. The high noise is caused by the similarity between the EEL spectra of resin and cell components. To illustrate this, Figure 5.22(d) plots a combined resin+cell profile, in which the noise is significantly reduced and the profile is in better agreement with XAS findings.

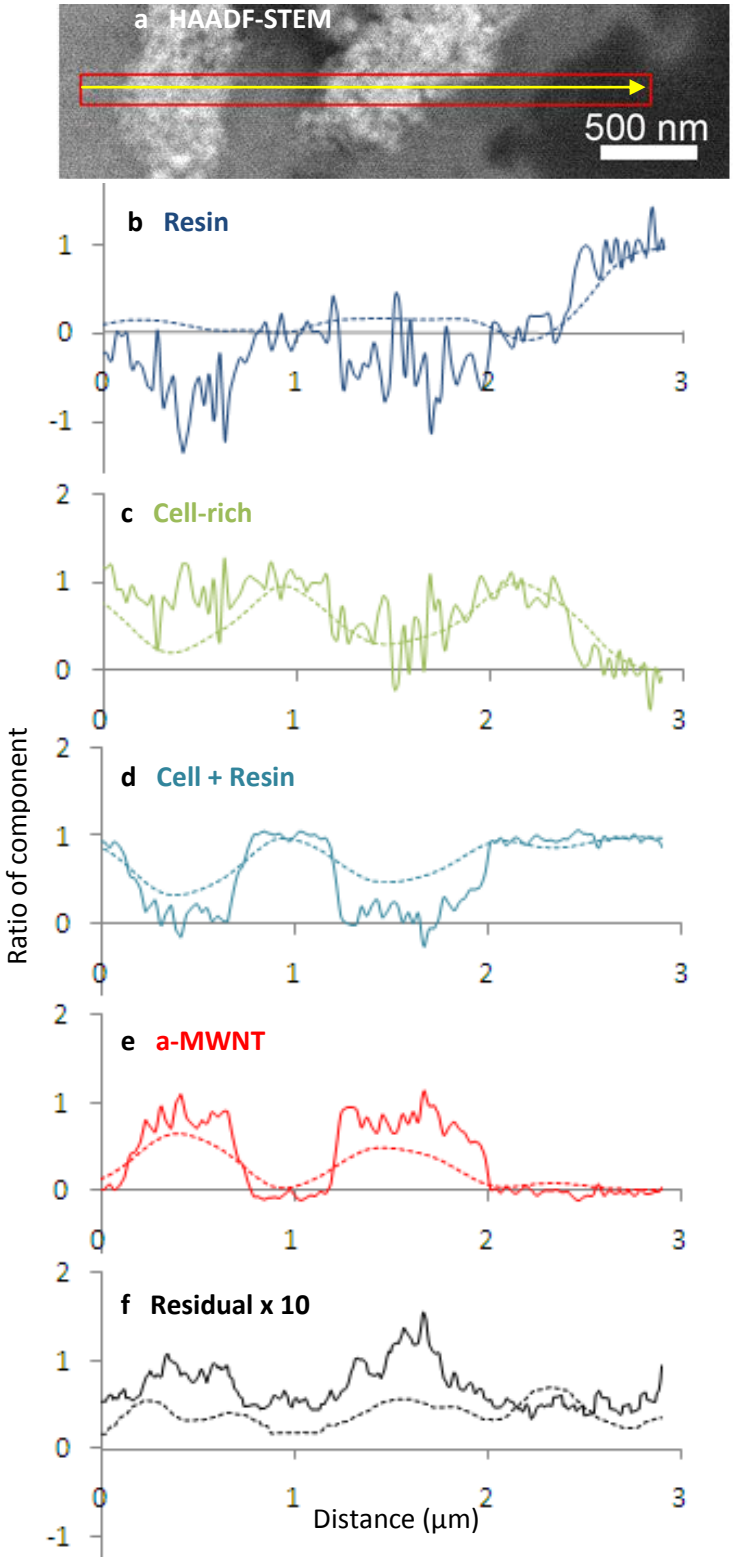


Figure 5.22 Profiles showing the spatial variation of chemical components as calculated from EELS (solid lines) and XAS experiments (dashed lines). (a) HAADF-STEM image of a section of the 14-day cell discussed previously. Profiles are calculated along the yellow arrow, and signals are summed over the width of the red box in order to reduce noise. (b) Resin and (c) cell-rich profiles are plotted, and show that EELS profiles have a low SNR. (d) Profiles of the combined resin and cell contributions, showing improved SNR in the EELS profile. (e) a-MWNT and (f) residual profiles. Note that the residual profile is multiplied by a factor of 10 to enhance its visibility.

The XAS a-MWNT profile shows gradual changes in concentration, which peak at ~80% in the centre of aggregates. The a-MWNT profile calculated from EELS data contains more sharply defined interfaces between aggregates and the cell. The noise is higher in the centre of aggregates, due to the low SNR of the experimental spectra in these regions. The residuals are both very low, though EELS residuals peak in the centre of aggregates. The XAS residual profile displays much less spatial variation.

Figure 5.23 shows the result of deconvolution of the XAS and EELS a-MWNT profile (Figure 5.22(e)). This gives an estimate of the instrument function, which takes into account the pixel size in the STXM stack, detector point spread function, and misalignments between X-ray absorption images. The full width at half-maximum of the central peak in this function is a measure of the effective spatial resolution of the X-ray data. This was measured to be 280 nm, which equates to 2.8 pixels.

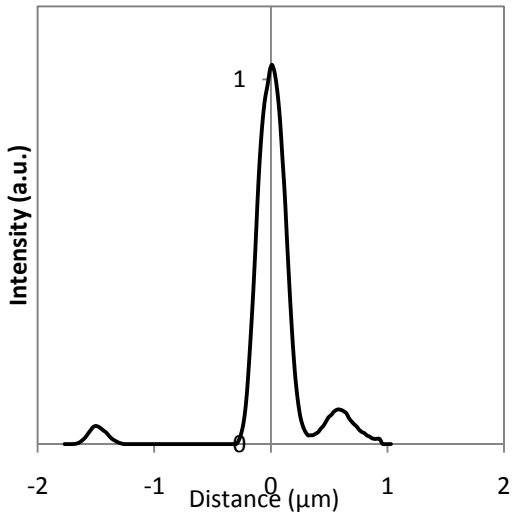


Figure 5.23 Deconvolution of EELS a-MWNT profile with the XAS a-MWNT profile from Figure 5.22(e). This gives an estimation of the instrument function of the STXM, which is found to have a full width at half maximum of 280 nm.

5.5. Discussion

5.5.1. Characterisation of a-MWNTs

The electronic structure of unexposed a-MWNTs was determined by XAS and EELS. Both spectra contained peaks at 285.5 and 292 eV, demonstrating that the graphitic structure of the tubes had been preserved during functionalisation and analysis. TEM imaging revealed that the CNTs had been

successfully shortened by oxidation, and both individual and aggregated tubes were observed. Aggregation was observed despite the increased dispersability of amine functionalised tubes [139], as well as the use of ultrasonication techniques to improve the dispersions prior to grid preparation. This may indicate that some aggregation does occur when a-MWNTs are dispersed in dextrose solution. An alternative explanation is that a-MWNTs were monodispersed in dextrose, but aggregated during drying on the TEM grid. To avoid potential drying artefacts, TEM samples could be prepared via a different route e.g. by performing cryo-TEM imaging of frozen samples. Other techniques such as dynamic light scattering (DLS) could also be employed to more directly characterise the quality of dispersion in the liquid state.

5.5.2. Uptake and Distribution of a-MWNTs

Aggregates of a-MWNTs were visible in the cell sections under both the X-ray and electron microscope. STXM and (S)TEM imaging of 1-day samples revealed that aggregates were internalised inside macrophage cells. This is consistent with previous studies which show that functionalised MWNTs are readily phagocytosed by macrophages [102, 140, 141].

After 14 days, aggregates were observed within the body of the cells. Additionally, TEM and STEM micrographs at higher spatial resolution were able to confirm that individual nanotubes were also present in the cells at both time points. Similar findings of individual and aggregated tubes within macrophage cells have been reported previously for oxidised-MWNTs [140] and a-MWNTs [130]. Although cell membranes could not be imaged in this study due to the lack of staining, a previous study on the same cell-NT system [141] using stained sections showed that as well as phagocytosis of MWNT aggregates, individual a-MWNTs enter the cell cytoplasm via penetration of cell and phagosome membranes.

5.5.3. Fate of a-MWNTs in macrophage cells

The fact that a large number of CNTs are present in this cell type as aggregates, and remain densely aggregated after 14 days, could have significant implications for their biostability. Tubes in the centre of aggregates might be expected to be somewhat protected from the oxidising environment of the phagolysosome, and so persist much longer in the cells. The finding that individual MWNTs enter cells by piercing the plasma membrane will also affect the biopersistence of these MWNTs, as nanotubes which enter the cell through this route may also not be exposed to phagolysosomal environments.

STXM and EELS were used to assess of the graphitic character of intracellular a-MWNT aggregates. Figure 5.13 and Figure 5.20 demonstrate that there was no significant loss in graphitic peaks in aggregate spectra after 1 and 14 days, which implies that aggregated nanotubes retained their graphitic structure during this time. There was also no spectroscopic evidence of changes in graphitic structure at different spatial positions across a-MWNT aggregates. This shows that the edges of the aggregates had not become amorphous inside the cells.

Studies of nanotube degradation in simulated phagolysosome environments have found that a range of enzymes are capable of degrading functionalised SWNTs and MWNTs [45, 117, 118, 121]. Degradation rates were highly dependent on the nature of the nanotube functionalisation as well as incubation conditions such as temperature and the concentration and type of enzyme. For example, complete degradation of oxidised-SWNTs in myeloperoxidase occurred after only 24 hours [122], while it took 90 days for similar tubes to be degraded by phagolysosomal stimulant fluid [117]. In general, SWNTs were degraded faster than MWNTs [118], and higher rates of degradation were observed in tubes with higher degrees of functionalisation [117]. It is unclear how well simulated environments in the above studies match the actual conditions within macrophage cells, and so *in vivo* studies might provide a better comparison.

When exposing HMMs to SWNTs functionalised with the antibody IgG, Kagan *et al.* recently reported exceptionally high rates of degradation, with 50% of the nanotubes degraded after just two days [122]. Such extreme degradation is not observed in this work, and could be a consequence of the IgG functionalisation of the CNTs. It is also possible that the harsh separation techniques used prior to the assessment of degradation further damaged the CNTs [142]. Another *in vivo* study used the more direct method of TEM imaging to characterise the degradation state of ox-SWNTs in HMMs [140]. This study found no signs of degradation after two days of exposure. This result is more consistent with the lack of detectable degradation observed here for a-MWNTs exposed to HMMs for one day. Further *in vivo* studies over longer exposure times are needed before any comparisons can be made with the 14-days exposure results presented here.

5.5.4. EELS versus XAS

The presence of graphitic structure in a-MWNT aggregates was confirmed by EELS using 1s-π* and σ* peaks at 285.5 and 292 eV respectively. Although the absolute intensity of these graphitic peaks could be used to quantify the degree of CNT degradation of an isolated CNT, the presence of carbon-rich background in the current samples makes such quantification much less straightforward. For example, for any pixel containing nanotube aggregates, the intensity of the 1s-π* peak will be

dependent on both the density of defects in the tubes, and the proportion of infiltrated cell and resin components in that volume which will also contribute to the spectrum. Due to these two effects, the degree of nanotube degradation could not be evaluated using the intensity of the 1s-π* (and σ*) peaks. However, these data have demonstrated that EELS has sufficient spectral sensitivity to map graphitic a-MWNT aggregates within the carbon-rich cell background at the carbon K edge.

The largest differences between XAS and EEL spectra (Figure 5.21) were seen in the resin and cell-rich spectra. Intense XAS peaks at 288 eV were not present in the EELS data, making it more difficult to distinguish between cellular and resin regions (Figure 5.18 and Figure 5.22(b,c)). As EELS data was acquired with an energy resolution of 0.3 eV, lower than the 0.1 eV resolution of the STXM, some blurring of features in EEL spectra is to be expected. However, due to the high intensity of the 288 eV peak in XAS, its absence in the EEL spectra cannot be explained by a degradation in energy resolution alone. We hypothesise that electron beam damage also contributed to the differences between XAS and EEL spectra of resin and cells. Additionally, the 1s-π* peak A (285.5 eV) in resin and cell components was more intense in EEL spectra compared to XAS. This is similar to the findings of van Schooneveld *et al*., who observed an unexpected 1s-π* peak in EELS measurements of saturated carbon chains. The greater intensity of the 1s-π* peak may also indicate increased damage from the electron microscope by the following mechanism [66]: knock-on damage may cause the removal of hydrogen from the CH_2 groups of saturated hydrocarbons, with the result that the remaining carbons form unsaturated C=C bonds. The formation of these C=C bonds would lead to an increased 1s-π* resonance at 285.5 eV.

The lack of fine structure in EEL spectra between 286 and 290 eV also reduces our ability to detect oxygen-containing functional groups associated with CNT degradation. Therefore, due to a combination of the reduced energy resolution and increased beam damage in EELS, it is not possible to track CNT degradation using features at ~287 eV under current experimental conditions. Radiolytic damage can be reduced by increasing the operating voltage [143], however operating at voltages above 86 kV [60] would result in knock-on damage in the graphitic lattice of the CNTs. To avoid this, the effects of radiolytic damage could instead be reduced by cooling TEM sections [143], and low temperature experiments could provide better results in future work.

As X-ray experiments were able to detect the carboxyl peaks at 288 eV in resin and cell spectra, X-ray experiments might provide higher chemical sensitivity to similar groups on degraded CNTs. However, the XAS residual profile in Figure 5.14(f), which can be interpreted as a relative measure of the goodness of fit, shows very little spatial variation across the sample. Notably, the residual signal does not increase towards the edges of nanotube aggregates. This indicates that both bulk

nanotube aggregates and *aggregate edges* can be described equally well by a linear combination of resin, cell-rich and *undegraded* a-MWNT components. Therefore, XAS results also provide no evidence of degradation of a-MWNTs in macrophages.

The effective spatial resolution of the STXM experiments was shown to be limited to ~280 nm (Figure 5.23). It is possible that CNT degradation may be occurring on a much smaller length-scale, and hence is not detected in the STXM data. Degradation on such a length-scale is supported by mechanistic experiments which predict layer-by-layer exfoliation of tubes [120]. To improve spatial resolution of STXM data, more advanced x-ray optics are needed. Increased sample stability, and hence less specimen warping, may also improve the spatial resolution in this data. Increased sample stability is often achieved by coating the sample with a layer of amorphous carbon [143]. Carbon-coating is not ideal in this situation as it will cover the whole of the cell section and contribute to the signal at the carbon K edge. Instead, extra support may be provided by using TEM grids covered with a holey or lacy carbon film. Regions of interest which fall over holes in the support film could then be chosen for the EELS experiments. This would increase sample stability without affecting the signal at the carbon K edge.

5.6. Conclusions

The fate of a-MWNTs in macrophage cells has been investigated using changes in fine structure at the carbon K edge. STXM-XAS and STEM-EELS independently revealed that a-MWNTs are internalised within macrophage cells after one day and 14 days, and that these a-MWNTs are present as aggregates at both time points. Individual a-MWNTs were also observed within macrophage cells by STEM imaging. Aggregates were found to retain their graphitic structure even after 14 days of exposure, and there is no evidence in this work of degradation at aggregate edges. However, these findings are limited by electron beam damage and the reduced energy resolution of EELS, as well as by the ~280 nm spatial resolution of STXM-XAS. Further work is required to determine if degradation of the a-MWNTs is occurring on smaller length-scales.

6. Functionalised Carbon Nanotubes

6.1. Introduction

A major barrier to fully realising the potential of carbon nanotubes in applications is their high tendency to aggregate in solutions [144]. Aggregated CNTs do not exhibit the same exceptional mechanical and chemical properties that an individual CNT will possess by virtue of its small size [145-147]. In order to access these properties, CNTs first need to be dispersed. This can be achieved by reducing the hydrophobicity of the CNT surface. One of the most frequently employed methods to improve dispersion is by oxidation of CNTs using acids such as nitric and sulphuric acid [148, 149]. As well as increasing CNT dispersibility, acid oxidation is also often employed to increase the purity of CNT samples by removing metallic catalyst and carbonaceous debris [150]. Additionally, oxidised tubes can then be further derivitised, introducing different functional groups for wide-ranging applications [151].

A thorough understanding of the effects of acid oxidation, *i.e.* the altered surface and physiochemical properties of oxidised CNTs (ox-CNTs), is important both for the applications of ox-CNTs and the ability to control the oxidation and subsequent functionalisation processes. Acid oxidation is known to open the ends of CNTs [152], cause length shortening, and to introduce structural defects such as atomic vacancies and deviations from hexagonal ring structures [153]. Changes to CNT dimensions and defect density following acid oxidation have been well characterised using techniques such as high resolution TEM and SEM [154, 155]. There is much ongoing work into developing protocols to characterise the oxygen-containing groups which are introduced on to the CNT walls during acid oxidation (Figure 6.1). The following section will briefly discuss the techniques currently used to identify and quantify functional groups on ox-CNTs. While these techniques have provided many insights into CNT functionalisation, current state of the art methods all have limitations, especially with regards to spatially-resolved information. Therefore there is a need for novel methods which allow characterisation of ox-CNTs at the nanometre scale. For more detailed reviews of CNT functionalisation the reader is referred elsewhere [156].

6.1.1. Identification of functional groups

Multiple complementary characterisation techniques are commonly used, often in combination, to probe the functional groups on CNTs. These include infrared (IR) spectroscopy, Raman spectroscopy, chemical derivatisation (CD), Boehm titration, thermogravimetric analysis (TGA), temperature programmed desorption (TPD), x-ray photoelectron spectroscopy (XPS) as well as x-ray absorption near-edge structure (XANES) [156]. Figure 6.1 shows the range of oxygen-containing functional groups which may be introduced on to CNTs during acid oxidation. The presence of many of these groups has been confirmed experimentally; for example, using IR spectroscopy, vibrational modes characteristic of carbonyls have been identified on SWNTs oxidised with H_2SO_4/HNO_3 [157], and alcohol groups have also been found on oxidised MWNTs (ox-MWNTs) [158]. Definitive assignments of other groups such as lactones can be difficult using IR spectroscopy due to overlapping peaks in the IR spectra [159]. A further limitation is that IR spectroscopy is generally not quantitative, as the variety of local environments and the low concentration of functional groups makes peak intensities difficult to compare between samples [158].

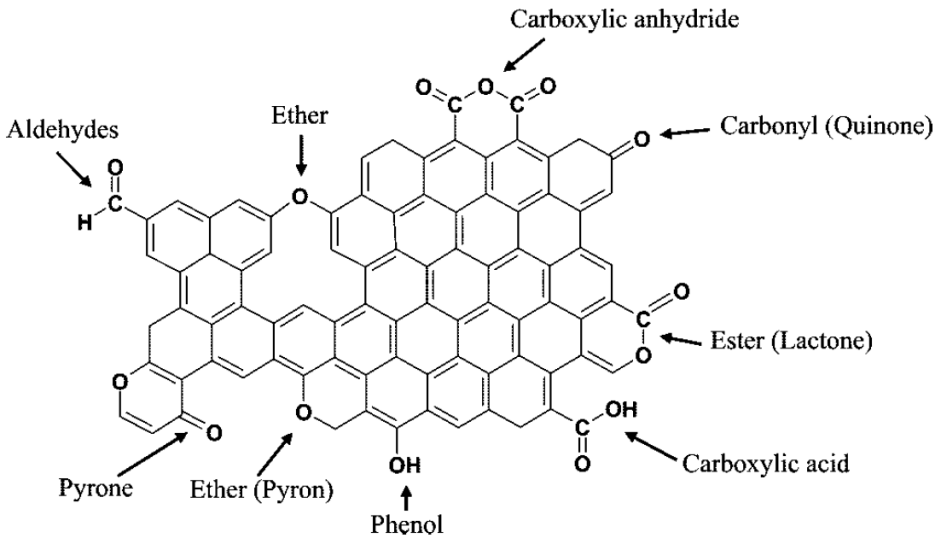


Figure 6.1 Schematic illustrating the variety of oxygen-containing groups which may be present on ox-MWNT surfaces. Reprinted with permission from [160]. Copyright 2008 American Chemical Society.

TGA is often used simply to determine the atomic oxygen content of ox-CNTs [156]. However, when TGA is used in combination with mass spectrometry to identify the evolved gases, it becomes possible to distinguish between different oxygen-containing groups. Using this technique, Martinez *et al.* reported the presence of carboxyl groups on HNO_3 oxidised SWNTs [161]. Carboxyl groups are easily identifiable by TGA-MS due to their characteristic evolution of CO_2 at relatively low

temperatures. However the identification of other oxygen groups is complicated by broad overlapping resonances and also the ability of a single functional group to undergo thermal decomposition through a number of routes, releasing different gases [156]. These factors also make quantification of functional groups difficult using TGA-MS.

XPS analysis can also be used to quantify the carbon to oxygen ratio in a CNT sample, or to quantify the presence of C-OH, C=O and COOH groups using the energy shifts of the different carbon species [156]. However the surface sensitivity of this technique means that only the top 0.5-5 nm of sample is probed [162], which may lead to difficulties in interpreting XPS results which are not truly 'bulk' measurements. Another difficulty is that the similar binding energies of the carbon species, and their relatively low concentrations can make the deconvolution of peaks difficult [156]. One solution is the use of chemical derivatisation, a technique whereby specific oxygen-containing functional groups are tagged with a unique chemical species (e.g. a compound containing fluorine) which is then quantified [156]. Chemical derivatisation of a range of MWNTs oxidised using different acids to reveal that functional groups such as COH, COOH, C=O were introduced in different proportions (Figure 6.2) [163]. Such CD methods rely on indirect tagging of the group of interest. They are therefore limited by the selectivity of the tag, and require knowledge of the efficacy of the derivatisation reaction if the concentration of functional groups it to be accurately quantified. In addition, not all functional groups can be targeted in this way [156].

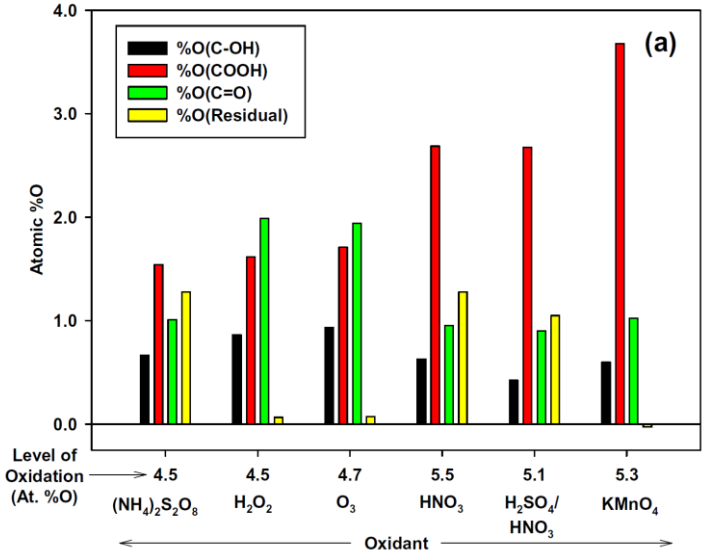


Figure 6.2 Graph showing the concentrations of different functional groups on the surface of MWNTs oxidised using a variety of acids. Functional groups were quantified using chemical derivatisation. Reprinted from [163] with permission from Elsevier.

Raman spectroscopy is commonly used to assess the functionalisation of CNTs using two resonances: the G band at 1500–1600 cm^{-1} and the D band at ~1350 cm^{-1} [164]. The G band originates from in-plane stretching vibrations of the carbon–carbon bonds in the CNT walls, whereas the D band is a measure of structural disorder arising from amorphous carbon and defects. Thus, the ratio of the intensities of the D and G bands is often used as a measure of the 'disorder density' of CNT samples [164]. While Raman measurements are invaluable for assessing the disorder in CNT samples, it has been reported that the G:D ratio is not directly related to the degree of functionalisation of the CNTs [165]. This is partly due to two competing effects during acid oxidation: a) the removal of amorphous carbon and b) the formation of defects, which raise and lower the G:D ratio respectively [163].

X-ray absorption spectroscopy provides identification and quantification of functional groups on ox-CNTs by studying variations in the fine structure of the carbon and oxygen K edges. XANES spectra of ox-CNTs exhibit peaks between 287 and 290 eV at the carbon K edge [132, 166-169]. Kuznetsova *et al.* found that these peaks decreased on heating the ox-CNTs, and that the disappearance of these peaks coincided with the disappearance of IR vibrations characteristic of carboxyl and carbonyl groups [132]. The intensity of the peaks between 287-290 eV has also been found to increase with the extent of CNT oxidation [166]. From these results it is possible to infer that XANES features between 287 and 290 eV are related to oxygen-containing functional groups on the surface of ox-CNTs. However, the exact oxygen-containing species which gives rise to each peak has yet to be identified unambiguously.

6.1.2. Distribution of functional groups

The techniques discussed above provide information on the identity and number of functional groups on the surface of ox-MWNTs, though information on the *spatial distribution* of the functional groups is not provided by these bulk methods. As many functional groups are charged, their spatial distribution will have a large influence on the electrostatic interactions between CNTs as well as between CNTs and their environment, e.g. interactions between CNTs and polymers in composites, or between CNTs and biomolecules or membranes in the field of nanomedicine. An understanding of the distribution of functional groups could also lead to increased control over the oxidation procedure.

The high curvature at the ends and bends of CNTs means that these sites, along with defect sites, are higher in energy than the sidewalls of a CNT. It is widely accepted that these regions are more easily

attacked during oxidation, resulting in a higher density of functional groups at these locations [170]. However, experimental evidence of this assumption is somewhat lacking. Menzel *et al.* used Au nanoparticles to tag sulphur-containing groups on CNTs, which were then imaged in the SEM (Figure 6.3) [171]. The decoration of the nanoparticles demonstrated that functionalisation occurred along the entire length of the CNTs. This technique is not quantitative however, as a one-to-one correlation between Au nanoparticles and functional groups is unlikely due to steric effects.

Although most XAS studies of ox-CNTs to date have not been spatially resolved, a brief study by Hitchcock *et al*. has demonstrated that STXM is able to map the distribution of functional peaks across individual MWNTs [168]. This opens up the possibility of in depth investigations of the spatial distribution of functional group, although the spatial resolution of this technique will limit the applicability of this technique to larger diameter CNTs (>50 nm). The higher spatial resolution of the electron microscope would be necessary for the study of smaller diameter nanotubes, however EELS is often considered to be too damaging to be applied to such functional groups [58, 172]. The aim of this work is to determine if differences in the electronic structure can be detected between pristine and oxidised MWNTs using low-dose EELS, and if these changes can be mapped across a MWNT.

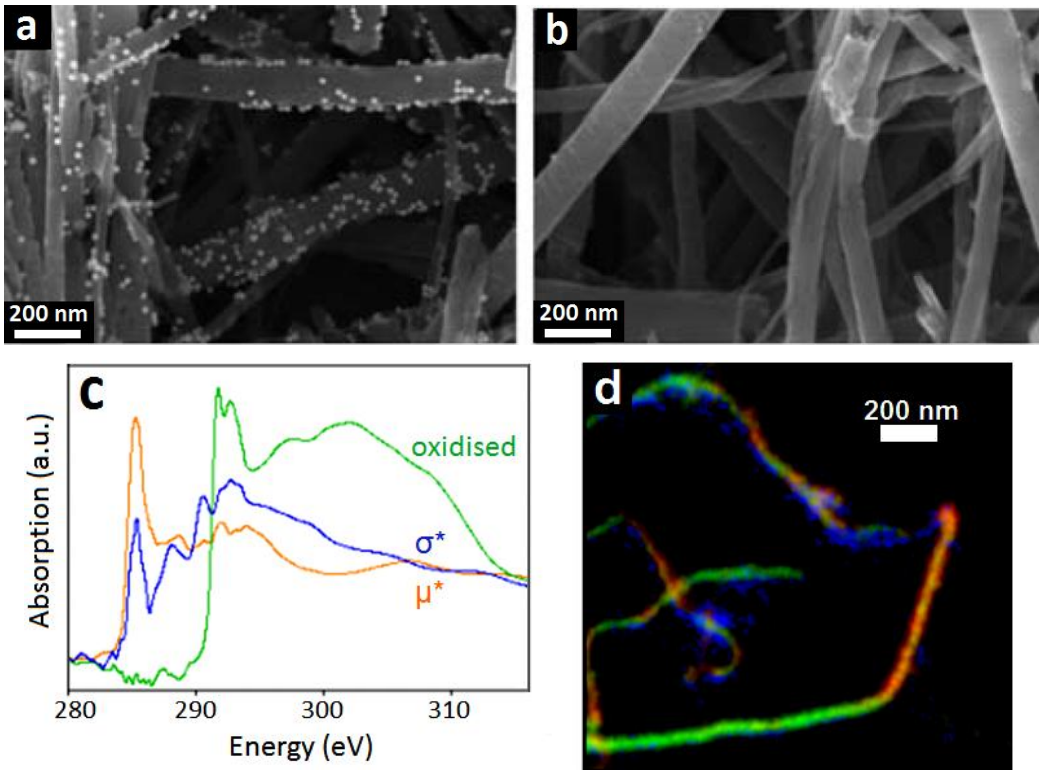


Figure 6.3 Studies of the spatial distribution of functional groups on MWNTs (a) SEM image of sulphur-functionalised MWNTs tagged with gold nanoparticles (b) SEM of MWNTs without sulphur containing groups (c) XANES of three chemical components present in a sample of ox-MWNTs and (d) STXM chemical map of the components showing the distribution of oxidizes carbon in blue. Adapted from [171] and [168].

6.2. The Carbon K edge

There are a number of features of the carbon K edge which can complicate the analysis of the MWNTs studied here. In this section, the effects of orientation dependence and chemical shifts will be discussed.

6.2.1. Orientation dependence

In anisotropic materials, the orientation-dependence of the density of unoccupied states becomes important. This is because the probability of transitions into unoccupied states, and hence the EEL spectrum, will be influenced by the direction of momentum transfer, $\underline{q}$, with respect to the sample. For small scattering angles, we can approximate the components of $\underline{q}$ ($q_{\parallel}$ parallel to the incident beam direction and $q_{\perp}$ perpendicular to it) as

$$q_{\parallel} = k_0 \theta_E \qquad \textit{Equation 6.1}$$

$$q_{\perp} \approx k_0 \theta \qquad \textit{Equation 6.2}$$

where k_0 is the wavevector of the incident electrons, θ is the scattering angle and θ_E is the characteristic scattering angle[‡‡] [7]. At the carbon K edge, θ_E is approximately 1.8 mrad. The collection semi-angles used in this work (~18 mrad) are much larger than θ_E, and so $q_{\perp} > q_{\parallel}$. Hence our EEL spectra mainly probe transitions in which the momentum transfer is *perpendicular* to the incident beam.

The π* and σ* orbitals in graphitic NTs are highly directional, as shown in Figure 6.4. MWNTs have relatively large diameters of ~10 nm, and hence the average curvature of the graphitic walls is small. The *local* structure of a MWNT is thus comparable to that of graphene[128]. For example, probing the centre of a CNT is analogous to probing graphite oriented so that the c-axis of the graphitic planes is parallel to the incident beam direction. In this orientation, the π* orbitals and $\underline{q}$ are orthogonal, and so we expect the 1s->π* transition to be forbidden. At the same time the transition to σ* orbitals, which lie in the graphitic plane, will be maximum at the centre of the MWNT. (In reality the curvature of the nanotube walls brings the σ* orbitals slightly out of the basal plane.)

Now we consider an EEL spectrum acquired at the edge of a CNT. As we are interested in momentum transfer perpendicular to the incident beam direction (z), $\underline{q}$ may lie anywhere in the x,y

[‡‡] The characteristic scattering angle corresponds to the mean energy loss, $\overline{E}$. For low beam energies E_0, it can be approximated by the equation $\theta_E = \overline{E}/2E_0$.

plane. This is referred to as the 'indetermination of the q-vector' [128]. If $\underline{q}$ lies along the x-axis, the probability of a transition into the π* orbitals will be high. If $\underline{q}$ lies along the y-axis then transitions into σ* orbitals will also occur. Therefore both π* and σ* resonances are expected at the edge of the CNT. EEL spectra from all positions across a MWNT will vary continuously between these two extremes.

This simple picture is complicated by a number of factors which reduce the full orientation dependence that might be expected from such highly directional MWNTs:

1. The STEM probe has a finite convergence angle of approximately 7 mrad in this work. Therefore the EEL spectrum at any one point on the CNT will be summed over a range of $\underline{k}_0$ (and hence $\underline{q}$), which effectively results in the orientation dependence becoming blurred [128].

2. In order to reduce the incident electron dose, EEL spectra were acquired from regions of ~25 nm^2. This has an averaging effect as each region will contain carbon atoms from multiple walls of the MWNTs, with a range of orientations (*Figure 6.4*(d)).

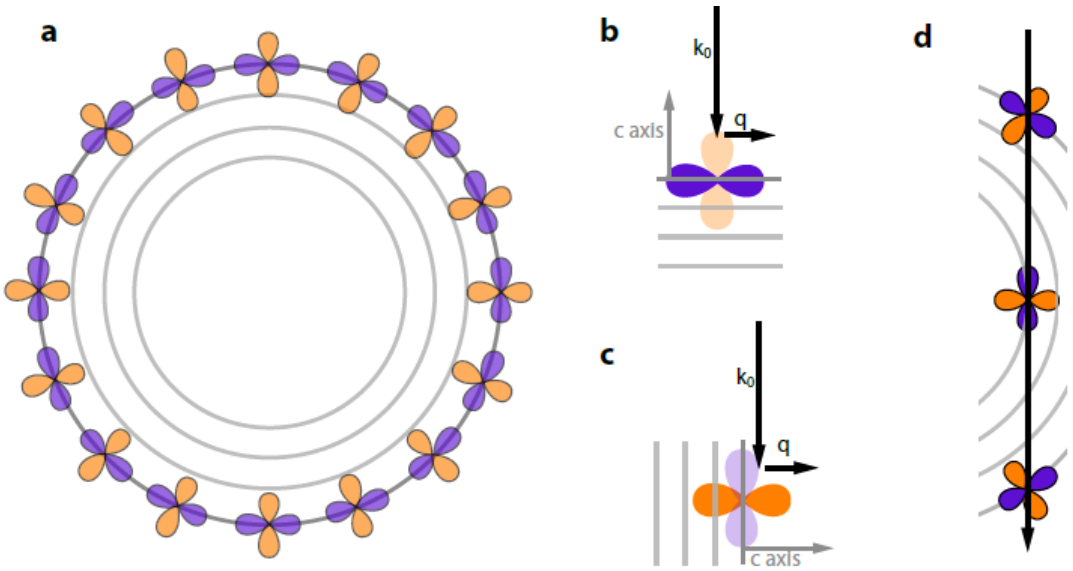


Figure 6.4 (a) Schematic showing the orientation of π (orange) and σ* (purple) orbitals when viewing a CNT end-on, along the long axis. The scattering geometry is illustrated for two situations: (b) when the electron probe is located in the centre of the MWNT and (c) when the probe is at the edge. (d) Shows the variation in orientation of the orbitals from the multiple carbon walls probed by an electron probe.*

One consequence of the variation in ELNES across a CNT diameter is that the intensity under the carbon K edge is no longer a function of the number of carbon atoms probed. Such quantitative analysis can only be performed when the orientation dependence is removed. This can be done by choosing the collection angle such that $q_{\parallel} = q_{\perp}$ which is known as the "magic angle" [173]. In this

work a range of collection and convergence angles were investigated, but no combination was found at which orientation effects were completely removed. Therefore the EEL spectra reported in this chapter were not collected using magic angle conditions.

6.2.2. Chemical Shifts

In section 5.2, bonding was explained by the creation of molecular orbitals, whose energies were different to the outer shell wavefunctions used to create them. Bonding can also shift the energy of the core states. The shift in energy of the core states is measured directly by XPS, in which the core electron is excited into the vacuum, and the kinetic energy that it possesses is a measure of the energy of the core level only [8]. This situation is more complicated in EELS and XAS, where the position of an ionization edge depends on both the energy of the core state and that of the unoccupied state [7, 8]. In graphitic samples, for example, proximity to a highly electronegative oxygen atom will withdraw electron density from the carbon atom, decreasing the shielding and therefore shifting the π* peak to higher energy-losses [8]. The energy position of ELNES features can provide information on the identity of the groups to which the carbon atom is bonded. Energy shifts of carbon K edge ELNES features for a number of functional groups are tabulated in Table 6.1. For each functional group, a range of energies is given as the exact position of a functional peak will be altered by different neighbouring atoms. As some of these energy ranges are overlapping, it can be difficult to assign some spectral features to a single functional group.

Table 6.1 XANES peak energies for a range of functional group, reproduced from [136].

Bond	Peak energy (eV)
C=O	283.0-284.5
C=C	284.9-285.5
C=O	285.8-286.2
C=C-OH	286.0-287.4
C=O	
R-(C=O)-R'	
C-H	287.0-287.6
R-COOH	288.0-288.7
COO	
C=O	
C-OH	289.2-289.5
COO^-	289.5-290.2

6.3. Methods

6.3.1. Sample history

A range of nanotubes was analysed in this study. Commercially produced MWNTs were functionalised using acid oxidation by two collaborators. Batch 1 was obtained from Prof. Kostas Kostarelos at the School of Pharmacy, University of London, and Batch 2 was functionalised by Dr. Shu Chen at the Department of Chemistry, Imperial College London. Their respective functionalisation methods are reproduced below. Samples of as-received commercial MWNTs were also obtained from each group, to act as control samples. These are referred to as pristine MWNTs (p-MWNTs) in the rest of the chapter. Ox-MWNTs were produced as follows.

Batch 1

Pristine MWNTs were purchased from Nanostructured and Amorphous Materials Inc. (Houston, USA) and had a purity of 94%. 2.5 g of MWNTs and 120 ml of concentrated H_2SO_4/HNO_3 (3/1, v/v) were sonicated for 24 h in a round-bottom flask placed in a water bath. The suspension was diluted with large amounts of water, and excess acid was then removed by centrifugation. The black solid was washed thoroughly with water and acetone until a pH value of about 6 was reached. The product was dried *in vacuo* at room temperature. 1.92 g of MWNT-COOH was obtained. TEM characterisation showed that the CNTs had been shortened by acid oxidation to a length of between 50 and 500 nm. Previously published IR spectra of the ox-MWNT samples confirmed the presence of carboxyl groups [129]. Ideally, Raman spectroscopy would also have been carried out on these samples. This would have provided more quantitative data, and allowed comparisons with Batch 2 to be made. Unfortunately, our collaboration ended before samples for Raman analysis could be obtained.

Batch 2

Pristine MWNTs were purchased from Arkema. 0.3 g of MWNTs and 30 ml of concentrated sulphuric (98%, Aldrich, A.R. grade) and nitric acid (65%, Fluka, puriss. p.a. plus) mixed at a volume ratio of 3:1 were heated to reflux at 120°C. After 30 minutes, the reaction solution was cooled and then diluted in ~500 ml of icy water. The ox-MWNTs were washed with distilled water through a sintered glass filter, using a 0.45 µm polycarbonate membrane, until the filtrate was colourless and the pH reached that of the distilled water (~5.5). Acid oxidation creates carbonaceous debris – highly functionalised aromatic fragments which coat the CNT walls but are not covalently attached [158]. In order to remove the debris, ox-MWNTs were washed with ~500 ml of 0.01 M sodium

hydroxide (BDH, AnalaR grade). This washing step produced a brown coloured filtrate and was continued until the filtrate ran clear. The ox-MWNTs were further washed with ~500 ml of 0.01 M hydrochloric acid (BDH, AnalaR grade) and finally the solution was neutralised by washing with 500 ml distilled water. Raman measurements performed by Dr. Shu Chen using an excitation of 632.8 nm found ox-MWNT samples to have a G:D peak ratio of 0.75 ± 0.05.

6.3.2. TEM grid preparation

TEM grids were prepared in the Department of Chemistry, Imperial College London with the help of Dr. Shane Bergin. All TEM grids were prepared from MWNT samples dispersed in HPLC-grade water. Water was used instead of the more common organic solvents or alcohols in order to avoid the possibility of contamination of TEM samples with functional groups from the solvent. As MWNTs are not easily dispersed in water, dispersions were first sonicated for 2-3 minutes using a sonic probe, and then samples were immediately dropped onto TEM grids. This procedure was found to provide adequate dispersions for the MWNTs used in this study. Samples were left to dry at room temperature before TEM analysis.

Lacey and holey carbon TEM grids from a number of suppliers were found to suffer from significant contamination if used as received from the manufacturers. Contamination was evident in STEM mode, but not TEM. It was characterised by a large build-up of material on the support film when exposed to a STEM probe, even for short periods of time (<1s) [174]. EELS analysis showed that this material contained only carbon and oxygen. The material was mobile, forming bridges into the vacuum, and coating nanotubes which lay over holes in the support film.

Carbonaceous contamination is particularly undesirable in this study as this contamination contributes to the carbon K edge. The large increase in sample thickness that is also associated with contamination could potentially mask ELNES from MWNTs. A number of routes to reduce the contamination of as-received TEM grids were investigated. These included washing in ethanol, plasma cleaning, and heating grids *in vacuo* in a tube furnace as well as a dedicated vacuum oven. Only heating in the vacuum oven to 120°C overnight was found to completely remove the carbon build-up. Therefore, all contaminating TEM grids were treated in this way before samples were dropped on to them.

6.3.3. Microscope parameters

An important damage mechanism is radiolysis, which is caused by inelastic scattering events which result in bond breakage. Thus the cross-section for radiolytic damage follows that of inelastic scattering, i.e. it is inversely proportional to the energy of the fast electron [143]. While it is true that lower energy electrons impart more radiolytic damage, the EELS signal to damage ratio is independent of electron energy. Therefore, the accelerating voltage in this work was chosen to minimise another damage mechanism, knock-on damage[§§] [2], whilst controlling radiolytic damage by lowering the temperature. Low temperature conditions are thought to reduce the effects of radiolytic damage, e.g. mass loss and structural damage, by lowering the mobility of the atoms liberated by bond breakage [143].

All EELS experiments were performed in the FEI Titan microscope at Imperial College London, using an accelerating voltage of 80 kV. This is below the 86 kV knock-on damage threshold of CNTs [60]. A Gatan liquid nitrogen cold stage was used to cool the sample. However, cooling to -170°C in the TEM resulted in the formation of a textured layer of contamination on the TEM grid and sample. Figure 6.5 (a) and (b) show a MWNT before and after electron illumination. EEL spectra at the carbon and oxygen K edges are shown in Figure 6.5(b) and (c). This effect has been reported previously [175] and is thought to arise from the condensation of residual molecules in the vacuum chamber, either water vapour or carbonaceous species. The similarity of the oxygen K edge to that of ice might suggest the former. At the carbon K edge, new ELNES features are present on the cooled support film compared to room temperature measurements. These additional peaks occur at 287.9 and 291 eV, where changes in bonding due to the functionalisation of MWNTs are also expected. The contamination layer was found to disappear, possibly due to sublimation, on heating the sample to -75°C. All EEL spectra presented in this chapter were acquired at -70°C to ensure that this contamination effect is eliminated.

[§§] Knock-on damage refers to the displacement of atoms from their lattice position [2].

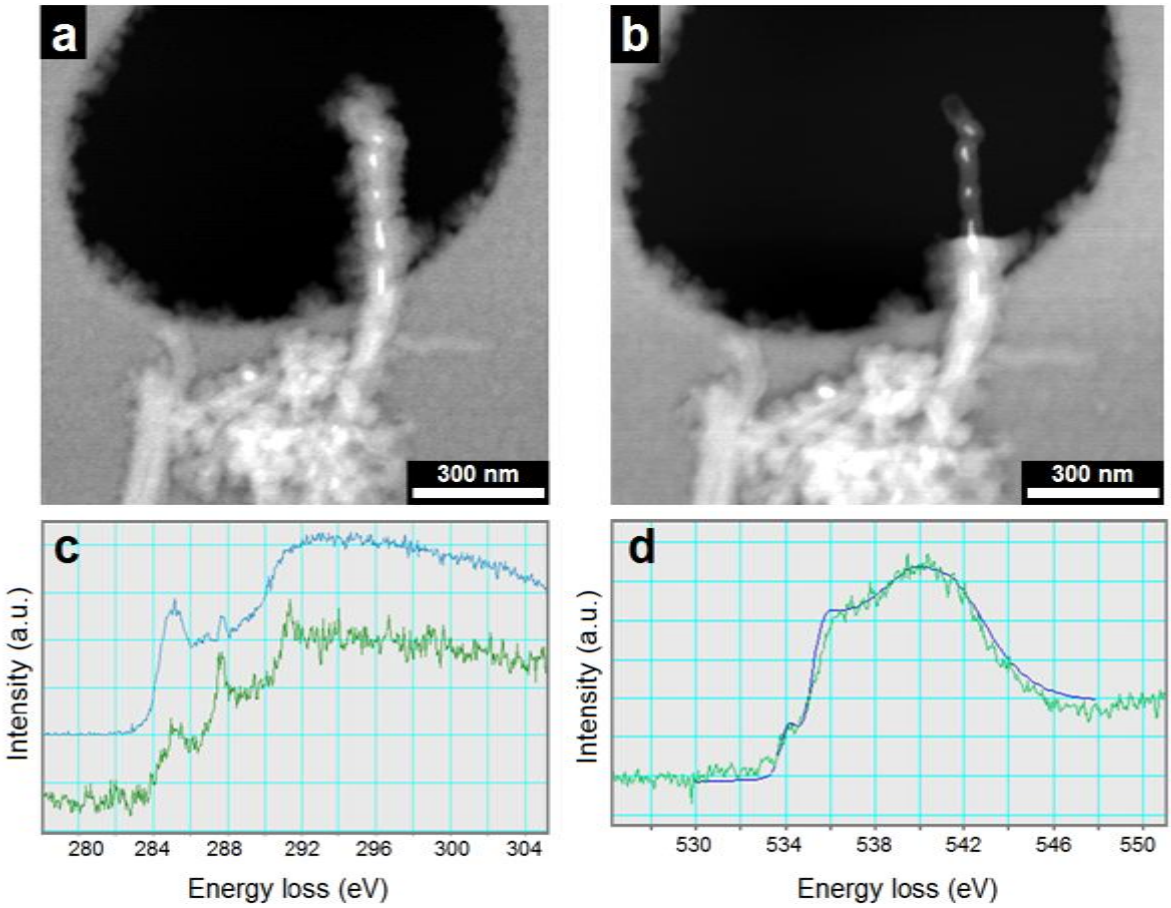


Figure 6.5 STEM and EELS analysis of ox-MWNT samples at -170°C (a) Dark field STEM image of MWNTs over a hole in the support film, and (b) STEM image of the same MWNT after exposure to an electron probe scanned over the tip. (c) Carbon K edge EEL spectrum of the support film (green) compared to a previously reported low-temperature spectrum (blue) [175] (d) Oxygen K edge spectrum of the support film (green) compared with EELS of ice (blue) from reference [175].

Further measures were used to minimise the electron dose applied to the specimen. Spectrum images were acquired using relatively large pixel sizes of 3 - 15 nm. Sub-pixel scanning was used, in which the probe is moved across the entire area of each pixel rather than held stationary at one spot. Additionally, high y-binning of 128 resulted in adequate SNR even for relatively short acquisition times of 0.5-2 s. By measuring the current on the fluorescent screen, the total electron dose was calculated, and ranged between 10^3 and 10^6 electronsÅ^{-2}. The variation in dose is caused by a) different choices of pixel size and spectrum acquisition times between spectrum images, and b) the increasing brightness of the probe, which could change by up to an order of magnitude throughout the day. The convergence and collection semi-angles used were 7 and 18 mrad respectively. Spectra from each pixel in a spectrum image were processed by removing background of the form AE^{-r}, and aligning the π* peak to 285.5 eV.

6.4. Results

6.4.1. EELS of ox-MWNTs

A number of EEL spectra obtained from each sample are shown in Figure 6.6. All MWNT spectra contain peaks A and C, at 285.5 eV and 292.7 eV respectively, which are characteristic of graphitic carbon. These features are in good agreement with previously reported XAS and EEL spectra of CNTs [67, 128, 132, 169], and have been discussed in more detail in section 5.4.1. The lower SNR of spectra from Batch 2 is a result of the smaller diameter MWNTs of this batch, effectively reducing the sample thickness and hence lowering the intensity under the carbon edge.

EEL spectra from ox-MWNT can be divided into two groups, those that appear to be very similar to p-MWNTs, and those that exhibit an additional peak labelled B', at 287.7 eV. This peak was observed in both batches of ox-MWNT, mostly as a relatively weak feature. However a number of spectra exhibited a sharp, intense peak B'. In a few instances, weak features at 287.7 eV were also observed in p-MWNT spectra e.g. the starred spectrum in Figure 6.6.

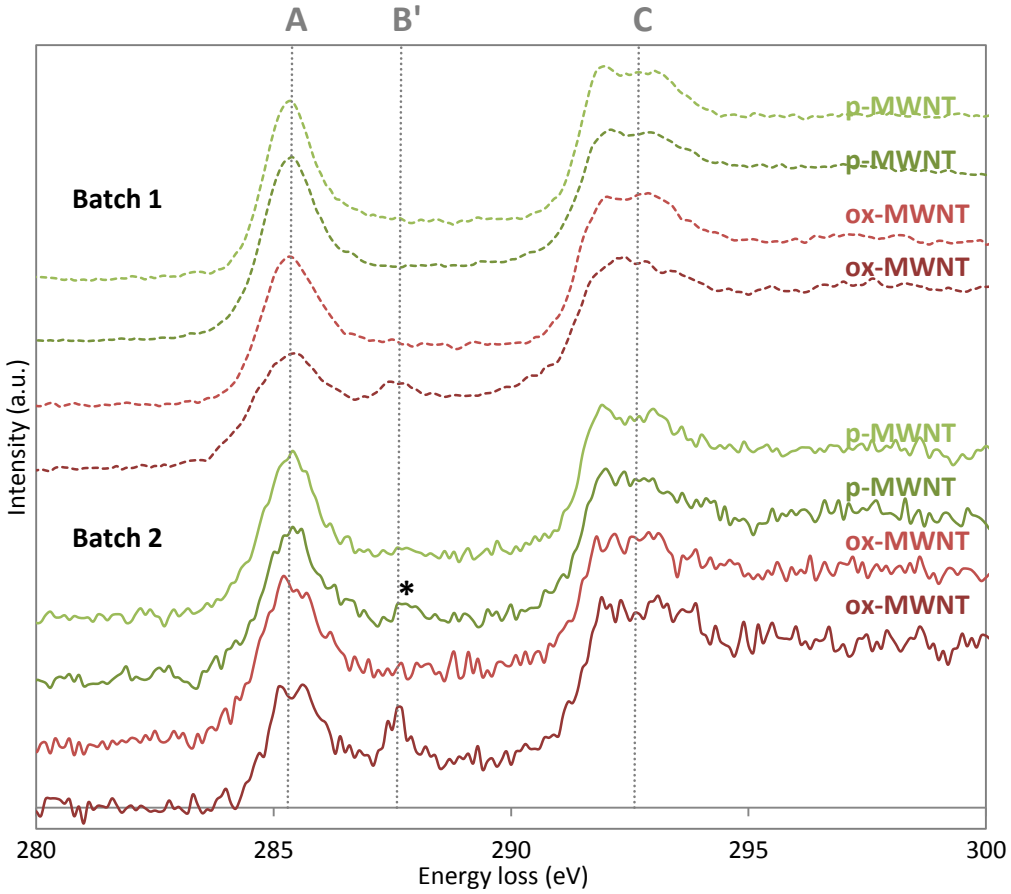


Figure 6.6 EEL spectra of the different MWNT samples. Two spectra of pristine (green) and oxidised (red) MWNTs from each batch are shown. Peaks corresponding to graphitic carbon at 285.5 and 292.7 eV are labelled. The peaks occurring at 287.7 eV are also marked.

6.4.2. Comparison with XANES literature

The features observed here could not be readily compared against previously published EELS studies of oxidised CNT systems, as the majority of these EELS studies employed much lower energy dispersions to investigate fine structure over a larger energy range of the carbon K edge. Therefore in this section our EELS results are compared with XANES studies of oxidised graphitic systems, including SWNTs, MWNTs and graphene sheets (Figure 6.7). Considering peaks A and C, there is relatively good agreement between EELS and all XANES spectra shown. However, the XANES features in the energy range *between* peaks A and C vary significantly across the different studies, and no clear trend between sample type and XANES features can be discerned. For example, a predominant feature in this energy region is a peak at ~288.7 eV, labelled B" in Figure 6.7. Most studies associate peak B" with the presence of oxygen-containing surface functional groups [132, 169], in particular COOH [132]. This peak is present in spectra of oxidised graphene, ox-MWNTs, and ox-SWNTs (i) and (ii), however it is absent in the spectra of ox-SWNT (iii) and (iv). The position of peak B" varies by about 2 eV between studies, and even ox-SWNT samples (i) and (ii) exhibit feature B" at different energies. Additionally, ELNES features at 288.7 eV were not observed in any of the EEL spectra recorded in this work.

A number of the XANES spectra in Figure 6.7 display increased intensity at 287.7 eV as well as the presence of peak B", although this is not always resolved as a separate peak. The XANES of ox-SWNTs (iii) contains a shoulder at 287.7 eV, which has been assigned to π^* transitions of oxidised carbon groups [132]. Ox-SWNT (ii) also exhibits a small peak B', which is only visible in the expanded spectrum shown in Figure 6.7(b) [69]. Again, this peak is attributed to oxygen rich surface groups. Interestingly, the XANES spectrum that most closely matches the shape of peak B' in our EELS data was recorded from the *unoxidised* graphene sheet. This feature was assigned to defects in the graphitic structure.

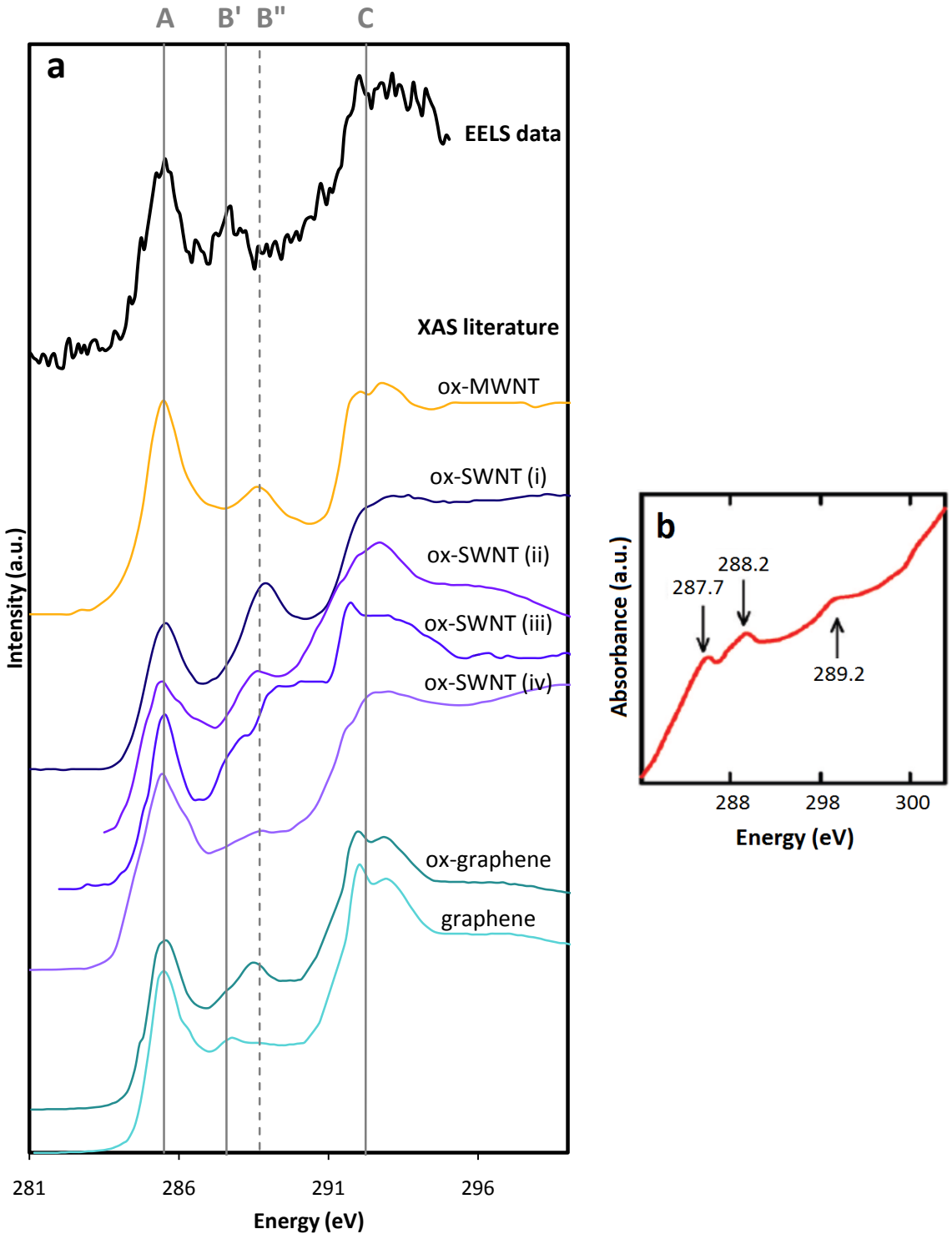


Figure 6.7 (a) EELS data of the ox-MWNTs investigated here are compared with XANES spectra from the literature, including acid oxidised MWNTs from reference [166], acid oxidised SWNTs (i)-(iv) from references [167], [67], [132] and [169] respectively, as well as oxidised and pristine graphene from reference [133]. The position of EELS peaks A, B' and C have been marked, as well as a new peak B" at ~288.7 eV which appears only in XANES data. (b) Expanded spectrum of the region between peaks A and C of ox-SWNT (ii) showing additional features at 287.7 and 288.2 eV.

6.4.3. Spatial distribution of peak B'

The spatial distribution of peak B' across the MWNT samples can be mapped by first decomposing each EEL spectrum into its constituent components. Linear decomposition is complicated by the orientation-dependence of the graphitic signal, which alters the relative intensities of peaks A and C as a function of position across the MWNT, as discussed in section 6.2.1. Figure 6.8 shows two EEL spectra taken from the edge and centre of a MWNT. Respectively, these spectra correspond to situations where $\underline{q}$ is parallel and perpendicular to the c axis of the graphitic sheets. The intensity of the π* peak has been normalised to emphasise the different π*/σ* ratios.

Linear combinations of these two spectra, $\underline{q} \parallel c\ axis$ and $\underline{q} \perp c\ axis$ were found to adequately describe EEL spectra from any position along the diameter of a MWNT. Figure 6.8 shows a number of EEL spectra obtained from different positions across the diameter of a single MWNT. Linear regression fitting was used to determine the ratio of the $\underline{q} \parallel c\ axis$ and $\underline{q} \perp c\ axis$ components. The fitted spectra are overlaid (dotted lines) for comparison.

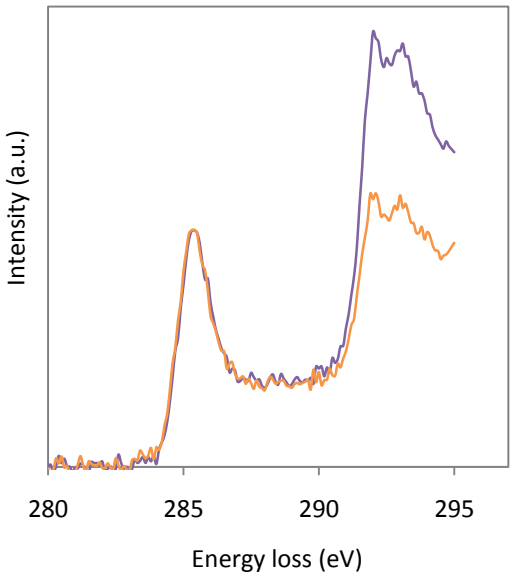


Figure 6.8 EEL spectra showing the orientation-dependence of MWNTs at the carbon K edge. The reference spectra were taken at the edge (orange) and centre (purple) of a MWNT.

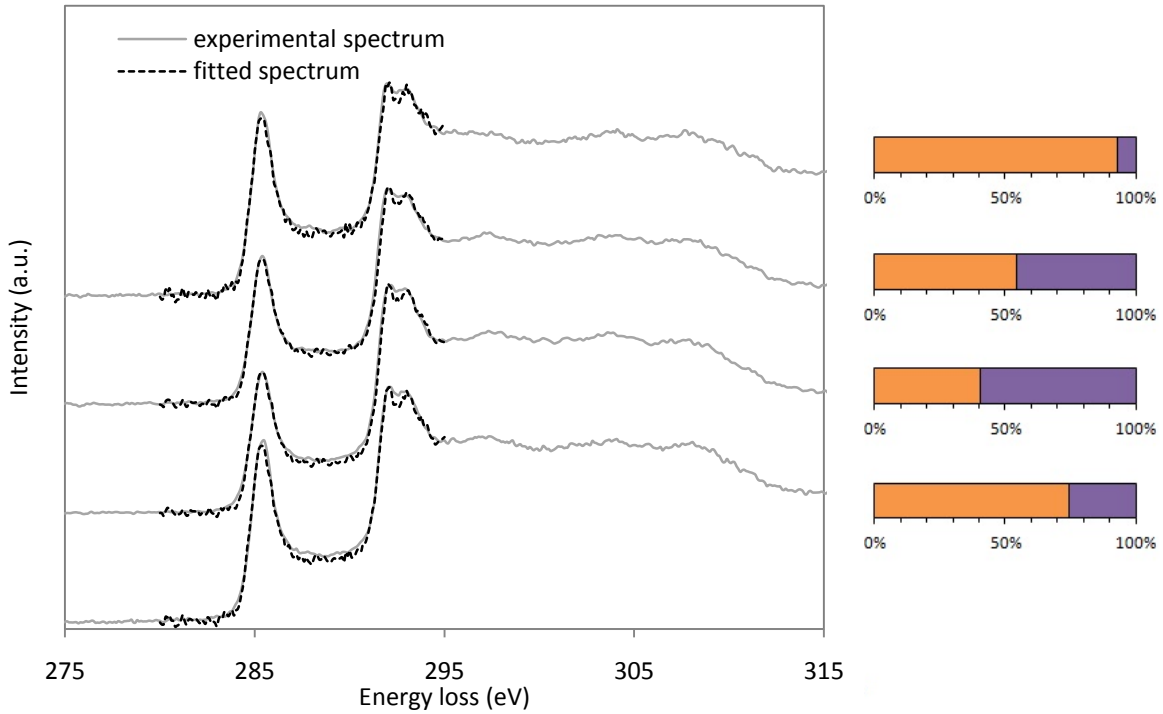


Figure 6.9 Four spectra taken at different positions across a MWNT (grey) overlaid with a linear superposition of the reference spectra from Figure 6.8. The coefficients of the reference spectra were calculated using linear decomposition, and are displayed in the bar graphs on the right.

Therefore, each EEL spectrum was decomposed into the following four components:

1. A Gaussian peak centred at 287.7 eV
2. Graphitic carbon where $\underline{q} \parallel c\ axis$
3. Graphitic carbon where $\underline{q} \perp c\ axis$
4. Amorphous carbon from the support film, defects and non-graphitic debris

These components are displayed in Figure 6.10(a), where components 2-4 have been normalised to an arbitrary 10000 counts between 282 and 295 eV. Figure 6.10(c) and (d) illustrate examples of the linear regression fitting, applied to two experimental spectra. Experimental spectra are overlaid with fitted spectra. Each component, scaled by the calculated regression coefficient, is also displayed. The difference between experimental and fitted spectra (grey line) is relatively featureless, demonstrating that the linear regression analysis well described all ELNES peaks.

In order to understand the spatial distribution of different components, EELS data were used to create chemical maps. By performing SVD analysis on selected SI datasets, the graphitic carbon concentration (the sum of of $\underline{q} \parallel c$ and $\underline{q} \perp c$ components) and the concentration of peak B' were mapped. Figure 6.11 and Figure *6.12* display these chemical maps for both ox-MWNT samples.

Chemical maps were also been combined to form a colour map where graphitic regions are green and regions which contain peak B' are red. Overlap between the two species appears yellow in the maps.

EELS SI chemical maps show that graphitic structure has been preserved along the entire length of the ox-MWNTs. Interestingly, peak B' at 287.7 eV appears to be inhomogeneously distributed across individual ox-MWNTs, and there is no evidence of higher concentrations of this peak at the ends of MWNTs. For comparison, the STXM maps recorded by Hitchcock *et al.* have been reproduced in Figure 6.13 [168]. Although the oxidised carbon spectrum displays features at different energies, the maps of this component display similar distribution pattern to our EELS maps.

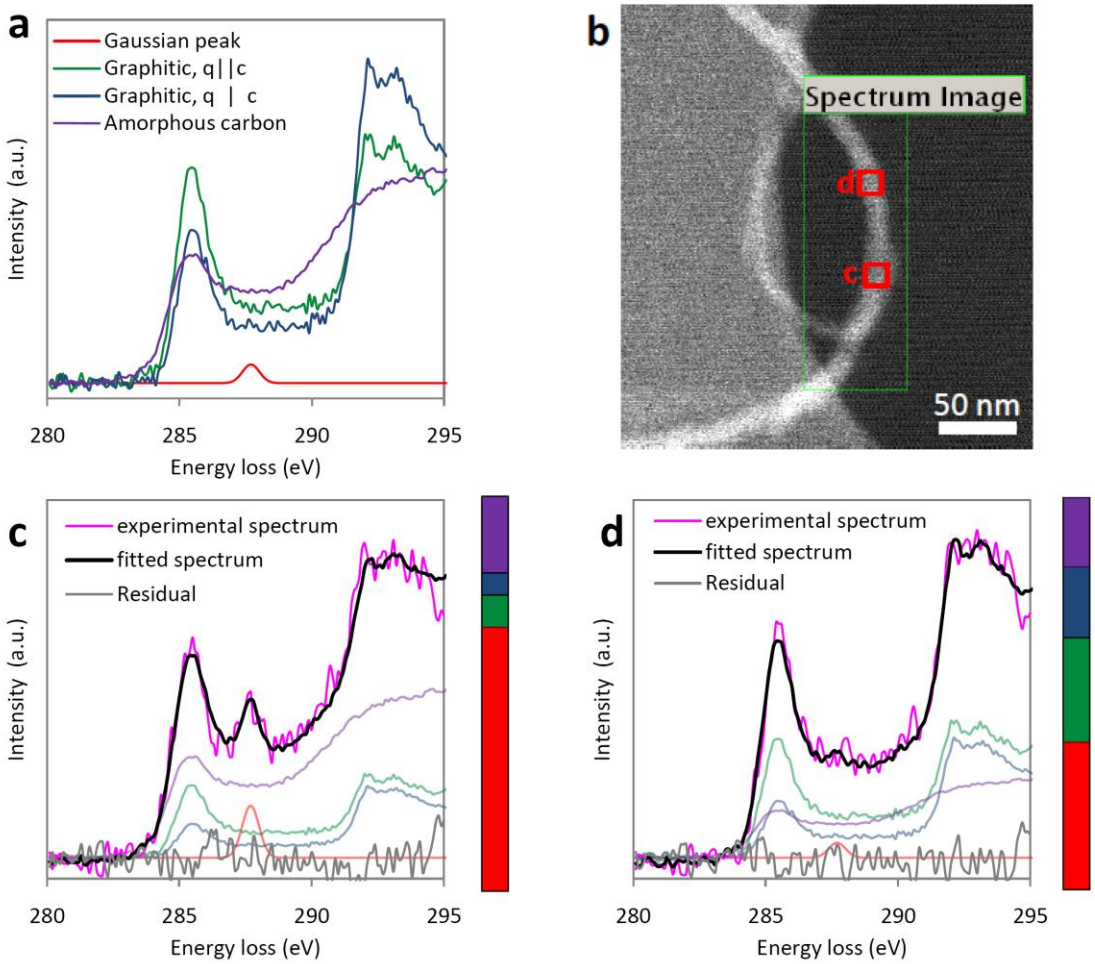


Figure 6.10 Linear regression analysis of the experimental spectra of ox-MWNTs. (a) The four reference spectra, gaussian peak (red) graphitic carbon from two positions: $\underline{q} \parallel c$ axis (green) and $\underline{q} \perp c$ axis (blue) and amorphous carbon (purple). (b) Dark field STEM image of a ox-MWNT, from which two EEL spectra are taken. (c-d) The fitted spectra and scaled reference components are overlaid. The difference between experimental and fitted spectra is plotted as the residual signal, in grey. Bar graphs to the right show the coefficients of each fitted component, where the colours correspond to the key in (a).

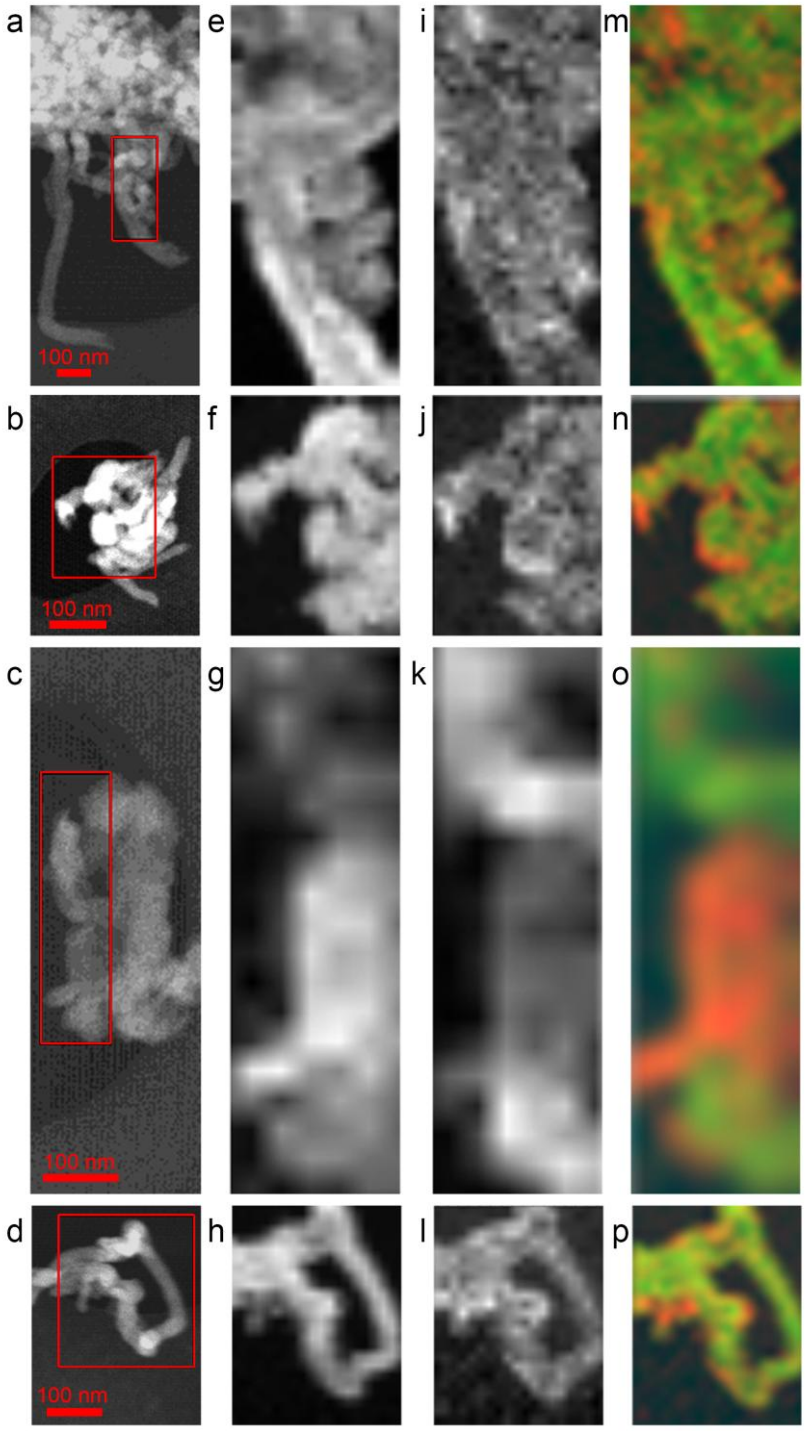


Figure 6.11 Chemical distribution maps across various ox-MWNTs from Batch 1. (a-d) Dark field STEM images of the MWNT bundles. Maps of (e-h) graphitic carbon and (i-l) peak B' are shown, and overlaid to form false colour images (m-p) where the graphitic carbon is green, and peak B' is red.

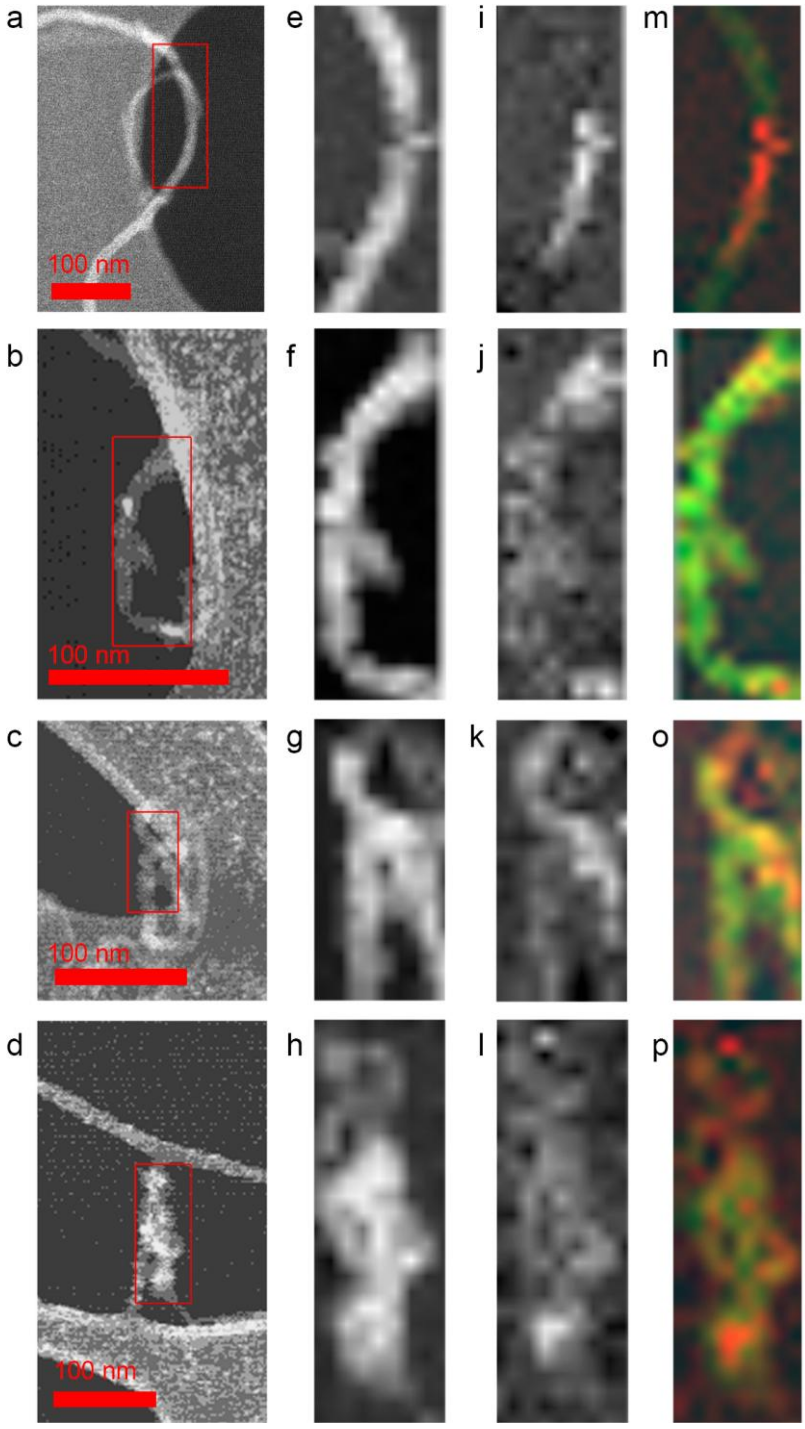


Figure 6.12 Chemical distribution maps across various ox-MWNTs from Batch 2. (a-d) Dark field STEM images of the MWNT bundles. Maps of (e-h) graphitic carbon and (i-l) peak B' are shown, and overlaid to form false colour images (m-p) where the graphitic carbon is green, and peak B' is red.

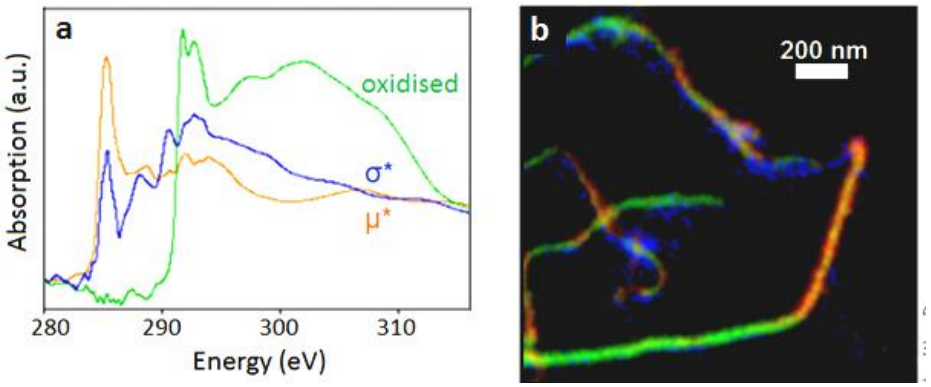


Figure 6.13 (a) XANES of the three chemical components present in a sample of ox-MWNTs and (b) STXM chemical map of the components showing the distribution of oxidizes carbon in blue. Adapted from [168].

6.4.4. Statistical analysis of peak B'

One issue with the EELS chemical maps presented here is that they are often noisy. This can be seen in the chemical map in Figure 6.12(p), where finite contrast is present in regions where there should be zero intensity (*i.e.* over the vacuum). Problems associated with noise are also apparent in Figure 6.10(d), where SVD analysis produced a non-zero gaussian peak coefficient, even though the experimental spectrum contained no obvious peak at 287.7 eV. In general, distinguishing between real, weak features and noise is difficult. In this section, statistical analysis was performed on all SI datasets in order to address this problem.

The criterion for a statistically significant peak B' was based on comparisons of the height of fitted gaussian peak, H, against the intensity of the noise. Noise was measured from the residual signal, which is the difference between an experimental spectrum and the fitted spectrum calculated by SVD in section 6.4.3. When the components in the regression fit well describe the experimental data, the difference between experimental and fitted spectra reveals the spectral noise. A large proportion of this noise originates from shot noise, which is proportional to the root of the signal intensity. Therefore the standard deviation of the noise was calculated between 286-290 eV only, where the EEL spectra of MWNTs are relatively flat. Peak B' was determined to be statistically significant if it satisfied the following requirement

$$H > 2.33 \times \sigma_{286\text{-}290} \qquad \textit{Equation 6.3}$$

where $\sigma_{286\text{-}290}$ is the standard deviation of the noise between 286 and 290 eV. The choice of 2.33σ corresponds to a probability of 99% that the height of peak B' cannot be explained by spectral noise.

In total, 15911 MWNT spectra were analysed, covering a total area of ~1.44 μm^2 of MWNTs. Figure 6.14 tabulates the percentage of EEL spectra which contain statistically significant peaks at 287.7 eV, for each MWNT sample. In both MWNT batches, the percentage of MWNT spectra which contained peak B' was higher in the ox-MWNTs samples compared to p-MWNTs. Spectra of p-MWNTs from Batch 1 contained no significant peaks at 287.7 eV, while a small percentage (0.4%) of p-MWNT spectra from Batch 2 contained peaks. The percentage of ox-MWNT spectra which contained significant peaks at 287.7 eV ranged from 11.3% for Batch 1 to 4.6% for Batch 2.

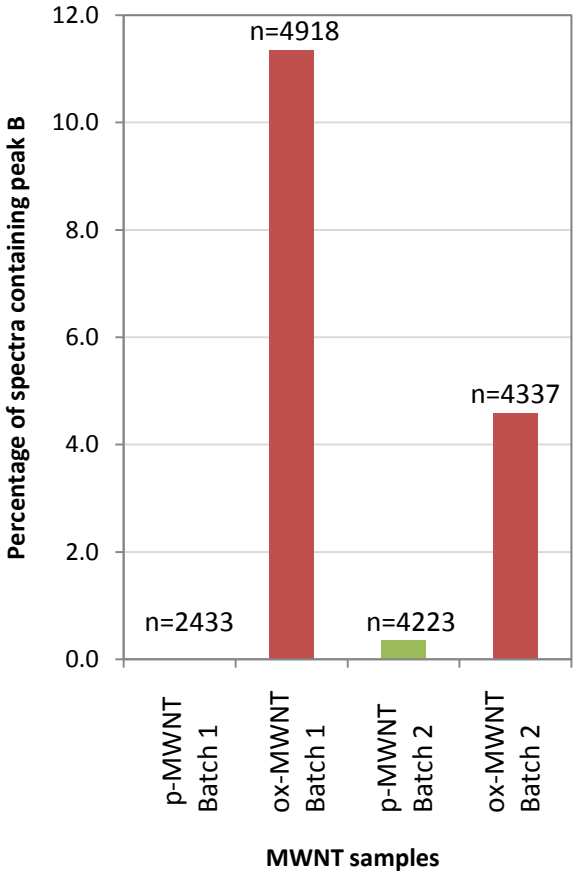


Figure 6.14 Bar graph showing the percentage of EEL spectra which contained a statistically significant peak B' at 287.7 eV.

6.5. Discussion

EEL spectra of pristine MWNTs from both batches were in good agreement with those previously reported in the XAS literature. p-MWNT spectra contained peaks at 285.5 and 292 eV which originate from the 1s-π* and 1s-σ* transitions of graphitic carbon. A small number of p-MWNT spectra also contained peaks at 287.7 eV, most likely due to a low concentration of defects present in the as-received commercial nanotubes. The spectra of ox-MWNTs could be divided into two

categories, where 1) ox-MWNT spectra closely resembled those of pristine MWNTs and 2) where an additional peak at 287.7 eV was observed, superimposed on the graphitic peaks. When present, peak B' was often weak, and the majority of EEL spectra of ox-MWNTs did not contain this peak at all. To the best of our knowledge, the peak at 287.7 eV has not previously been reported in EELS studies of ox-MWNTs.

6.5.1. Assignment of peak B'

The ELNES features between peaks A and C are distinct from the reported XANES spectra of oxidised graphitic materials. A number of XAS studies have reported raised intensity at 287.7 eV, and this peak has been attributed to "oxygen-containing surface functional groups" [69, 132] or (unspecified) defects in the graphitic structure [133]. From these XANES studies, as well as peak assignments determined from a range of organic reference standards (Figure 6.7), it is likely that peak B' observed in this work is caused by deviations from graphitic structure, and could indicate the presence of C-O or C-H bonds in the MWNT walls.

Interestingly, the dominant feature in most XANES spectra of the oxidised graphitic materials occurs at a higher energy-loss, ~288.5 eV. Peaks at ~288.5 eV were not observed in any EELS data recorded in this study. The cause of the discrepancy between XANES and EELS features is unknown, and further work is needed. The XANES peak at ~288.5 eV most likely originates from carboxyl groups. From IR spectroscopy, we have confirmed the presence of carboxyl groups in our ox-MWNTs. Therefore the absence of this feature in EEL spectra is unexpected. One possible explanation for the lack of a carboxyl peak could be a higher susceptibility to electron beam damage in the TEM. Further EELS experiments at lower electron doses are needed to confirm this hypothesis. The different sample preparation routes and sample environments (the lower temperature and higher vacuum in the TEM compared to the X-ray beamline) may also contribute to the differences in ELNES and XANES structure observed in this energy region.

6.5.2. Spatial distribution of peak B'

Using linear regression analysis, experimental spectra were decomposed into four components, thus separating peak B' from the rest of the carbon edge. In this way it was possible to map the intensity of peak B', as well as the graphitic carbon signals, across the samples (Figure 6.11 andFigure *6.12*). The chemical maps demonstrate that the graphitic character of the MWNTs was preserved during acid oxidation. Peak B' was found to be *inhomogeneously* distributed along the ox-MWNTs. This result seems to be similar to the oxidised carbon STXM maps reported by Hitchcock *et al*. [168]. The

commonly quoted prediction of higher functional group loading at the ends and kinks of MWNTs [176, 177] does not seem to be supported by the spatial distribution of peak B'. However, only a very small area has been sampled in this work, and more experiments are necessary to confirm any trends in the spatial distribution of the peak. Additionally, as different functional groups (species as well as location on the graphitic wall) have different sensitivities to electron beam damage, peak B' might only map a subset of all the different functional groups present in the samples. Rigorous damage studies are required to determine whether *all* functional groups are detectable under the current STEM acquisition conditions.

6.5.3. Frequency of occurrence of peak B'

Statistical analysis was performed on all SI datasets to determine the frequency with which significant peaks were observed at 287.7 eV, as peak B' was often weak and on the background noise was high. This analysis was used to determine the number of measurements in which significant peaks were found. A fully quantitative interpretation of these results was not possible in this work due to:

a) complications from orientation dependent effects. The total volume of MWNT sampled differed from pixel to pixel, due to the changing MWNT thickness at various positions across the cylindrical tubes. Additionally, clusters of MWNTs were also studied in which the total thickness of MWNT sampled in a given pixel was unknown. Due to the orientation dependence of the EELS measurements, it is not straightforward to determine the number of carbon atoms present by integration over the carbon K edge. Therefore the relative amount of carbon atoms in each EEL spectrum was not quantified, and thus the ratio of the number of carbon atoms giving rise to peak B' against all graphitic carbon atoms could not be calculated.

b) variations in electron doses used to acquire different EEL spectra. This was caused by variations in the monochromated probe current through the course of the day, as well as small variations in pixel size and acquisition times between different spectrum images. Therefore comparisons between spectra can only be made if the effects of electron beam damage do not vary in the dose range 10^3 and 10^6 electronsÅ^{-2}.

Nevertheless, the results of the statistical analysis show that ox-MWNTs of both batches contained higher concentrations of the functional group than p-MWNTs. This provides further evidence that the peak at 287.7 eV is caused by the acid oxidation process. Therefore, although peak B' has not yet been identified to an exact chemical species, we have shown that its presence can be used as a

signature of the oxidation process. There are indications that ox-MWNTs of Batch 1 contain more functional groups than those of Batch 2 (Figure 6.14). These differences highlight the difficulty of sourcing ox-MWNTs from different laboratories as the oxidation process is not always reproducible. For example, the higher concentration of functional groups in Batch 1 could be caused by the differences in the washing procedures carried out after oxidation: the oxidation procedure for Batch 2 contained a base-washing step, whilst Batch 1 was not base-washed. It has been shown that without base-washing, highly functionalised aromatic debris remains adsorbed to MWNT walls, and this debris could contribute to the signal observed at 287.7 eV. However, further work is necessary to allow a more quantitative comparison of functional group loading between the two ox-MWNT batches.

6.6. Conclusions

Using 80 kV STEM-EELS at -70°C, peak B' at 287.7 eV was observed on spectra of MWNT oxidised using H_2SO_4/HNO_3. This peak was less frequently found on samples of MWNT prior to acid oxidation. It is likely that this feature arises from the presence of oxygen-containing functional groups on the MWNT surface. These data demonstrate that differences in ELNES can be detected between pristine and oxidised MWNT samples. The peak at 287.7 eV has been mapped across the MWNT samples at a spatial resolution of ~5 nm, showing that these groups are inhomogeneously distributed across the entire length of the MWNTs, with no preferential functionalisation occurring at the ends of the MWNTs.

7. Characterising wear debris from MOM hips

7.1. Introduction

One million hip replacements are performed worldwide every year, with the majority of these using metal-on-polyethylene (MOP) bearings [178, 179]. However, the micrometre-sized polyethylene wear debris generated by these hips causes chronic inflammation, which in turn leads to bone death (osteolysis) and loosening of the prosthesis [180, 181]. This limits the lifetime of MOP hips to around 10 years. Therefore, alternatives to polyethylene have been sought, and metal-on-metal (MOM) hip replacements made of cobalt-chromium-molybdenum alloys (60, 30, 7 at% respectively) have become an increasingly popular option, especially for younger patients [182, 183].

While wear rates of MOM bearings are up to 100 times lower than MOP bearings [180], and incidence of failure due osteolysis is almost non-existent [184], MOM hips have exhibited high rates of failure through a different route: patients develop unexplained pain within the first few years of implantation, requiring the prosthesis to be revised [185-187]. This is a considerable human problem, as unexplained pain causes 28% of all MOM hip resurfacing failures [188].

It is hypothesised that poor human biocompatibility with CoCr wear debris is responsible for the early failure of all types of MOM hips [185, 186]. The nanometre size of the metal debris also raises concerns about their possible increased capacity for corrosion, dissemination and cell infiltration [184, 189-191]. However it is not known how wear debris interacts with the tissue, nor which metallic species is responsible for device failure [186, 192, 193]. An important step towards understanding the effect of wear particles on the body is to characterise the chemistry, morphology and ultrastructural distribution of the *individual* particles in the tissue.

7.1.1. Morphological characterisation

There have been many studies to characterise the morphology of wear particles. TEM and scanning electron microscopy (SEM) have shown rounded or irregular particles with mean diameters of approximately 50 nm [183, 194] and aggregates measuring 0.1-5 µm [182]. Due to the difficulty of locating nanoparticles in the comparatively large volumes of explanted tissue, most studies employ isolation protocols in which alkaline or enzymatic treatments digest the organic matter, leaving behind the wear debris [194, 195]. These techniques have been shown to alter the size and chemistry of wear debris [195], and information on the location of particles with respect to cell structure is lost. It is possible to avoid using these isolation techniques by studying wear debris within the surrounding tissue. As it is often impractical to survey large volumes of sample using high spatial resolution techniques such as TEM, a correlative approach across multiple length-scales becomes vital for locating nano-scale debris.

7.1.2. Chemical characterisation

Popular methods for chemical analysis of wear debris are atomic absorption spectroscopy and mass spectrometry [191, 196], but these are destructive and show only bulk composition [197]. An EDX study of explanted tissue found variable proportions of cobalt to chromium in different wear particles. The proportion of cobalt present was often much lower than that in the original alloy [197]. This, coupled with the fact that circulating levels of cobalt and chromium ions are elevated [198], indicates that metal wear particles undergo corrosion.

The methods above are capable of determining only the elemental composition of particles; however the oxidation states of the metals will also have important implications for their toxicity. For example, Cr(VI) is much more toxic than Cr(III), and can lead to denaturing of proteins and breakage of chromosomes [182]. Co(II) has also recently been shown to affect DNA damage across intact cellular barriers [199]. In previous EDX studies, speciations are inferred indirectly from the ratios of the constituent elements. However as the cell environment also contains common complexing elements such as oxygen and phosphorus, oxidation states inferred in this way can give ambiguous results. To more accurately characterise the oxidation state of the debris, direct methods are needed. A recent report showed, using microfocussed x-ray absorption spectroscopy (XAS), that chromium (III) phosphate was the *predominant* species in the tissue [200]. The hard x-rays used in this study limited the spatial resolution of the chemical analysis, and so it was not

possible to determine if the Co and Cr signals arose from intra-cellular or extra-cellular particles, nor the morphological form of the debris. In order to obtain information of individual wear particles, new techniques are required to probe the chemical state of particles on a more appropriate energy- and length-scale.

In this study, soft x-ray STXM-XAS and STEM-EELS were used to locate wear debris in periprosthetic tissue, and comparisons were made between these two techniques. The specific aims were to determine the location of particles with respect to the cells and their organelles, and the oxidation state of the metal species.

7.2. The transition metal $L_{2,3}$ edge

As MOM hips are mainly composed of cobalt and chromium, in this work we will track changes in the chemical state of wear debris using the Cr and Co $L_{2,3}$ edges. $L_{2,3}$ edges involve transitions from 2p states [7]. As both XAS and EELS transition operators have a dipole form, these p electrons can access s- and d-like states. The 2p electron is most likely to be excited into a 3d state, due to the large overlap between 2p and 3d wave functions. Therefore the $L_{2,3}$ edge is dominated by 2p → 3d transitions [201].

3d states in transition metals have high densities and narrow bandwidths, giving rise to sharp intense peaks known as white lines [8]. Unlike fine structure at the K edge (section 5.2), $L_{2,3}$ fine structure is not well explained by the unoccupied density of states [202]. Due to the highly localised 3d states and the strong overlap of the incompletely filled 2p and 3d wave functions, electron-electron effects need to be dealt with explicitly [201, 203]. We turn to *atomic multiplet theory* to understand these edge structures.

Consider the transition from a ground state $2p^6 3d^n$ into a final state $2p^5 3d^{n+1}$. There are six ways to arrange five electrons (or alternatively, one hole) in the 2p shell. Additionally, the number of ways to arrange n+1 electrons in a 3d shell is given by [203]:

$$\frac{10!}{\big(10-(n+1)\big)!\,(n+1)!} \qquad \textit{Equation 7.1}$$

This means that for a Cr(III) ion, for example, the $2p^6 3d^3 \rightarrow 2p^5 3d^4$ transition has 1260 possible final states (though only the subset of these states which satisfy rules such as the dipole selection rule

will contribute to the $L_{2,3}$ edge). These final states are not degenerate; their energies are split by a number of interactions [201, 203]:

1. Electron-electron interactions

   This interaction accounts for both the direct Coulomb repulsion, as well as the Coulomb exchange interaction between each pair of electrons in the atom. Coulomb exchange arises from a quantum mechanical requirement for the overall wave function of two indistinguishable fermions to be anti-symmetric. The electron-electron Hamiltonian, H_{ee}, has the form

$$H_{ee} = \sum_{pairs} \frac{e^2}{4\pi\varepsilon_o \underline{r}_{ij}} \qquad \textit{Equation 7.2}$$

   Where $\underline{r}_{ij}$ is the vector between electrons i and j and ε_o is the permittivity of free space.

2. Spin orbit coupling

   Spin orbit (S-O) coupling results from the interaction between the magnetic moment associated with the spin of the electron, and the magnetic field produced by the electron's motion. This is a relativistic effect which adds the following term to the Hamiltonian:

$$H_{ls} = \sum_{i=1}^{N} \zeta(\underline{r}_i) l_i \cdot s_i \qquad \textit{Equation 7.3}$$

   Where l_i and s_i are the orbital and spin angular momenta of electron i, respectively, and $\zeta(\underline{r}_i)$ is the spin orbit coupling constant of the atom. S-O coupling at the core hole is large, and greatly affects the $L_{2,3}$ spectrum. The 2p core hole has orbital angular momentum $l = 1$, spin $s = 1/2$ and thus total angular momentum j = 1/2 or 3/2 (as $j = l \pm s$). S-O coupling splits the 2p edge into two white lines, L_3 and L_2, corresponding to the $2p_{3/2}$ and $2p_{1/2}$ states respectively. The degeneracy of states is given by 2j+1, implying that the L_3:L_2 intensity ratio should be 4:2. However, additional coupling between the 2p core hole and 3d wave functions mixes the S-O split states and therefore alters this intensity ratio.

3. Crystal field effects

   Crystal field theory (CFT) describes the effect of any ligands which surround a metal ion. In CFT, individual ligands are replaced by a static electric field which surrounds the metal ion. As the crystal field typically has lower symmetry than a free metal ion, the degeneracy of the 3d states is broken. The relative energy of each 3d state will depend on its orientation with

respect to the crystal field. Figure 7.1 illustrates the effect of an octahedral crystal field on 3d states.

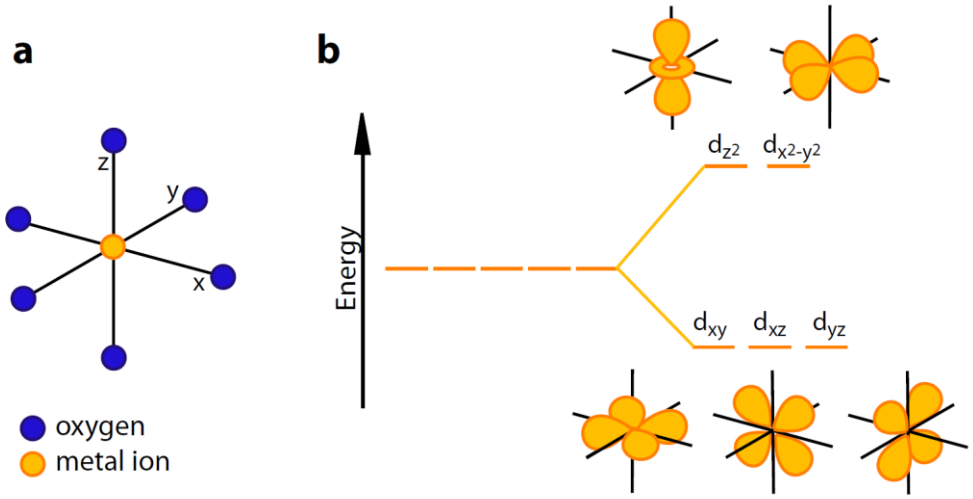


Figure 7.1 Schematic describing the effect of an octahedral crystal field on 3d energy levels. a) Example of octahedral geometry, in which six oxygen ligands surround a central metal ion. b) Energy level diagram of 3d levels showing the loss of five-fold degeneracy due to the different orientations of the d-orbitals with respect to the ligands. Diagram adapted from [204].

Thus, the $L_{2,3}$ edge is very sensitive to changes in electronic structure, and analysis of the fine structure at the edge provides information about the oxidation state of the 3d transition metal ions. Crystal field effects may also provide information on the co-ordination environment. In this chapter fine structure at the $L_{2,3}$ edge has been used as a fingerprint for different oxidation states of the transition metals.

7.3. Sample History and Methods

Tissue samples were obtained from Mr. Alister Hart of the London Implant Retrieval Centre and Imperial College London. Histological analysis and sample embedding was performed by Dr. Ann Sandison at Charing Cross Hospital. Details of sample retrieval and processing are as follows.

Hip capsule tissue was retrieved from patients with failed MOM hip resurfacing arthroplasties during implant revision surgery. Tissue samples were fixed in 10% neutral buffered formalin, and processed to paraffin wax. 3-4 µm thick sections were cut and stained with haematoylin and eosin, which stains nuclear regions blue and the cell cytoplasm and other proteins various shades of pink. Histological analysis was then carried out to identify regions of interest for further TEM and XAS studies. These regions of tissue were de-waxed and fixed in 3% glutaraldehyde in cacodylate buffer. Tissue was post-fixed in 1% osmium tetroxide, which binds to lipids, allowing cell ultrastructure such

as lipid bilayers to be visualised. Samples were then dehydrated through a graded series of ethanol, and embedded in Araldite epoxy resin. Ultramicrotomed sections nominally 150 nm thick were collected on to standard copper TEM grids.

7.3.1. Wear debris identification

Sections from three patients were examined using the JEOL 2000FX TEM at 120 kV under bright field imaging conditions. Electron-dense particles of the right length scale (~50 nm) were further examined using an INCAx-sight™ EDX detector to determine their chemical composition. Samples from one patient were selected for further detailed analysis with FIB-SEM, EELS and STXM.

Slice and View (S&V) data were acquired by David Wall at FEI Company, Eindhoven. A 6 µm × 6 µm × 8 µm volume of embedded tissue was studied using an FEI Helios Nanolab™ with fully automated Slice and View program. Sequential slices, 10 nm thick, were milled away using a 30 kV ion beam. Backscattered electron SEM images were acquired of each successive exposed surface using a 2 kV beam. Stack alignment was performed using ImageJ software [205], and Amira® 3D visualisation software (Mercury Computer Systems, France) was used to reconstruct the volume. Quantitative analysis of particle sizes and morphology was performed using ImageJ software.

7.3.2. STXM-XAS

STXM experiments were carried out at beamline 10ID-1 at the Canadian Light Source (CLS). Sections had been previously mapped in the TEM to enable regions of high particle concentration to be located quickly. Serial sections, not previously exposed to an electron beam, were also analysed. The x-ray probe size was 25 nm and spectral data were acquired in transmission mode. Areas of approximately 10 µm × 10 µm were analysed by acquiring absorption images over the chromium and cobalt $L_{2,3}$ edges. Spectra of a number of reference compounds were also collected: Cr_2O_3, $K_2Cr_2O_7$, $CrPO_4$, $(AcO)_7Cr_3(OH)_2$ and CoO.

7.3.3. STEM-EELS

The *same* sections from the STXM experiments were subsequently examined in the FEI Titan (S)TEM at Imperial College London. All data were acquired at an operating voltage of 300 kV. Bright field TEM and HAADF-STEM images were acquired of the debris within cells. All EELS data were recorded on a GIF Tridiem spectrometer as spectrum images. Unmonochromated spectra were acquired with convergence and collection semi-angles of 7 and 18 mrad respectively, and an energy resolution of of 0.7 eV. Monochromated spectra were also acquired at an improved energy resolution of 0.2 eV.

7.3.3.1. EELS processing

DigitalMicrograph™ (DM) software was used to process all EEL spectra by removing background of the form AE^{-r} and performing quantitative analysis as illustrated in figure 7.2. First, plural scattering was removed from each elemental edge individually. As the Cr $L_{2,3}$ edge lies within ~35 eV of the O K edge, the background signal under the Cr $L_{2,3}$ edge did not follow the power law form, and the O K edge was removed before further analysis. This was done by linear regression fitting of the oxygen signal using DM software. The fitted oxygen edges were subsequently removed from every spectrum in an SI in MATLAB. A typical oxygen-subtracted spectrum is shown in Figure 7.2(b).

The absolute number of oxygen, chromium and cobalt atoms per nm^2 of sample (which was nominally 150 nm thick) was quantified in DM using the equation:

$$I_k(\Delta) = N\sigma_k(\Delta)I(\Delta) \qquad \textit{Equation 7.4}$$

where N is the areal concentration (atoms / nm^2) of the atoms giving rise to the ionization edge k, I_k is the integrated intensity of the edge (over a 40 eV window), I is the integrated intensity of the low loss region including the zero-loss peak (over a 40 eV window), and σ_k is the partial inelastic scattering cross-section. The Hartree-Slater model was chosen to calculate the oxygen K edge cross-section while the 'hydrogenic white line' model was used to calculate the cross-sections of the metals. These models calculate the energy-differential cross section of an edge using tabulated GOS values, and a semi-empirical model based on hydrogenic cross sections, respectively [206]. Fitting windows and the calculated cross-sections are shown for each elemental edge in Figure 7.2.

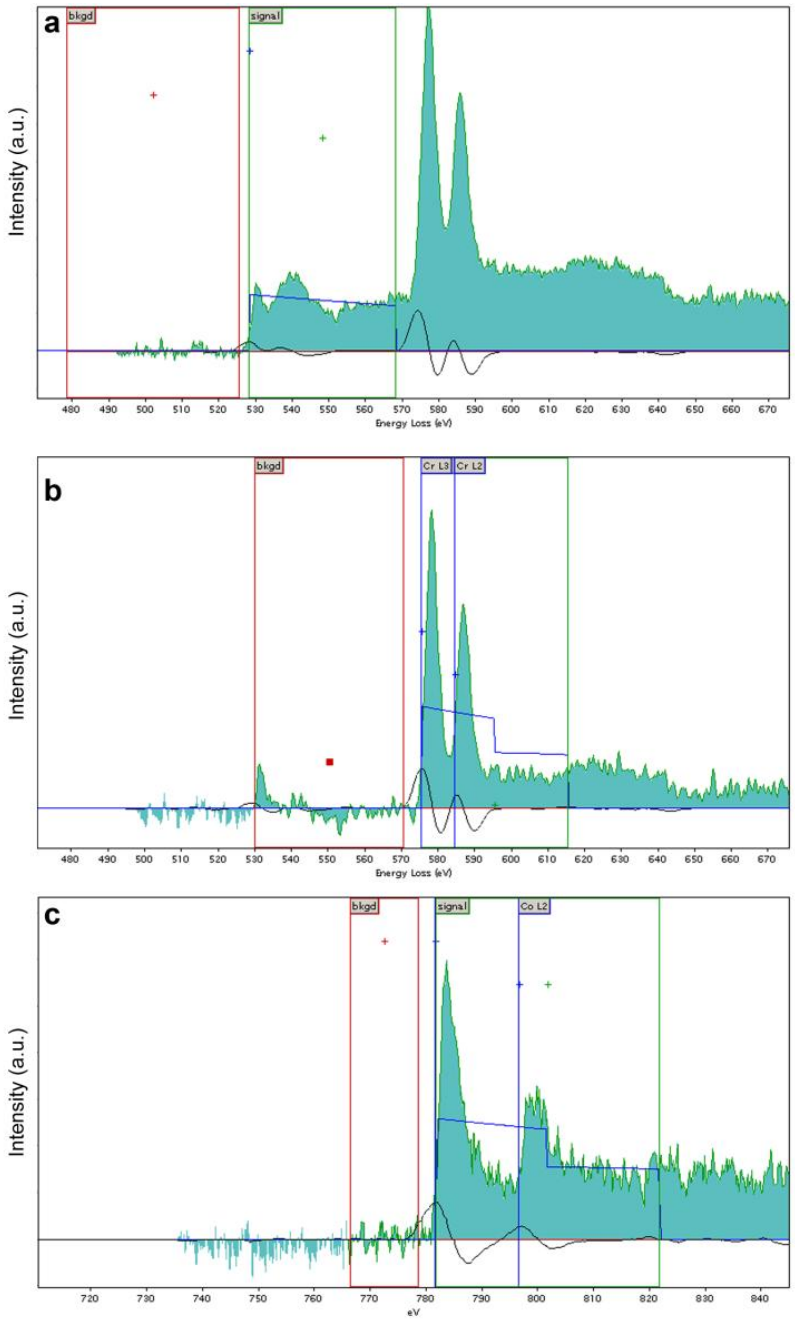


Figure 7.2 Examples of elemental quantification in Digital Micrograph. All spectra have been deconvolved with low loss spectra in order to remove the effects of plural scattering. The background-removed edges are shown in green, the first derivative in black, and the calculated edge in blue. (a) and (c) show the oxygen K and Co $L_{2,3}$ edges. (b) Quantification at the Cr $L_{2,3}$ edge was more difficult due to the proximity of the O K edge. Background of the form AE^{-r} was removed from the O K edge, after which the O K edge itself was fitted and subtracted from the experimental spectrum. The fitting at the onset of the O K edge is poor (seen as the peak at ~530 eV), however this procedure results in a relatively flat signal in the region 540-570 eV showing that the oxygen signal has been removed effectively in this region.

7.3.4. STEM-EDX methods

STEM-EDX experiments were carried out by Dr. Huikai Cheng and Prof. David McComb in a Tecnai Osiris (S)TEM microscope equipped with a Super-X EDX detector at FEI headquarters, Oregon, USA. This EDX detector system achieves state of the art sensitivity due to the large collection angle (0.9 srad) offered by its four silicon drift detectors. The microscope was operated at 200 kV, with a nominal probe size of 0.3 nm and a probe current of 0.3 nA. EDX maps were acquired with pixel sizes of 5 nm and dwell times of 50 µs per pixel.

7.4. Results

7.4.1. Locating wear debris

The light micrographs in Figure 7.3 illustrate how regions of interest within a hip capsule sample were located for spectroscopic studies. The histological sections show a cross-section of the synovial surface – the interface between soft tissue and the synovial fluid that surrounds the hip joint. A sub-surface band of macrophage cells is present in Figure 7.3(a), and higher magnification images revealed that these macrophages contained dark regions of up to 1 µm in diameter (Figure 7.3(b)). As light microscopy had insufficient spatial resolution to characterise these regions fully, e.g. whether dark regions were single particles or aggregates of smaller particles, tissue from this macrophage band was processed for further analysis in the TEM.

Figure 7.4 shows HAADF-STEM and bright field TEM images of osmicated sections. The hip capsule tissue was composed of a collagen fibre matrix, and contained many macrophage cells. Most macrophages contained large volumes of electron dense particles, which have high intensity in the HAADF-STEM images and low intensity in the bright field TEM images. Mitochondria appeared to be swollen, with abnormal cristae structure (Figure 7.4 (c,d)). A few macrophages were also found to have abnormal nuclear membrane structure, where the outer nuclear membrane is separated from the inner membrane (Figure 7.4 (a,b)). Despite the high loading of particles and abnormal cell ultrastructure, no necrotic cells were observed in the multiple sections surveyed.

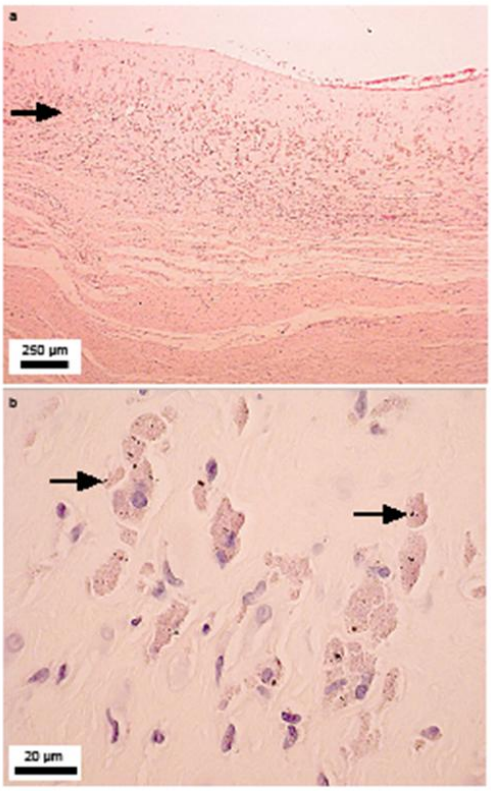


Figure 7.3 Light micrographs showing a section of hip capsule tissue across the synovial surface. (a) The presence of a subsurface band (arrow) of macrophage cells indicates an inflammatory response in the tissue sections. (b) Higher magnification image of the macrophages, revealing dark regions (arrows) in the cell cytoplasm.

Most of the electron dense material could be categorised into two distinct morphologies: denser rounded nanoparticles, and diffuse material. A few high aspect ratio 'needles' of up to 5 µm in length were also observed. Many particles were aggregated in regions of typically 1 µm in diameter. EDX spectra were acquired from electron dense particles, and representative spectra are shown in Figure 7.4 (e-h). Particles were found to be composed *mainly* of Cr. A minority of particles also contained Co in varying proportions, although Cr was mostly found in isolation. No significant Mo signals were observed in the TEM-EDX data, possibly due to sensitivity limitations of the EDX detector, and dilution effects from the relatively large volume sampled by a condensed TEM beam (see section 7.5). The presence of Cr and Co signals in EDX data confirms that the electron dense particles are debris originating from the hip prosthesis.

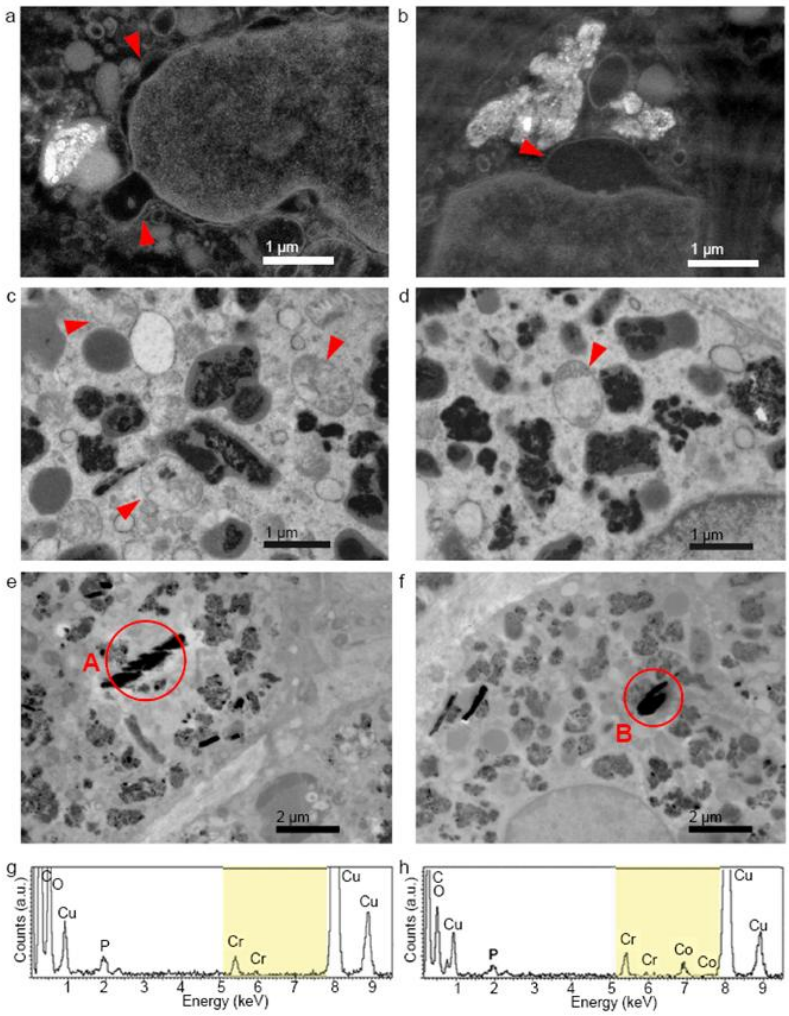


Figure 7.4 Electron micrographs of wear debris contained in macrophage cells. (a-b) HAADF-STEM imaging shows that macrophages are laden with wear debris (bright particles). The arrows indicate abnormal nuclear membrane structures, where the outer nuclear membrane is separating from the inner membrane. (c-f) Bright field TEM images in which the wear debris is imaged as dark particles. Debris is seen clustered in the cytoplasm. Mitochondria with damaged ultrastructure are marked with arrows. (g-h) EDX analysis of the circled particles in (e) and (f) shows that particle A contains Cr while particle B contains both Cr and Co. The high Cu signal originates from the TEM grid.

The limitation of characterising a three-dimensional (3D) particle using TEM imaging is that TEM images are projections in only two dimensions. In order to fully characterise the 3D morphology and intracellular distribution of the wear debris within the cell, S&V was performed in a dual beam focused ion beam (FIB) instrument.

The 3D reconstruction of the debris within a volume of macrophage cell cytoplasm is shown in Figure 7.5, where green regions are more electron dense, and blue regions are less dense. The reconstruction confirmed that particles were internalised inside membrane bound compartments within macrophage cells. Particles occupied a large proportion (12% ± 2%) of the cell volume. The size distribution of particles was large and ranged from a few nanometres in size to a few

micrometres. Analysis of the 2D SEM slices showed that particles had a mean aspect ratio of 1.8 and a mean diameter of 30 nm. The thresholding procedure used to identify particles was not sensitive to particles smaller than 10 × 10 nm, and therefore the calculated mean diameter represents an upper limit to the true mean diameter of the particles. In most cases the particles were spherical in morphology. The large needle-like particle that is visible at the bottom of the SEM images turned out to be plate-like in 3-D.

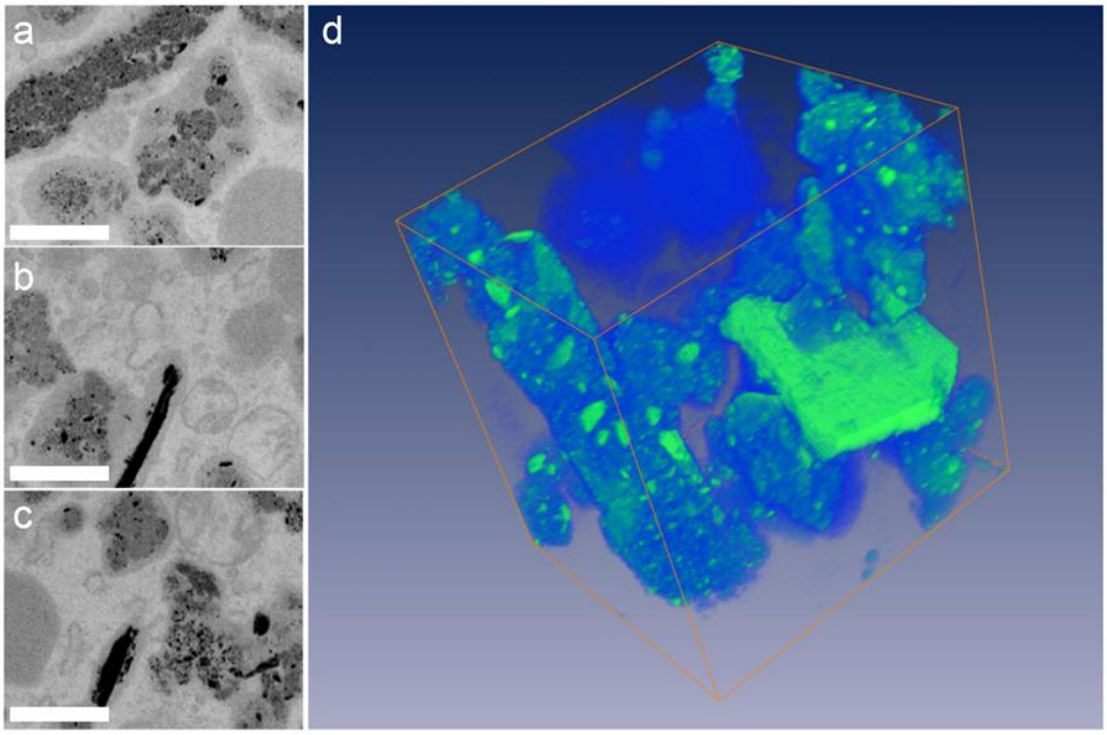


Figure 7.5 FIB-SEM analysis of a volume of macrophage cell containing wear debris, in two and three dimensions. (a-c) Three backscattered electron images, from a set of 200 slice-and-view images, are shown. (scale bars 750 nm) Wear debris (dark particles) and lipid bilayers are visible. (d) A snapshot of a 3D reconstruction of the volume, showing the distribution of wear particles (green).

7.4.2. STXM-XAS results

XAS data were acquired for five cells from different ultramicrotome sections. No difference in XANES at the Cr or Co $L_{2,3}$ edges was found between sections which had previously been mapped in the TEM, and those which had not been exposed to the electron beam. This showed that the low-dose TEM mapping had not changed the chemical state of the debris. XAS analysis of one representative cell (Figure 7.6) will be presented here. XAS stacks of this cell were acquired over the chromium and cobalt $L_{2,3}$ edges. SVD and PCA analysis were used to map the spatial distribution of characteristic chemical components throughout the cell.

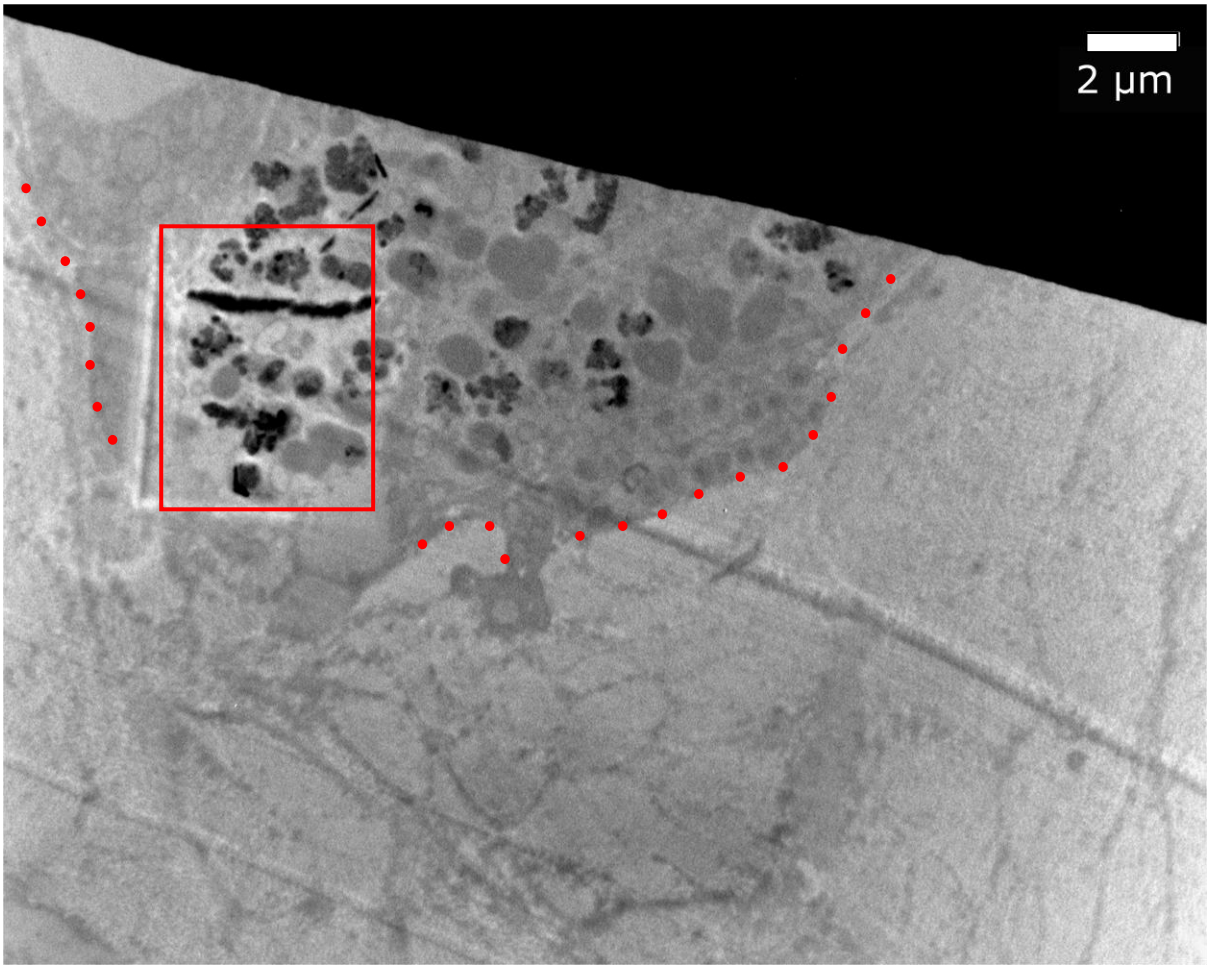


Figure 7.6 Bright field TEM micrograph of a representative macrophage cell laden with wear debris, where the cell membrane is marked (red dots). Although STXM-XAS and STEM-EELS data were acquired from multiple cells, for ease of comparison, all subsequent data presented in this chapter were acquired within the boxed region of this macrophage cell.

Three distinct components for SVD analysis were identified at the Cr $L_{2,3}$ edge (Figure 7.7). While PCA analysis identified a relatively large number of clusters, these could be grouped into three unique chemical signatures, as seen in the SVD analysis. The three components present in the sample describe the cellular background (blue) and two particle phases (red and green).

The cell background was found to contain no chromium. To determine the oxidation state of the chromium species in the particle phases, component spectra were compared to a number of reference compounds (Figure 7.9(a)). Comparing the positions of edge onsets and the height and energy splitting of the multiplet peaks, the chromium species in the green phase corresponds most closely to Cr(III) reference compounds. As the Cr $L_{2,3}$ spectra of chromium phosphate and hydroxide references are very similar, it is only possible to identify the valence of the chromium in the green phase, but not the exact complexing ligand.

The Cr $L_{2,3}$ edge of the red phase was very similar to that of the green, suggesting that this phase also contained significant amounts of Cr(III). However, as the red phase exhibits a slightly higher peak at 576 eV, this phase is best recreated by a combination of Cr(III) and *metallic* chromium as show in Figure 7.10. Linear regression fitting was used to determine the exact composition of the red phase as 70% Cr(III) and 30% Cr metal.

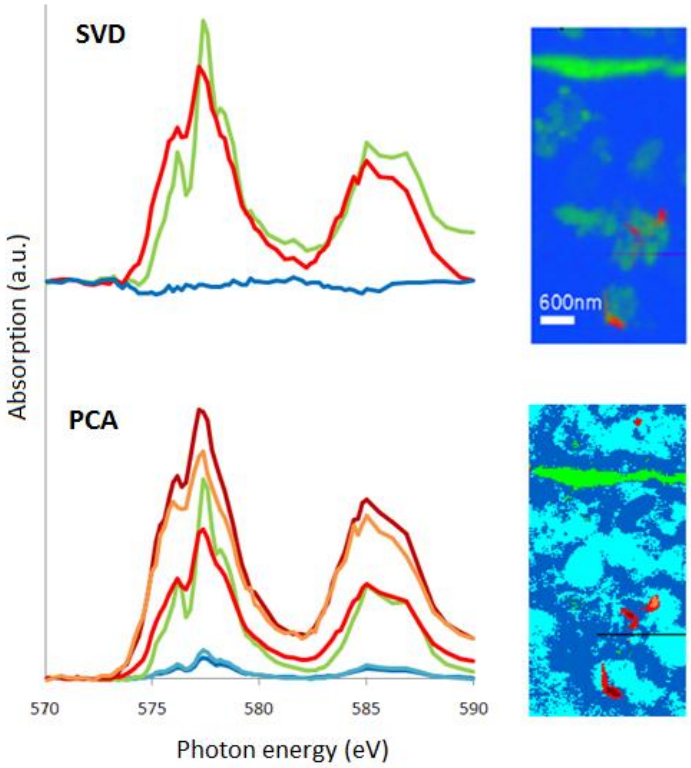


Figure 7.7 SVD and PCA analysis of a STXM stack at the Cr $L_{2,3}$ edge. (a) The three component spectra (red, green and blue) used for SVD fitting are shown, along with an RGB image displaying the spatial distribution of these components. (b) Seven PCA clusters were identified, and cluster spectra and locations are shown.

SVD and PCA analysis of the Co stack also revealed three unique chemical species: cellular background which contained no Co, and two chemical phases localised to the particles (Figure 7.8). Most particles are described by the green phase, whose spectrum contains very faint Co L_2 and L_3 white lines. The Co L_3 edge of this phase was blue-shifted by 6 eV. Such a large shift in edge onset was not observed in any of the recorded reference spectra, nor in the XAS literature (Figure 7.9(c)). Therefore we can only conclude that this phase contains trace amounts of Co in a high (but unknown) oxidation state. A small number of particles were described by the red phase. The asymmetry of the L_2 and L_3 peaks in this phase closely matches the spectrum of the metallic Co reference.

In summary, green-phase debris was composed of Cr(III) and trace amounts of oxidised Co, while red-phase particles contained Cr(III) and also metallic Cr and Co.

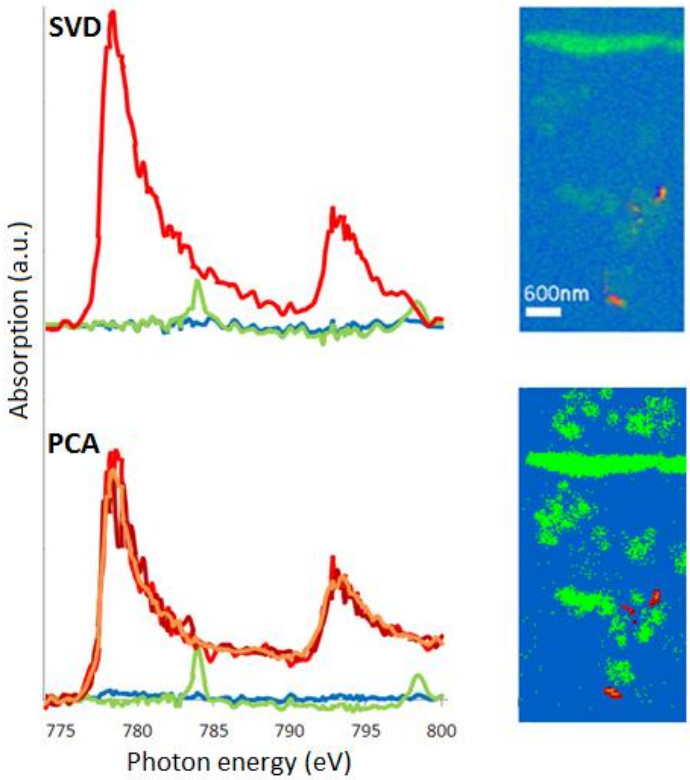


Figure 7.8 SVD and PCA results of a STXM stack at the Co $L_{2,3}$ edge. (a) The three component spectra used for SVD fitting are shown, along with an RGB image displaying the spatial distribution of these components. (b) Spectra of the PCA clusters and a map of the cluster locations.

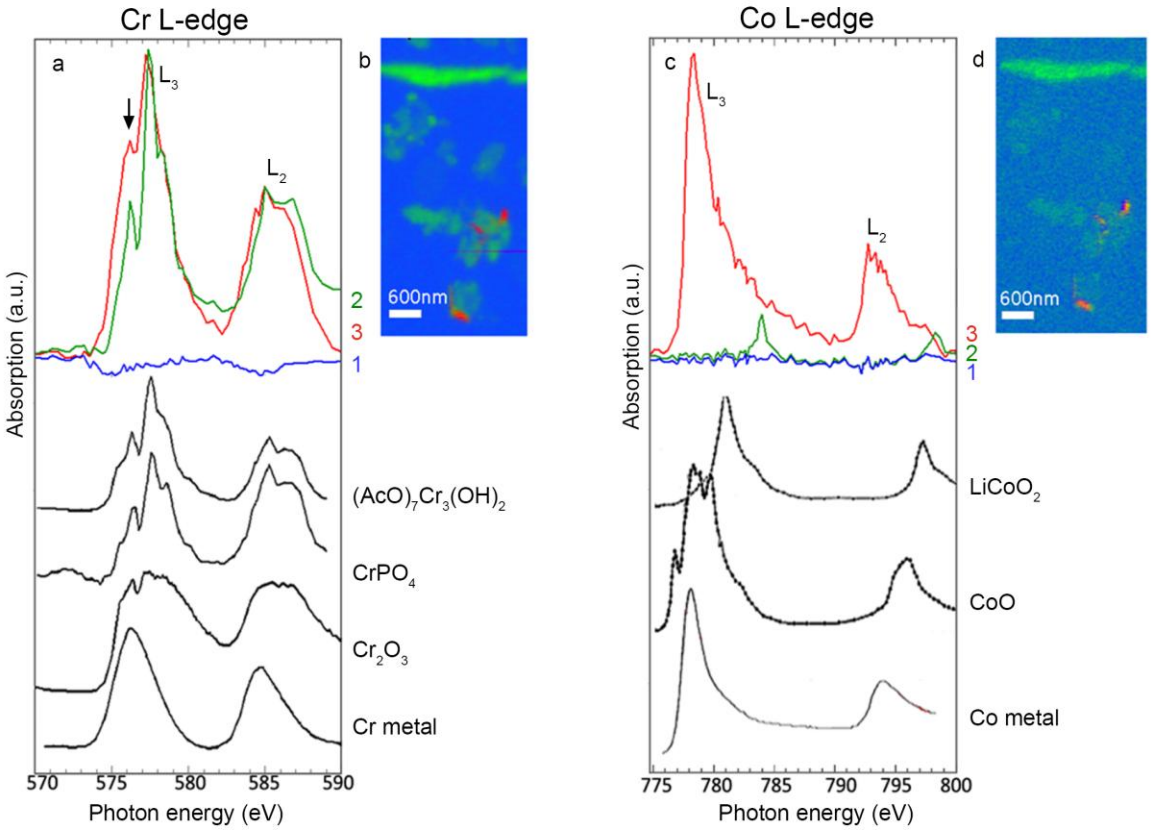


Figure 7.9 Comparison of experimental XAS spectra with reference compounds. (a) At the Cr $L_{2,3}$ edge, the blue phase contains no Cr and corresponds to the cell cytoplasm. The green phase is most similar to the Cr(III) reference compounds. The red phase is similar to the green spectrum, but exhibits a more intense peak at 576 eV (arrow). (b) At the Co $L_{2,3}$ edge, the red phase matches the spectrum of Co metal, while the green phase contains only trace amounts of Co and does not correspond to any reference samples studied. The $LiCoO_2$ and CoO reference spectra are taken from Morales et al. [207].

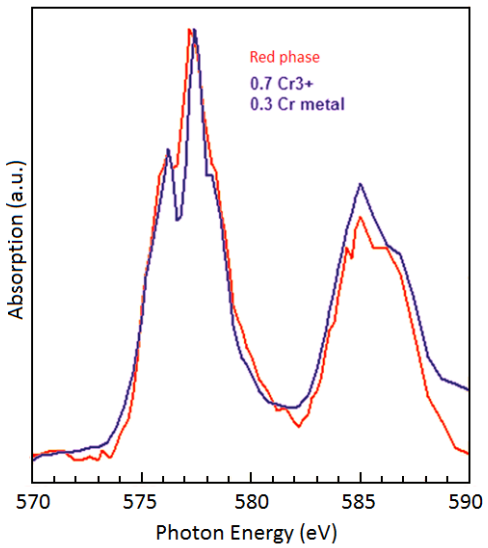


Figure 7.10 Comparison of the Cr $L_{2,3}$ edge of the red phase with a linear combination of 70% Cr(III) and 30% Cr metal. Ratios of each component were calculated using linear regression fitting.

7.4.3. STEM-EELS results

Figure 7.11 displays TEM and STEM images acquired of the *exact same region* of the sample that was analysed in section 7.3.2. These electron micrographs provide much more information on the morphology of the particles than the corresponding x-ray absorption image. Cellular structures such as lipid membranes are also better resolved in the electron microscope. Micrographs acquired using different modes and with different collection angles also provide different information about the sample. Bright field TEM images contain contrast variations from different densities as well as diffraction from crystalline regions, while HAADF-STEM images do not contain any diffraction contrast. The intensity in a HAADF-STEM image is proportional to Z^n where n~2, and so this micrograph can be considered to contain some chemical contrast, as elements with higher Z will appear brighter.

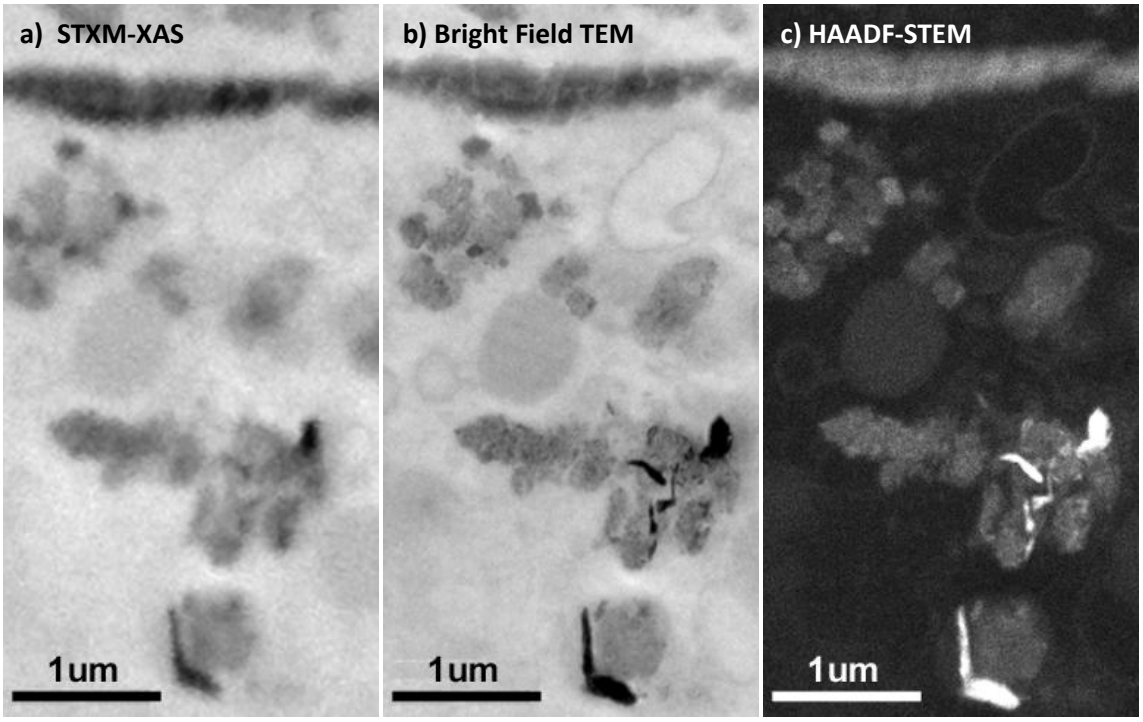


Figure 7.11 Comparison of images of the same cellular region, taken with STXM and (S)TEM. (a) X-ray absorption image taken with 540 eV photons. (b) Bright field TEM image and (c) HAADF-STEM image taken with an inner collection semi-angle of 129 mrad, showing the morphology of debris and cellular ultrastructure on a higher length scale.

Direct comparison of STXM chemical maps with HAADF-STEM images (Figure 7.12) revealed that the particles composed of the oxidised green phase were found to have diffuse morphology in the STEM. The more metallic red phase particles were also more electron dense, and had high aspect ratios.

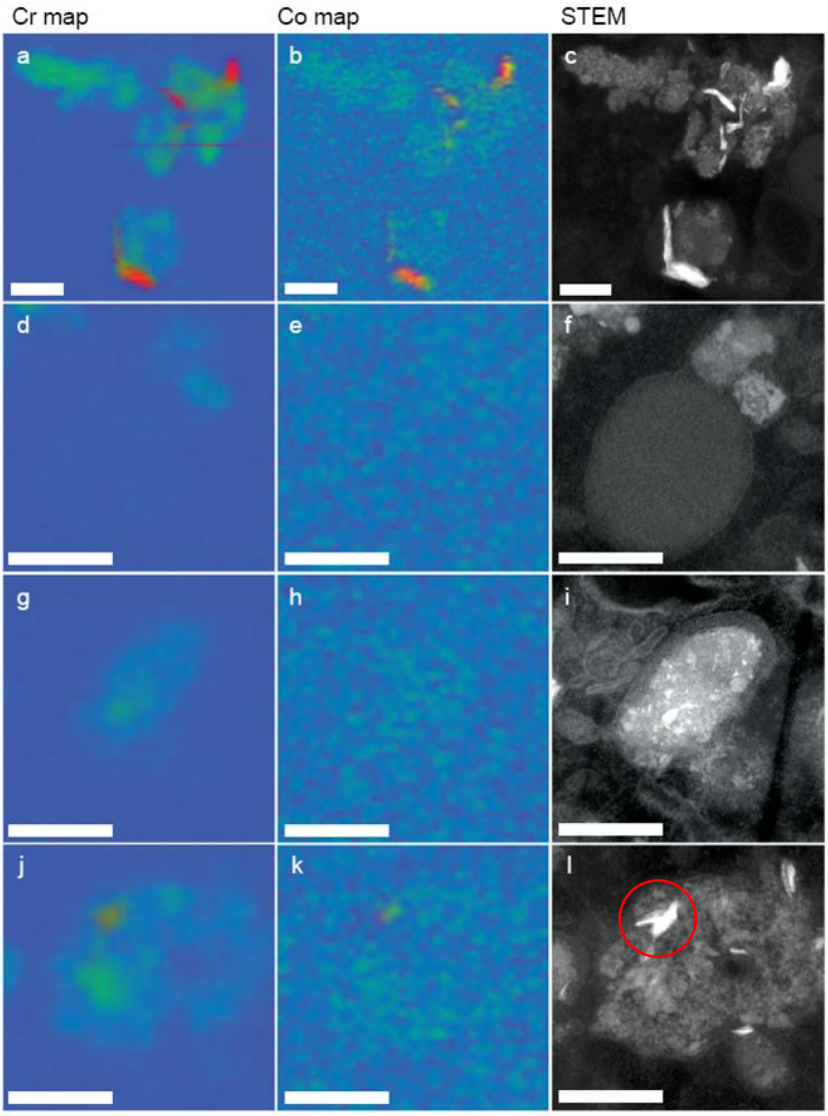


Figure 7.12 Different clusters of wear debris analysed by STXM and dark field STEM) (scale bars 400 nm). Cr (a,d,g,j) and Co (b,e,h,k) chemical thickness maps and dark field STEM images (c,f,i,l) of wear debris clusters are correlated. Circled particles in (l) were selected for further EELS analysis (see Figure 7.15).

Monochromated EELS spectra were recorded from the two different debris phases as identified by XAS. These EEL spectra are shown in Figure 7.13, overlaid with the corresponding XAS data. When removing the background from XAS data, the linear background was chosen so as to match the L_3:L_2 peak ratio determined by EELS. At the Cr $L_{2,3}$ edge, EEL spectra of both phases have the same overall shape as x-ray spectra. However, some of the multiplet peaks which are well resolved in XAS (e.g. Cr L_3 peaks at 576.3, 577.4 and 578.3 eV) are only present as shoulders in EEL spectra, or not resolved at all. EEL spectra of both Co phases show good agreement with XAS data.

Figure 7.14 shows that the differences between EELS and XAS at the Cr $L_{2,3}$ edges can be explained by a degradation in energy resolution. XA spectra were convolved with Gaussian functions of various widths. Comparing the shape of the shoulder at 576.3 eV, the best agreement is achieved when a Gaussian with FWHM = 0.6 eV was used.

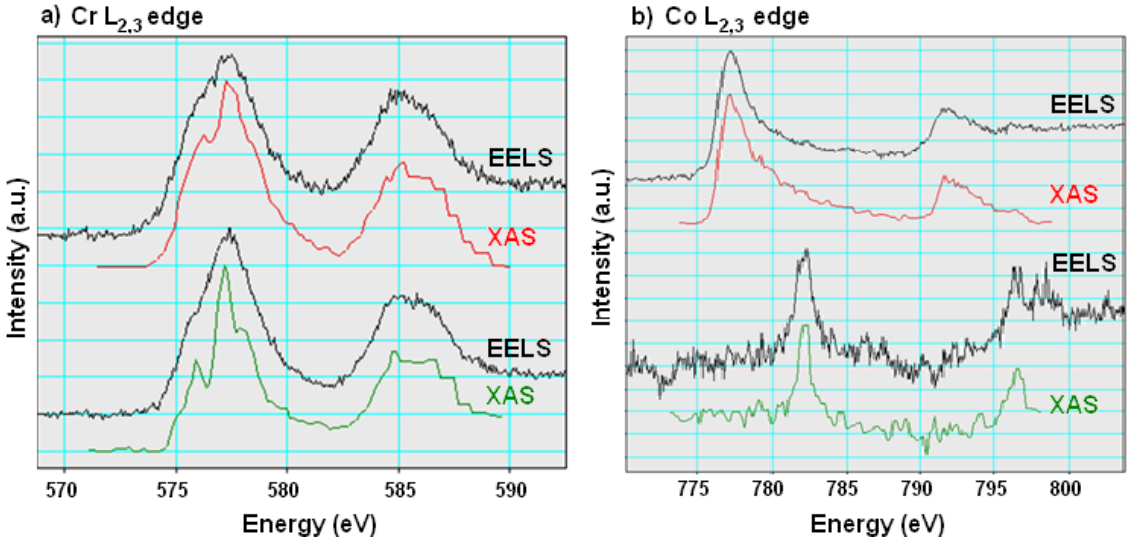


Figure 7.13 Comparison of XAS and EEL spectra of the different chemical phases of the wear debris at the Cr $L_{2,3}$ edge (a) and the Co $L_{2,3}$ edge (b).

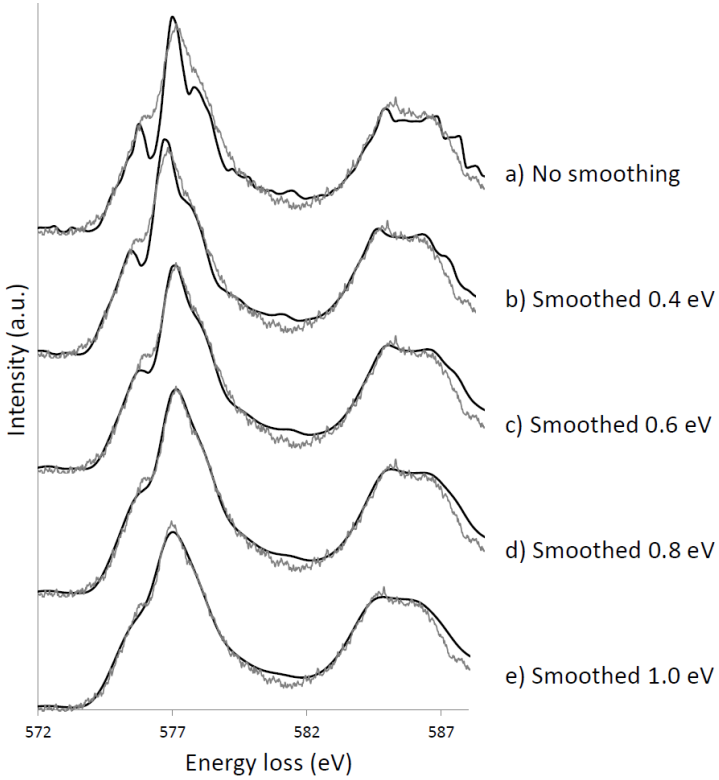


Figure 7.14 XAS spectra of the green phase at the Cr $L_{2,3}$ edge, after different degrees of smoothing. Spectra have been overlaid with corresponding EELS for comparison.

7.4.4. EELS Quantification

Quantitative EELS analysis was carried out the two particles circled in Figure 7.12(l). The XAS chemical maps show no spatial variation over this region, suggesting that the particles are composed of a homogeneous mixture of Cr(III) and metallic Cr and Co. However, the additional spatial resolution of EELS revealed that these particles are in fact more complex. Variations in the chemical composition were quantified and mapped across one 50 nm particle. The profiles in Figure 7.15 show the absolute number of O, Co and Cr atoms present in each nm^2 of sample. They demonstrate that while oxygen and chromium signals are present throughout the 50 nm diameter of the particle, Co is present only in the centre ~20 nm. In this central region the Co:Cr ratio is ~0.66 compared to a ratio of 2 in the bulk alloy. Additionally, the profile of the oxygen signal decreases in the centre of the particle. This could be explained by the presence of an oxygen-rich (and cobalt-deficient) shell surrounding the particle.

STEM-EDX data acquired by Dr. Huikai Cheng largely confirmed the elemental distributions of O, Cr and Co from previous STXM and STEM-EELS analysis (Figure 7.16). In addition, this technique was capable of mapping elemental Mo, revealing that Mo was largely absent from wear debris. The few particles which were found to contain Mo also contained Co and Cr.

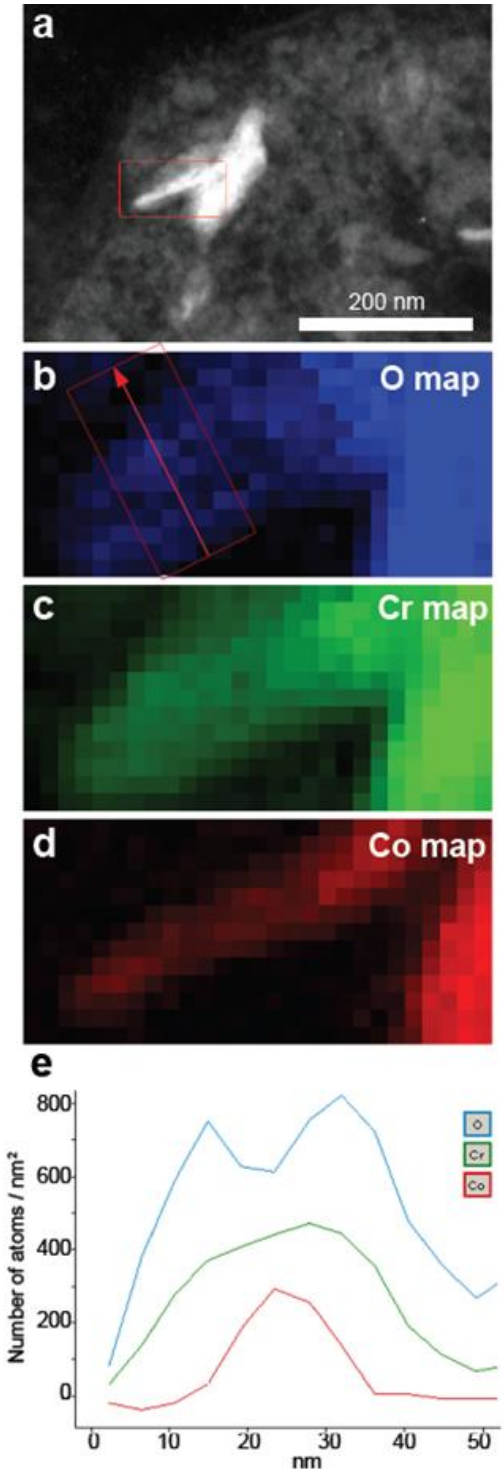


Figure 7.15 Quantitative EELS analysis of a 50 nm wear particle. (a) Higher magnification HAADF-STEM image of the wear particles shown in Figure 7.12(j-l). EEL spectra were acquired at each pixel in the boxed area. (b-d) Chemical maps showing the distribution of oxygen, chromium and cobalt were calculated. (e) Absolute numbers of atoms per unit area are plotted as a function of distance across the nanoparticle (red arrow in (b)). The chemical composition changes through the particle, showing an oxygen-rich and cobalt-deficient shell.

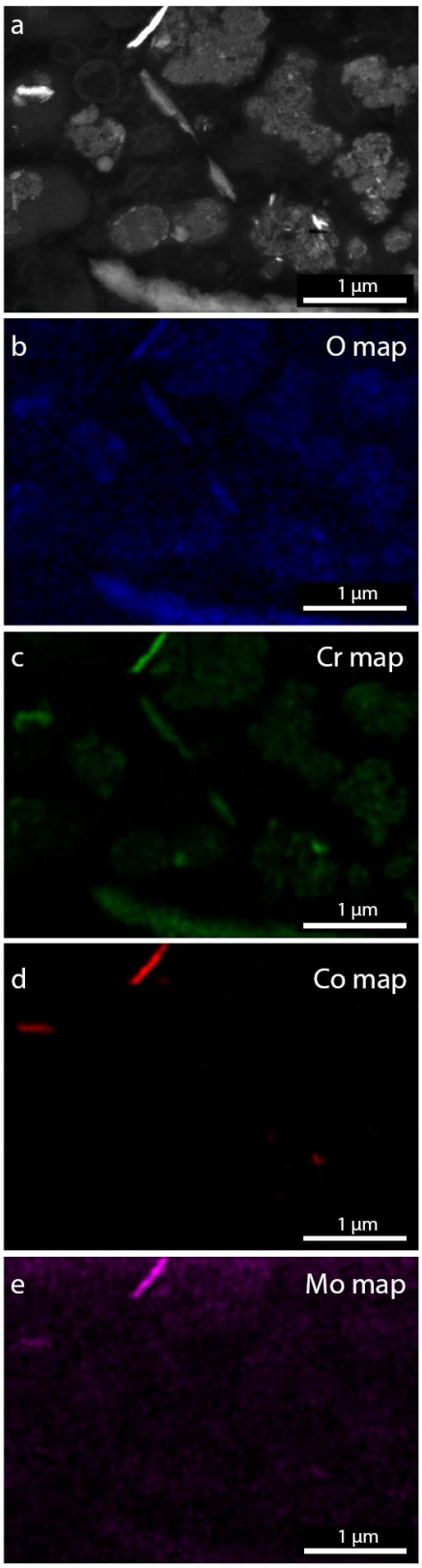


Figure 7.16 STEM-EDX analysis of wear debris in an adjacent area of cell. (a) HAADF-STEM image and corresponding EDX maps of elemental O, Cr, Co and additionally, Mo (b-e).

7.5. Discussion

Analysis of hip capsule tissue sections by light microscopy revealed disruption to the synovial surface and the presence of a sub-surface band of macrophages (Figure 7.3). These results are consistent with previous histological findings [186, 208]. Dark regions within macrophage cells have also been previously reported [186, 208], and have been assumed in these reports to be prosthesis wear debris. Here, TEM-EDX analysis of serial tissue sections provided chemical confirmation that the dark regions seen in light micrographs contain nanoparticles composed of Co and Cr. As Co and Cr occur naturally in the human body only in trace amounts [209], the particles can be unambiguously identified as originating from the MOM hip prosthesis. Additionally, EDX results showed variable Co:Cr ratios between wear particles. The majority of particles contained mainly Cr, with no detectable Co. This is in agreement with previous studies [194, 197], and indicates that significant Co dissolution is occurring. No significant Mo signal was detected using TEM-EDX, however Mo peaks were visible in later STEM-EDX spectra (Figure 7.16). The lack of detectable Mo is a reflection of the poorer detection limit of TEM-EDX (and the higher sensitivity of the Super-X EDX detector), rather than complete Mo dissolution.

A combination of FIB-SEM and TEM analysis was used to assess the anatomical distribution of debris within macrophages, and any changes to the structure of cell organelles. High loadings of wear debris were found inside macrophage cells. No debris was observed within mitochondria, nor the cell nucleus. Papegeorgiou *et al.* reported the inclusion of CoCr nanoparticles in the nucleus of fibroblast cells in tissue culture experiments [210]. The lack of evidence here for intranuclear debris may suggest that wear debris cannot gain access to the nucleus of macrophage cells *in vivo*. Alternatively such events may occur, rarely, but have not been observed here as the volumes sampled are small compared to the total tissue volume. This is an inherent limitation of TEM.

Quantification of one cell using FIB-SEM found that 12% of the cell volume was made up of wear debris. As a rough guide, this is equivalent to 600 μm^3 of wear debris in a 5000 μm^3 macrophage cell [211]. Despite such high particle loadings, none of the characteristics of macrophage necrosis or apoptosis described by Hardwick *et al.* were observed in TEM micrographs [212]. Plasma membrane integrity was preserved, though cells displayed abnormal ultrastructure in their mitochondria, and occasionally at the nuclear membrane. These findings are consistent with the effects of oxidant stress [213], and the generation of high concentrations of reactive oxygen species (ROS) such as hydroxyl radicals [210]. The observation that CoCr particles cause mitochondrial toxicity in the absence of cytotoxicity has been reported in fibroblast cells in cell culture experiments [199, 210].

STXM-XAS was used to probe the speciation of wear debris within tissue samples. As x-ray irradiation is known to cause photoreduction in some metals, the possibility of such x-ray damage in these samples should be considered. Reference standards were studied using the same photon doses as the tissue experiments, and their XAS spectra were found to be in good agreement with published spectra in terms of edge onsets and fine structure [207, 214, 215]. Therefore we can conclude that changes in oxidation state are not induced at the photon doses used in these studies, and that XAS results reflect the true chemical state of the debris.

Wear debris was present in cells in two distinct chemical states. The chemical state mapped in red in Figure 7.9 and Figure 7.12 contained Cr(III) as well as metallic Cr and metallic Co. The state mapped in green in Figure 7.9 and Figure 7.12 contained Cr(III) and trace levels of Co. The 6 eV shift in edge onset of this Co species was not seen in any Co standard studied, nor in the XAS literature. The large edge shift is indicative of Co in a high oxidation state, although the exact species could not be identified unambiguously. Similar large shifts in binding energy have been observed in Co(II) compounds studied by XPS. However comparison of XPS binding energies with XAS chemical shifts is not straightforward: the former reflects energy shifts in core level only, whilst the latter is the net energy shifts of both core and final states [37]. Further XAS experiments of additional standards are needed to confirm the Co oxidation state of this phase. The chemical states identified here are in good agreement with the hard x-ray XANES findings of Hart *et al.*, who used a microfocussed probe to study wax-embedded tissue sections [200]. Hart *et al.* also found some metallic Cr, and a predominance of Cr(III), which they identified as Cr orthophosphate using Cr K edge XANES and EXAFS. Co was detected as well, though its oxidation state was again difficult to determine, this time due to beam damage from the higher energy photons. Additionally, because of the low spatial resolution of the hard x-ray microprobe, it was not possible to determine whether the different chemical species were present in the same particle, nor whether these particles were located within the macrophage cells.

To provide higher spatial resolution structural information, STEM imaging after STXM analysis allowed the co-registration of chemical (STXM) and spatial (STEM) information. This revealed that the oxidised phase is diffuse in nature and that the particles containing metallic Co and Cr are dense, rounded nanoparticles with high aspect-ratios.

STEM-EELS analysis allowed independent confirmation of the chemical state of the particles as determined by STXM-XAS. The chemical states determined using EELS agree well with XAS results, demonstrating that electron irradiation also does not alter the state of Cr or Co in the wear debris. However, differences between EELS and XAS were observed, in the fine structure of the white lines.

Figure 7.13 shows that the multiplet peaks are less well resolved in EEL spectra. This is particularly evident at the Cr $L_{2,3}$ edge, making the variation in the Cr(III):Cr metal ratio more challenging to identify. The main cause of poorly resolved multiplet peaks is most likely the lower energy resolution of EELS. Although the energy resolution of EELS, measured from the FWHM of the zero-loss peak (ZLP), was 0.2 eV, XAS data needed to be smoothed by a further 0.6 eV to obtain good agreement with EEL spectra. The lower effective resolution of EELS measurements at the Cr $L_{2,3}$ edge data may have been caused by misalignments of the spectrometer introduced when the EEL spectrum was shifted by >500 eV to the Cr $L_{2,3}$ edge. Re-alignment of the spectrometer at the relevant energy shift may result in improved resolution of EELS fine structure.

The advantage of using EELS is its higher spatial resolution. Results of elemental mapping with 25 nm resolution suggests a core-shell structure of some debris particles, where the centre of the particle contains high concentrations of Co as well as Cr, and the outer shell is composed mainly of Cr and O. Quantitative analysis also provided the absolute number of Co, Cr and O atoms within the sample. For inhomogeneous and irregular particles, projected EELS data still do not provide enough information to deduce, for example, whether the core of this particle has the same composition as the original alloy. For this, we would need chemical information in three dimensions. As EELS signals satisfy the linear projection requirement, it is possible to combine SI imaging with tomography. This involves collecting a spectrum image at a range of sample tilt angles, from which the 3D distribution can be calculated. This has been done in the x-ray microscope [216], and 4D STEM-EELS has been demonstrated using core loss EELS [217]. Before carrying out 4D experiments on the current samples, it would be important to determine whether the very high electron doses required for 4D experiments will alter the chemical state of the Co/Cr debris. Difficulties may also arise from the beam-sensitive tissue sections in which the debris is located. Hole formation and section ripping can occur at high electron doses. Additionally, the sections will experience shrinkage due to the cross-linking of resin, although this will stop after the first few minutes of electron irradiation.

So far, the STXM-XAS and STEM-EELS experiments focussed on the two major alloy components, Co and Cr, while Mo had been neglected. In the former case, this is because the position of the Mo $L_{2,3}$ edge (located at ~2500 eV) would have required significant realignments of the STXM. This was impractical due to time constraints. It is also difficult to study the Mo $L_{2,3}$ edge using EELS, as the signal to background ratio is very low at such high energy losses. The results obtained by STEM-EDX (Figure 7.16), with its extremely high spectral dispersion, show that this is technique is well suited to studying the distribution of Mo in the tissue. The ability of STEM-EDX to detect Mo while TEM-EDX

failed is partly due to the higher brightness of the STEM probe and higher sensitivity of the four-detector system. Additionally, the relatively large areas sampled by TEM-EDX would effectively dilute the concentration of Mo, and it is possible that this effect also contributed to the lack of significant Mo signal in the TEM-EDX results.

Combined chemical analysis (STXM-XAS, STEM-EELS and STEM-EDX) shows that nanoparticulate wear debris is present within macrophage cells in hip capsule tissue. The lowered Co:Cr ratio throughout the debris particles provides evidence that significant dissolution of Co has occurred. This contrasts with the corrosion behaviour of the bulk alloy, in which Co is protected from corrosion by the passivating effect of Cr. Additionally, the altered valence state of both Co and Cr shows that oxidation has occurred at the surface of particles. As tissue samples are only collected at revision surgery, this is the only time point at which the chemical state of periprosthetic debris can be determined. It is important to correlate these results with other methods such as mass spectrometry analysis of blood and joint fluid samples, which may be collected at various stages throughout the lifetime of the prosthesis. Many of these studies have reported the presence of Cr and Co ions in the blood and synovial fluid [218]. It is possible that the cells studied in this report would also have been exposed to soluble metal ions. It is then unclear which species - soluble ions or residual debris - is responsible for the oxidative stress, and ultimately the failure of the hip prosthesis.

Soluble ions are not preserved by the sample preparation techniques used here; buffer and solvent washes will remove soluble ions from the intracellular space [219]. Alternative sample preparation routes, such as high pressure freezing followed by freeze substitution [220], would be necessary to study any soluble ions present within the cells.

These data provide vital insights into both the mechanism of dissolution of wear debris, and also the nature of the biointerface presented to the cell. These results could aid the design of future cell culture experiments in terms of determining clinically relevant sizes, speciation and doses of particles.

7.6. Conclusions

In conclusion, using a combination of light microscopy, TEM and FIB-SEM we have confirmed that wear debris is present within macrophage cells in hip capsule tissue, and that these cells display damage to mitochondrial and nuclear membrane structure. Correlation of STEM-EELS and STXM data has been performed for the first time in this field. This approach allowed the co-registration of chemical (STXM) and spatial (STEM) information, and revealed two types of wear debris. Diffuse

debris was found to contain mainly oxidised Cr(III) with trace amounts of oxidised Co. Dense particles were found to contain *metallic* Co and Cr as well as Cr(III). The majority of particles were near-devoid of Co, suggesting that significant dissolution of Co was occurring in the cellular environment. These results demonstrate the power of such a correlative multi-scale approach across both length and energy resolutions.

8. Conclusions and further work

The present work has explored a correlative approach to chemical characterisation on the nanoscale, using STEM-EELS and STXM-XAS. Acquisition of both an STXM stack and an EELS SI over the same nanostructures has made it possible to take advantage of the higher spatial resolution of STEM-EELS and the (often) superior chemical sensitivity, and different damage properties, of STXM-XAS. In this way a more complete understanding has been gained of a number of nanoscale systems. The extent of the benefits to be gained from this correlative approach greatly depends on the system, i.e. the length scale at which chemical information is required, or the electron and x-ray damage properties of the different sample materials. In this chapter, implications of this work for each system – CNT toxicity, CNT functionalisation and MOM implants – will be discussed individually. Conclusions relating to the correlative spectroscopic approach as a whole will then be drawn.

8.1. Fate of MWNTs in cells

In chapter 5, a correlative EELS/XAS approach was applied to amino functionalised MWNTs (a-MWNTs) within macrophage cells. The electronic structure of intracellular a-MWNTs was studied as a function of both exposure time and a-MWNT aggregation state. This is the first core loss spectroscopy study of intracellular MWNTs using either EELS or XAS, though low loss EELS has been reported on SWNT-cell systems [124]. Both STEM-EELS and STXM-XAS were capable of distinguishing between graphitic carbon nanotubes and the carbon-rich background of cell/resin at the carbon K edge, allowing a-MWNT aggregates to be mapped within the cell. The two techniques provided independent confirmation that a-MWNTs aggregates were present within macrophage cells, and that they did not become amorphous even after 14 days (section 5.4.2). The relative biopersistence of the a-MWNT aggregates observed in this work does not seem to fit well with the high rates of MWNT degradation reported in previous studies [121, 221]. This discrepancy could be due to differences in the functional groups present on the nanotube samples, or the different techniques used to characterise nanotube degradation. Additionally, it is likely that the aggregation state of MWNTs will also have a large effect on MWNT biopersistence [222], as this will determine what fraction of MWNTs are exposed to the cellular environment. The aggregation state of intracellular CNTs is rarely considered in the toxicity literature. However, as this study

demonstrates, it is not sufficient to characterise the aggregation state of a CNT sample prior to cell exposure only; the supposedly well dispersed [98] a-MWNTs studied here did not remain monodispersed within the cellular environment (figures 5.11 and 5.12). Therefore, there is a clear need for techniques such as STEM-EELS and STXM-XAS which are able to characterise both the electronic structure and the aggregation state of CNTs within cells.

No evidence was found of altered electronic structure at aggregate edges using either EELS or XAS, even though MWNTs here would have been exposed to the oxidising environment of the phagolysosome (section 5.4.3). Due to the significant rates of degradation reported in similar studies [121, 221], and the high defect density present in the a-MWNTs, it is unlikely that no degradation is occurring at the edges of aggregates. Therefore, the lack of detectable degradation is probably due to the (different) limitations of the EELS and XAS techniques. For STXM-XAS, degradation occurring on small length scales may be below the detection limit of the STXM, with its effective spatial resolution of 280 nm (figure 5.23). In the case of EELS, this technique may not have sufficient chemical sensitivity to distinguish between cellular carbon and degraded a-MWNT: from studies of MWNTs in simulated phagolysosomal fluids, nanotube degradation is expected to create defects in the graphitic lattice as well as the addition of oxygen-containing functional groups [221]. The chemical species in degraded a-MWNTs may thus be similar to those present in the cell, although the groups will differ in their local chemical environment, and so subtle differences in fine structure are expected. While XAS even had the chemical sensitivity to distinguish between the similar chemical signatures of cell and resin (figure 5.22b-d), EELS was less able to distinguish between these two components. This reduced chemical sensitivity of EELS could also limit its ability to assess the degradation of MWNTs in cells.

Further work is required to determine if EELS and XAS, under different sample conditions, could be suitable techniques for monitoring MWNT degradation. This could be done by applying both techniques to test systems in which more severe MWNT degradation is induced. In vitro enzymatic digestion studies could provide ideal samples to determine the spectroscopic signature of degraded MWNTs, whilst avoiding the complication of a carbon-rich cell background. MWNTs functionalised with different groups, engineered to provide greater chemical contrast, may also facilitate the tracking of degradation in both microscopes. Additionally, if enzymatic degradation can be induced on an appropriate timescale, a further avenue of research might be to study MWNT degradation in situ, within liquid cells in the TEM or STXM.

8.2. Functionalised CNTs

It is often assumed that EELS is too damaging to study fine structure at the carbon K edge [57, 58, 172]. In the field of CNTs, there have been many detailed XANES studies concerned with identifying the different functional groups present on CNTs [69, 132], however the scope of EELS studies has been largely limited to characterising the degree of graphitic structure of CNT samples only [128]. In chapter 6, low dose EELS methods were employed in order to determine whether covalently bonded functional groups on oxidised MWNTs could be detected at the carbon K edge. STEM-EEL spectra revealed peaks related to the graphitic structure of the MWNTs, as well as a new peak labelled B' at 287.7 eV (figure 6.6) which to our knowledge has not been studied previously. From the energy position of peak B', and its greater incidence in oxidised MWNT samples compared to pristine MWNTs (section 6.4.4), it is likely that this feature arises from oxygen-containing functional groups or defects introduced during the acid oxidation process. There was also a non-zero occurrence of peak B' in the pristine MWNT samples (figure 6.14), which may be explained by the presence of low concentrations of defects in the pristine MWNT samples. The occurrence of the peak at 287.7 eV was mapped across small clusters as well as individual MWNTs (figures 6.11 and 6.12), and was found to be inhomogeneously distributed along the entire length of the MWNTs. If the distribution of peak B' does correlate with the location of oxygen-containing functional groups, then our result appears to contrast with the common assumption[***] that the sidewalls of covalently-functionalised CNTs have a uniform distribution of functional groups [223]. Additionally, no evidence was found of higher concentrations of the peak B' at the ends of MWNTs, nor at MWNT kinks, contrary to another theory that these sites are the most heavily functionalised during oxidation [176, 177]. These results raise the possibility that the actual distribution of functional groups on an oxidised MWNT is more complicated than a simple "ends and kinks" model.

It is notable that the features observed in a number of separate XANES studies of similarly oxidised CNTs occurred at a different energy, around 288 eV (figure 6.7). The origin of this difference between EELS and XAS spectra remains to be determined: one explanation is that, due to different electron and x-ray damage mechanisms, different stages in the degradation of the original chemical species are observed in the different spectroscopes. Alternatively, variations in CNT synthesis and functionalisation, or in sample environment, could alter the identity of the chemical species present on the CNTs at the start of the experiments. Further work to elucidate the reason for this discrepancy could involve repeating the EELS measurements at even lower electron doses, which

[***] This assumption is implicit in many chemical schemes of CNT functionalisation, and has also been expressed explicitly [223].

could be achieved without loss of spatial resolution with the use of a more sensitive EELS detector. The use of a lower operating voltage, e.g. 60 kV, which is below the threshold for knock-on damage in graphitic carbon [60], would minimise this mode of irradiation damage. It has also been suggested that cooling samples to liquid helium temperatures, rather than liquid nitrogen temperatures, can further reduce beam damage [224].

8.3. MOM hip debris

In chapter 7, direct STXM-EELS correlation was used to successfully determine the chemical nature of the nanoparticle debris in tissue surrounding metal-on-metal hip prostheses. This is the first study to investigate the chemical speciation of the metal particles at the nanometre level. Both XANES and EELS provided sufficient spectral resolution to resolve multiplet peaks at the Cr and Co $L_{2,3}$ edges, and hence determine the oxidation state of the elements (figure 7.6). Additionally, EELS was capable of mapping changes in the concentration of different elements across individual nanometre-sized debris particles (section 7.4.4). STEM-EDX was used to map Mo, and thus the combination of STXM, EELS and EDX results provided a more complete characterisation of the CoCr nanoparticles. This work employed a multi-scale correlative approach including optical, x-ray and electron micro-spectroscopy techniques, which was essential for tracing the exact localisation of nanoparticles from the whole body level down to the nanoscale.

The detailed chemical speciation analysis presented here has only been carried out for debris in tissue explanted during prosthesis revision, after the device has failed. Therefore few conclusions about particle generation and chemical evolution before this time point can be drawn. It is important to be able to characterise debris at all stages, from generation to dissolution, as the biological response to these particles at each stage will be closely dependent on particle size and speciation. Future work could involve investigations of debris from the synovial fluid of patients, which would provide an earlier time point, and give insight into the amount of dissolution that occurs within this environment. The chemical state of particles that are subsequently presented to periprosthetic tissue could also be determined. Such results would be invaluable in targeting future cell culture experiments to the most biologically relevant species. The use of different sample preparation routes which enable soluble ions to be retained could also be important for understanding the speciation of any dissolved ions within the cell. Direct links between the generation of wear debris and unexplained pain leading to MOM failure also need to be drawn. The correlation between pain on the whole body level, implant misalignment on the joint level, and

physico-chemical state of wear debris on the nano-scale needs to be investigated in order to shed light on the primary causes of implant failure.

8.4. Correlative EELS/XAS

In summary, it has been possible to perform both STXM-XAS and STEM-EELS analysis on the same nanostructures. Practically, this has required careful mapping of specimens at low magnification prior to analysis, either in the TEM or in an optical microscope, in order to locate the same nanostructures in a reproducible manner. For future studies, such mapping could be greatly facilitated by the use of finder grids in which subsections of the grid are labelled. Additionally, access to STXM facilities which enable samples to be loaded in TEM sample rods would avoid the problems associated with removing taped TEM grids, e.g. ripping of microtomed cell sections.

The combination of these two independent, complementary techniques to probe electronic structure is invaluable. In systems which do not require the highest spatial or spectral resolutions, where electron and x-ray damage is negligible, the information obtained from EELS and XAS is equivalent and allows cross-validation of findings. For systems in which the required spatial and/or energy resolution cannot be met by STEM-EELS or STXM-XAS alone, such as investigations of interfaces (chapter 5) or of multiplet splittings in transition metals (chapter 7), correlation of the two techniques becomes essential for bridging the spatial and spectral gaps. Even for biological or polymer samples which are challenging to characterise using EELS due to electron beam damage, correlations between STXM-XAS chemical maps and TEM imaging can greatly assist understanding.

There are a number of extensions to these techniques which have not been explored in this thesis, and which may afford greater benefits to future correlative studies. Due to their higher interaction cross-sections, low loss EELS can greatly reduce the electron doses that a sample is exposed to. This could enable further insights to be gained into the more electron sensitive samples. Whilst low loss EEL spectra do not have a direct equivalent in soft x-ray spectroscopy, correlation of low loss EELS data with core loss XAS would provide high spatial resolution electronic structure information over a much wider energy range. The use of gas and liquid cells in both microscopes, as discussed in section 3.6, would also provide the opportunity to probe dynamic systems in situ, and together with the different detection modes available for surface-sensitive measurements (such as TEY) or trace element analysis (XFS), correlative STEM-EELS/STXM-XAS has the potential to become a very powerful and flexible tool for the materials scientist.

Appendix 1

This appendix deals with the properties of a Fresnel zone plate lens, and is based on *Soft x-rays and extreme ultraviolet radiation* by D. T. Attwood [81]. Here we will derive the focal length and spatial resolution of a zone plate of N zones, and an outermost zone width of Δr.

Consider figure A1 . By the Pythagorean theorem, we obtain the relation

$$f_m{}^2 + r_n{}^2 = \left(f_m + \frac{mn\lambda}{2}\right)^2 \qquad \textit{Equation A1}$$

which can be expanded as follows:

$$r_n{}^2 = mn\lambda f_m + \frac{m^2 n^2 \lambda^2}{4} \qquad \textit{Equation A2}$$

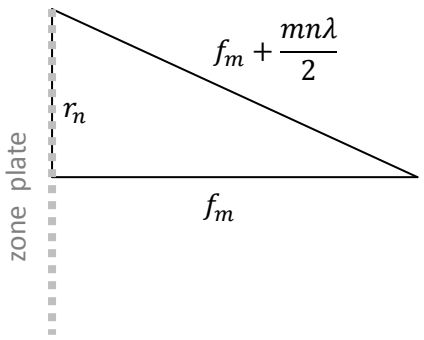


Figure A1 Diagram of a Fresnel zone plate showing the optic axis and the path from the n^{th} zone.

For large focal lengths, $f_m \gg m^2 n^2 \lambda^2 / 4$, and so the second term in Equation A2 can be ignored.

$$r_n{}^2 = mn\lambda f_m \qquad \textit{Equation A3}$$

Now, the outermost zone width, Δr, is defined as

$$\Delta r \equiv r_N - r_{N-1} \qquad \textit{Equation A4}$$

for $n \to N$. Substituting this definition into equation A3 for both r_N and r_{N-1}, we get

$$r_N{}^2 - r_{N-1}{}^2 = mN\lambda f_m - m(N-1)\lambda f_m = m\lambda f_m \qquad \textit{Equation A5}$$

The term r_{N-1} can be replaced using equation A4. As $\Delta r \ll r_N$ for large N, we get

$$r_N{}^2 - (r_N - \Delta r)^2 = 2r_N\Delta r - (\Delta r)^2 \approx 2r_N\Delta r \qquad \textit{Equation A6}$$

Combining equations A5 and A6, we obtain

$$2r_N\Delta r \approx m\lambda f_m \qquad \textit{Equation A7}$$

The focal length of the m^{th} order is then given by a combination of equations A3 and A7

$$f_m \approx \frac{4N(\Delta r)^2}{\lambda} \qquad \textit{Equation A8}$$

The numerical aperture of a lens is defined as

$$NA \equiv \sin\theta \qquad \textit{Equation A9}$$

Thus, from equation A3, the numerical aperture of a zone plate lens can be expressed as

$$NA \approx \frac{r_N}{f_m} \approx \frac{m\lambda}{2\Delta r} \qquad \textit{Equation A10}$$

The far field diffraction pattern from circular apertures is described by an Airy pattern, illustrated in figure A2. This pattern has a minimum at radius r_{null}, which, for a zone plate, occurs at

$$r_{null} = \frac{0.61\lambda}{NA} \qquad \textit{Equation A11}$$

One measure of the resolution of a lens is given by ability to distinguish between two mutually incoherent point sources. If each point source produces an Airy pattern, then the two are just resolved when peak of one lies on the null of the other. This is known as the Rayleigh criterion. Using equations A10 and A11, the Rayleigh resolution limit, δ, of a zone plate is given by

$$\delta \approx r_{null} = \frac{1.22\Delta r}{m} \qquad \textit{Equation A12}$$

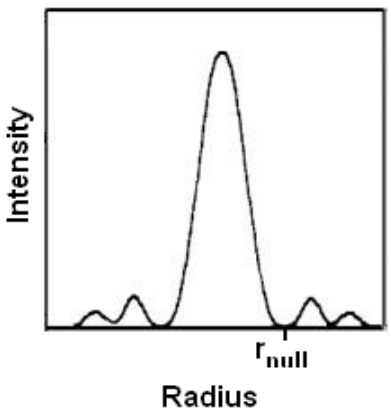


Figure A2 Diagram of an Airy pattern, describing the intensity at the focal plane created by a zone plate.

References

1. de Groot, F.M.F., et al., *In-situ Scanning Transmission X-Ray Microscopy of Catalytic Solids and Related Nanomaterials.* Chemphyschem, 2010. **11**(5): p. 951-962.
2. Williams, D.B. and C.B. Carter, *Transmission Electron Microscopy*. 2004: Plenum Press.
3. Nellist, P.D., et al., *Direct sub-angstrom imaging of a crystal lattice.* Science, 2004. **305**(5691): p. 1741-1741.
4. Bertsch, P.M. and D.B. Hunter, *Applications of synchrotron-based X-ray microprobes.* Chemical Reviews, 2001. **101**(6): p. 1809-1842.
5. Chao, W.L., et al., *Soft X-ray microscopy at a spatial resolution better than 15nm.* Nature, 2005. **435**(7046): p. 1210-1213.
6. Walther, T., et al., *Comparison of monochromated electron energy-loss with X-ray absorption near-edge spectra: ELNES vs. XANES*

EMC 2008 14th European Microscopy Congress 1–5 September 2008, Aachen, Germany. 2008, Springer Berlin Heidelberg. p. 65-66.

7. Brydson, R., *Electron Energy Loss Spectroscopy*. Microscopy Handbook. 2001, New York: Taylor & Francis.
8. Egerton, R.F., *Electron energy-loss spectroscopy in the electron microscope*. 1986, New York: Plenum Press. xii, 410 p.
9. Keast, V.J., et al., *Electron energy-loss near-edge structure - a tool for the investigation of electronic structure on the nanometre scale.* Journal of Microscopy, 2001. **203**: p. 135-175.
10. Lerotic, M., et al., *Cluster analysis of soft X-ray spectromicroscopy data.* Ultramicroscopy, 2004. **100**(1-2): p. 35-57.
11. Tanaka, I. and T. Mizoguchi, *First-principles calculations of x-ray absorption near edge structure and energy loss near edge structure: present and future.* Journal of Physics-Condensed Matter, 2009. **21**(10).
12. Egerton, R.F., *Electron energy-loss spectroscopy in the TEM.* Reports on Progress in Physics, 2009. **72**(1).
13. Maigne, A. and R.D. Twesten, *Review of recent advances in spectrum imaging and its extension to reciprocal space.* Journal of Electron Microscopy, 2009. **58**(3): p. 99-109.
14. Hitchcock, A.P., et al., *Comparison of NEXAFS microscopy and TEM-EELS for studies of soft matter (vol 39, pg 311, 2008).* Micron, 2008. **39**(6): p. 741-748.
15. Haines, B.M., et al., *Development of Surface Sensitive Scanning X-ray Microscopy at the CLS*, in *Canadian Light Source 2008 Activity Report*. 2008. p. 154-155.
16. Goodhew, P.J., F.J. Humphreys, and R. Beanland, *Electron Microscopy and Analysis*. 2001: Taylor & Francis.
17. Egerton, R.F., *Limits to the spatial, energy and momentum resolution of electron energy-loss spectroscopy.* Ultramicroscopy, 2007. **107**(8): p. 575-586.
18. Muller, D.A. and J. Silcox, *Delocalization in Inelastic-Scattering.* Ultramicroscopy, 1995. **59**(1-4): p. 195-213.
19. Pennycook, S.J., et al., *Materials advances through aberration-corrected electron microscopy.* Mrs Bulletin, 2006. **31**(1): p. 36-43.
20. Scherzer, O., *Über einige Fehler von Elektronenlinsen.* Zeitschrift für Physik 1936. **101**(9-10): p. 593-603
21. Egerton, R.F., H. Qian, and M. Malac, *Improving the energy resolution of X-ray and electron energy-loss spectra.* Micron, 2006. **37**(4): p. 310-315.
22. Freitag, B., et al., *Breaking the spherical and chromatic aberration barrier in transmission electron microscopy.* Ultramicroscopy, 2005. **102**(3): p. 209-214.
23. Haider, M., et al., *Electron microscopy image enhanced.* Nature, 1998. **392**(6678): p. 768-769.
24. [cited 08/2012]; Available from: http://www.er-c.org/centre/micfac/frames/titanp.htm.

25. Warwick, T., et al., *A scanning transmission x-ray microscope for materials science spectromicroscopy at the advanced light source.* Review of Scientific Instruments, 1998. **69**(8): p. 2964-2973.
26. Margaritondo, G., *Introduction to synchrotron radiation*. 1988: Oxford University Press.
27. Farge, Y. and P.J. Duke, *European synchrotron radiation facility - the scientific case*. 1979, Strasbourg: European Science Foundation.
28. Jacobsen, C., J. Kirz, and S. Williams, *Resolution in Soft-X-Ray Microscopes.* Ultramicroscopy, 1992. **47**(1-3): p. 55-79.
29. Hitchcock, A., *Chemical mapping with soft X-ray spectromicroscopy.* American Laboratory, 2001. **33**(16): p. 30-+.
30. Warwick, T., et al., *Soft x-ray spectromicroscopy development for materials science at the advanced light source.* Journal of Electron Spectroscopy and Related Phenomena, 1997. **84**(1-3): p. 85-98.
31. Kaznatcheev, K.V., et al., *Soft X-ray spectromicroscopy beamline at the CLS: Commissioning results.* Nuclear Instruments & Methods in Physics Research Section a-Accelerators Spectrometers Detectors and Associated Equipment, 2007. **582**(1): p. 96-99.
32. Kirz, J., et al., *Illumination for coherent soft X-ray applications: the new X1A beamline at the NSLS.* Journal of Synchrotron Radiation, 2000. **7**: p. 395-404.
33. Krause, M.O. and J.H. Oliver, *Natural Widths of Atomic K-Levels and L-Levels,K-Alpha X-Ray-Lines and Several Kll Auger Lines.* Journal of Physical and Chemical Reference Data, 1979. **8**(2): p. 329-338.
34. Gasiorowicz, S., *Quantum Physics*. 3 ed. 2003: John Wiley & Sons.
35. Meitzner, G., *Experimental aspects of X-ray absorption spectroscopy.* Catalysis Today, 1998. **39**(4): p. 281-291.
36. Su, D.S., et al., *High resolution EELS using monochromator and high performance spectrometer: comparison of V2O5 ELNES with NEXAFS and band structure calculations.* Micron, 2003. **34**(3-5): p. 235-238.
37. McComb, D.W., et al., *The use of XANES and ELNES for the characterisation of stabilised zirconia.* Electrically Based Microstructural Characterization Iii, 2002. **699**: p. 161-166.
38. Brydson, R., *A brief review of quantitative aspects of electron energy loss spectroscopy and imaging.* Materials Science and Technology, 2000. **16**(10): p. 1187-1198.
39. Suenaga, K., et al., *Element-selective single atom imaging.* Science, 2000. **290**(5500): p. 2280-+.
40. Acremann, Y., et al., *Time-resolved imaging of spin transfer switching: Beyond the macrospin concept.* Physical Review Letters, 2006. **96**(21).
41. Gainsforth, Z., et al., *Combined STEM/STXM Elemental Quantification for Cometary Particles.* Microscopy and Microanalysis, 2010. **16**(SupplementS2): p. 922-923.
42. Hitchcock, A.P., et al., *Improving Sensitivity in Soft X-ray STXM Using Low Energy X-ray Fluorescence.* Microscopy and Microanalysis, 2010. **16**(SupplementS2): p. 924-925.
43. Gloskovskii, A., et al., *Spectroscopic and microscopic study of vanadium oxide nanotubes.* Journal of Applied Physics, 2007. **101**(8).
44. Terrones, M., et al., *Novel nanoscale gas containers: encapsulation of N(2) in CN(x) nanotubes.* Chemical Communications, 2000(23): p. 2335-2336.
45. Zhou, J.G., et al., *Imaging Nitrogen in Individual Carbon Nanotubes.* Journal of Physical Chemistry Letters, 2010. **1**(11): p. 1709-1713.
46. Park, J., et al., *Release of N-2 from the carbon nanotubes via high-temperature annealing.* Journal of Physical Chemistry B, 2005. **109**(5): p. 1683-1688.
47. Gai, P.L., et al., *Atomic-resolution environmental transmission electron microscopy for probing gas-solid reactions in heterogeneous catalysis.* Mrs Bulletin, 2007. **32**(12): p. 1044-1050.

48. Janbroers, S., et al., *Insights into the nature of iron-based Fischer-Tropsch catalysts from quasi in situ TEM-EELS and XRD.* Journal of Catalysis, 2009. **268**(2): p. 235-242.
49. Topsøe, H., *Developments in operando studies and in situ characterization of heterogeneous catalysts.* Journal of Catalysis, 2003. **216**(1-2): p. 155-164.
50. Janbroers, S., et al., *A model study on the carburization process of iron-based Fischer-Tropsch catalysts using in situ TEM-EELS.* Applied Catalysis B-Environmental, 2011. **102**(3-4): p. 521-527.
51. de Groot, F.M.F., et al., *Nanoscale chemical imaging of a working catalyst by scanning transmission X-ray microscopy.* Nature, 2008. **456**(7219): p. 222-U39.
52. Creemer, J.F., et al., *Atomic-scale electron microscopy at ambient pressure.* Ultramicroscopy, 2008. **108**(9): p. 993-998.
53. Lawrence, J.R., et al., *Scanning transmission X-ray, laser scanning, and transmission electron microscopy mapping of the exopolymeric matrix of microbial biofilms.* Applied and Environmental Microbiology, 2003. **69**(9): p. 5543-5554.
54. Leapman, R.D. and S.Q. Sun, *Cryoelectron Energy-Loss Spectroscopy - Observations on Vitrified Hydrated Specimens and Radiation-Damage.* Ultramicroscopy, 1995. **59**(1-4): p. 71-79.
55. Dynes, J.J., et al., *Correlative Microscopy of Quantum Dot Labelled Biofilms*, in *CLS Activity Report 2005-2006*. 2006. p. 116-118.
56. Hunter, R.C., et al., *Mapping the Speciation of Iron in Pseudomonas aeruginosa Biofilms Using Scanning Transmission X-ray Microscopy.* Environmental Science & Technology, 2008. **42**(23): p. 8766-8772.
57. Braun, A., et al., *Advantages of soft X-ray absorption over TEM-EELS for solid carbon studies - a comparative study on diesel soot with EELS and NEXAFS.* Carbon, 2005. **43**(1): p. 117-124.
58. Alexander, D., et al., *The Real Carbon K-Edge.* Microscopy and Microanalysis, 14 (Suppl. 2), 2008: p. 674-675.
59. Rightor, E.G., et al., *Spectromicroscopy of poly(ethylene terephthalate): Comparison of spectra and radiation damage rates in x-ray absorption and electron energy loss.* Journal of Physical Chemistry B, 1997. **101**(11): p. 1950-1960.
60. Smith, B.W. and D.E. Luzzi, *Electron irradiation effects in single wall carbon nanotubes.* Journal of Applied Physics, 2001. **90**(7): p. 3509-3515.
61. Hitchcock, A.P., et al., *Quantitative Evaluation of Radiation Damage to Polyethylene Terephthalate by Soft X-rays and High-energy Electrons.* Journal of Physical Chemistry B, 2009. **113**(7): p. 1869-1876.
62. Porter, A.E., et al., *Visualizing the uptake of C-60 to the cytoplasm and nucleaus of human monocyte-derived macrophage cells using energy-filtered transmission electron microscopy and electron tomography.* Environmental Science & Technology, 2007. **41**(8): p. 3012-3017.
63. Goode, A.E., et al., *Correlating EELS spectrum imaging with x-ray microscopy*, in *EDGE 2009 Poster*. 2009.
64. Luzzi, D.E. and B.W. Smith, *Electron irradiation effects in single wall carbon nanotubes.* Journal of Applied Physics, 2001. **90**(7): p. 3509-3515.
65. Suenaga, K. and M. Koshino, *Atom-by-atom spectroscopy at graphene edge.* Nature, 2010. **468**(7327): p. 1088-1090.
66. van Schooneveld, M.M., et al., *Imaging and quantifying the morphology of an organic-inorganic nanoparticle at the sub-nanometre level.* Nature Nanotechnology, 2010. **5**(7): p. 538-544.
67. Hitchcock, A.P., et al., *Characterization of Single-Walled Carbon Nanotubes by Scanning Transmission X-ray Spectromicroscopy: Purification, Order and Dodecyl Functionalization.* Journal of the American Chemical Society, 2010. **132**(26): p. 9020-9029.
68. Shaffer, M.S.P., et al., *A versatile, solvent-free methodology for the functionalisation of carbon nanotubes.* Chemical Science, 2010. **1**(5): p. 603-608.

69. Najafi, E., et al., *Characterization of Single-Walled Carbon Nanotubes by Scanning Transmission X-ray Spectromicroscopy: Purification, Order and Dodecyl Functionalization.* Journal of the American Chemical Society, 2010. **132**(26): p. 9020-9029.
70. FEICompany, *Titan – Condenser manual*. 2004: Eindhoven.
71. Brydson, R., *Aberration-corrected Analytical Electron Microscopy*. RMS - Royal Microscopical Society. Vol. Volume 3. 2011: John Wiley & Sons.
72. Gatan, *ORIUS™ SC 1000 CCD Camera User's Guide*. 2006, Gatan, Inc.: Pleasanton, CA.
73. Mullejans, H. and J. Bruley, *Electron-Energy-Loss Spectroscopy (Eels) - Comparison with X-Ray-Analysis.* Journal De Physique Iv, 1993. **3**(C7): p. 2083-2092.
74. von Harrach, H.S., et al., *An integrated Silicon Drift Detector System for FEI Schottky Field Emission Transmission Electron Microscopes.* Microscopy and Microanalysis, 2009. **15**: p. 208-209.
75. McGuire, E., *Imaging Disease-related Protein Aggregates Inside Human Cells Using a Selenium Label*, in *Department of Materials*. 2011, Imperial College London.
76. Tiemeijer, P., *Monochromator Manual Titan*. 2008, FEI Company.
77. [cited Jan 2012]; Available from: http://www.gatan.com/analysis/gif_tridiem865.php.
78. Wiesemann, U., *The scanning transmission x-ray microscope at BESSY II.* 2003.
79. [cited Feb 2012]; Available from: http://xray1.physics.sunysb.edu/~micros/beamline/node8.html.
80. [cited 2012]; CLS beamline webpage]. Available from: http://exshare.lightsource.ca/sm/Pages/SM-Home.aspx.
81. Attwood, D.T., *Soft x-rays and extreme ultraviolet radiation*. 2000: Cambridge University Press.
82. Kirz, J., *Phase Zone Plates for X-Rays and Extreme Uv.* Journal of the Optical Society of America, 1974. **64**(3): p. 301-309.
83. Spector, S.J., C.J. Jacobsen, and D.M. Tennant, *Process optimization for production of sub-20 nm soft x-ray zone plates.* Journal of Vacuum Science & Technology B, 1997. **15**(6): p. 2872-2876.
84. Chao, W., *Demonstration of 12 nm resolution Fresnel zone plate lens based soft x-ray microscopy*. 2010.
85. Kiskinova, M., et al., *Imaging with spectroscopic micro-analysis using synchrotron radiation.* Analytical and Bioanalytical Chemistry, 2007. **389**(4): p. 1121-1132.
86. Hitchcock, A.P., et al., *Quantitative mapping of structured polymeric systems using singular value decomposition analysis of soft X-ray images.* Journal of Physical Chemistry B, 2002. **106**(21): p. 5358-5364.
87. Turchini, S., et al., *Soft-X-Ray Absorption-Spectroscopy in Transmission Mode - Ce M(4,5) Edges.* Journal of Electron Spectroscopy and Related Phenomena, 1995. **71**(1): p. 31-37.
88. Jacobsen, C., et al., *Soft x-ray spectroscopy from image sequences with sub-100 nm spatial resolution.* J Microsc, 2000. **197**(Pt 2): p. 173-84.
89. *aXis2000 is written in Interactive Data Language (IDL), and is available from http://unicorn.mcmaster.ca/aXis2000.html*.
90. Osanna, A. and C. Jacobsen, *Principal component analysis for soft X-ray spectromicroscopy.* X-Ray Microscopy, Proceedings, 2000. **507**: p. 350-357.
91. Koprinarov, I.N., et al., *Quantitative mapping of structured polymeric systems using singular value decomposition analysis of soft X-ray images.* Journal of Physical Chemistry B, 2002. **106**(21): p. 5358-5364.
92. Bosman, M., et al., *Mapping chemical and bonding information using multivariate analysis of electron energy-loss spectrum images.* Ultramicroscopy, 2006. **106**(11-12): p. 1024-1032.
93. Angelika, O. and J. Chris, *Principal component analysis for soft x-ray spectromicroscopy.* AIP Conference Proceedings, 2000. **507**(1): p. 350-357.

94. Baughman, R.H., A.A. Zakhidov, and W.A. de Heer, *Carbon nanotubes - the route toward applications.* Science, 2002. **297**(5582): p. 787-792.
95. Klingeler, R. and R.B. Sim, *Carbon Nanotubes for Biomedical Applications*. Carbon Nanostructures. 2011: Springer Berlin Heidelberg.
96. Bianco, A., K. Kostarelos, and M. Prato, *Applications of carbon nanotubes in drug delivery.* Current Opinion in Chemical Biology, 2005. **9**(6): p. 674-679.
97. Kostarelos, K., et al., *Cellular uptake of functionalized carbon nanotubes is independent of functional group and cell type.* Nature Nanotechnology, 2007. **2**(2): p. 108-113.
98. Wu, W., et al., *Targeted delivery of amphotericin B to cells by using functionalized carbon nanotubes.* Angewandte Chemie-International Edition, 2005. **44**(39): p. 6358-6362.
99. Heister, E., et al., *Triple functionalisation of single-walled carbon nanotubes with doxorubicin, a monoclonal antibody, and a fluorescent marker for targeted cancer therapy.* Carbon, 2009. **47**(9): p. 2152-2160.
100. Lam, C.W., et al., *A review of carbon nanotube toxicity and assessment of potential occupational and environmental health risks.* Crit Rev Toxicol, 2006. **36**(3): p. 189-217.
101. Xu, H.Y., et al., *Subcutaneous injection of water-soluble multi-walled carbon nanotubes in tumor-bearing mice boosts the host immune activity.* Nanotechnology, 2010. **21**(14).
102. Sato, Y., et al., *Influence of length on cytotoxicity of multi-walled carbon nanotubes against human acute monocytic leukemia cell line THP-I in vitro and subcutaneous tissue of rats in vivo.* Molecular Biosystems, 2005. **1**(2): p. 176-182.
103. Gambhir, S.S., et al., *A pilot toxicology study of single-walled carbon nanotubes in a small sample of mice.* Nature Nanotechnology, 2008. **3**(4): p. 216-221.
104. Mcclellan, R.O. and T.W. Hesterberg, *Role of Biopersistence in the Pathogenicity of Man-Made Fibers and Methods for Evaluating Biopersistence - a Summary of 2 Round-Table Discussions.* Environmental Health Perspectives, 1994. **102**: p. 277-283.
105. Oberdorster, G., *Determinants of the pathogenicity of man-made vitreous fibers (MMVF).* International Archives of Occupational and Environmental Health, 2000. **73**: p. S60-S68.
106. Shukla, A., M. Ramos-Nino, and B. Mossman, *Cell signaling and transcription factor activation by asbestos in lung injury and disease.* International Journal of Biochemistry & Cell Biology, 2003. **35**(8): p. 1198-1209.
107. [cited 10/2011]; macrophage diagram]. Available from: http://bio1152.nicerweb.com/Locked/media/ch43/phagocytosis.html.
108. Porter, A.E., et al., *Direct imaging of single-walled carbon nanotubes in cells.* Nature Nanotechnology, 2007. **2**(11): p. 713-717.
109. Cherukuri, P., et al., *Near-infrared fluorescence microscopy of single-walled carbon nanotubes in phagocytic cells.* Journal of the American Chemical Society, 2004. **126**(48): p. 15638-15639.
110. Jia, G., et al., *Cytotoxicity of carbon nanomaterials: Single-wall nanotube, multi-wall nanotube, and fullerene.* Environmental Science & Technology, 2005. **39**(5): p. 1378-1383.
111. Dumortier, H., et al., *Functionalized carbon nanotubes are non-cytotoxic and preserve the functionality of primary immune cells (vol 6, pg 1522, 2006).* Nano Letters, 2006. **6**(12): p. 3003-3003.
112. Kagan, V.E., et al., *Direct and indirect effects of single walled carbon nanotubes on RAW 264.7 macrophages: Role of iron.* Toxicology Letters, 2006. **165**(1): p. 88-100.
113. Shvedova, A.A., et al., *Inhalation vs. aspiration of single-walled carbon nanotubes in C57BL/6 mice: inflammation, fibrosis, oxidative stress, and mutagenesis.* American Journal of Physiology-Lung Cellular and Molecular Physiology, 2008. **295**(4): p. L552-L565.
114. Nerl, H.C., et al., *Imaging methods for determining uptake and toxicity of carbon nanotubes in vitro and in vivo.* Nanomedicine, 2011. **6**(5): p. 849-865.

115. Kunzmann, A., et al., *Toxicology of engineered nanomaterials: Focus on biocompatibility, biodistribution and biodegradation.* Biochimica Et Biophysica Acta-General Subjects, 2011. **1810**(3): p. 361-373.
116. Coleman, J.N., et al., *Quantitative evaluation of surfactant-stabilized single-walled carbon nanotubes: Dispersion quality and its correlation with zeta potential.* Journal of Physical Chemistry C, 2008. **112**(29): p. 10692-10699.
117. Hurt, R.H., X.Y. Liu, and A.B. Kane, *Biodurability of single-walled carbon nanotubes depends on surface functionalization.* Carbon, 2010. **48**(7): p. 1961-1969.
118. Bianco, A., et al., *Oxidative biodegradation of single- and multi-walled carbon nanotubes.* Nanoscale, 2011. **3**(3): p. 893-896.
119. Star, A., et al., *Biodegradation of Single-Walled Carbon Nanotubes through Enzymatic Catalysis.* Nano Letters, 2008. **8**(11): p. 3899-3903.
120. Zhao, Y., B.L. Allen, and A. Star, *Enzymatic Degradation of Multiwalled Carbon Nanotubes.* Journal of Physical Chemistry A, 2011. **115**(34): p. 9536-9544.
121. Allen, B.L., et al., *Mechanistic Investigations of Horseradish Peroxidase-Catalyzed Degradation of Single-Walled Carbon Nanotubes.* Journal of the American Chemical Society, 2009. **131**(47): p. 17194-17205.
122. Kagan, V.E., et al., *Carbon nanotubes degraded by neutrophil myeloperoxidase induce less pulmonary inflammation.* Nat Nanotechnol. **5**(5): p. 354-9.
123. Kateb, B., et al., *Internalization of MWCNTs by microglia: possible application in immunotherapy of brain tumors.* Neuroimage, 2007. **37 Suppl 1**: p. S9-17.
124. Porter, A.E., et al., *Uptake of Noncytotoxic Acid-Treated Single-Walled Carbon Nanotubes into the Cytoplasm of Human Macrophage Cells.* Acs Nano, 2009. **3**(6): p. 1485-1492.
125. Atkins, P.W. and J. de Paula, *Atkins' Physical Chemistry*. 8th Edition ed. 2006, Oxford: Oxford University Press.
126. Husain, S., *Site specific characterisation of hydrocracking catalysts using nanoanalytical electron microscopy*, in *Materials*. 2010, Imperial College London: London.
127. [cited 2011 2011]; MO to Band]. Available from: http://www.chembio.uoguelph.ca/educmat/chm729/band/concept.htm.
128. Stephan, O., et al., *Electron energy-loss spectroscopy on individual nanotubes.* Journal of Electron Spectroscopy and Related Phenomena, 2001. **114**: p. 209-217.
129. Li, S.P., et al., *Adsorption of carbon nanotubes on active carbon microparticles.* Carbon, 2008. **46**(7): p. 1091-1095.
130. Al-Jamal, K.T., et al., *Cellular uptake mechanisms of functionalised multi-walled carbon nanotubes by 3D electron tomography imaging.* Nanoscale, 2011. **3**(6): p. 2627-2635.
131. Stephan, O., et al., *Curvature-induced bonding changes in carbon nanotubes investigated by electron energy-loss spectrometry.* Physical Review B, 1996. **53**(20): p. 13824-13829.
132. Kuznetsova, A., et al., *Oxygen-containing functional groups on single-wall carbon nanotubes: NEXAFS and vibrational spectroscopic studies.* Journal of the American Chemical Society, 2001. **123**(43): p. 10699-10704.
133. Coleman, V.A., et al., *Defect formation in graphene nanosheets by acid treatment: an x-ray absorption spectroscopy and density functional theory study.* Journal of Physics D-Applied Physics, 2008. **41**(6).
134. Li, Z.R., et al., *Spectroscopic Characteristics of Differently Produced Single-Walled Carbon Nanotubes.* Chemphyschem, 2009. **10**(13): p. 2296-2304.
135. Solomon, D., et al., *Carbon (1s) NEXAFS Spectroscopy of Biogeochemically Relevant Reference Organic Compounds.* Soil Science Society of America Journal, 2009. **73**(6): p. 1817-1830.
136. Heymann, K., et al., *C 1s K-edge near edge X-ray absorption fine structure (NEXAFS) spectroscopy for characterizing functional group chemistry of black carbon.* Organic Geochemistry, 2011. **42**(9): p. 1055-1064.

137. Boese, J., et al., *Carbon edge XANES spectroscopy of amino acids and peptides.* Journal of Electron Spectroscopy and Related Phenomena, 1997. **85**(1-2): p. 9-15.
138. Solomon, D., et al., *Carbon (1s) NEXAFS Spectroscopy of Biogeochemically Relevant Reference Organic Compounds.* Soil Sci. Soc. Am. J., 2009. **73**(6): p. 1817-1830.
139. Georgakilas, V., et al., *Amino acid functionalisation of water soluble carbon nanotubes.* Chemical Communications, 2002(24): p. 3050-3051.
140. Boncel, S., et al., *Tunable chemistry and morphology of multi-wall carbon nanotubes as a route to non-toxic, theranostic systems.* Biomaterials, 2011. **32**(30): p. 7677-7686.
141. Al-Jamal, K., et al., *Imaging Plasma Membrane Translocation of Functionalised Multi-Walled Carbon Nanotubes by 3D Electron Tomography.* Nanoscale, 2011. **8**(3(6)): p. 2627-35.
142. Huang, W.J., et al., *Sonication-assisted functionalization and solubilization of carbon nanotubes.* Nano Letters, 2002. **2**(3): p. 231-234.
143. Egerton, R.F., P. Li, and M. Malac, *Radiation damage in the TEM and SEM.* Micron, 2004. **35**(6): p. 399-409.
144. Giordani, S., et al., *Debundling of single-walled nanotubes by dilution: Observation of large populations of individual nanotubes in amide solvent dispersions.* Journal of Physical Chemistry B, 2006. **110**(32): p. 15708-15718.
145. Liew, K.M., C.H. Wong, and M.J. Tan, *Tensile and compressive properties of carbon nanotube bundles.* Acta Materialia, 2006. **54**(1): p. 225-231.
146. Tan, P.H., et al., *Optical properties of nanotube bundles by photoluminescence excitation and absorption spectroscopy.* Physica E-Low-Dimensional Systems & Nanostructures, 2008. **40**(7): p. 2352-2359.
147. Kim, K., et al., *Characterization of oxygen containing functional groups on carbon materials with oxygen K-edge X-ray absorption near edge structure spectroscopy.* Carbon, 2011. **49**(5): p. 1745-1751.
148. Hernadi, K., et al., *Reactivity of different kinds of carbon during oxidative purification of catalytically prepared carbon nanotubes.* Solid State Ionics, 2001. **141**: p. 203-209.
149. Zhang, J., et al., *Effect of chemical oxidation on the structure of single-walled carbon nanotubes.* Journal of Physical Chemistry B, 2003. **107**(16): p. 3712-3718.
150. Rinzler, A.G., et al., *Large-scale purification of single-wall carbon nanotubes: process, product, and characterization.* Applied Physics a-Materials Science & Processing, 1998. **67**(1): p. 29-37.
151. Prato, M., K. Kostarelos, and A. Bianco, *Functionalized carbon nanotubes in drug design and discovery.* Accounts of Chemical Research, 2008. **41**(1): p. 60-68.
152. Jia, Z.J., et al., *Production of short multi-walled carbon nanotubes.* Carbon, 1999. **37**(6): p. 903-906.
153. Saito, T., K. Matsushige, and K. Tanaka, *Chemical treatment and modification of multi-walled carbon nanotubes.* Physica B-Condensed Matter, 2002. **323**(1-4): p. 280-283.
154. Forrest, G.A. and A.J. Alexander, *A model for the dependence of carbon nanotube length on acid oxidation time.* Journal of Physical Chemistry C, 2007. **111**(29): p. 10792-10798.
155. Furtado, C.A., et al., *Debundling and dissolution of single-walled carbon nanotubes in amide solvents.* Journal of the American Chemical Society, 2004. **126**(19): p. 6095-6105.
156. Wepasnick, K.A., et al., *Chemical and structural characterization of carbon nanotube surfaces.* Analytical and Bioanalytical Chemistry, 2010. **396**(3): p. 1003-1014.
157. McPhail, M.R., et al., *Charging Nanowalls: Adjusting the Carbon Nanotube Isoelectric Point via Surface Functionalization.* Journal of Physical Chemistry C, 2009. **113**(32): p. 14102-14109.
158. Verdejo, R., et al., *Removal of oxidation debris from multi-walled carbon nanotubes.* Chemical Communications, 2007(5): p. 513-515.
159. Boehm, H.P., *Surface oxides on carbon and their analysis: a critical assessment.* Carbon, 2002. **40**(2): p. 145-149.

160. Kundu, S., et al., *Thermal Stability and Reducibility of Oxygen-Containing Functional Groups on Multiwalled Carbon Nanotube Surfaces: A Quantitative High-Resolution XPS and TPD/TPR Study.* Journal of Physical Chemistry C, 2008. **112**(43): p. 16869-16878.
161. Martinez, M.T., et al., *Sensitivity of single wall carbon nanotubes to oxidative processing: structural modification, intercalation and functionalisation.* Carbon, 2003. **41**(12): p. 2247-2256.
162. Moulder, J.F., *Handbook of x-ray photoelectron spectroscopy*. 1992: Physical Electronics Division, Perkin-Elmer Corp.
163. Wepasnick, K.A., et al., *Surface and structural characterization of multi-walled carbon nanotubes following different oxidative treatments.* Carbon, 2011. **49**(1): p. 24-36.
164. Osswald, S., M. Havel, and Y. Gogotsi, *Monitoring oxidation of multiwalled carbon nanotubes by Raman spectroscopy.* Journal of Raman Spectroscopy, 2007. **38**(6): p. 728-736.
165. Graupner, R., *Raman spectroscopy of covalently functionalized single-wall carbon nanotubes.* Journal of Raman Spectroscopy, 2007. **38**(6): p. 673-683.
166. Liang, X., K. Ibrahim, and Z. Wu, *XANES study of multi-walled carbon nanotubes modified by HNO3 vapor.* Materials Letters, 2012. **72**: p. 131-133.
167. Zhong, J., et al., *A XANES characterization of structural defects in single-walled carbon nanotubes.* Radiation Physics and Chemistry, 2006. **75**(11): p. 1861-1865.
168. Hitchcock, A.P., et al., *Scanning Transmission X-ray Microscopy of Individual Multi-Walled Carbon Nanotubes: Linear Dichroism and Functionalization Chemistry.* Microsc Microanal, 2008. **14**((Suppl 2)).
169. Abbas, M., et al., *X-ray absorption and photoelectron spectroscopy studies on graphite and single-walled carbon nanotubes: Oxygen effect.* Applied Physics Letters, 2005. **87**(5).
170. Banerjee, S., T. Hemraj-Benny, and S.S. Wong, *Covalent surface chemistry of single-walled carbon nanotubes.* Advanced Materials, 2005. **17**(1): p. 17-29.
171. Menzel, R., et al., *A versatile, solvent-free methodology for the functionalisation of carbon nanotubes.* Chemical Science, 2010. **1**(5): p. 603-608.
172. Braun, A., et al., *Radiation damage from EELS and NEXAFS in diesel soot and diesel soot extracts.* Journal of Electron Spectroscopy and Related Phenomena, 2009. **170**(1-3): p. 42-48.
173. Daniels, H., et al., *Experimental and theoretical evidence for the magic angle in transmission electron energy loss spectroscopy.* Ultramicroscopy, 2003. **96**(3-4): p. 523-534.
174. McGilvery, C.M., et al., *Contamination of holey/lacey carbon films in STEM.* Micron, 2012. **43**(2-3): p. 450-455.
175. Nicholls, R.J., *Electron energy loss spectroscopy of fullerene materials* in *Mathematical,Physical & Life Sciences Division - Materials*. 2006, University of Oxford.
176. Tsang, S.C., P.J.F. Harris, and M.L.H. Green, *Thinning and Opening of Carbon Nanotubes by Oxidation Using Carbon-Dioxide.* Nature, 1993. **362**(6420): p. 520-522.
177. Srivastava, D., et al., *Predictions of enhanced chemical reactivity at regions of local conformational strain on carbon nanotubes: Kinky chemistry.* Journal of Physical Chemistry B, 1999. **103**(21): p. 4330-4337.
178. *Annual Report*. 2009, Australian Orthopaedic Association National Joint Replacement Registry.
179. *6th Annual Report*. 2009, National Joint registry for England and Wales.
180. Amstutz, H.C., et al., *Mechanism and clinical-significance of wear debris-induced osteolysis.* Clinical Orthopaedics and Related Research, 1992(276): p. 7-18.
181. Schmalzried, T.P., M. Jasty, and W.H. Harris, *Periprosthetic bone loss in total hip-arthroplasty - polyethylene wear debris and the concept of the effective joint space.* Journal of Bone and Joint Surgery-American Volume, 1992. **74A**(6): p. 849-863.
182. Cobb, A.G. and T.P. Schmalzreid, *The clinical significance of metal ion release from cobalt-chromium metal-on-metal hip joint arthroplasty.* Proceedings of the Institution of Mechanical Engineers Part H-Journal of Engineering in Medicine, 2006. **220**(H2): p. 385-398.

183. Brown, C., et al., *Characterisation of wear particles produced by metal on metal and ceramic on metal hip prostheses under standard and microseparation simulation.* Journal of Materials Science-Materials in Medicine, 2007. **18**(5): p. 819-827.
184. Ingham, E. and J. Fisher, *Biological reactions to wear debris in total joint replacement.* Proceedings of the Institution of Mechanical Engineers Part H-Journal of Engineering in Medicine, 2000. **214**(H1): p. 21-37.
185. Hart, A.J., et al., *The painful metal-on-metal hip resurfacing.* Journal of Bone and Joint Surgery-British Volume, 2009. **91B**(6): p. 738-744.
186. Willert, H.G., et al., *Metal-on-metal bearings and hypersensitivity in patients with artificial hip joints - A clinical and histomorphological study.* Journal of Bone and Joint Surgery-American Volume, 2005. **87A**(1): p. 28-36.
187. Milosev, I., et al., *Survivorship and retrieval analysis of Sikomet metal-on-metal total hip replacements at a mean of seven years.* Journal of Bone and Joint Surgery-American Volume, 2006. **88A**(6): p. 1173-1182.
188. Hart, A.J., et al., *Circulating levels of cobalt and chromium from metal-on-metal hip replacement are associated with CD8+ T-cell lymphopenia. (vol 91, pg 835, 2009).* Journal of Bone and Joint Surgery-British Volume, 2009. **91B**(12): p. 1641-1641.
189. Firkins, P.J., et al., *A novel low wearing differential hardness, ceramic-on-metal hip joint prosthesis.* Journal of Biomechanics, 2001. **34**(10): p. 1291-1298.
190. Tipper, J.L., et al., *Quantitative analysis of the wear and wear debris from low and high carbon content cobalt chrome alloys used in metal on metal total hip replacements.* Journal of Materials Science-Materials in Medicine, 1999. **10**(6): p. 353-362.
191. Germain, M.A., et al., *Comparison of the cytotoxicity of clinically relevant cobalt-chromium and alumina ceramic wear particles in vitro.* Biomaterials, 2003. **24**(3): p. 469-479.
192. Toms, A.P., et al., *MRI of early symptomatic metal-on-metal total hip arthroplasty: a retrospective review of radiological findings in 20 hips.* Clin Radiol, 2008. **63**(1): p. 49-58.
193. Witzleb, W.C., et al., *Neo-capsule tissue reactions in metal-on-metal hip arthroplasty.* Acta Orthop, 2007. **78**(2): p. 211-20.
194. Doorn, P.F., et al., *Metal wear particle characterization from metal on metal total hip replacements: Transmission electron microscopy study of periprosthetic tissues and isolated particles.* Journal of Biomedical Materials Research, 1998. **42**(1): p. 103-111.
195. Catelas, I., et al., *Effects of digestion protocols on the isolation and characterization of metal-metal wear particles. I. Analysis of particle size and shape.* Journal of Biomedical Materials Research, 2001. **55**(3): p. 320-329.
196. Busse, B., et al., *Allocation of nonbirefringent wear debris: Darkfield illumination associated with PIXE microanalysis reveals cobalt deposition in mineralized bone matrix adjacent to CoCr implants.* Journal of Biomedical Materials Research Part A, 2008. **87A**(2): p. 536-545.
197. Shahgaldi, B.F., et al., *In-vivo corrosion of cobalt-chromium and titanium wear particles.* Journal of Bone and Joint Surgery-British Volume, 1995. **77B**(6): p. 962-966.
198. Vendittoli, P.A., et al., *Chromium and cobalt ion release following the Durom high carbon content, forged metal-on-metal surface replacement of the hip.* Journal of Bone and Joint Surgery-British Volume, 2007. **89B**(4): p. 441-448.
199. Bhabra, G., et al., *Nanoparticles can cause DNA damage across a cellular barrier.* Nat Nanotechnol, 2009. **4**(12): p. 876-83.
200. Hart, A.J., et al., *The chemical form of metallic debris in tissues surrounding metal-on-metal hips with unexplained failure.* Acta Biomaterialia, 2010. **6**(11): p. 4439-4446.
201. Vanderlaan, G. and I.W. Kirkman, *The 2p Absorption-Spectra of 3d Transition-Metal Compounds in Tetrahedral and Octahedral Symmetry.* Journal of Physics-Condensed Matter, 1992. **4**(16): p. 4189-4204.
202. Pennycook, S.J. and N. P.D., *Scanning Transmission Electron Microscopy: Imaging and Analysis*. 2011: Springer.

203. de Groot, F. and A. Kotani, *Core level spectroscopy of solids*. Advances in condensed matter science, ed. D.D. Sarma, G. Kotliar, and Y. Tokura. 2008: CRC press.
204. [cited; Available from: http://chemed.chem.purdue.edu/genchem/topicreview/bp/ch12/crystal.php.
205. Rasband, W.S., *ImageJ*. 1997-2012: U. S. National Institutes of Health, Bethesda, Maryland, USA, .
206. *EELS Analysis User's Guide*, Gatan, Inc.
207. Morales, F., et al., *In situ x-ray absorption of Co/Mn/TiO2 catalysts for Fischer-Tropsch synthesis.* Journal of Physical Chemistry B, 2004. **108**(41): p. 16201-16207.
208. Campbell, P., et al., *Histological Features of Pseudotumor-like Tissues From Metal-on-Metal Hips.* Clinical Orthopaedics and Related Research, 2010. **468**(9): p. 2321-2327.
209. Chang, R., *Chemistry*. 6th Edition ed. 1998, Boston, Mass. : McGraw-Hill.
210. Papageorgiou, I., et al., *The effect of nano- and micron-sized particles of cobalt-chromium alloy on human fibroblasts in vitro.* Biomaterials, 2007. **28**(19): p. 2946-2958.
211. [cited 01/2012]; Available from: http://bionumbers.hms.harvard.edu/bionumber.aspx?&id=103566&ver=4.
212. Hardwick, S.J., *Apoptosis in human monocyte-macrophages exposed to oxidized low density lipoprotein (vol 179, pg 294, 1996).* Journal of Pathology, 1996. **180**(1): p. 114-114.
213. Akao, M., et al., *Mechanistically distinct steps in the mitochondrial death pathway triggered by oxidative stress in cardiac myocytes.* Circ Res, 2003. **92**(2): p. 186-94.
214. Soriano, L., et al., *Chemical-Analysis of Passivated and Oxidized Layers on Fecr and Feti Alloys by Soft-X-Ray Absorption-Spectroscopy.* Surface and Interface Analysis, 1993. **20**(1): p. 21-26.
215. Daulton, T.L. and B.J. Little, *Determination of chromium valence over the range Cr(0)-Cr(VI) by electron energy loss spectroscopy.* Ultramicroscopy, 2006. **106**(7): p. 561-573.
216. Obst, M., J.A. Wang, and A.P. Hitchcock, *3-d chemical imaging with STXM tomography.* 9th International Conference on X-Ray Microscopy, 2009. **186**.
217. Jarausch, K., et al., *Four-dimensional STEM-EELS: Enabling nano-scale chemical tomography.* Ultramicroscopy, 2009. **109**(4): p. 326-337.
218. Davda, K., et al., *An analysis of metal ion levels in the joint fluid of symptomatic patients with metal-onmetal hip replacements.* Journal of Bone and Joint Surgery-British Volume, 2011. **93B**(6): p. 738-745.
219. Daulton, T.L., et al., *Electron energy loss spectroscopy techniques for the study of microbial chromium(VI) reduction.* Journal of Microbiological Methods, 2002. **50**(1): p. 39-54.
220. Gillot, I., et al., *Quantitative X-Ray-Microanalysis of Calcium in Sea-Urchin Eggs after Quick-Freezing and Freeze-Substitution - Validity of the Method.* Histochemistry, 1989. **92**(6): p. 523-529.
221. Kagan, V.E., et al., *Carbon nanotubes degraded by neutrophil myeloperoxidase induce less pulmonary inflammation.* Nature Nanotechnology, 2010. **5**(5): p. 354-359.
222. Johnston, H.J., et al., *A critical review of the biological mechanisms underlying the in vivo and in vitro toxicity of carbon nanotubes: The contribution of physico-chemical characteristics.* Nanotoxicology, 2010. **4**(2): p. 207-246.
223. Pantarotto, D., et al., *Synthesis, structural characterization, and immunological properties of carbon nanotubes functionalized with peptides.* Journal of the American Chemical Society, 2003. **125**(20): p. 6160-6164.
224. Stark, H., F. Zemlin, and C. Boettcher, *Electron radiation damage to protein crystals of bacteriorhodopsin at different temperatures.* Ultramicroscopy, 1996. **63**(2): p. 75-79.